NOVEL SEMICONDUCTOR BASED LIGHT SOURCES

Andrew Douglas McRobbie

**A Thesis Submitted for the Degree of PhD
at the
University of St. Andrews**

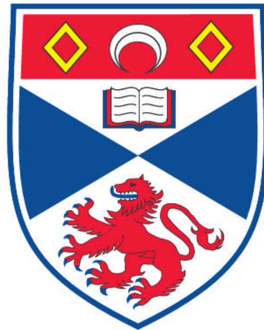

2008

**Full metadata for this item is available in the St Andrews
Digital Research Repository
at:
https://research-repository.st-andrews.ac.uk/**

**Please use this identifier to cite or link to this item:
http://hdl.handle.net/10023/565**

This item is protected by original copyright

**This item is licensed under a
Creative Commons License**

Novel semiconductor based light sources

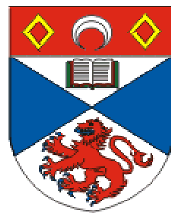

Thesis presented for the degree of Doctor of Philosophy

to the University of St Andrews

by

Andrew Douglas McRobbie

School of Physics and Astronomy

University of St Andrews

May 2008

Declarations

I, Andrew Douglas McRobbie, hereby certify that this thesis, which is approximately fifty thousand words in length, has been written by me, that it is the record of work carried out by me and that it has not been submitted in any previous application for a higher degree.

Date   Signature of candidate

I was admitted as a research student and as a candidate for the degree of Doctor of Philosophy in October, 2004; the higher study for which this is a record was carried out in the University of St Andrews between 2004 and 2008.

Date   Signature of candidate

In submitting this thesis to the University of St Andrews I understand that I am giving permission for it to be made available for use in accordance with the regulations of the University Library for the time being in force, subject to any copyright vested in the work not being affected thereby. I also understand that the title and abstract will be published, and that a copy of the work may be made and supplied to any bona fide library or research worker, that my thesis will be electronically accessible for personal or research use, and that the library has the right to migrate my thesis into new electronic forms as required to ensure continued access to the thesis. I have obtained any third-party copyright permissions that may be required in order to allow such access and migration.

Date   Signature of candidate

I hereby certify that the candidate has fulfilled the conditions of the Resolution and Regulations appropriate for the degree of Doctor of Philosophy in the University of St Andrews and that the candidate is qualified to submit this thesis in application for that degree.

Date   Signature of supervisor

for

Annie

Abstract

The research described in this thesis relates to the design, fabrication and testing of novel semiconductor-based light sources that have been designed for the generation of infra-red light. The thesis is formatted to account for two distinct components of my work, where the first part concerns sources producing coherent light by direct laser emission, notably, ultrashort-pulse quantum-dot lasers. These types of lasers continue to show considerable promise as efficient, compact sources of ultrashort pulses with durations of hundreds of femtoseconds, while giving rise to unique and interesting electronic properties such as low lasing thresholds through the quantum nature of their density of states.

At the outset a study of the most relevant aspects of the lasing dynamics of an optically pumped quantum-dot laser is outlined. Pumping of the device with intense discrete optical pulses leads to output from multiple electronic states, each having a characteristic wavelength and temporal properties. I show that pulses produced by excited-state emission have shorter durations (24 ps) and arrive earlier in time than those due to transitions from the ground state, which themselves have durations of around 180 ps. Investigations are then made on two different mode-locked quantum-dot laser systems. One is an all-quantum-dot external-cavity laser that is mode locked using a quantum-dot SESAM device at a repetition frequency of 860 MHz with output power approaching 20 mW. This is followed by a study of a monolithic two-section quantum-dot laser that is mode locked stably in a wide temperature range of 20°C to 70°C. The excellent performance characteristics presented serve to demonstrate both the versatility of quantum-dot material as components in mode-locked laser systems and the temperature stability of such laser devices.

The second part of the thesis relates to structures that are designed to take advantage of nonlinear frequency conversion in GaAs-based semiconductors. This material system possesses a nonlinear coefficient of ~170 pm/V and is transparent from around 0.9 μm through to 17 μm, making it attractive for the realisation of a new class of efficient, integrable, quasi-phase-matched, optical parametric oscillator devices. Initially, ion implantation is utilised as a vector to create a periodically-switched nonlinear ridge waveguided device. The observation is made that in the course of implantation the transmissive properties of the device are severely degraded.

Unfortunately, the high losses incurred, which reached 250 dB/cm, could not be removed without also destroying the modulation in nonlinearity.

During the course of this investigation, significant technological advances were made on the production of orientation-patterned GaAs structures. By recognising the elegance and potential of this new orientation-patterned (OP) methodology, a study of its implications and applicability in the context of my project is initiated.

Table of Contents

Declerations II

Abstract IV

Contents VI

List of Publications XI

Acknowledgements XIV

1 Introduction 1

1.1. Background 1
1.1.1 Optoelectronic sources 2

1.2 Direct laser emission – Ultrashort-pulse mode-locked quantum-dot lasers 4
1.2.1 Uses of Ultrashort-pulse quantum-dot lasers 4
1.2.2 Mode-locked lasers 8

1.3 State-of-the-art ultrashort-pulse lasers 10

1.4 Quantum-dot ultrashort-pulse semiconductor lasers 12

1.5 Nonlinear properties of semiconductor material 15
1.5.1 Uses of nonlinear frequency conversion 16

1.6 Semiconductor materials for nonlinear optics 18

1.7 State-of-the-art nonlinear frequency conversion in semiconductors 19

1.8 Work contained in this thesis on nonlinear optical frequency conversion 24

1.9 Thesis overview 25

References 26

2 Underpinning theory of ultrashort-pulse quantum-dot lasers 32

2.1 Laser Pulses 32
2.1.1 Mathematical description of an optical pulse 33
2.1.2 Linear pulse propagation 34
2.1.3 Nonlinear pulse propagation 36

2.1.4 Self phase modulation in semiconductor lasers 36
2.1.5 Dispersion compensation 38

2.2 Methods of obtaining ultrashort-pulse operation in lasers 40
2.2.1 Gain switching 40
2.2.2 Q-switching 41
2.2.3 Mode locking 42

2.3 Mode locking techniques in quantum-dot lasers 44
2.3.1 Passive mode locking 45
2.3.2 Semiconductor saturable absorber mirrors and saturable Bragg reflectors 46
2.3.3 Important SESAM parameters for successful mode locking 47
2.3.4 Ideal SESAM parameters for a semiconductor laser 51

2.4 Ultrashort-pulse measurement 52
2.4.1 The two-photon autocorrelator 52

2.5 Conclusions 55

References 56

3 Fabrication 58

3.1 Molecular beam epitaxy 58

3.2 Photolithography 60

3.3 Chemically-assisted Ion-beam etching 64

3.4 Ion Implantation 71

3.5 Analytical tools 73

3.6 Concluding remarks 75

References 76

4 Properties of quantum-dot materials 77

4.1 Background Semiconductor Physics 77
4.1.1 The p-n junction 78
4.1.2 Recombination 80

4.2 Semiconductor Diode Lasers 80

4.3 Quantum Confinement **81**
4.3.1 Additional Quantum Confinement – Dots 82
4.3.2 Self-organised Growth (Stranski-Krastanow [S-K]) 84

4.4 Investigation of the Transition Dynamics of Quantum-dot Material **86**
4.4.1 Motivation 86
4.4.2 Sample Growth 88
4.4.3 Experimental Assessment 89

4.5 Results **91**

4.6 Future work and conclusions **99**

References **101**

5 All-quantum-dot, External-cavity, mode-locked laser 104

5.1 Introduction **104**

5.2 Motivation **105**
5.2.1 Advantages of external-cavity configurations 105

5.3 The Quantum-dot SESAM **109**

5.4 Material Description **112**

5.5 Experimental setup **114**

5.6 Results **116**

5.7 Additional work on quantum-dot lasers **130**

5.8 Conclusions and future work **133**

References **136**

6 Nonlinear Frequency Conversion Theory 139

6.1 Polarisation **139**

6.2 Nonlinear Polarisation Response **140**

6.3 The Coupled-wave Equations **141**

6.3.1 Solving the Coupled-wave Equations for Second Harmonic generation 143
6.3.2 Solving the Coupled-wave Equations for the Case of Difference-frequency Generation 144

6.4 The Manley-Rowe Relations **145**

6.5 Phase Matching **146**
6.5.1 Refractive-index Dependence on Wavelength 147
6.5.2 Birefringent Phase Matching 149
6.5.3 Quasi-phase Matching (QPM) 151

6.6 Optical Parametric Oscillation **154**

6.9 Conclusions **156**

References **157**

7 Nonlinear Frequency Conversion Experimental 158

7.1 PSN Concept **158**

7.2 Ion implantation for destruction of nonlinear coefficient **161**

7.3 Design and Calculations **162**
7.3.1 Ion implantation calculations 163
7.3.2 Phase matching calculations 164

7.4 Sample Preparation **166**

7.5 Linear-loss experimental setup and technique **168**
7.5.1 Fourier analysis loss method 170

7.6 Ion Implantation and Thermal Annealing **175**

7.7 Assessment of nonlinear optical properties **177**

7.8 Orientation-patterned GaAs **180**
7.8.1 Sample Preparation 181
7.8.2 Sample Preparation 2 184

7.9 Conclusions and Future Work **187**

References **190**

8 Summary and outlook 192

8.1 Mode-locked quantum-dot lasers 192
8.2 Nonlinear Frequency Conversion 195

References 198

Appendix A 200

List of Publications

Recent publications

Self-sustained pulsation in the oxide-confined vertical-cavity surface-emitting lasers based on submonolayer InGaAs quantum dots

Kuzmenkov, A. G. Ustinov, V. M. Sokolovskii, G. S. Maleev, N. A. Blokhin, S. A. Deryagin, A. G. Chumak, S. V. Shulenkov, A. S. Mikhrin, S. S. Kovsh, A. R. McRobbie, A. D. Sibbett, W. Cataluna, M. A., Rafailov, E. U.

Appl Phys Lett Vol 91,12, 121106 (2007)

High power all-quantum-dot based external cavity mode-locked laser
A. D. McRobbie, M. A. Cataluna, S.A. Zolotovskaya, D.A. Livshits, W. Sibbett, E.U. Rafailov
IEE Electronics Letters, Vol. 43(15), p812-813 (2007).

Stable modelocked operation up to 80°C from an InGaAs quantum-dot laser
E. U. Rafailov, M. A. Cataluna, A. D. McRobbie, W. Sibbett, D. A. Livshits and A.R. Kovsh
IEEE Photonic Technology Letters, Vol. 18(14), p1500-1502 (2006).

Investigation of transition dynamics in a quantum-dot laser optically pumped by femtosecond pulses
E. U. Rafailov, A. D. McRobbie, M. A. Cataluna, L. O'Faolain, W. Sibbett and D. A. Livshits
Cover image for Applied Physics Letters 23 Jan 2006 and featured article
Appl. Phys. Lett. Vol. 88, 041101 (2006).

This paper was also selected to be published on:

Virtual Journal of Nanoscale Science & Technology, 13, issue 5 (2006) and

Virtual Journal of Ultrafast Science, 5, issue 2 (2006).

Recent conference and poster presentations

Self-starting femtosecond Cr4+:YAG laser mode locked with a GaInNAs saturable Bragg reflector
C. G. Leburn, A. D. McRobbie, A. A. Lagatsky, S. Calvez, D. Burns, C. T. A. Brown, H. D. Sun, J. A. Gupta, G. C. Aers, M. D. Dawson and W. Sibbett
Advanced Solid-State Photonics (ASSP), Vancouver, Canada (2007)

Self-sustained pulsation and signal peaking in the oxide-confined VCSELs based on submonolayer InGaAs quantum dots
G.S.Sokolovskii, N.A.Maleev, A.G.Kuzmenkov, S.A.Blokhin, A.D.McRobbie, M.A.Cataluna, A.G.Deryagin, S.V.Chumak, .S.Shulenkov, S.S.Mikhrin, A.R.Kovsh, V.I.Kuchinskii, V.M.Ustinov, W.Sibbett, E.U.Rafailov
CLEO/Europe 2007, Munich, Germany, CB7-6-WED, 2007.

All-quantum-dot based external cavity mode locked laser
McRobbie, A.D., M.A. Cataluna, S.A. Zolotovskaya, D.A. Livshits, W. Sibbett, and E.U. Rafailov
SIOE'07. Cardiff, UK. (2007)

High power all-quantum-dot based external cavity mode-locked laser
A. D. McRobbie, M. A. Cataluna , S. A. Zolotovskaya, D. A. Livshits, W. Sibbett, E.U.Rafailov
LEOS annual meeting, Montreal, Canada, Th J4 (2006)

Low-loss GaInNAs saturable Bragg reflector for femtosecond mode locking of a Cr4+:YAG laser
C.G. Leburn, A.D. McRobbie, A.A. Lagatsky, C.T.A. Brown, W. Sibbett,
QEP 17/Photon 06,LTE7 16:15, Manchester, UK, 2006

New mode locking regime in a quantum-dot laser: enhancement by simultaneous cw excited-state emission
M. A. Cataluna, A. D. McRobbie, W. Sibbett, D. A. Livshits, A. R. Kovsh and E. U. Rafailov
CLEO 2006, Paper CThH3, Long Beach, USA (2006).

Investigation of Transition Dynamics in a Quantum dot laser optically pumped by femtosecond pulses
E. U. Rafailov, A. D. McRobbie, L. O'Faolain, M. A. Cataluna, W. Sibbett and D. A. Livshits
European Network of Excellence on Photonic Integrated Components and Circuits, Pontresina, Switzerland (2006)

Femtosecond semiconductor quantum-dot lasers
M. A. Cataluna, E. U. Rafailov, A. D. McRobbie, W. Sibbett, ,D. A. Livshits, and A. R. Kovsh
Ultrafast Photonics Collaboration Meeting, Glasgow, (2006).

Investigation of Transition Dynamics in a Quantum dot laser optically pumped by femtosecond pulses
E. U. Rafailov, A. D. McRobbie, L. O'Faolain, M. A. Cataluna, W. Sibbett and D. A. Livshits
LEOS Annual Meeting, Sydney, Australia ThN4 (2005)

Ground and excited-state modelocking in a two-section quantum-dot laser
M. A. Cataluna, E. U. Rafailov, A. D. McRobbie, W. Sibbett, D. A. Livshits, and A. R. Kovsh
LEOS 2005, Sydney, Australia, ThS2 (2005).

Design parameters of periodically-switched nonlinear structures for efficient nonlinear process
Edik U. Rafailov, A. D. McRobbie, Wilson Sibbett, David Artigas and Pablo Loza-Alvarez
OSA Trends in Optics and Photonics Series, Advanced Solid-State Photonics, I. Sorokina Ed., 98, p86-91, 2005.

Acknowledgements

I have enjoyed my PhD studies immensely. During their course, I have had the opportunity to interact with some fantastic people who have made the experience as a whole, one of the most fulfilling.

First and foremost I am extremely indebted to my supervisors Prof Thomas Krauss and Prof Wilson Sibbett for giving me the opportunity to be part of their respective research groups. Their enormous experience and intellect have been a constant restorative force for me, ensuring that I move in a forwards direction at all times. Secondly, my most sincere gratitude is reserved for Dr Edik Rafailov, now affiliated with Dundee University. His deep knowledge of the particular details of my project, enthusiasm and practical skills were of great use on countless occasions.

Throughout my studies, I have been fortunate to be surrounded by extremely learned postdoctoral researchers and academic staff who have always surprised and delighted me with their patience and eagerness to share the benefit of their bountiful experience. For this reason I am very grateful to (in no particular order) Dr Alexander Lagatsky, Dr Liam O'Faolain, Dr Tom Brown, Dr Christopher Leburn, Dr Maria Ana Cataluna, Dr Ben Agate and Dr Arvydas Ruseckas.

Throughout the course of my PhD I have been in the constant debt of the technical staff of the School of Physics and Astronomy. I am particularly grateful for the talents of Mr George Robb and Mr Stevie Balfour whose ability to fix almost anything ensured the smooth running of the cleanroom facility which was essential to the day to day activities of my project.

I am also indebted to the skilled researchers with whom I was fortunate enough to collaborate, particularly Dr Nianhua Peng of the University of Surrey who assisted with the ion implantation work; Dr John Roberts at the National III-V semiconductor facility in Sheffield who helped with various aspects of my project and Dr Alexey Zhukov at the Ioffe institute who provided access to an excellent epitaxial growth facility.

Special thanks must also go to the members of both the microphotonics and ultrashort pulsed-laser research groups for their friendship, advice, empathy and good humour.

On a personal level, I am very grateful to my parents and extended family for their unwavering support and advice over the last three and a half years. My Mum and Dad have been endlessly compassionate and for this I will be eternally thankful.

My final and most sincere thanks go to my wife Annie, for being the counterpoint to my odd personality and for supporting me in all my endeavours. She has been my closest confidante throughout my PhD and the writing of this thesis, sharing the moments of joy and counselling me - injecting her perspective and realism into moments of despair. Her ‘gentle’ pushes towards the computer have allowed me to reach the conclusion of this PhD with all of my mental faculties intact. And so, with all my love, I dedicate this, the last thesis I will *ever* write, to Annie and the future we share.

Chapter 1 Introduction

1.1 Background

An impressive amount of optoelectronic devices are in use in the modern world. The fact that they are ubiquitous bears strong testimony to both their versatility and reliability. It is because of these virtuous qualities that mankind and equipment based on optoelectronic technology have become inexorably linked. Indeed, to compile a list of instruments, used even in a domestic capacity, that contain optoelectronic-based components would be an exhaustive, lengthy process. From somewhat trivial applications such as the light emitting diodes used in household appliances through laser diodes used in CD players to globe-spanning pieces of technology such as the internet, optoelectronic devices contribute to the lives of people in many ways each and every day.

Optoelectronics is defined as the basic physics of light and matter and their interactions [1], whether in a specific device or in a more general context. A large amount of study in the last 50 years or so has led to an explosion in this field with significant milestones being the development of the p-n junction [2], the laser [3] and more recently the growth of fibre optic communications and biophotonics.

The research undertaken in this project is a continuation of earlier work done in the Microphotonics and Ultrashort-Pulse Laser research groups at the University of St Andrews. The Microphotonics group is concerned with the fabrication of structures on scales ranging from several nanometres to several micrometres. These structures are applied in areas such as photonic crystal research and biophotonics. The Ultrashort-Pulse Laser research group is involved in the development and characterisation of mode-locked laser systems that operate over a wide spectral range. These lasers are often developed with telecommunications or time-resolved spectroscopic applications in mind.

1.1.1 Optoelectronic sources

The application and further development of modern technology requires many different light sources that exhibit various properties. Applications as diverse as remote sensing, medical research and telecommunications have rather different requirements, so the light sources used in these different areas should accommodate these requirements via differing characteristics. In spectroscopic applications, the high degree of spectral purity inherent to a narrow linewidth source is a necessary feature [4]; the operating wavelength is also of great importance depending on the absorption or scattering properties of the sample to be analysed.

In the case of the lasers used in commercial CD players, small size, efficiency, reliability and low manufacturing costs are the key factors. This of course is why semiconductor diode lasers are so well suited to this particular application. Hence, if we consider the myriad of possible characteristics that sources should exhibit, it is not surprising that there exists a plethora of research into sources throughout the electromagnetic spectrum. Figure 1.1 shows a green laser pointer device which is an example of a compact optoelectronic product combining much of the physics pertinent to my project. This device has ferroelectric crystals at its core whereas my project specifically exploits semiconductor media as a base material.

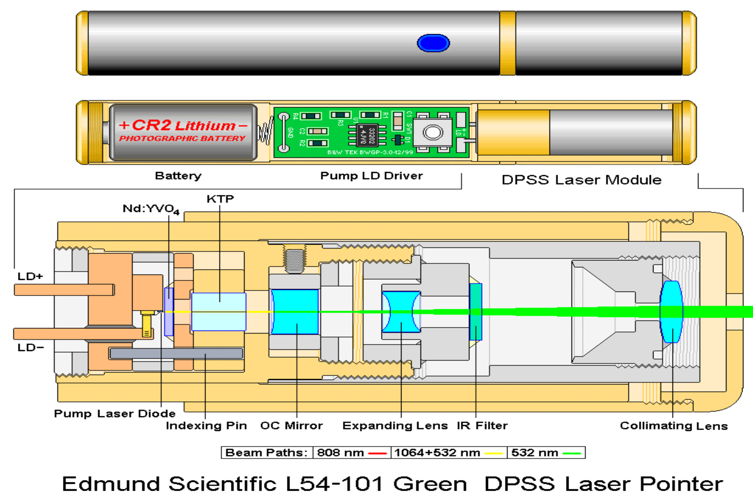

Figure 1.1. Green laser pointer consisting of a frequency doubled diode-pumped solid state laser and nonlinear crystal. Image taken from http://www.repairfaq.org/sam/laserdio.htm

This thesis comprises two main parts; the first half concerns ultrashort-pulse semiconductor lasers where I studied the fundamental physics of compact, low-threshold quantum-dot semiconductor material and its utilisation as a gain material in a mode-locked laser configuration. Study of the fundamental material properties was performed by the investigation of the transition dynamics of an optically pumped quantum-dot (QD) laser. The unique three-dimensional carrier confinement in quantum-dot material, produces discrete electronic states with distinct spectral and temporal characteristics. This knowledge is then applied to two mode-locked QD laser systems. In quantum-dot material, broad gain bandwidths and ultrafast carrier dynamics allow the generation of ultrashort pulses. I managed to show that in a quantum-dot laser, lasing transitions from different electronic states happen on different timescales. I then demonstrated mode-locked operation from an all-quantum-dot external cavity laser. In a separate investigation, I showed stable mode locking over a wide operating temperature range in a monolithic QD laser.

The second part of my thesis concerns the use of the nonlinear χ^2 properties of semiconductor material. Novel GaAs-based quasi-phase-matched structures were designed, manufactured and tested. The use of semiconductor material for this application type paves the way for a new class of low threshold waveguide based optical parametric oscillator (OPO) system operating in the infra-red region of the spectrum. Here I investigated a system based on periodic switching of χ^2 and another based on orientation-patterning.

Integration of a quantum-dot pump source with a semiconductor frequency conversion structure could result in a very compact, highly efficient device which would be a milestone in the development of mid-infra-red sources. While the fabrication of an entirely monolithic device is perhaps beyond what can be currently achieved with semiconductor processing, other, less demanding integration schemes are possible (for example a pump source could be butt-coupled to a nonlinear waveguide structure). Before this can be done, it is important to understand the physics of the individual components allowing optimisation of their performance.

1.2 Direct laser emission – Ultrashort-pulse mode-locked quantum-dot lasers

Semiconductors are excellent candidates as laser gain materials, capable of producing light over a large range of wavelengths depending on which of the many possible material configurations are implemented. These range from sub-400 nm wavelength emission for GaN-based devices to the mid-and far infrared for quantum cascade devices. In comparison with other laser materials, semiconductor lasers are typically several orders of magnitude smaller and are mainly monolithic electrically-pumped devices. It is these types of lasers, operated in pulse regimes around 1.3 microns that were investigated as part of this work. The gain material is based on self-assembled quantum dots.

1.2.1 Uses of ultrashort-pulse quantum-dot lasers

Optical communications

Since the 1990s, optical technology has become increasingly important in the areas of telecommunications and more recently in data communications due to the tremendous growth enjoyed in this area over the last ten years or so. Modern systems incorporate lasers that are used to transmit pulses of light through optical fibres in preference to conducting electrical signals in copper wire. The use of light as a transmission vector allows for faster transmission speeds due to the bosonic nature of photons. These pulses are encoded in a digital pattern which is used to represent bits of data.

Wavelength division multiplexing (WDM) involves combining several signals at different wavelengths into one amalgamated signal for sending. This signal is then broken apart into its constituent signals at the receiving end and each segment decoded in turn. WDM allows the sender to transmit the information at a far higher rate than is possible with a single bit stream since in theory, the maximum rate obtainable from a multiplexed system will be equal to the maximum single channel rate multiplied by the number of channels. Here, the inhomogeneously broadened

emission bandwidth of QD lasers could be exploited to allow multiplexed channels of data comprised of many different bit streams [5].

An alternative scheme operating in the time domain is referred to as optical time division multiplexing (OTDM). In this scheme, several lower repetition frequency signals are joined together by the use of variable delay lines, again to form a composite signal containing all the information of the others. This can then be transmitted as a single very high repetition frequency signal using the one transmission line and then split up back into its constituent parent signals after receiving. Quantum-dot lasers could be particularly well suited to this application because their inherent short cavity length allows them to be incorporated in high repetition-rate schemes. Low jitter is also an advantage here as it allows improved bit error rates.

These endeavours are undertaken in order to improve the amount of data that can be transmitted with an optical fibre. A large volume of work has been done on developing wide emission bandwidth laser sources operating in telecoms windows of 1.3 μm and 1.5 μm. Silica optical fibres have low loss and low dispersion at these wavelengths, sources were therefore developed to capitalise on this. As we see below in figure 1.2, the optical fibre exhibits its lowest propagation losses at around 1.5 microns. At 1.3 microns the fibre exhibits zero dispersion, a criterion ensuring that pulses of light propagating down the fibre undergo minimal broadening in the temporal domain. A specific advantage of QD lasers at 1.3 μm is that unlike quantum-well (QW) lasers, they can be grown in GaAs as opposed to InP, avoiding the problem of Auger recombination [6]. An additional advantage of diode lasers in this area is their inherent simplicity and robustness.

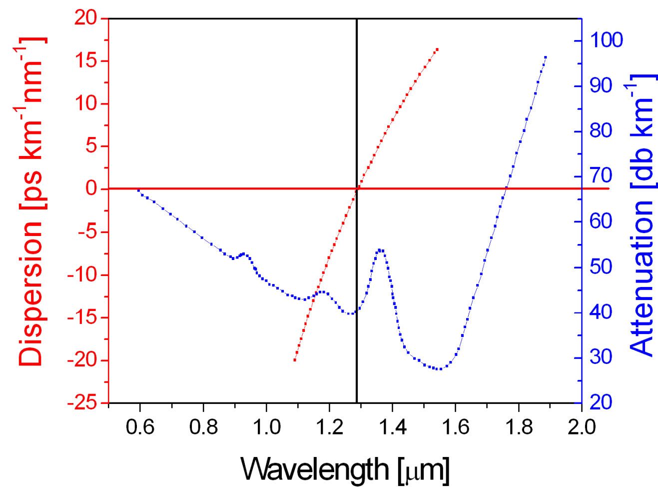

Figure 1.2. Dispersion and loss of silica-based optical fibre

Recently, OFS optics have pioneered the development of what they describe as 'AllWave' fibre. Conventional silica fibre displays increased loss between 1300 nm and 1400 nm due to OH^- absorption. However, improvements in manufacturing technology allows AllWave fibre to exhibit a flat low-loss profile from 1280 nm to 1625 nm with no increased loss between 1300 nm 1400 nm. This improvement allows the potential to expand the capacity of optical networks [7].

Biophotonics

Another important application of pulsed lasers is in the area of biophotonics. Ultrashort pulses have been used, for example, to transfect DNA into living cells [8] and to cause two-photon ablation of biological tissue [9]. This type of application is becoming more commonplace as scientists realise the possible ways in which short pulses of light can be used to study biological processes.

Another potential biophotonics-related application is the field of optical coherence tomography. Here, a laser beam shone into tissue can be used to provide information about its composition due to the backscattered signal. The resolution of this technique is proportional to the bandwidth of the source of illumination. Sources exhibiting a short coherence length are also of particular use for the same reason [10, 11].

In biophotonic applications, it is also important to tailor the emission of the laser to the properties of the medium under investigation. The absorption profile of

water makes lasers operating in the near infra-red well suited to cellular investigation. Specific wavelengths have demonstrated advantages in terms of cell viability when compared with others. For example, Neuman and Block state in their review of optical trapping that 830nm and 970 nm [12]. In this work viability was quantified by measuring the cloning efficiency of E.coli and Chinese hamster ovarian cells after 5 mins trapping as a function of wavelength. While these wavelengths are not possible in the quantum-dot system I studied, other types of semiconductor laser can readily produce these wavelengths.

Currently, solid-state and fibre lasers dominate these types of applications since they satisfy the power, bandwidth and coherence length criteria. Mode-locked quantum-dot lasers with their small size and inexpensive manufacturing costs could allow for the creation of biophotonics systems with reduced complexity, size and cost. While quantum-dot lasers currently struggle to match the peak power and bandwidths available from their solid-state counterparts, the continued development of techniques such as chirped-pulse amplification and engineering of the inhomogeneous broadening of QD material could allow these systems system to become competitive [13, 14].

Recently, QD lasers operating in a continuous wave configuration were integrated with microfluidic channels to create an integrated optical trap for the study of biological matter [15]. Using radiation pressure from the laser beams, cellular material was manipulated and subsequently interrogated. The QD laser system was intrinsically aligned for optimal trapping allowing a layperson to use the system with minimal training. This is in contrast to macroscopic optical trap systems which require skilled laser experts to operate and maintain. The system was also very small in size and the low numbers of components mean that it would be cheap to mass produce. While this is not a specific example of pulsed laser implementation, this type of small-footprint, turn-key operation is one of the key advantages of diode lasers in biophotonics applications.

Optical switching and datacomms

Ultrashort-pulse quantum-dot lasers can be utilised in a variety of applications in optically interconnected systems. As modern technology demands ever faster switching capabilities and processing speeds in CPUs, electronic means are struggling

to keep pace. For example, current CPUs are clocked at around 2-4 GHz and are preferentially employed in dual core configurations since it is easier to link two slower processors together than construct one faster element [16]. The high repetition rates and short pulse durations coupled with the small footprint of QD lasers could be of enormous advantage in these areas. Small, electrically-pumped quantum-dot lasers could be used, e.g. for generating and distributing the clock around an electronic microcircuit.

1.2.2 Mode-locked lasers

Despite the many ways of generating short pulses from a laser, such as Q-switching or gain switching, the technique of mode locking is the only currently available method of producing ultrashort (femtosecond) pulses directly from a laser without external compression. These methods will be discussed in further depth in Chapter 2 with a specific emphasis on mode locking and the factors that influence it.

For now I will define the features of a mode-locked laser and introduce the parameters that play an important role in pulse shaping. This will enable a comparison of the different ultrashort pulse mode-locked laser systems currently available and how these pulse defining characteristics apply to each laser system. More importantly, it will help to identify differences between various laser systems and provide valuable insights into the optimal parameters required for the developments of the quantum-dot lasers described in this thesis.

Requirements for mode locking

In addition to the usual laser requirements of a laser gain medium - optical feedback and some mechanism to pump the system, a mode-locked laser requires a mechanism to periodically modulate the loss of the laser at its round-trip frequency. In a mode-locked laser, the longitudinal modes of the laser are forced into a fixed-phase relationship. This results in the laser emitting a series of intense pulses separated by the round trip time of the cavity. Passive mode locking results from the laser cavity containing an element which responds to changes in the intensity of the circulating

laser field such that pulsed operation is favoured over continuous wave. Other important schemes include active and hybrid mode locking. Furthermore, the production of ultrashort pulses in the femtosecond regime requires that the gain material and saturable absorber satisfy additional criteria.

Pulse duration is fundamentally limited by the width of the stimulated emission bandwidth of the gain material. A wide emission bandwidth can support shorter pulses than one of narrower extent. Traditional solid-state sources, such as Cr^{4+}:YAG or Ti:sapphire lasers, that generate femtosecond pulses possess emission bandwidths that can support the evolution of pulses having durations below 30fs. In the case of Ti:sapphire, pulse durations as short as 5 fs have been produced [17]. Quantum-dot semiconductor material can exhibit gain bandwidths that are capable of supporting ultrashort pulses [18].

Sources of ultrashort pulses also need to have very fast acting mechanisms to initiate pulse evolution. The Kerr-lensing mechanism used in some solid-state lasers can be considered to be instantaneous in its response since the nonlinear focusing effect adapts to changes in intensity immediately. In the case of lasers which use a saturable absorber element to initialise mode locking, the absorber must recover from a bleaching event long before the next pulse arrives.

Saturable absorbers based on QD material have also been able to demonstrate ultrafast recovery, indicating their ability to act as mode locking elements [19-21]. This has enabled absorbers based on QD material to successfully mode lock a variety of laser systems from solid-state-based systems through fibre based lasers to semiconductor lasers [22-24]. The size of modulation introduced to the circulating field is also of crucial importance to the process. The magnitude of modulation required is related to the gain per unit length of the laser gain material which is lower in the case of solid-state lasers than in the case of semiconductor or fibre lasers. The fact that QD absorbers have been utilised successfully in all three of these systems bears testament to their versatility.

Gain narrowing also plays a part in limiting the minimum pulse durations obtainable from mode-locked lasers. This manifests itself because the gain lineshape falls off faster than the atomic lineshape of the gain material due to mode competition [25]. Intracavity spectral shaping techniques have been employed to attempt to circumvent this problem such as the work of Delfyett *et al* where pulses having durations of 250 fs were produced by means of an intracavity Fabry-Perot etalon [26].

The spacing of the etalon is fixed such that its loss profile matches the inverse of the laser gain profile, resulting in a subsequently flat resultant gain and loss product. This technique however, requires a significant increase in the complexity of the system.

Another key requirement of any optimised mode-locked laser is the need to control or compensate the dispersive properties of the gain material. In semiconductor lasers, the nonlinear refractive index is strongly dependent on the numbers of carriers present locally in the material. Variations in this nonlinear index lead to chirping of the pulse frequency and subsequent pulse lengthening. In the gain section of a semiconductor laser, this chirping is positive in that the instantaneous frequency of the pulse increases with time. This is one of the fundamental limiting factors in the generation of femtosecond pulses from semiconductor lasers. With appropriate dispersion compensation, chirped pulses with picosecond durations can be compressed dramatically into the femtosecond domain [27].

1.3 State-of-the-art ultrashort-pulse lasers

Favourable characteristics such as emission bandwidth have helped establish solid-state lasers as the most widely used sources of ultrashort pulses. The gateway to exceptionally short pulses was the discovery of Kerr lens mode locking by Spence, Kean and Sibbett [28]. This method has now also been employed at the telecoms windows through gain materials such as Cr^{4+}:Forsterite operating at 1.3 μm and Cr^{4+}:YAG operating at 1.5 μm. These have both been utilised to produce pulses in the femtosecond domain [29, 30]. Some of the shortest pulses ever produced at optical frequencies use solid-state lasers that have been mode locked using the Kerr lens technique [17].

Perhaps the natural successors to Kerr-lens mode-locked systems are lasers containing semiconductor saturable absorber mirrors (SESAMs) as mode-locking elements. These elements are easier to implement in mode-locking regimes since there are less stringent demands placed on cavity alignment and have been successfully employed at both 1.3 and 1.5 microns to produce femtosecond pulses [22, 31]. The pulses produced by these means are not as short as those available through KLM. This is due to the difficulty in producing a SESAM which provides an even loss modulation over the sorts of wide gain bandwidths required to equal the

performance of a KLM system. The durations available and increased operational tolerance in the mode locking parameters in SESAM-based lasers however, makes this type of laser configuration suitable for many applications.

Ultrashort-pulse semiconductor lasers

The lasers described above are all quite large and because none is directly electrically pumped, the wall plug efficiency is low, typically below 25% [32]. Semiconductor lasers, being small compared to solid-state lasers, offer much higher pulse repetition frequencies but their high efficiencies really set them apart. Furthermore, a monolithic device cannot be internally tweaked or become misaligned over a period of time, which makes them very robust for practical implementations.

Most ultrashort-pulse semiconductor lasers prior to 2001 incorporated quantum wells. These devices have been operated mainly in a picosecond regime using a variety of schemes involving passive mode locking [33] and colliding pulse passive mode locking [34] and typical pulse durations have been between 1-2 picoseconds and even less in the case of the work of Chen *et al* [35]. It is possible to use QW lasers to generate even shorter pulses by incorporating an external cavity to compress the pulses further after they have been produced. This can be done with prisms or a grating [36] or indeed by using rather more complicated schemes to control the precise shape of spectra from the laser.

In this thesis, I will concentrate on quantum-dot-based InAs/GaAs gain media as investigated by Goldstein *et al* [37]. Systems based on this combination of materials are by far the best developed of the various types of QD configurations currently being investigated for ultrashort pulse production.

Quantum-dot laser gain material possesses material gain which can be around one order of magnitude higher than in typical single-quantum-well laser, but a much broader gain bandwidth due to the large inhomogeneous broadening characteristic [13, 38]. In addition, saturable absorbers based on QD material demonstrate saturation fluences around a factor of 2-5 times lower than similar QW based structures . Low fluence is important for lasers with low gain. Quantum-dot material also displays lower amplified spontaneous emission (ASE) noise than QW material due to the discrete nature of the electronic states [39]. ASE gives rise to increases in pulse timing jitter because photons produced by spontaneous emission are random in

nature and not governed by the discrete timing characteristics of a pulse profile. Timing jitter is a particular problem in passively mode-locked devices as there is no external 'clocking' signal [40]. Improved ASE levels have thus allowed QD lasers to display considerably lower timing jitters than those reported for the alternative QW-based devices [41]. These factors suggest that equivalent and even potentially superior pulse performance could be obtained from a quantum-dot laser compared to a quantum-well device.

1.4 Quantum-dot ultrashort-pulse semiconductor lasers

Some of the subject matter in this section is extracted from the content of the review paper recently co-authored by Rafailov *et al* and the thesis of M.A. Cataluna on the topic of mode-locked QD lasers [6, 42]. The results are shown in table 1.1 below in chronological order. Those deemed to be of particular importance are also briefly discussed.

Several authors have investigated passively mode-locked configurations for QD semiconductor lasers. For instance, Huang *et al* were among the first to explore this type of laser and reported the generation of 17 ps pulses which had a time-bandwidth product of around 3, indicating highly frequency-chirped pulses [24]. Shortly after this, in 2004, Thompson *et al* demonstrated 10 ps pulses with a time – bandwidth product of 0.315, indicating that the pulses from their passively mode-locked system were transform limited [43]. This difference in time-bandwidth product is connected to the very good balance of pulse broadening and compression mechanisms which must have been achieved between the gain section and absorber in the latter result.

A significant result using this type of system was obtained by Rafailov *et al* also in 2004. Their system produced pulses with a duration as short as 390 fs, a significant improvement on previous results with QD lasers. The success of this work can be attributed to the excellent characteristics of the device, which allowed it to emit 45 mW of average power in the mode-locked regime. The resilience of the diode laser meant that high absorber biasing conditions could be applied and the device operated well above threshold, allowing a more thorough investigation of the interplay between absorber and gain sections than had previously been possible [44]. The high forward

bias on the gain section meant that a broad spectral bandwidth of 14 nm was created (the broadest mode-locked spectrum at that time) which could potentially support shorter pulses. The high values of reverse bias used in this work assisted in the optimal recovery of the absorber which is an important pulse shaping mechanism. The pulses were still slightly frequency chirped, indicating that yet shorter pulses are possible from similar systems. Since this breakthrough, several other groups have also reported subpicosecond pulses with durations around 700 fs [45, 46]. These serve to illustrate that it is possible to produce exceptionally short pulses using a simple and self-contained device configuration.

Another important factor in the assessment of sources for ultrafast applications is the repetition frequency of the laser. QD lasers have shown an ability to deliver ultrashort pulses with impressively high repetition frequencies. Currently, the highest observed value from a simple two-section QD laser configuration under the conditions of passive mode locking is 80 GHz [45]. Still higher repetition frequencies have been obtained using a variation of colliding-pulse mode locking (CPM) (schemes where the saturable absorber section is in the centre of the laser) called harmonic mode locking. In such CPM configurations, multiple pulses circulate within the cavity and so the repetition frequency is equal to the product of the round-trip frequency and the number of circulating pulses. Using this technique, Rae *et al* mode-locked a QD laser diode at the 6th harmonic with a pulse repetition frequency of 238 GHz [47]. There is however still has some way to go to match the impressive result of Yanson *et al*, who realised a pulse repetition frequency of 2.1 THz from a compound-cavity harmonically-mode-locked quantum-well device [48]

As mentioned previously, QD lasers also have the capability to deliver improved performance in the timing jitter. When employed in a harmonic, actively mode-locked configuration, QD lasers have been shown to deliver the lowest timing jitter values demonstrated by any semiconductor laser (7.5 fs) [49] and considerably lower than is possible from a QW system in passive and active configurations. The reason for this is the increased confinement of carriers to the dots and subsequent reduction in spontaneous emission possible when compared to a QW device.

Laser type and Mode locking configuration	Pulse width (ps)	Peak power (mW)	Spectral bandwidth (nm)	Time Bandwidth product (dimensionless)	Repetition frequency (GHz)	Ref #
Monolithic passive	17	7	1	3.1 G	7.4	[24]
Monolithic Hybrid/passive	<14.2 (hybrid)	4 (hybrid)	0.8 (hybrid)	< 2.78 G (hybrid)	10 (hybrid)	[50]
Monolithic passive	10	2.5	0.2	0.315 S	18	[43]
Monolithic Hybrid/passive	12/7	N/A/6	0.18/NA	N/A	20/35	[51]
Monolithic passive	2	1100	N/A	N/A	21	[44]
Monolithic passive	0.39	3000	14	~1 G	21	[44]
Monolithic Hybrid/passive	3	6	N/A	N/A	20/50	[52]
Monolithic assive	1.7	57	0.86	0.27 L	9.7	[53]
Monolithic passive	5.7	290	~5	~5	5.17	[54]
Monolithic Colliding pulse	7	13	0.32	0.54 G	20	[55]
Monolithic (flared waveguide)	0.79	500	3.6	0.5 G	24	[46]
External cavity + SOA + compressor	1.2	1220	3.1	0.69 G	4.95	[56]
Monolithic + SOA hybrid	0.7	130	8.5	1.1 S	20	[45]
Monolithic + SOA hybrid	3.3	26	6.5	3.9 S	20	[45]
Monolithic + SOA hybrid	1.9	14	2.2	0.7 S	40	[45]
Monolithic + SOA passive	2.2	11	4.2	1.5 S	80	[45]
Monolithic	1.3	10	1.4	0.45 S	238	[47]
Monolithic	6.4	224	1.8	3.4	42.4	[57]

Table 1.1. Table showing state of the art in QD performance. S, G and L refer to a $sech^{2}$, Gaussian and Lorenzian pulse shapes respectively.

One interesting point of note is that the 390 fs result of Rafailov *et al* still remains the shortest pulse duration achieved directly from a QD laser to my knowledge at the time of writing this thesis. This is despite the fact that many other researchers have investigated lasers with very similar characteristics. The precise mechanisms leading to these very short pulses are not currently fully understood. It is also worth pointing out that lasers exhibiting the smallest TBP do not necessarily yield the shortest pulses given that a suitable combination of a wide emission bandwidth and chirp control is required for optimal pulse duration.

These results confirm that a great deal more work is required to understand the processes at work within mode locked quantum-dot lasers and implement them in the sorts of simple monolithic configurations which best exploit their comparative advantage. The ultimate realisation of this would be a monolithic semiconductor laser capable of producing pulses of the order of 100 fs. If this could be achieved and pulse amplification techniques employed to boost the peak power, then QD lasers could be truly competitive with existing solid-state systems in a broad range of applications.

1.5 Nonlinear optical properties of semiconductor material

The second thrust of my project concerned the use of semiconductor material for nonlinear optical frequency conversion (NLOFC) applications in the mid infrared where there is a relative lack of practical optical sources. NLOFC is a “parametric” nonlinear process - a term that has been derived from electrical engineering. In electronic parametric amplifiers, signals of differing frequency interact in a nonlinear manner dictated by the parameters of the circuit. In the case of optical parametric processes, the nature of the nonlinear process depends on the characteristics of the material and of the interacting waves.

Current materials used for these processes are ferroelectric crystalline materials such as lithium niobate ($LINbO_3$), potassium titanyl phosphate (KTP) and lithium tantalate (LT). These are well developed technologies implemented in many commercial systems used in applications like scientific research and sensing yielding high efficiencies [58] and output powers [59]. I hypothesise, however, that the excellent nonlinear properties of GaAs which are to its large nonlinear polarisation

response, will allow this material to be used as the basis for devices that may be shown to be superior to those currently available.

1.5.1 Uses of nonlinear frequency conversion

As stated previously, nonlinear means are used to produce light in regions of the spectrum where it is difficult to generate coherent light otherwise. Reliable efficient sources are important to many types of applications. One of the principal uses of nonlinear optical wavelength generation is in spectroscopic applications. These demand light sources whose wavelength can be precisely matched to the absorption resonances pertaining to particular molecular species. By variation of materials and methods, parametric processes can deliver light with wavelengths ranging from the ultraviolet right through to the far infrared.

This technique is central to the area of trace gas detection. Recently, Stothard *et al* demonstrated a continuous wave OPO for the detection of Methane gas [60]. This system produced an output of approximately 50 mW from around 900 mW of pumping at 1064 nm. Another application is in the detection of explosive vapours [61]. This system operated in a pulsed configuration with pulse energies of up to 1 mJ. By directing light at a target area, small changes in transmission caused by the presence of minute quantities of gas can be detected. These can then be compared to known absorption spectra thus enabling identification. This could be applied for example in a luggage scanning capacity, allowing detection and identification potentially dangerous compounds. These systems could also be used to locate leaks in gas pipes.

Figure 1.3. Visible light LIDAR system used to probe the sky during strong aurora activity in Antarctica. Image taken from http://www.aad.gov.au/default.asp?casid=2933.

Another spectroscopic application is that of light detection and ranging (LIDAR). This can be thought of as radar but done at optical frequencies. An example of the use of LIDAR is for atmospheric monitoring. By directing a light beam at the sky and collecting the back-scattered signal, one can gather information on the distribution and movement of clouds and aerosols. In addition, by employing a differential absorption methodology (DIAL), it is possible to ascertain the nature of the species present. This enables the monitoring of air quality, by detection of specific molecules indicative of things such as smog [62]. Atmospheric LIDAR operates over large distances, requiring sources delivering several Watts of average power [63]. Other types of LIDAR such as those used for more close range analysis would require less power to function effectively.

Like QD lasers, NLOFC is also useful in the area of telecommunications to allow WDM. Optical parametric oscillators (OPOs) can generate sets of equally spaced optical frequencies in frequency combs. These combs are produced by applying a modulated electric field to an anisotropic crystal. When polarised light then passes through the crystal, this modulation is experienced by the light in the form of electro-optically induced refractive index changes at a frequency equal to that of the modulation. This amounts to a phase modulation that results in the production of a series of frequency sidebands that are equidistant about the fundamental frequency of the incident polarised light. The separation of these sidebands in frequency is then equal to that of the modulated electric field giving rise to the effect [64]. This comb

can then be used as the channels of a WDM system. Due to its complexity, this system would be quite bulky if implemented using currently available technology.

From the above, it is clear that nonlinear frequency conversion has many applications due to the versatility of the approach to arbitrary wavelength regimes. In terms of scientific research, tunable parametric sources represent excellent investments as they can be applied to many different tasks. With the use of new materials, new wavelengths can be generated and new applications can be explored, further enhancing the usefulness of the approach.

1.6 Semiconductor materials for nonlinear optics

Despite the success of current ferroelectric materials such as $LiNbO_3$, there are several reasons for considering nonlinear processes in semiconductors (GaAs), such as transparency window, photo-stability and nonlinear conversion efficiency, typically described by χ^2.

The second-order nonlinear susceptibility χ^2 of a material describes how the material develops a nonlinear polarisation under the influence of an external electric field. This nonlinear polarisation subsequently gives rise to frequencies in addition to that of the fundamental driving field through the coupled wave equations which are covered in Chapter 6. GaAs has a χ^2 coefficient of around an order of magnitude larger than that of $LiNbO_3$ (d_{36} GaAs = 170 pm/V whereas $d_{31}LiNbO_3$=4.6 pm/V d_{33} $LiNbO_3$=25.2 pm/V) [65]. The second advantage of semiconductor material relates to the transparency range. For instance, GaAs is transparent from its band edge at around 870 nm through to about 17 μm [66]. Correspondingly, the transparency range of $LiNbO_3$ lies between around 320 nm and around 4 μm [67].

Ferroelectric nonlinear materials suffer from effects such as green infra-red absorption (GRIIRA) [68]. This causes promotion of electrons to forbidden states in the material causing degradation in performance and visible 'damage' to the material in the form of a haze where the pump beam is incident. Heating of the material can repair these effects by giving electrons sufficient thermal energy to escape the forbidden states [69]. This technique can also be applied in real time to prevent their occurrence [70-72]. This problem can also be circumvented by the use of MgO doped

crystals [68]. Semiconductor materials do not suffer from these effects due to their different electronic structure, but do exhibit lower damage thresholds.

An extremely important advantage of using semiconductor material is the inherent ability of integration, which offers the potential to realise a monolithic frequency conversion device comprising an integrated pump laser and 'nonlinear' section. This goal is aided by the ability in semiconductor to fabricate waveguide structures less than 10 μm wide of high optical quality, exhibiting low losses. This technology can be readily applied in order to produce a semiconductor based nonlinear waveguide, providing efficient conversion due to the high intensity of light propagating within. With these advantages it is easy to understand why there is significant research interest worldwide in harnessing semiconductor materials for NLOFC

1.7 State-of-the-art nonlinear frequency conversion in semiconductors

GaAs has been and continues to be investigated as a potential nonlinear material because of the attractive properties outlined above. It possesses some disadvantages because GaAs is optically isotropic. This means that a simple GaAs chip will exhibit no birefringence and hence cannot be deployed in conventional birefringently phase-matched arrangements. Nevertheless, *form birefringence* has been exploited by several authors in GaAs systems for phase matching to overcome the chromatic dispersion between the propagating waves of differing wavelength. Form birefringence is created in multilayered structures consisting of layers of material with differing refractive indices. The layering introduces anisotropy into the structure for light polarised parallel or perpendicular to the layers. Transverse electric (TE) and transverse magnetic (TM) modes will experience different indices such that if the fundamental is polarised in the TE direction and the second harmonic in the TM direction, phase matching is possible. This approach was first proposed in 1975 [73], but practical demonstration of the technique was initially not possible due to the lack of constituent multilayer structures possessing high enough index contrasts and nonlinear coefficients [74]. Fiore *et al* [75] were the first to demonstrate nonlinear conversion in a selectively oxidised form birefringent GaAs/AlAs waveguide. The

oxidation was performed on the AlAs sections to increase the index contrast between these areas and those of GaAs [75]. Parametric amplification was demonstrated with up to 80 nW of difference frequency generated (DFG) power at 1058 nm using 0.4 mW and 11.6 mW of Nd:YAG and Titanium sapphire pump power respectively. [76]. After this initial demonstration, several other authors also used form birefringence for second-harmonic-generation (SHG), producing an efficiency of 1.3% and 650 μW of second-harmonic power at 1μm [77] as well as optical parametric generation (OPG) where 4 nW from 50 mW of pump power at λp = 1060 nm [78] were demonstrated

Modal phase matching (MPM) is another way to compensate for dispersion and achieve phase matching. This technique utilises careful design in multimode waveguide structures such that the differing propagation speeds of transverse modes in the waveguide can be exploited. The refractive index experienced by higher-order modes is smaller and the propagation speed higher than that of lower order modes. Also, in a material exhibiting normal dispersion, a second-harmonic beam will propagate more slowly than the fundamental. By then engineering a situation where, the SH field propagates in a higher-order mode than the fundamental, the two fields can experience the same phase velocity and are thus phase matched.

This method has the advantage of being an 'all optical' method of achieving phase matching where there is no complicated processing of the structure to engineer the phase matching effect. Instead, the geometry of the waveguide causes the difference in mode velocities which balances the dispersion. This was first demonstrated practically in 1971 producing SHG from a CO_2 pump [79]. Several other authors have since also utilised the effect in NLOFC applications. Recently, Moutzouris *et al* demonstrated 10 μW of SHG from 65 mW input power with a fundamental frequency of 1.55 μm [80]. Due to the simple nature of this method, it offers (in comparison to other GaAs NLOFC schemes) ease of monolithic integration.

The final method of phase matching in GaAs discussed here is quasi-phase-matching (QPM). QPM is also the method for realising a NLOFC that was chosen in my project. This method can generally allow higher nonlinear coefficients to be accessed than with alternative phase-matching methods and can be employed at essentially any wavelength provided the host material exhibits transparency and the necessary poling period can in some way be defined [67].

Normally, in ferroelectric materials such as $LiNbO_3$ or KTP, this is achieved by periodic electric poling of the material, which acts to alter the material properties such that the sign of the nonlinearity is changed [81]. It is normally achieved through applying an electric field to the material through the use of patterned electrodes. Periodic poling, allows continued conversion from pump to converted wave by resetting the phase slip between propagating waves every coherence length.

Given that GaAs is non-ferroelectric, the poling approach cannot be used. Alternative methods are thus required to achieve domain inversion and QPM operation. One novel way to perform QPM in non-ferroelectric materials such as GaAs is to employ a periodic switching of the nonlinearity (PSN) in the material between a low and high value every coherence length. This allows a net gain in the converted field over two coherence lengths. Switching the nonlinearity can be done by a variety of methods including regrowing domains of material with a nonlinear coefficient which alternates between a high and low value. This is less technically demanding than the micron scale reorienting demanded in order to create periodically poled material in non- ferroelectric materials. This method has been explored from a theoretical perspective [82] and utilised to produce SHG in an AlGaAs/GaAs waveguide crystal [83]. Despite the fact that this method is inherently half as efficient as periodic poling due to only providing a net gain in converted field every 2 coherence lengths, the higher nonlinear coefficients available in GaAs could in principle allow this method to be more efficient than a periodically poled $LiNbO_3$ system.

On the other hand, GaAs is a zincblende type structure. This means that the orientation of the atoms in its crystal lattice can be visualised as two face centred cubic (FCC) sublattices, one containing As atoms and the other with Ga atoms. These sublattices each penetrate the space occupied by the other, as shown below in figure 1.4.

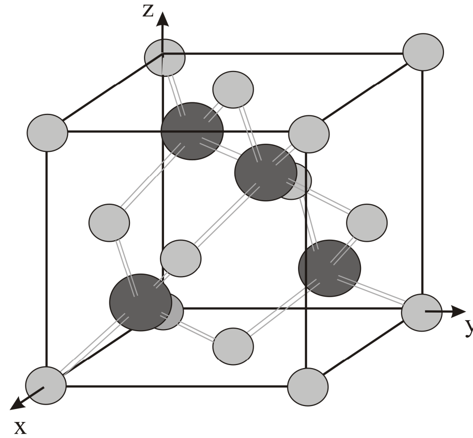

Figure 1.4. Diagram showing zincblende crystal structure such as in GaAs

The two different sizes of atoms shown in the diagram represent the Ga and As atoms present in the structure. It is possible to replicate the effect of periodic poling (reversing the sign of the nonlinear coefficient) by inverting the crystal domain, thus turning the crystal through 180 degrees. Inverting the crystal domain can be achieved by rotating the structure about the x ([100]) direction by 90 degrees [84].

Early approaches for achieving domain inversion and subsequent QPM in GaAs involved the stacking of plates of alternating domain. This was first demonstrated experimentally in 1976 by Szilagyi *et al* who showed SHG of 10.6 μm CO_2 laser light using a stack of plates with a thickness of 308 μm which gave third order QPM [85]. These early attempts operated with coherence lengths of hundreds of microns. To truly exploit the vast transparency range of GaAs it was necessary to formulate a method capable of producing far thinner plates of material (<10 μm).

In 1993, diffusion bonding was first used by Fejer's group to join together plates of GaAs into a continuous slab of material. This proof of concept paper exhibited reduced losses due to the elimination of reflections at the boundaries between adjacent plates [86]. The authors managed to demonstrate slabs as thin as 3 μm in AlGaAs, performing SHG [87] and DFG [88]. The former was able to produce an efficiency of 4.9 %, generating around 2μW at a wavelength of 1466 μm. Due to the inescapable problems in aligning adjacent slabs with sufficient accuracy, this method suffers from considerable problems with losses. Novel alternative schemes for achieving QPM in GaAs include using phase shifts upon reflection in thin sections of material – so called Fresnel birefringence [89] and the use of quantum-well intermixing which was utilised to produce 110 nW of thirdorder second-harmonic

power from 2.3 mW of fundamental power at around 1.5 μm [90]. Here, third-order refers to the fact that in this case the quasi-phase-matching acts over every third coherence length of the material.

A key breakthrough in the quest to obtain low loss periodically orientation inverted material was the development of so-called sublattice reversal epitaxy (SRE) [91], or orientation patterning (OP) as it is otherwise known. The SRE/OP technique (which underwent significant development during the timeframe of this thesis) allows the creation of epitaxially grown material with alternating domains required for QPM. This can be thought of as 'periodic poling for non ferroelectric materials'. Developed independently by groups at Stanford University and the University of Tokyo, the basis of the technique is growth of GaAs in antiphase to the material beneath.

Using this technique, Fejer's group at Stanford University demonstrated SHG with an internal conversion efficiency of around 33%[92] and DFG, producing a cw idler power level just 2.8 times lower than theory predicted [93]. They also demonstrated optical parametric generation [94]. In this work they utilised the broad transparency range of GaAs with a pulsed pump at 1.9 μm generating light from 2.28 and 9.14 μm with a maximum output energy of over 3 μJ (idler) from around 60 μJ of pump. This broad range was then further extended into the IR by exploiting pump wavelengths connected with zero group velocity dispersion. This allowed the generation of light from 4.5 – 10.7 μm. Recently, a French group using this technique managed to recreate the work, producing the highest slope efficiency and output from an OPGaAs system producing 57% and 1.2W (signal and idler combined) respectively [95]. These devices are all based on bulk material. In this configuration, the pump light has relatively low intensity. By operating in a waveguide configuration, the pump intensity is dramatically increased due to the smaller cross sectional area when comparing waveguide to bulk.

The waveguide approach was followed by Kondo's group at Tokyo University where they produced SHG and optical parametric fluorescence [96] in waveguide devices 5 μm wide. Despite the increases in pump intensity provided by the waveguide approach, the results were considerably poorer than those shown by Fejer *et al.* , with demonstrated conversion efficiencies of around one order of magnitude less than suggested by theory. Reasons for this include differences in etching and regrowth procedures coupled with losses brought about by the formation

of the waveguide. Improvements in both of these could lead potentially to significant increases in efficiencies.

1.8 Work contained in this thesis on NLOFC

Two methods for achieving nonlinear frequency conversion were investigated in my project work. Initially, a PSN methodology was investigated using ion implantation to selectively destroy the nonlinear coefficient in patterned GaAs waveguides. The underlying research hypothesis was that NLOFC waveguides fabricated in this manner would have low losses due to the fact that no regrowth is required. Once the active region is grown, it is modified rather than removed and replaced as in orientation-patterned schemes or in PSN schemes such as [83]. These waveguides were then studied with a view to measuring OPG and SHG.

While this work was in progress, the orientation-patterning technique discussed in the previous section reached a level of prominence such that its utilisation was considered in the context of my project. The approach was recognised as being very practical and offered the prospect of twice the efficiency of an identical PSN system. Orientation-patterned GaAs frequency conversion waveguide chips were therefore explored as an additional and potentially superior method of nonlinear parametric generation. This work will be described in Chapter 7.

Both methods employed extensively the technique of chemically-assisted ion-beam etching (CAIBE) because this method can produce very high quality etches with excellent sidewall verticality compared with wet etching. This method of etching offers excellent selectivity, and is routinely being employed for the fabrication of photonic crystal devices, which is very demanding. CAIBE was therefore seen as an excellent candidate to fabricate not only the waveguides but also to establish the gratings required to produce the modulation or reversal in the nonlinear coefficient for PSN and orientation patterning respectively.

1.9 Thesis overview

The overarching theme of my project activities was the development of novel GaAs-based light sources, either by direct laser action or by nonlinear conversion. Concentrating first on semiconductor devices that produce light by direct means, ultrashort-pulse quantum-dot-based semiconductor lasers were explored. In Chapter 2 I deal with the physics of the operation and ultrashort-pulse production of quantum-dot lasers. Chapter 3 provides a summary of the main fabrication techniques used in my work to fabricate both quantum-dot devices and structures suitable for NLOFC applications. In Chapter 4 I describe how these ideas were used to investigate quantum-dot, gain-switched lasers that were optically pumped by femtosecond pulses. With research colleagues, I then investigated how emission from the ground and excited states evolved and what type of temporal differences could be observed in QD devices. The subject matter of Chapter 5 is a description of the mode locking of a semiconductor quantum-dot laser in an external cavity scheme and how mode locking could be achieved over a broad temperature range for a monolithic laser.

The physics of nonlinear optics is then briefly described in Chapter 6. Here, the origin of the nonlinear polarisation is discussed, leading into the coupled- wave equations and the different methods to achieve phase matching and Chapter 7 contains a description of the PSN and orientation-patterned devices that were fabricated and tested. The thesis concludes with Chapter 8 in which the main findings of the work are summarised together with suggestions for possible avenues for future research, including schemes where quantum-dot lasers could be used as the pump sources for parametric applications.

References

1. Wilson. J., Hawkes. P., *Optoelectronics an introduction*. 3rd ed.: Prentice hall. 1998,
2. Hoddeson, L., *The origins of the pn junction*, *IEEE SPECTRUM*. 1997. p. 46 - 51.
3. Maiman, T.H., *Stimulated optical radiation in ruby.* Nature, 1960. **187**(4736): p. 493-494.
4. McAleavey, F.J., et al., *Narrow linewidth, tunable Tm3+ - doped fluoride fiber laser for optical-based hydrocarbon gas sensing.* IEEE Journal of Selected Topics in Quantum Electronics, 1997. **3**(4): p. 1103-1111.
5. Liu, J., et al., *Uniform 90-channel multiwavelength InAs/InGaAsP quantum dot laser.* Electronics Letters, 2007. **43**(8): p. 458 - 460.
6. Rafailov, E.U., M.A. Cataluna, and W. Sibbett, *Mode-locked quantum-dot lasers.* Nature Photonics, 2007. **1**(7): p. 395-401.
7. Chang, K. and W.M. Flegal. *Full spectrum fibre performance today and tomorrow with OFS AllWave fibre*, 2003 http://www.ofsoptics.com/resources/hydrogenaging-0503web.pdf.
8. Stevenson, D., et al., *Femtosecond optical transfection of cells:viability and efficiency.* Optics Express, 2006. **14**: p. 7125 - 7133.
9. Fischer, P., et al., *Two-photon ablation with 1278 nm laser radiation.* Journal of Optics A-Pure and Applied Optics, 2007. **9**(6): p. S19-S23.
10. Wikipedia. *Optical coherence tomography*. 2008, http://en.wikipedia.org/wiki/Optical_coherence_tomography .
11. Drexler, W., *Ultrahigh-resolution optical coherence tomography.* Journal of Biomedical Optics, 2004. **9**(1): p. 47-74.
12. Neuman, K.C. and S.M. Block, *Optical Trapping.* Review of Scientific Instruments, 2004. **75**(9): p. 2787-2809.
13. Kovsh, A., et al., *Quantum dot laser with 75 nm broad spectrum of emission.* Optics Letters, 2007. **32**(7): p. 793-795.
14. Kim, K., S. Lee, and P.J. Delfyett, *eXtreme chirped pulse amplification - Beyond the fundamental energy storage limit of semiconductor optical amplifiers.* IEEE Journal of Selected Topics in Quantum Electronics, 2006. **12**(2): p. 245-254.
15. Cran-McGreehin, S.J., K. Dholakia, and T.F. Krauss, *Monolithic integration of microfluidic channels and semiconductor lasers.* Optics Express, 2006. **14**(17): p. 7723 - 7729.
16. Kronlund, D. *Dual core processing: Over-simplified, demystified and explained*. 2004 http://icrontic.com/articles/dual_core
17. Ell, R., et al., *Generation of 5-fs pulses and octave-spanning spectra directly from a Ti : sapphire laser.* Optics Letters, 2001. **26**(6): p. 373-375.
18. Rossetti, M., et al., *Quantum dot superluminescent diodes emitting at 1.3 mu m.* IEEE Photonics Technology Letters, 2005. **17**(3): p. 540-542.
19. Rafailov, E.U., et al., *Fast quantum-dot saturable absorber for passive mode-locking of solid-state lasers.* IEEE Photonics Technology Letters, 2004. **16**(11): p. 2439-2441.
20. Malins, D.B., et al., *Ultrafast electroabsorption dynamics in an InAs quantum dot saturable absorber at 1.3 mu m.* Applied Physics Letters, 2006. **89**(17).

21. Borri, P., et al., *Ultrafast carrier dynamics in InGaAs quantum dot materials and devices.* Journal of Optics a-Pure and Applied Optics, 2006. **8**(4): p. S33-S46.
22. McWilliam, A., et al., *Quantum-dot-based saturable absorber for femtosecond mode-locked operation of a solid-state laser.* Optics Letters, 2006. **31**(10): p. 1444-1446.
23. Herda, R., et al. *Quantum-dot based saturable absorber for mode locking of fibre lasers*. IEEE *LEOS 2005*. Paper ThN5. Sydney, Australia.
24. Huang, X.D., et al., *Passive mode-locking in 1.3 mu m two-section InAs quantum dot lasers.* Applied Physics Letters, 2001. **78**(19): p. 2825-2827.
25. Siegman, A., *Lasers*. 1986: University Science Books. 1283.
26. Gee, S., et al., *Ultrashort pulse generation by intracavity spectral shaping and phase compensation of external-cavity modelocked semiconductor lasers.* IEEE Journal of Quantum Electronics, 2000. **36**(9): p. 1035-1040.
27. Matsui, Y., M.D. Pelusi, and A. Suzuki, *Generation of 20-fs optical pulses from a gain-switched laser diode by a four-stage soliton compression technique.* IEEE Photonics Technology Letters, 1999. **11**(10): p. 1217-1219.
28. Spence, D.E., P.N. Kean, and W. Sibbett, *60-Fsec Pulse Generation from a Self-Mode-Locked Ti-Sapphire Laser.* Optics Letters, 1991. **16**(1): p. 42-44.
29. Tong, Y.P., P.M.W. French, and J.R. Taylor, *All-solid-state Kerr lens mode-locked Cr4+:forsterite laser.* Electronics Letters, 1996. **32**(8): p. 737-738.
30. Leburn, C.G., et al., *Femtosecond Cr4+: YAG laser with 4GHz pulse repetition rate.* Electronics Letters, 2004. **40**(13): p. 805-807.
31. Lebum, C.G., et al. *Self-starting Cr4+:YAG laser mode-locked with a GaInNAs saturable Bragg reflector*. *Advanced solid state photonics*, 2007 Paper WA6 ,Vancouver Canada
32. RPPhotonics. *Encyclopedia of laser physics and technology article : Wall plug efficiency*. http://www.rp-photonics.com/wall_plug_efficiency.html,
33. Ogawa, K., et al., *Pulse characterisation of a quantum-well mode-locked laser diode by two-photon absorption frequency-resolved optical gating.* Optical and Quantum Electronics, 2001. **33**(7-10): p. 727-733.
34. Wu, M.C., et al., *Transform-Limited 1.4 Ps Optical Pulses from a Monolithic Colliding-Pulse Mode-Locked Quantum-Well Laser.* Applied Physics Letters, 1990. **57**(8): p. 759-761.
35. Chen, Y.K., et al., *Subpicosecond Monolithic Colliding-Pulse Mode-Locked Multiple Quantum-Well Lasers.* Applied Physics Letters, 1991. **58**(12): p. 1253-1255.
36. Ludwig, R. and A. Ehrhardt, *Turn-Key-Ready Wavelength, Repetition Rate and Pulsewidth-Tunable Femtosecond Hybrid Modelocked Semiconductor-Laser.* Electronics Letters, 1995. **31**(14): p. 1165-1167.
37. Goldstein, L., et al., *Growth by Molecular-Beam Epitaxy and Characterization of Inas/Gaas Strained-Layer Superlattices.* Applied Physics Letters, 1985. **47**(10): p. 1099-1101.
38. Kirstaedter, N., et al., *Gain and differential gain of single layer InAs/GaAs quantum dot injection lasers.* Applied Physics Letters, 1996. **69**(9): p. 1226-1228.
39. Berg, T.W. and J. Mork, *Quantum dot amplifiers with high output power and low noise.* Applied Physics Letters, 2003. **82**(18): p. 3083-3085.

40. Derickson, D.J., et al., *Comparison of Timing Jitter in External and Monolithic Cavity Mode-Locked Semiconductor-Lasers.* Applied Physics Letters, 1991. **59**(26): p. 3372-3374.
41. Thompson, M.G., et al. *Absorber length optimisation for sub-picosecond pulse generation and ultra-low jitter performance in passively mode-locked 1.3 /spl mu/m quantum-dot laser diodes*. *Optical fibre communication conference.* 2006. Paper OThG3 .
42. Cataluna, M.A., *Ultrashort-pulse generation from quantum-dot semiconductor diode lasers*,PhD Thesis, *School of Physics and Astronomy*, 2007, University of St Andrews: St Andrews,.
43. Thompson, M.G., et al., *Transform-limited optical pulses from 18GHz monolithic modelocked quantum dot lasers operating at similar to 1.3 mu m.* Electronics Letters, 2004. **40**(5): p. 346-347.
44. Rafailov, E.U., et al., *High-power picosecond and femtosecond pulse generation from a two-section mode-locked quantum-dot laser.* Applied Physics Letters, 2005. **87**(8).
45. Laemmlin, M., et al., *Distortion-free optical amplification of 20-80 GHz modelocked laser pulses at 1.3 mu m using quantum dots.* Electronics Letters, 2006. **42**(12): p. 697-699.
46. Thompson, M.G., et al., *Subpicosecond high-power mode locking using flared waveguide monolithic quantum-dot lasers.* Applied Physics Letters, 2006. **88**(13). p. 133119
47. Rae, A.R., et al. *Harmonic Mode-Locking of a Quantum-Dot laser diode*. in *LEOS annual meeting,* 2006, Paper ThR5. Montreal Canada.
48. Yanson, D.A., et al., *Terahertz repetition frequencies from harmonic mode-locked monolithic compound-cavity laser diodes.* Applied Physics Letters, 2001. **78**(23): p. 3571-3573.
49. Choi, M.T., et al., *Ultralow noise optical pulse generation in an actively mode-locked quantum-dot semiconductor laser.* Applied Physics Letters, 2006. **88**: p. 131106.
50. Thompson, M.G., et al., *10GHz hybrid modelocking of monolithic InGaAs quantum dot lasers.* Electronics Letters, 2003. **39**(15): p. 1121-1122.
51. Kuntz, M., et al., *35 GHz mode-locking of 1.3 mu m quantum dot lasers.* Applied Physics Letters, 2004. **85**(5): p. 843-845.
52. Kuntz, M., et al., *Direct modulation and mode locking of 1.3 mm quantum dot lasers.* New Journal of Physics, 2004. **6**.
53. Gubenko, A.E., et al. *Mode-locking at 9.7 GHz repetition rate with 1.7 ps pulse duration in two-section QD lasers*. *Semiconductor laser conference,* 2004. Paper ThB1.
54. Zhang, C., L., et al. *Low timing jitter, 5 GHz optical pulses from monolithic two-section passively mode-locked 1250/1310 nm quantum dot lasers for high-speed optical interconnects*. *Optical Fiber Communication Conference,* 2005. *Paper* OWM4.
55. Thompson, M.G., et al., *Colliding-pulse modelocked quantum dot lasers.* Electronics Letters, 2005. **41**(5). P 248-250
56. Choi, M.T., et al., *Ultrashort, high-power pulse generation from a master oscillator power amplifier based on external cavity mode locking of a quantum-dot two-section diode laser.* Applied Physics Letters, 2005. **87**(22).
57. Xin, Y.C., et al., *Reconfigurable quantum dot monolithic multi-section passive mode-locked lasers.* Optics Express, 2007. **15**(12): p. 7623-7633.

58. Taverner, D., et al., *Highly efficient second-harmonic and sum-frequency generation of nanosecond pulses in a cascaded erbium-doped fiber periodically poled lithium niobate source.* Optics Letters, 1998. **23**(3): p. 162-164.
59. Katz, M., et al., *Vapor-transport equilibrated near-stoichiometric lithium tantalate for frequency-conversion applications.* Optics Letters, 2004. **29**(15): p. 1775-1777.
60. Stothard, D.J.M., M.H. Dunn, and C.F. Rae, *Hyperspectral imaging of gases with a continuous-wave pump-enhanced optical parametric oscillator.* Optics Express, 2004. **12**(5): p. 947-955.
61. Owano, T.G.T., M.W. Paldus, B.A. Vodopyanov, K.L. *Ultrasensitive detection of explosives vapor using mid-IR cavityring-down spectroscopy. Conference on lasers and electro-optics. CLEO'01*. 2001. Technical Digest, page 591-520. Baltimore USA.
62. Butler, C.F. *Lidar Atmospheric Sensing Experiment (LASE): Measuring Water Vapor, Aerosols and Clouds*., 2007 http://asd-www.larc.nasa.gov/lase/ASDlase.html
63. Nuphoton.com. *NP3000MOPA-4.0 4W LIDAR Source*. 2008 http://www.nuphoton.com/NP3000MOPA4W.html
64. Spurr, M.B., *Frequency comb generation in a pump enhanced optical parametric oscillator*, PhD Thesis. *School of physics and astronomy*. 2005, University of St Andrews: St Andrews. p. 231.
65. Shoji, I., et al., *Absolute scale of second-order nonlinear-optical coefficients.* Journal of the Optical Society of America B-Optical Physics, 1997. **14**(9): p. 2268-2294.
66. Kuo, P.S., et al., *Optical parametric generation of a mid-infrared continuum in orientation-patterned GaAs.* Optics Letters, 2006. **31**(1): p. 71-73.
67. Hum, D.S. and M.M. Fejer, *Quasi-phasematching.* Comptes Rendus Physique, 2007. **8**(2): p. 180-198.
68. Furukawa, Y., et al., *Green-induced infrared absorption in MgO doped LiNbO3.* Applied Physics Letters, 2001. **78**(14): p. 1970-1972.
69. Stothard, D.J.M., Personal communication, 2008
70. Jermann, F., M. Simon, and E. Kratzig, *Photorefractive Properties of Congruent and Stoichiometric Lithium-Niobate at High Light Intensities.* Journal of the Optical Society of America B-Optical Physics, 1995. **12**(11): p. 2066-2070.
71. Ashkin, A., et al., *Optically induced refractive index inhomogeneities in LiNbO3 and LiTaO3.* Applied Physics Letters, 1966. **9**(1): p. 72 - 74.
72. Myers, L.E. and W.R. Bosenberg, *Periodically poled lithium niobate and quasi-phase-matched optical parametric oscillators.* IEEE Journal of Quantum Electronics, 1997. **33**(10): p. 1663-1672.
73. van der Ziel, J.P., *Phase-Matched Harmonic-Generation in a Laminar Structure with Wave-Propagation in Plane of Layers.* Applied Physics Letters, 1975. **26**(2): p. 60-61.
74. Rao, S.V., K. Moutzouris, and M. Ebrahimzadeh, *Nonlinear frequency conversion in semiconductor optical waveguides using birefringent, modal and quasi-phase-matching techniques.* Journal of Optics A-Pure and Applied Optics, 2004. **6**(6): p. 569-584.
75. Fiore, A., et al., *Huge birefringence in selectively oxidized GaAs/AlAs optical waveguides.* Applied Physics Letters, 1996. **68**(10): p. 1320-1322.

76. Fiore, A., et al., *Phase matching using an isotropic nonlinear optical material.* Nature, 1998. **391**(6666): p. 463-466.
77. Moutzouris, K., et al., *Efficient second-harmonic generation in birefringently phase-matched GaAs/Al2O3 waveguides.* Optics Letters, 2001. **26**(22): p. 1785-1787.
78. De Rossi, A., et al., *Parametric fluorescence in oxidized aluminum gallium arsenide waveguides.* Applied Physics Letters, 2001. **79**(23): p. 3758-3760.
79. Anderson, D.B. and J.T. Boyd, *Wideband Co2 Laser Second Harmonic Generation Phase Matched in Gaas Thin-Film Waveguides.* Applied Physics Letters, 1971. **19**(8): p. 266-8.
80. Moutzouris, K., et al., *Second-harmonic generation through optimized modal phase matching in semiconductor waveguides.* Applied Physics Letters, 2003. **83**(4): p. 620-622.
81. Fejer, M.M., et al., *Quasi-Phase-Matched 2nd Harmonic-Generation - Tuning and Tolerances.* IEEE Journal of Quantum Electronics, 1992. **28**(11): p. 2631-2654.
82. Artigas, D., et al., *Periodically switched nonlinear structures for frequency conversion: Theory and experimental demonstration.* IEEE Journal of Quantum Electronics, 2004. **40**(8): p. 1122-1130.
83. Rafailov, E.U., et al., *Second-harmonic generation from a first-order quasi-phase-matched GaAs/AlGaAs waveguide crystal.* Optics Letters, 2001. **26**(24): p. 1984-1986.
84. Kondo, T. and I. Shoji, *Study on wavelength conversion by compound semiconductor based quasi phase matching devices*:*Photonics Based on Wavelength Integration and Manipulation*. IPAP. 2005 p. 151 - 160.
85. Szilagyi, A., A. Hordvik, and H. Schlossberg, *Quasi-Phase-Matching Technique for Efficient Optical Mixing and Frequency Doubling.* Journal of Applied Physics, 1976. **47**(5): p. 2025-2032.
86. Gordon, L., et al., *Diffusion-Bonded Stacked Gaas for Quasi-Phase-Matched 2nd-Harmonic Generation of a Carbon-Dioxide Laser.* Electronics Letters, 1993. **29**(22): p. 1942-1944.
87. Yoo, S.J.B., et al., *Quasi-Phase-Matched 2nd-Harmonic Generation in Algaas Wave-Guides with Periodic Domain Inversion Achieved by Wafer-Bonding.* Applied Physics Letters, 1995. **66**(25): p. 3410-3412.
88. Yoo, S.J.B., et al., *Wavelength conversion by difference frequency generation in AlGaAs waveguides with periodic domain inversion achieved by wafer bonding.* Applied Physics Letters, 1996. **68**(19): p. 2609-2611.
89. Haidar, R., P. Kupecek, and E. Rosencher, *Nonresonant quasi-phase matching in GaAs plates by Fresnel birefringence.* Applied Physics Letters, 2003. **83**(8): p. 1506-1508.
90. Helmy, A.S., et al., *Quasi phase matching in GaAs-AlAs superlattice waveguides through bandgap tuning by use of quantum-well intermixing.* Optics Letters, 2000. **25**(18): p. 1370-1372.
91. Kondo, T. and I. Shoji, *Study on wavelength conversion by compound-semiconductor-based quasi phase-matching devices*, in *Photonics Based on Wavelength Integration and Manipulation*. 2005. IPAP. p. 151 - 160.
92. Skauli, T., et al., *Measurement of the nonlinear coefficient of orientation-patterned GaAs and demonstration of highly efficient second-harmonic generation.* Optics Letters, 2002. **27**(8): p. 628-630.

93. Levi, O., et al., *Difference frequency generation of 8-mu m radiation in orientation-patterned GaAs.* Optics Letters, 2002. **27**(23): p. 2091-2093.
94. Vodopyanov, K.L., et al., *Optical parametric oscillation in quasi-phase-matched GaAs.* Optics Letters, 2004. **29**(16): p. 1912-1914.
95. Faye, D., et al. *Highly efficient mid-infrared OPO based on low-loss Orientation-Patterned GaAs samples*. in *CLEO-IQEC 2007.* Technical digest p 1 . Munich, Germany.
96. Kondo, T. and I. Shoji, *Study on Wavelength Conversion by Compound-Semiconductor -Based Quasi Phase-Matching Devices*, *Photonics Based on Wavelength Integration and Manipulation*. 2005. IPAP. p. 151 - 160.

Chapter 2 Underpinning theory of ultrashort-pulse quantum-dot lasers

In Chapter 1 I introduced the overarching aims of my PhD project, describing the performance of state-of-the-art quantum dot devices and introducing my work within this research area. Chapters 4, 5 will detail the particular assessments undertaken by me in this topic. To be in a position to understand these devices properly, a basic understanding of the physics governing the operation of pulsed lasers is required. There already exist comprehensive sources of relevant information in publications such as those of references [1] and [2]. It therefore suffices here to summarise the most important concepts and their implications. Given that I am interested mainly in the development of ultrashort-pulse lasers, I will forego any discussion of constant-intensity lasing behaviour. I therefore begin by examining the different mechanisms which affect a pulse as it propagates through a dielectric medium and then discuss the different methods that can be used to initiate and sustain ultrashort-pulse generation. Specifically, I concentrate on gain switching then mode locking before going on to explore active and passive mode locking with a particular emphasis on saturable absorber induced mode locking in the context of quantum-dot lasers. This chapter concludes by describing methods used to measure the output characteristics of such lasers.

2.1 Laser pulses

A number of techniques exist for the characterisation of laser pulses, ranging from the interpretation of the longitudinal mode spectrum to nonlinear interactions such as autocorrelations. Understanding these techniques begins by considering how pulses of light propagate in optical media.

2.1.1 Mathematical description of an optical pulse

The following mathematical description of an optical pulse is based on that of Siegman [1]. An expression for the time-dependent electric field associated with such a pulse is shown below:

$$E(t) = \varepsilon(t)\exp[i\phi(t)]\exp[-i\omega_0 t] \qquad 2.1$$

In this expression, $\varepsilon(t)$ is the slowly-varying electric field envelope, ω_0 is the optical carrier frequency and $\phi(t)$ is the temporal phase variation across the pulse. We assume that the pulse envelope varies slowly with respect to the carrier frequency (slowly varying envelope approximation). If we Fourier transform the temporal field amplitude of such a pulse, we obtain its optical spectrum. It is therefore clear that changes in the temporal characteristics of a pulse such as phase must also be manifested in the spectral characteristics of the pulse. The relationship between these two factors is known as the bandwidth theorem and is described by the time-bandwidth product (TBP), which describes the minimum pulse duration that a specific spectral bandwidth can support [2]:

$$\begin{aligned} &\Delta\nu\Delta\tau_p \geq K \\ &K = 0.441 \text{ for a gaussian pulse} \\ &K = 0.315 \text{ for a } \sec h^2 \text{pulse} \end{aligned} \qquad 2.2$$

The expression states that the product of the spectral bandwidth $\Delta\nu$ and the pulse width $\Delta\tau_p$ must be greater than or equal to a constant *K,* with *K* depending on the specific pulse shape. The pulse shape itself depends on the nature of the pulse-forming mechanisms within the laser cavity and indeed the shape of the laser emission spectrum. For a given spectral bandwidth, the shortest possible pulse given by equation 2.2, is said to be transform-limited. A pulse exhibiting a TBP greater than *K* is not optimally short and is said to be frequency chirped.

The chirp of an optical pulse is the time-dependence of its instantaneous frequency and is an effect of propagation through a transparent dispersive medium. If a pulse possesses positive chirp, then its instantaneous frequency will increase with time (up-chirping). Control of this chirp is vital for the production of ultrashort pulses. Therefore, we can explore the factors that can give rise to frequency chirp in pulses propagating within a laser resonator and how this can be compensated.

As a pulse propagates through an optical resonator, it will interact with the various elements within the cavity. The manner in which interactions occur is accounted for by the induced polarisation:

$$P(E(r,t)) = \varepsilon_0[\chi_1 E(r,t) + \chi_2 E^2(r,t) + \chi_3 E^3(r,t) + ...] \qquad 2.3$$

Here, P is the total induced polarisation per unit volume, ε_0 is the permittivity of free space, χ is the susceptibility of the material and E is the electric field. The first term inside the brackets describes the linear optical properties of the material and describes phenomena such as refraction and linear dispersion. Higher-order terms inside the brackets describe the nonlinear behaviour induced in the material by intense optical fields. Understanding the contribution made by all these terms is crucial to the design of the devices fabricated and evaluated in my project.

2.1.2 Linear pulse propagation

When passing through a linearly dispersive optical medium, a pulse will experience a phase change $\phi(\omega)$ that depends on the frequency spectrum of the pulse [1].

$$\phi(\omega) = \frac{\omega}{c} L n_0(\omega) = \frac{2\pi L n_0(\lambda)}{\lambda} = \beta(\omega) L \qquad 2.4$$

In the above expression, ω is the angular frequency of propagating light, λ is its wavelength, L is length and c is the speed of light. The quantity $n_0(\lambda)$ is the wavelength dependent linear refractive index. These parameters define the propagation constant $\beta(\omega)$, where:

$$\beta(\omega) = \frac{n_0(\omega)\omega}{c} = \frac{2\pi n_0(\lambda)}{\lambda} \qquad 2.5$$

If we perform a Taylor series expansion of β about a centre frequency ω_0, we obtain the following:

$$\beta(\omega) = \beta_0 + \beta_1(\omega - \omega_0) + \tfrac{1}{2}\beta_2(\omega - \omega_0)^2 + \tfrac{1}{6}\beta_2(\omega - \omega_0)^3 + ... \qquad 2.6$$

These coefficients of β describe the different aspects of pulse propagation through a material. Firstly, the term β_0 is related to the phase velocity ν_ϕ in the medium. This parameter represents the velocity of the phase fronts of waves propagating inside the

dielectric as well as the velocity with which the central frequency of the pulse propagates. It is given by the following expression:

$$\beta_0 = \frac{\omega_0}{\upsilon_\phi} \tag{2.7}$$

The second term in the expansion is related to the group velocity ν_g of the propagating pulse in the dielectric medium and describes the speed of propagation of the envelope of the pulse. In a non-dispersive medium or a vacuum, the group and phase velocities exhibited by a pulse would be equal. However, in a dispersive dielectric medium, this is not the case. A pulse is made up from different frequency components; each having a different phase velocity ν_ϕ. Their superposition forms the pulse envelope which propagates through the medium with the following speed:

$$\beta_1 = \frac{d\beta}{d\omega} = \frac{1}{c}\left(n + \omega\frac{dn}{d\omega}\right) = 1/\nu_g \tag{2.8}$$

β_2 describes changes in shape of the pulse envelope as it propagates through the medium. This arises because different wavelength components of the pulse will experience different refractive indices and will not propagate with the same phase velocity. This is called the group velocity dispersion (GVD) and is given by the following expression:

$$\beta_2 = \frac{d\beta_1}{d\omega} = \frac{d^2\beta_0}{d\omega^2} = \frac{1}{c}\left(2\frac{dn}{d\omega} + \omega_0\frac{d^2n}{d\omega^2}\right) = GVD \tag{2.9}$$

In most dielectric materials, the GVD will be positive, which is referred to as "normal" dispersion. The effect of GVD in this configuration is that longer wavelength components in a pulse will propagate faster than those with a shorter wavelength. Transform-limited pulses travelling through a dielectric will experience a frequency dependent phase change, resulting in the pulse becoming frequency up-chirped. If β_2=0, an optical pulse can propagate indefinitely without broadening in the temporal domain, and the shape of the pulse envelope is thus unchanged. There are several dielectric materials such as some types of glasses which display this property for certain wavelengths. This was shown in figure 1.2 of Chapter 1 for fused silica. Third-order dispersive effects only become important when managing pulses with very short durations, typically around 10fs since the very broad bandwidths required to support such pulses mean that the frequency dependence of the group

velocity dispersion becomes important. These are described by the third term in the expansion.

$$\beta_3 = \frac{d\beta_2}{d\omega} = \frac{1}{c}\left(3\frac{d^2n}{d\omega^2} + \omega\frac{d^3n}{d\omega^3}\right) \qquad 2.10$$

2.1.3 Nonlinear pulse propagation

If we now start to consider more intense incident optical fields, we need to concern ourselves with higher-order terms in equation 2.3. These terms cover the situation in which the polarisation response to the incident field becomes nonlinear and gives rise to, for example, an intensity dependent refractive index, which is important for the pulse shaping of solid state lasers such as the titanium sapphire laser described in Chapter 4. In semiconductor lasers, carrier induced phenomena dominate at much lower powers and are of prime concern here, because pulse broadening tends to be dominated by carrier induced effects.

2.1.4 Self phase modulation in semiconductor lasers

A semiconductor laser pulse depletes carriers and hence the available gain as it propagates through the material. As such, the rear of the pulse experiences a higher refractive index than the front. Following the propagation of an optical pulse, the gain and refractive index recover to the initial steady-state levels. The relationship between gain and refractive index in semiconductor materials can be explained by Drude theory. The refractive index of a material is intrinsically linked to the polarisability of the material. In turn, this polarisability depends on the numbers of charge carriers present in the material. Thus, a change in carrier density causes an instantaneous alteration in refractive index.

This carrier dependent change in index also causes a phase shift in the pulse and a change in frequency. To analyze this, we consider the example of a plane wave:

$$E(t,x) = E_0 \exp i\phi(t) = E_0 \exp i(\omega_0 t - kx) \qquad 2.11$$

In the above expression, ϕ is the phase of the wave, ω_0 is the central angular frequency and $k = \omega_0 n(t)/c$. If we allow the refractive index to vary with time, we

have set up the requirements to allow the study of the SPM effect. Taking the time derivative of the phase, we will arrive at the instantaneous optical frequency. Applying this to 2.11:

$$\omega(t) = \frac{d\phi(t)}{dt} = \frac{d}{dt}(\omega_0 t - kx) = \omega_0 - \frac{\omega_0}{c}\frac{dn(t)}{dt} \qquad 2.12$$

Carrier depletion by an intense optical pulse alters the instantaneous frequency of the pulse. In semiconductor lasers, carrier depletion by a pulse tends to cause positive chirp in the gain section of a device. SPM does not directly increase the pulse duration, but since the additional frequency components are subject to additional GVD, higher chirp and longer pulse duration results. Thus, we see how the interplay between SPM and GVD causes pulse broadening in both spectral and temporal domains. It is worth noting that in special circumstances, these same factors can also balance to produce optical solitons, which exhibit zero broadening of both its temporal and spectral properties .

The parameter used to quantify the change in index with respect to changes in carrier density/gain is known as the linewidth enhancement factor α. It is described by the following expression:

$$\alpha = \frac{-4\pi}{\lambda}\left[\frac{\frac{dn}{dN}}{\frac{dg}{dN}}\right] \qquad 2.13$$

Here, n is the material refractive index, N is the carrier density and g is the gain per unit length [3]. This parameter was introduced when early investigations led to the observation that the emission linewidth of semiconductors exhibited broadening that could not be attributed to thermal effects. The work of Henry explained this phenomenon as a coupling between the gain of the laser and the refractive index [4].The parameter dg/dn that features in the equation is the differential gain of the system and can be thought of as the gain per carrier. One method to reduce the α factor and the resultant frequency chirp is to increase the differential gain of the material. Several authors have recently discussed the care required when assigning a linewidth enhancement factor to QD devices since it is strongly dependent on the pumping conditions and varies significantly from device to device in quantum-dot material from values much lower than those found in quantum-wells to significantly higher [5]. This is due to the varying contributions from the quantum states at

differing pumping strengths. As such, the linewidth enhancement factor loses some of its significance when considering quantum-dot material. However, it can still be of use provided that it is applied to a limited parameter range of laser operation.

2.1.5 Dispersion compensation

To obtain transform-limited pulses, we must introduce additional GVD of a sign and magnitude such that the net GVD is zero, or, in other words, compensate for the inherent GVD of the material. Semiconductor gain media exhibit positive GVD, therefore components with a negative GVD are required to offset this. There are a number of techniques that can provide this negative dispersion.

In monolithic semiconductor lasers, mode locking is often initiated by a reverse biased section [6]. Given that the carrier effects in this section are the opposite from those found in the gain section, so too will be the effects on wavelength chirp. There is therefore a degree of balancing of chirp between the gain and absorption sections which in an ideal case can lead to transform-limited pulse durations. However, this fine balance is hard to obtain in practice. Instead, mode-locked semiconductor lasers tend to exhibit net positive frequency chirp, resulting in pulse broadening and non-transform limited pulses.

To overcome this, external pulse compression schemes are often used. Such schemes tend to compromise the small size and inherent simplicity of the monolithic design. Pairs of diffraction gratings have been employed successfully to provide dispersion compensation by allowing the slower shorter wavelength components to experience effectively shorter paths around the cavity than their faster long wavelength counterparts [7]. Other techniques include the use of chirped mirrors [8] and Gires-Tournois interferometers [9]. The most common approach is to use pairs of prisms. First reported by Fork *et al*, this method places pairs of prisms in the cavity to provide the negative GVD required [10, 11]. A typical configuration for this scheme in a travelling-wave resonator is shown below in figure 2.1.

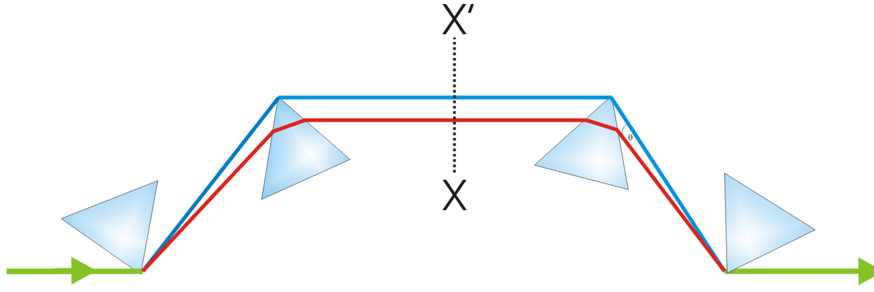

Figure 2.1. Typical 4-prism dispersion compensation scheme

In this system, the angle of light emerging from the first prism is dictated by its wavelength. Shorter wavelength components take a sharper exit angle than longer wavelength rays. This allows the shorter components to pass through less of the second prism. This amounts to a difference in optical path for short components compared with those of longer wavelength. By using this technique, carefully choosing the prism positions relative to each other, a negative, geometrically induced GVD can be introduced to the cavity. The plane XX' defines a plane of symmetry for the remaining two prisms. By placing a mirror at this position, two prisms can be made to perform the same task of four.

Looking at the mathematics of the system, the total dispersion of the prism sequence is given by:

$$D = \left(\frac{\lambda}{cL}\right)\frac{d^2P}{d\lambda^2} \qquad 2.14$$

where, P is the optical path length and L is the physical path length. The derivative in the expression depends on the different exit angles of blue parts of the pulse spectrum compared with red parts θ, the prism refractive index and the tip to tip separation of the prisms l. The total dispersion of the system is given in terms of femtoseconds[2].

$$\frac{d^2P}{d\lambda^2} = 4l\left\{\left(\frac{d^2n}{d\lambda^2} + \left(2n - \frac{1}{n^3}\right)\left(\frac{dn}{d\lambda}\right)^2\right)\sin(\theta) - 2\left(\frac{dn}{d\lambda}\right)^2\cos(\theta)\right\} \qquad 2.15$$

If the tip-to-tip separation, l, of the prisms is increased to a sufficiently large value, the overall dispersion introduced by the prisms becomes negative[1].

[1] Prisms are usually made from material that exhibits positive material dispersion. However, fused silica prisms exhibit negative dispersion when used at 1.3μm

2.2 Methods of obtaining ultrashort-pulse operation in lasers

This section covers the main approaches used to obtain ultrashort-pulse operation in semiconductor lasers. In my project, the primary method of interest is mode locking. A gain switching technique is also employed, although this is done mainly to provide an insight into the development of better mode-locked laser configurations.

2.2.1 Gain switching

Perhaps the simplest method for obtaining ultrashort pulses from a QD laser is to pump it with a short but powerful pump pulse. This can take the form of a short current pulse or alternatively a short, intense optical pulse. Such a short pump causes a large population inversion to build up rapidly from noise.

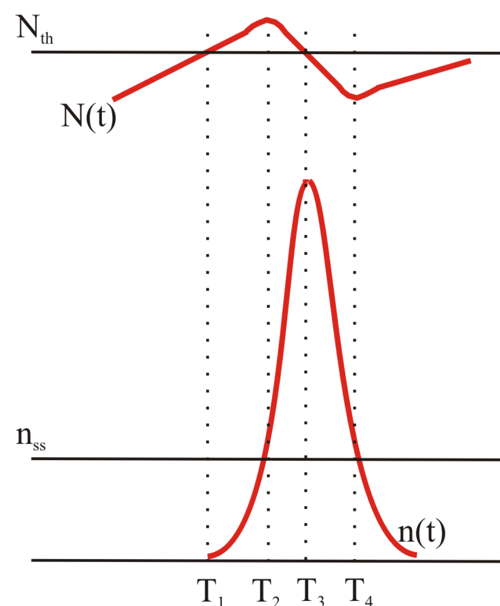

Figure 2.2. Evolution of population inversion N(t) and the corresponding cavity photon number n(t) (pulse profile). The population inversion rises above threshold at time T_1, corresponding to the leading edge of the pump pulse. This causes the number of photons in the cavity to increase. By T_2, the population inversion has reached its peak. Here, the rate of stimulated emission is equal to the rate of stimulated absorption and hence the number of photons in the cavity is equal to the steady-state value. At this level the field intensity inside the cavity is using up the population inversion faster than it can be replenished by the current pulse. This causes the number of photons in the cavity to grow at a very fast rate. At T_3, despite the fact that the inversion is no longer at a maximum, it is still above the threshold value and therefore the photon number continues to increase, further depleting the inversion. Then, when the inversion drops below the threshold value, the photon number in the cavity rapidly drops off. Finally, at T_4, the photon number drops below the steady-state value and the inversion begins to build up again slowly.

The result is the emission of an intense pulse of light as the large population inversion is rapidly lost due to the strong stimulated emission. The physics behind this is essentially the same as those relating to spiking and relaxation oscillations in lasers [1]. A diagram depicting population and photon number in side the cavity is shown above for an intense pump pulse.

Provided that the pump pulse is sufficiently short, it is possible to push the laser above threshold for only a very short period during the pumping cycle. This allows the extraction of a short, intense gain-switched pulse while subsequent smaller relaxation oscillations in the pumping cycle are suppressed. This simple method is capable of producing pulses directly from the device with picosecond durations provided the carrier dynamics in the gain material are sufficiently fast. Exceptionally, pulses as short as 20fs have been produced by a gain switched laser diode system employing a four-stage compression technique [12]. It is notable that prior to compression, the pulses produced by this system were 7.5 ps in duration – a typical duration for a gain-switched semiconductor laser [13, 14]. As such, this work is perhaps more a demonstration of the capability of pulse compression techniques as opposed to the fast dynamics of gain switching.

2.2.2 Q-Switching

The quality factor Q of a laser oscillator is given by the ratio of the power stored inside the oscillator to the power lost per optical cycle. If initially, the losses of the cavity are kept high by the inclusion of some sort of attenuator in the cavity the Q factor of the resonator is low and lasing is suppressed. In this regime, a lot of gain can be stored inside the cavity, filling the upper level of the laser to create a very large population inversion. By then reducing rapidly the losses of the resonator, it is possible to extract all the stored energy into one intense pulse. With the losses switched to a lower level, a laser energy field rapidly builds up in the resonator by stimulated emission of the stored up inversion, but this high level of emission cannot be maintained and the pulse dies off again. In diode lasers, Q-switching can be implemented in two-section diode lasers, providing picosecond pulses at high repetition rates [15, 16]. In solid-state lasers, Q-switching is often achieved by means of an electro-optic switch inside the cavity. Pulses produced by this method typically

have nanosecond durations. The 1 μm Nd:YAG laser used in chapter 7 operated using Q switching.

2.2.3 Mode locking

Mode locking is the most widely used technique for the operation of lasers that can produce ultrashort pulses. The basic premise of the method is to force the different longitudinal modes of the laser to enter into a fixed, stable phase relationship with one another. This causes ultrashort, intense pulses to be emitted with a separation determined by the cavity round-trip period [17].

One way to understand mode locking is to examine a standing-wave cavity as shown below in figure 2.2 below. In this simple configuration, it is evident that since the longitudinal modes of the laser are also standing modes of the cavity, the wavelength of these modes will be determined by the spacing between the mirrors.

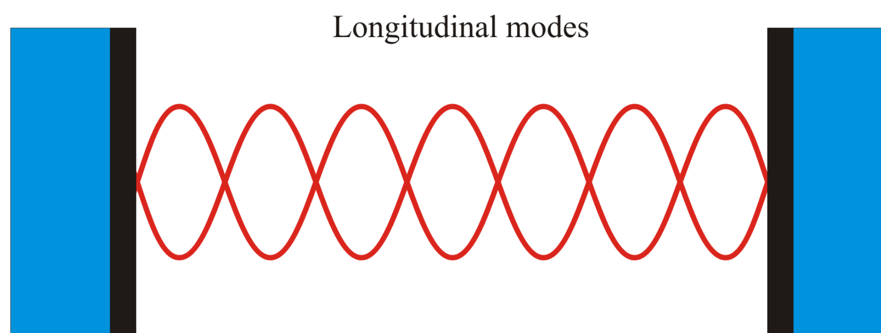

Figure 2.3. Simple two-mirror cavity showing standing modes

This means that the frequency separation between adjacent longitudinal modes of the laser in will be given by the following.

$$\Delta\upsilon = \frac{c}{2nl} = 1/\tau_{RT} = f_{cav} \qquad 2.16$$

In terms of wavelength, the spacing between adjacent modes is then given by

$$\Delta\lambda = \frac{\lambda^2}{2nl} \qquad 2.17$$

In the above expressions, c is the speed of light, l is the cavity length and n is the average refractive index. The quantities τ_{RT} and f_{cav} are the cavity round-trip delay and cavity frequency spacing, respectively. The precise operating wavelength of a laser is thus determined by a combination of both the emission bandwidth of the gain material and the cavity length.

In mode-locked lasers, broad gain bandwidths allow many modes to participate in the lasing process. If we consider a simplified situation where N contributing longitudinal modes have equal amplitude, we can express the output electric field from the laser as a function of time in the following manner.

$$E_{tot}(t) = \sum_{n=1}^{n=N-1} (E_0) \exp[i(\omega_n t + \phi_n)] \qquad 2.18$$

Here, ω_n and ϕ_n are the angular frequency and phase of the n_{th} longitudinal mode. In an unmode-locked regime, the relative phases of the contributing modes are all varying randomly. In this case, the total intensity is equal to the sum of the modal intensities. The total intensity at any given time will remain relatively constant.

By contrast, in a mode-locked laser, the relative phase of the participating modes is fixed. Using this in expression 2.18 and simplifying the resulting power series, we arrive at the following expression for the electric field as a function of time.

$$E_{tot}(t) = (E_0) \exp[i(\omega t)] \left[\frac{\sin(N\Delta\omega t/2)}{\sin(\Delta\omega t/2)} \right] \qquad 2.19$$

Hence, the total intensity as a function of time is given by the following.

$$I_{tot}(t) = [E_{tot}(t)]^2 = (E_0)^2 \left[\frac{\sin^2(N\Delta\omega t/2)}{\sin^2(\Delta\omega t/2)} \right] \qquad 2.20$$

We see that the intensity is directly proportional to the number of modes N. Plotting the output intensity as a function of time now produces a series of discrete and intense pulses. This is shown below in figure 2.4 for the case of a relatively small number of longitudinal modes.

The narrow peaks in the output intensity occur at time intervals where many longitudinal modes in the laser are in phase with one another. The separation of the pulses is given by the inverse of the round-trip frequency of the laser. The duration of the pulse is determined fundamentally by the number of modes that are locked in phase. It is for this reason that lasers with broad emission bandwidths are capable of producing ultrashort pulses, but also why a large GVD is so detrimental to the operation, because it inhibits the modes from maintaining the necessary phase relationship.

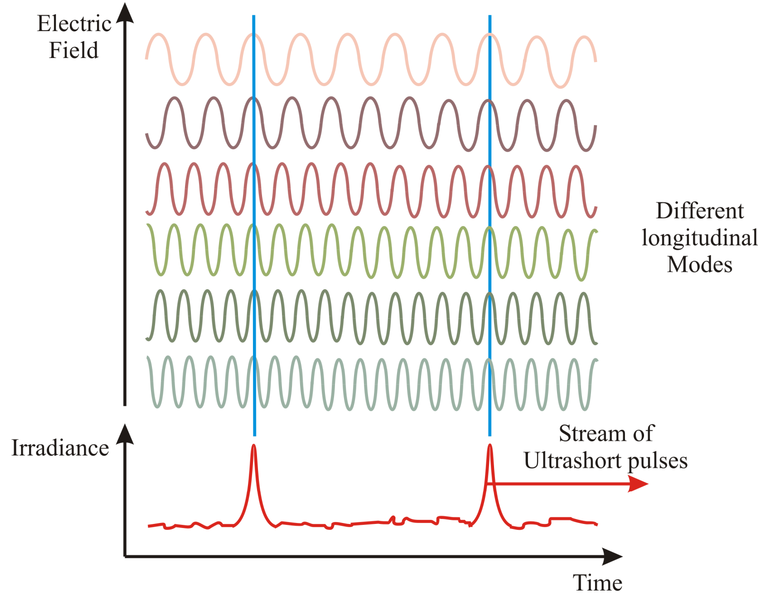

Figure 2.4. Mode-locked laser output and phase relationship between a small number of contributing modes

Ideally, all of the laser energy should be concentrated in the pulses with interpulse energy that is essentially zero. The relationship between the average power emitted by the laser and the peak power contained in an ultrashort pulse is as follows [18].

$$P_{Pk} = 0.92\frac{E_p}{\Delta\tau_p} = \frac{0.92P_{av}}{\Delta\tau_p f_{cav}} \qquad 2.21$$

Here, P_{Pk} and P_{av} refer to the peak and average power of the system and E_p is the energy contained in the pulse. If we consider a system with a pulse duration of 100 fs, a round trip time of 10 ns and an average power of 100 mW, this would give a peak power of 9.2 KW! This assumes a Gaussian pulse shape. For a hyperbolic secant pulse shape, the factor of 0.92 in equation 2.26 becomes 0.88. The numerical factors arise because in real pulses, a significant portion of the pulse energy can reside in its wings.

2.3 Mode locking techniques in quantum-dot lasers

Having looked at the basic principles, we will now explore the different methods used to facilitate mode locking. The main techniques that are used are described as active, passive or a mixture of both, namely hybrid, mode locking. Active mode locking uses externally applied modulation of the gain applied at the cavity frequency f_{cav}. This

gives a high degree of control over the various parameters of the modulating signal. In addition, the external modulation signal provides a reference signal which can be useful for signal processing and telecommunications. Unfortunately, it is very difficult to generate very fast RF signals, making this technique less practical for the mode-locking of lasers that have very short cavities. Active mode locking is also fundamentally limited by the fact that the characteristics of the modulation imposed on the laser field are determined solely by the external electronic modulating element. While this modulation can be accurately tuned to the laser repetition frequency, it is inflexible in that it does not depend on the specific conditions in the cavity and cannot adapt itself to provide a suitably optimized degree of modulation.

2.3.1 Passive mode locking

Passive mode locking (PML) overcomes these limits by using a saturable absorber element to provide self–amplitude-modulation (SAM) of the laser field. This is most easily understood by considering a simple two mirror cavity as in figure 2.2 but with the addition of a saturable element as introduced above. When the laser output is initialised, the phases of the constituent modes are random. This causes the output of the laser to behave in an essentially continuous wave manner. There will be random fluctuations and perturbations in the total field inside the resonator, however, that produce random noise fluctuations in the internal field. If one, or as is more often the case, a group of these noise fluctuations has an energy density sufficient to bleach the absorber, it will experience lower loss than the peripheral lower amplitude areas of the noise and will experience a higher round-trip gain. Once established, this process repeats itself and promotes the formation of a sequence of pulses. The balance between loss and gain once a pulse is established is shown in figure 2.5. below. The fact that gain is outstripped by loss in between periods of pulse formation explains why no other sets of pulses are able to form.

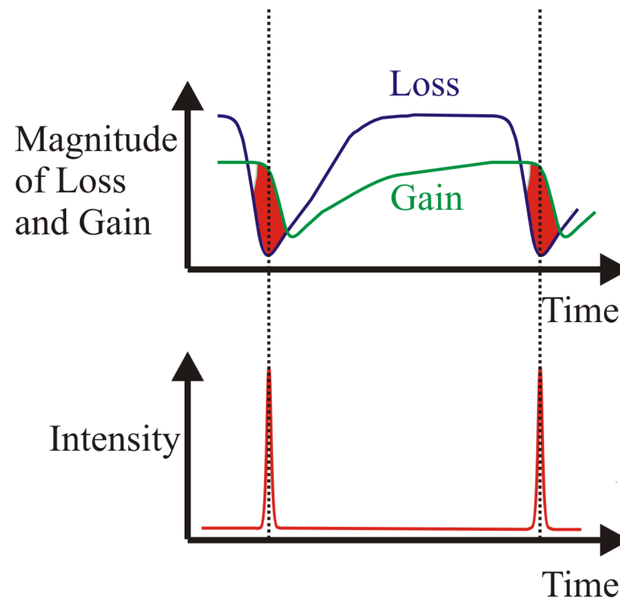

Figure 2.5. Illustration of saturable absorber loss and laser gain as a function of time and resultant pulse production. Shaded areas in the top sketch indicate areas where gain outstrips loss and pulses are produced. A necessary requirement is thus that the loss saturates faster than the gain. Semiconductor lasers display slow saturable absorption behaviour because their gain and absorption sections are made from similar material [19].

There are several methods of creating an absorber in a semiconductor laser. In monolithic devices, one can use ion implantation to modify one of the laser facets [20]. This creates additional trap states which behave as an absorber. Another method involves constructing a split contact laser. The active region is split into two sections, each electrically isolated from the other. The laser gain section is forward biased in the normal manner while the intended absorber section has either zero bias or a reverse bias applied. In this configuration, carriers in the absorber section are pushed out of the absorber by the internal electrostatic forces. A reverse biased absorber recovers to its original highly attenuating rest state more quickly than in the unbiased case. This is due to the increased tunnelling of carriers out of the dot states taking place in the reverse biased case [21].

2.3.2 Semiconductor saturable absorber mirrors and saturable Bragg reflectors

Semiconductor lasers can be mode-locked in additional ways. Through exploitation of molecular beam epitaxy (MBE) and metal-organic vapour phase epitaxy (MOVPE), it is possible to tailor the linear and nonlinear optical properties of ultrathin layer

structures. Such growth techniques can be used to integrate a semiconductor saturable absorber directly onto a mirror structure which then provides both feedback and acts as a mode locking element

Both semiconductor saturable absorber mirrors (SESAMs)[22] and saturable Bragg reflectors (SBRs) [23] exhibit an intensity dependent reflectivity, favouring operation in a pulse regime. Both SESAMs and SBRs have been used extensively to mode-lock solid state lasers without being subject to the stringent cavity alignment required for Kerr-lens mode locking. Both types of device are very similar in terms of their structure and the principles governing their operation. As such, SBRs can be thought of as a subcategory of SESAMs. Any differences between the two are to be found in the specific details of their growth and post production. Details of their differences can be found in the review paper by Keller [22].

2.3.3 Important SESAM parameters for successful mode locking

There are five factors that define the performance of SESAM or SBR devices.

i) Ultrafast carrier dynamics are essential for any saturable absorber because successful operation requires that an absorber should be saturated on a short timescale and recover to its original state of high loss (relax) on an equally short timescale. By this token, the recovery time of the absorber τ_A, after a pulsed induced saturation is of critical importance to the production of ultrashort pulses. Ideally, after complete saturation by a pulse, the absorber should be able to completely relax long before the arrival of the next pulse. Therefore the recovery time of the absorber must be less than the round trip period of the cavity. A similar condition applies to the gain if differential amplification instabilities are to be avoided. Semiconductor lasers can have very short cavity lengths. For instance, a 3mm long laser has a cavity frequency of around 15 GHz and this corresponds to less than 60 ps for its round-trip period.

ii) Another very important factor is the saturation fluence F_{satA}, which is defined as the pulse fluence required, such that the remaining fractional unsaturated loss of the absorber after such a pulse is equal to $1-e^{-1}$. This dynamic process can also be understood in the context of pulse energy. The saturation fluence is equal to the saturation energy E_{satA} per unit area of the laser mode cross section. To initiate and maintain stable mode locking, the energy required to saturate the absorption of the

gain should be less than that required to saturate the gain as outlined in the expressions below.

$$E_{satA} = \frac{h\nu A}{a/N} < E_{satG} = \frac{h\nu A}{g/N} \qquad 2.22$$

In the above expression, ν is the optical frequency of the laser, h is Planck's constant while a,g/N are the differential loss and gain i.e. the loss and gain per carrier. In satisfying 2.27 the existence of the gain window shown in figure 2.5 is allowed. Fortunately, in semiconductor material this favourable situation is ensured since $\frac{\partial \alpha}{\partial n} > \frac{\partial g}{\partial n}$ [24]. In this project, the specific design of the external cavity for the QD SESAM mode-locked QD lasers enables the fluence to be varied somewhat by varying the cavity length and making small adjustments to the spot size on the SESAM.

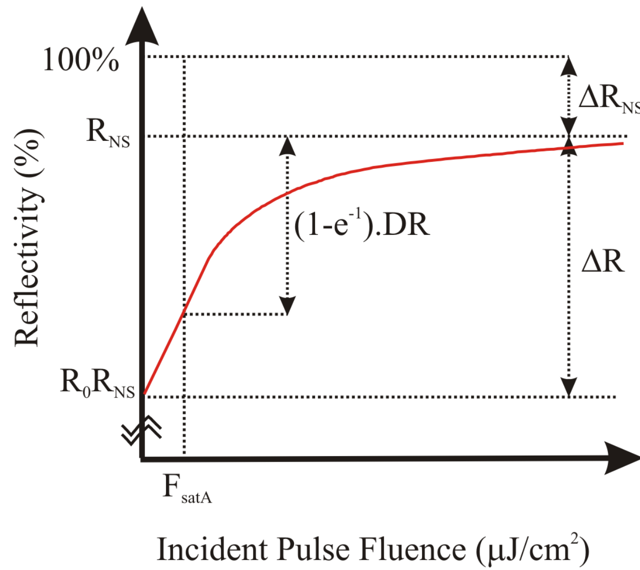

Figure 2.6. SESAM reflectivity as a function of incident pulse fluence

Concentrating specifically on mirror based saturable absorbers; there are three main parameters that describe how such absorbers perform (figure 2.6). The modulation depth ΔR of the SESAM is the maximum change in reflectivity between the relaxed absorber state and that exhibited when a pulse with large fluence fully bleaches the absorber. The pulse will have an energy density which is larger than the saturation fluence of the absorber $F_{satA.}$ By using SESAMs with large modulation depths, strong modulation of the laser field can be achieved however, excessive modulation depths can cause problems such as an increase in Q-switching instabilities

[25]. These occur because the modulation of the laser field becomes strong enough or the recovery of the gain slow enough such that successive pulses experience differing levels of attenuation. The consequence of this is that the mode-locked pulse train becomes subject to further modulation by the comparatively slowly varying Q-switched envelope [22].

The non-saturable loss, ΔR_{NS}, is the loss of the device which remains after bleaching by a highly intense pulse. The magnitude of this loss factor is strongly related to the manner in which the device has been designed. Various factors including scattering losses, residual absorption and the reflectivity of the bottom Bragg mirror are taken into account in ΔR_{NS}. The quantity R_0R_{NS} is the reflectivity of the device when the pulse fluence incident on the device is close to zero. By a similar token, R_{NS} is the device reflectivity when a very highly fluent pulse fully saturates the absorber.

Finally, we consider the spectral bandwidth of the SESAM. The spectral bandwidth determines the upper limit on the number of modes which the SESAM can lock together and consequently the minimum pulse duration obtainable with that particular SESAM. This parameter is usually limited by the reflection bandwidth of the Bragg mirror located beneath the absorber layer. Several methods such as selective oxidation have been utilised in order to increase the refractive index contrast between the layers of the mirror stack and thus increasing the bandwidth of the device. In Chapter 5 I describe the use of a QD SESAM that features a very wide spectral bandwidth.

There are several types of commonly used SESAM structures. The first types of SESAM were high finesse antiresonant Fabry-Perot structures (HFA-FPSA). The basic material structure of such a device is shown below in figure 2.7a [26].

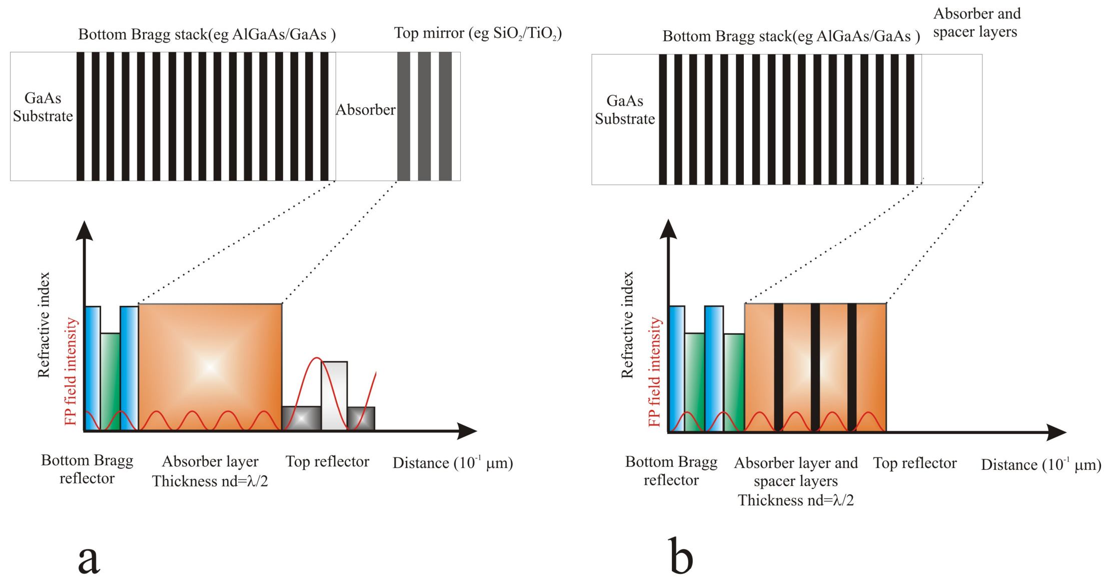

Figure 2.7. (a) HFA-FPSA material structure and (b) LFA-FPSA material structure.

In the case of 2.7a, a bottom Bragg reflector consisting of very thin alternating layers of GaAs and AlGaAs with thickness λ/4 is grown on top of a GaAs substrate. The absorber layer typically consists of a quantum well, multiple wells or layers of quantum dots grown on top of this. Finally a top mirror is provided by a highly reflecting SiO_2/TiO_2 Bragg structure. This creates a Fabry-Perot (FP) type of structure in the absorber region of the device. The thickness of this region is chosen such that it is antiresonant at the wavelength of operation, meaning that minima in the electric field intensity are located at the edges of the Fabry-Perot structure. When this is satisfied, the device exhibits broadband reflection and minimal group velocity dispersion [22, 26]. The bandwidth of the SESAM is limited in most cases by either the reflection bandwidth of the Bragg mirrors or by the free spectral range of the Fabry-Perot cavity. The inclusion of spacer layers between the absorbing layer(s) and the Bragg mirrors can alter the saturation fluence of the device by changing the distribution of the electric field maxima in relation to the absorbing layers of the device.

An alternative SESAM configuration involves the removal of the upper highly reflecting mirror. In this configuration, shown in figure 2.7b, Fresnel reflections provide the feedback at the top of the Fabry-Perot cavity. This low finesse structure requires a thinner absorber and a bottom mirror exhibiting higher reflectivity to minimise losses [22]. In the figure, the absorber areas are placed at positions of

maxima in the F.P. field. The saturation fluence can be altered by changing the position of the absorbing section relative to the maximum of the standing wave inside the Fabry-Perot cavity. Because different wavelengths will have different nodal positions in the standing-wave profile, this can be used to reduce the wavelength dependence of the absorber edge, thereby giving improved broadband performance.

SESAM structures can also be designed to operate in resonance. This is achieved by careful choice of both cavity length and the layer of material terminating the cavity. In this configuration, the standing wave inside the Fabry-Pérot cavity has an anti-node of intensity at the Fabry-Pérot boundary. These types of devices exhibit different GVD behaviour and typically lower saturation fluences due to the enhanced Fabry-Pérot field [27].The quantum-dot SESAM discussed in Chapter 5 was designed to operate close to resonance.

2.3.4. Ideal SESAM parameters for a semiconductor laser

Now that I have outlined the important SESAM parameters that define their performance, it is useful to have in mind the approximate values these should take in order to mode-lock optimally the semiconductor lasers in which we are interested. Ideally, we would like the spectral bandwidth of the SESAM to be as wide as possible, and it is worth noting that a bandwidth of 13nm is capable of producing 200fs pulses at 1300nm for an assumed Gaussian pulse shape. Secondly, and as previously stated, the absorber must recover faster than the round trip period of the cavity. In the case of the quantum-dot based SESAM device described in Chapter 5, this condition is easily satisfied due to the ultrafast carrier dynamics of the absorber. A rule of thumb as far as saturation energy is concerned according to Keller is that laser pulses incident on the SESAM should provide in the region of 3 – 5 times the saturation fluence of the absorber [22]. This helps suppress the likelihood of Q-switching stabilities manifesting themselves. For a semiconductor laser with a length of 3mm, average power of 20mW and pulse duration of 200fs, this corresponds to a pulse energy of around 1pJ. This results in a saturation energy of around 0.25pJ. In the case of the external-cavity QD laser described in Chapter 5, the cavity round-trip period is considerably longer which results in a higher pulse energy. We require a modulation depth in the structure that is higher than that required to mode-lock a

solid-state laser (typically 1% - 3%) and considerably less than that needed for a fibre laser (15 - 20%). In the case of the non-saturable loss of a SESAM, the higher gain of a semiconductor laser perhaps makes this less important than in low gain lasers, but in general, it is best to operate in a low-loss regime for optimal performance.

2.4 Ultrashort-pulse measurement

Four of the most important parameters defining the operation of an ultrashort pulse laser are as follows: average power, optical output spectrum, repetition frequency and pulse duration. Average power can be measured simply by a power meter and is the most trivial of the measurements. The optical spectrum can be determined with an optical spectrum analyser while the repletion frequency can be obtained by the use of a fast photodiode and a radio frequency spectrum analyser. All of these are very quick and easy measurements to perform.

The most demanding quantitative measurement is that of the pulse duration because this cannot be done electrically for the ultrashort pulse durations involved. One solution is a technique known as autocorrelation [28] where the pulse duration is calculated for an assumed pulse shape by using the pulse itself as an instrument of metrology. It is very important for accurate measurements when using this method that the shape of the pulses being investigated is known. Despite the fact that sech^2 pulses and ones with a Gaussian profile may look similar, significant differences exist (see equation 2.7) in their time-bandwidth products.

2.5.1 The two-photon autocorrelator

Figure 2.8 below shows the basic set up for the two-photon autocorrelator that is at the heart of the method.

In this scheme, which is basically a Michelson type of optical delay line, an incoming pulse is split at the beam splitter. One copy of the pulse strikes a static mirror and is reflected into a detector. The other copy of the pulse strikes a movable mirror. Because mirror M2 is moving backwards and forwards, the optical path difference between the two pulse copies is constantly changing.

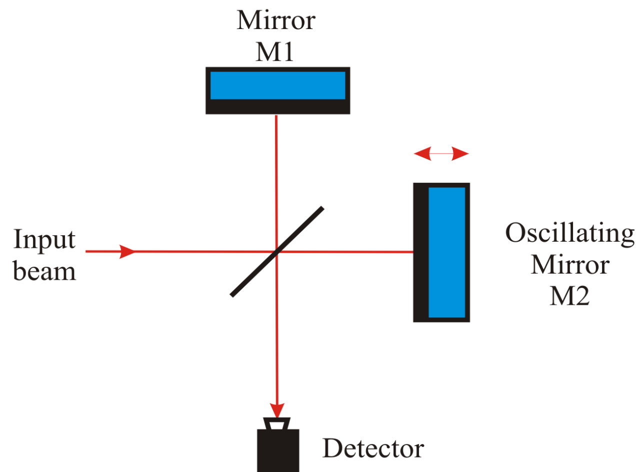

Figure 2.8. Two-photon autocorrelator.

At times when the path difference is zero, the two copies will be completely overlapping and interfere constructively, and destructively for a phase difference of π. When a path difference exists, the two copies will be out of sync with each other by an amount given by this optical path difference. When the pulses overlap, there will be significantly higher intensity incident on the detector resulting in a nonlinear response. This nonlinear response will only be produced for the period of overlap of the pulses. This is intrinsically connected to the width of the pulse.

Typical ways to achieve this nonlinearity are through the use of a second harmonic crystal placed before the detector or through the use of a diode which will give a quadratic response by means of two-photon absorption. One difficulty in using a nonlinear crystal is that additional alignment must be performed to ensure correct phase-matching in the crystal. In addition, when measuring ultrashort pulses, thin crystals have to be used to ensure that the phase matching bandwidth of the crystal is large compared to the frequency bandwidth of the pulse. When looking for the two-photon signal produced by a laser diode, incident photons with energy greater than the bandgap of the diode will be absorbed in a linear manner for low intensities of light. However, should a suitably intense signal be incident on the detector, then less energetic photons with energies given by $\frac{1}{2} E_g < E < E_g$ will be absorbed by a nonlinear two-photon process. This will produce the required quadratic response. This approach is polarisation insensitive and is inherently broad bandwidth. It is also cheaper than the SHG crystal approach since an additional photomultiplier tube is not required.

Provided that the two arms of the autocorrelator are aligned perfectly, the detector will measure a signal which is related to the degree of overlap of the two pulse copies. This can be described by the following expression.

$$G(\tau) = \int_{-\infty}^{\infty} \left| \left[E(t) + E(t-\tau) \right]^2 \right|^2 d\tau \qquad 2.23$$

In the above expression, G(τ) is the degree of overlap which is a function of the delay time τ between pulses. E(t) represents the electric field of the pulse as a function of time. Provided that the autocorrelator is calibrated for a relatively slow frequency response, the device will measure a time averaged intensity autocorrelation. This is defined as follows:

$$G_i(\tau) = 1 + 2g(\tau)$$

where

$$g(\tau) = \frac{\int_{-\infty}^{\infty} I(t)I(t-\tau)dt}{\int_{-\infty}^{\infty} I(t)^2 dt} \qquad 2.24$$

In the above expressions, g(τ) is the background free autocorrelation function. This measurement uses equations which contain information purely regarding intensity. This method contains no information regarding the frequency chirp of the signal. A ratio of 3:1 exists between signal level and background for values of τ=0 and ±∞ respectively in equation 2.9. This defines the contrast ratio for an intensity autocorrelation. We find that the relationship between the pulse duration $\Delta\tau_p$ and the width of the autocorrelation Δt trace is given by:

$$\Delta\tau_p = \frac{\Delta t}{k} \qquad 2.25$$

k is the intensity autocorrelation conversion factor which depends on the shape of the pulse. For a Gaussian pulse, k=1.414 and a $sech^2$ pulse has k=1.543. This allows us to calculate the actual pulse duration from the trace assuming a specific shape. Figure 2.9 shows a typical intensity autocorrelation trace.

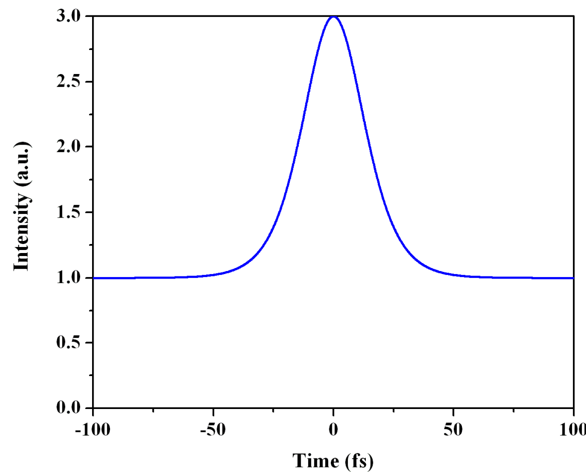

Figure 2.9. Intensity autocorrelation trace showing 3:1 ratio displaying a FWHM of approximately 30fs

The intensity autocorrelation is the simplest of the autocorrelation techniques and also contains the least information. More complicated techniques such as interferrometric autocorrelations can be employed in order to provide additional information about the pulse, such as its frequency chirp profile.

2.5. Conclusions

In this chapter I set out to describe the various mechanisms affecting an optical pulse as it propagates through a dispersive medium. These processes such as dispersion and self-phase modulation determine the spectral and temporal characteristics of propagating pulses. With these mechanisms in place, I outlined the different ways in which one can instigate ultrashort pulse generation in a laser and how such pulses can be characterised. These will be of direct relevance to the work described in subsequent chapters of the thesis.

This provides a motivation for my work together with the theoretical descriptions of the mechanisms that underpin the operation of ultrashort pulse semiconductor lasers. In Chapter 3, I will describe the techniques required to fabricate both ultrashort pulsed semiconductor lasers and how these techniques can also be applied to fabricate structures for nonlinear frequency conversion.

References

1. Siegman, A., *Lasers*. University Science Books 1983
2. Trager, F., *Springer Handbook of lasers and Optics*.: Springer Science + Business Media, LLC New York, 2007
3. Melnik, S. and G. Huyet, *The linewidth enhancement factor alpha of quantum dot semiconductor lasers.* Optics Express, 2006. **14**(7): p. 2950 - 2955.
4. Henry, C.H., *Theory of the Linewidth of Semiconductor-Lasers.* IEEE Journal of Quantum Electronics, 1982. **18**(2): p. 259-264.
5. Gioannini, M. and I. Montrosset, *Numerical analysis of the frequency chirp in quantum-dot semiconductor lasers.* IEEE Journal of Quantum Electronics, 2007. **43**(10): p. 941-949.
6. Rafailov, E.U., et al., *High-power picosecond and femtosecond pulse generation from a two-section mode-locked quantum-dot laser.* Applied Physics Letters, 2005. **87**(8).
7. Treacy, E.B., *Optical pulse compression with diffraction gratings.* IEEE Journal of Quantum Electronics, 1969. **5**(9): p. 454 - 458.
8. Ripin, D.J., et al., *Generation of 20-fs pulses by a prismless Cr4+: YAG laser.* Optics Letters, 2002. **27**(1): p. 61-63.
9. Szipocs, R., et al., *Negative dispersion mirrors for dispersion control in femtosecond lasers: chirped dielectric mirrors and multi-cavity Gires-Tournois interferometers.* Applied Physics B-Lasers and Optics, 2000. **70**: p. S51-S57.
10. Fork, R.L., O.E. Martinez, and J.P. Gordon, *Negative Dispersion Using Pairs of Prisms.* Optics Letters, 1984. **9**(5): p. 150-152.
11. Martinez, O.E., R.L. Fork, and J.P. Gordon, *Theory of Passively Mode-Locked Lasers Including Self-Phase Modulation and Group-Velocity Dispersion.* Optics Letters, 1984. **9**(5): p. 156-158.
12. Matsui, Y., M.D. Pelusi, and A. Suzuki, *Generation of 20-fs optical pulses from a gain-switched laser diode by a four-stage soliton compression technique.* IEEE Photonics Technology Letters, 1999. **11**(10): p. 1217-1219.
13. Downey, P.M., et al., *Picosecond Dynamics of a Gain-Switched Ingaasp Laser.* IEEE Journal of Quantum Electronics, 1987. **23**(6): p. 1039-1047.
14. Arakawa, Y., et al., *Picosecond pulse generation (<1.8 ps) in a quantum well laser by a gain switching method.* Applied Physics Letters, 1987. **51**(17): p. 1295 - 1297.
15. Cakmak, B., *Passively Q-switched operation of a double contact tapered InGaAs/GaAs diode laser.* Microelectronic Engineering, 2003. **65**(3): p. 273-278.
16. Yang, S.H., et al., *Generation of high-power picosecond pulses from a gain-switched two-section quantum-well laser with a laterally-tapered energy-storing section.* IEEE Photonics Technology Letters, 1996. **8**(3): p. 337-339.
17. Keller, U., *Ultrafast solid state lasers*, *Progress in Optics* 2004, Elsevier B. V.
18. RPPhotonics, Article on peak power, 2008 *http://www.rp-photonics.com/peak_power.html*.
19. Haus, H.A., *Theory of Mode-Locking with a Slow Saturable Absorber.* IEEE Journal of Quantum Electronics, 1975. **11**(9): p. 736-746.

20. Deryagin, A.G., et al., *Generation of 110 GHz train of subpicosecond pulses in 1.535 mm spectral region by passively modelocked InGaAsP/InP laser diodes.* Electronics Letters, 1994. **30**: p. 309 - 311.
21. Malins, D.B., et al., *Ultrafast electroabsorption dynamics in an InAs quantum dot saturable absorber at 1.3 mu m.* Applied Physics Letters, 2006. **89**(17).
22. Keller, U., et al., *Semiconductor saturable absorber mirrors (SESAM's) for femtosecond to nanosecond pulse generation in solid-state lasers.* IEEE Journal of Selected Topics in Quantum Electronics, 1996. **2**(3): p. 435-453.
23. Tsuda, S., et al., *Mode-locking ultrafast solid-state lasers with saturable Bragg reflectors.* IEEE Journal of Selected Topics in Quantum Electronics, 1996. **2**(3): p. 454-464.
24. Yu, S.F. and E.H. Li, *Influence of the lateral field on the relaxation oscillation frequency of semiconductor lasers.* IEEE Journal of Quantum Electronics, 1996. **32**(1): p. 1 - 3.
25. Honninger, C., et al., *Q-switching stability limits of continuous-wave passive mode locking.* Journal of the Optical Society of America B-Optical Physics, 1999. **16**(1): p. 46-56.
26. Keller, U., et al., *Solid-State Low-Loss Intracavity Saturable Absorber for Nd-Ylf Lasers - an Antiresonant Semiconductor Fabry-Perot Saturable Absorber.* Optics Letters, 1992. **17**(7): p. 505-507.
27. Spuhler, G.J., et al., *Semiconductor saturable absorber mirrir structures with low saturation fluence.* Applied Physics B-Lasers and Optics, 2005. **81**: p. 27 - 32.
28. Barry, L.P., et al., *Autocorrelation of ultrashort pulses at 1.5 mu m based on nonlinear response of silicon photodiodes.* Electronics Letters, 1996. **32**(20): p. 1922-1923.

Chapter 3 Fabrication

In this Chapter I will describe the processes necessary to fabricate the devices used in this PhD research project. While I do not discuss the particular fabrication requirements of each device type in this chapter (the experimental details can be found in the specific chapters), I give an overview of the main techniques employed. This can then be used as a reference for the sample fabrication work discussed in the subsequent experimental descriptions.

3.1 Molecular Beam Epitaxy

Since its conception in the 1960s at Bell labs, molecular beam epitaxy (MBE) has become perhaps *the* key enabler in the development of a wide range of semiconductor devices. It allows the formation of extremely high quality single crystalline material, due to the system permitting material to be grown layer by atomic layer. It also allows the formation of heterostructures of arbitrary composition. A diagram of an MBE system is shown below in Figure 3.1. The basic process underlying the technique is quite simple. Material which is to be deposited is held in effusion cells. These are heated until the material inside undergoes evaporation. This hot beam of molecules is then incident on a heated substrate such that these molecules diffuse over this surface and eventually adhere, becoming part of the material [1].

For a high quality single crystalline material to be formed, growth must occur in an ultra high vacuum environment which is naturally very low in impurities. Evaporated material should not interact with any other molecules during transit from the effusion

cells to the target material. It follows, therefore, that the mean free path of the molecules should be larger than the physical size of the MBE chamber. Typical pressures used in MBE systems are of the order of 10^{-11} mbar.

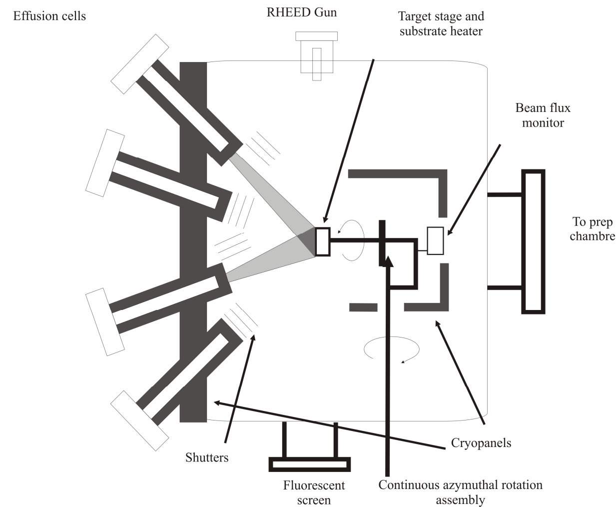

Figure 3.1. Diagram of key MBE system components. Image adapted from

http://www.elettra.trieste.it/experiments/beamlines/lilit/htdocs/people/luca/tesihtml/node24.html

To achieve this extremely low pressure, a long bake out at several hundred degrees Celsius is required in conjunction with a multi-stage evacuation process. These ensure that the chamber is adequately devoid of undesirable molecules. As seen in figure 3.1, the target substrate is held on a heated stage which rotates to ensure uniform deposition on the material. Beams of evaporated material emerge from the effusion cells and are directed towards the sample stage. The stage is also cryogenically screened to prevent unwanted fluxes of material being deposited. Deposition rates are monitored by reflection high energy electron diffraction (RHEED). Given that multiple molecular species can be deposited simultaneously by using more than one effusion cell at once, for example, by utilising three cells, containing aluminium, gallium and arsenic and varying their flux contributions, it is possible to deposit AlGaAs material with varying proportions of its constituent elements.

An alternative approach for the fabrication of epitaxially grown layers is metal organic vapour phase epitaxy (MOVPE). This is widely used in the manufacture of laser diodes and uses chemical reactions as a vector for layer formation as opposed to physical deposition, as is the case with MBE. Also, while molecular beam epitaxial growth is conducted at very low pressures, MOVPE takes place at pressures that are much more comparable to atmospheric pressure.

Epitaxial growth was the starting point for the fabrication of all of the devices used in my project because high quality heterostructures were central to both the ultrashort pulsed lasers and frequency conversion structures that I investigated. MBE was also used to produce the domain inversion central to the orientation patterned structures that will be discussed in Chapter 7. Once these epitaxially grown wafers have been produced, it is necessary to lithographically pattern them, not only to form ridge waveguides but to assist (where required) in the production of the desired nonlinear effects. The principal lithographical technique employed in this project was photolithography.

3.2 Photolithography

Photolithography, one of the most widely used methods for patterning semiconductor materials, utilises a photosensitive resist. This resist is spun onto the semiconductor material and then by subjecting this resist to incident light of a specific wavelength, an induced chemical reaction alters the physical properties of the resist. A liquid substance known as a developer is then used, in the case of a positive resist, to remove the resist that has been exposed to the light. Conversely, in the case of a negative

resist, exposure to the light causes the properties of the resist to be altered in such a way as it becomes resistant to the developer. This is known as cross-linking.

A mask, typically made of glass, coated with metal on one side, is used to expose a desired pattern on the semiconductor material. The mask is held in close proximity to the material such that opaque areas on the mask prevent the light from interacting with the corresponding area of photoresist underneath. Conversely, transparent areas allow the material underneath to become exposed.

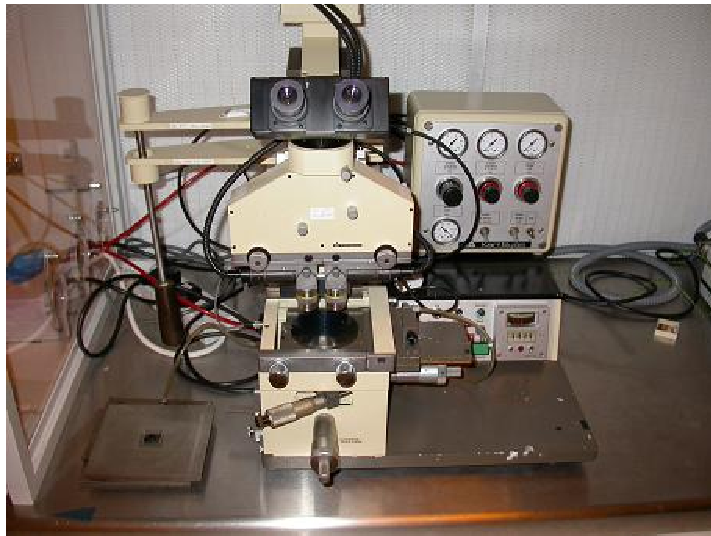

Figure 3.2. Picture of mask aligner

A mask aligning machine is used to correctly orient the sample with respect to the mask. Pictured above in Figure 3.2, the Karl Suss MJB3 mask aligner used in this work. It comprises a moveable x-y-z stage, allowing micrometer precision adjustments to the sample position in three dimensions. The mask is held above, suspended from a plate by a vacuum. Alignment is done by eye using a movable microscope objective and light from a shutter-controlled ultraviolet lamp provides the exposure. By careful control of the distance between sample and mask and the length of exposure to the UV light, patterns can be transferred accurately from the mask. The mask aligner had interchangeable mask holders, each with a different seized viewing window, ranging from 1 sq in up to 3 sq in. The ultraviolet lamp used to perform the exposures emitted light with an intensity of 3.1 ± 0.1 mW cm−2 and 5.3 ± 0.1 mW cm−2, at 365 nm and 400 nm, respectively. Under optimal conditions, the mask

aligner had a resolution of around 2 microns, thus providing a comfortable tolerance for the manufacturing I performed in this thesis. For the work covered in this Thesis, the positive resists SR 1805 which forms a layer 500 nm thick and SR 1818, which forms a layer 1.8 microns thick were used. These resists are commercially available from ROHM HAAS Electronic materials [2]. Below in table 3.1, is a description of the basic processes used when utilising these types of resist.

Resist type	SR-1805	SR-1818
Spin speed	5000 RPM	5000 RPM
Bake time/temperature	1min/100° C	1min/100° C
Exposure time	9.5 ± 1 seconds	25 ± 2 seconds
Development time	30 seconds	30 seconds
Development solvent	MF319	MF319
Resist removed by	Acetone (rinsed off in IPA)	Acetone (rinsed off in IPA)

Table 3.1. Processing requirements for positive resist types used

The parameters in the above table assume that the U.V. bulb in the mask aligner has been allowed approximately 15 mins to equilibrate and is not approaching the end of its lifetime, when its output tended to vary in intensity.

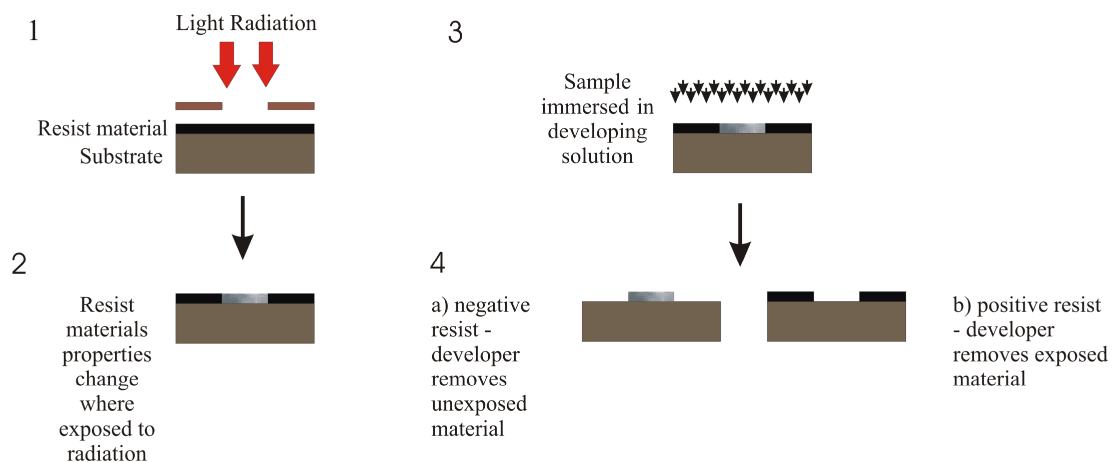

Figure 3.3 – The process of applying, exposing and developing both negative (a) and positive (b) resists.

[2] http://www.rohmhaas.com/wcm/products/browse.page?

A typical process (shown in Figure 3.3) for patterning material using SR1805 resist is as follows. The resist is placed on the material using a dropper. This is then spun at 5000 rpm for 1 minute, forming a uniform layer about 500 nm thick. To drive off solvents, the sample (which is now coated with resist) is then heated to a temperature of 100°C and baked for 1 min. At this time, the quality of the resist layer is checked through optical inspection. Any bubbles or specks of dust in the resist are severely detrimental to the quality of exposure obtainable and subsequently the quality of structure obtainable. If necessary, the resist is easily washed off the sample with acetone at this stage, the sample cleaned and a new resist layer applied. Low magnification and an ultraviolet filter must be employed to prevent accidental exposure of the resist during inspection

The sample is then ready for exposure to the ultraviolet light in the mask aligner lithography machine. Care is needed to find the optimum exposure dose/time because incorrectly exposing the resist will result in features that do not correspond precisely to those on the mask. For a 500 nm thick resist, an exposure time of around 9.5 seconds was found to be sufficient. When using SR1818 resist, which produces a 1.8 μm thick resist layer, a 23 second exposure is used. The sample is then placed in developing solution (here MF319) for approximately 30 seconds. As the resists used in this work are positive in nature, areas of the resist which were exposed to the light are removed by the developer, leaving the unexposed areas. Again, careful optical inspection is employed at this stage to check the quality of the transferred pattern.

Considerable project time and effort were dedicated to the optimisation of the photolithography steps in the sample fabrication processes. For some aspects of my work, large samples were fabricated containing very small features throughout and, in this case, great care was needed to ensure that the exposure was balanced across the

whole of the surface of the sample, with features on the mask being transferred accurately to the sample surface uniformly over the material. Several factors were important when trying to achieve this. It is essential that mask and sample are parallel to each other, with the photomask in flat contact with the material. Any angular deviation between the two, results in mask and sample having different vertical separations at either end. This will inevitably cause a non-uniform exposure. With small samples, this source of error can be ignored as the two ends of the sample are sufficiently close together. However, for the sample sizes involved here, this is an important point to consider.

Due to the nature of the spinning process used to apply photoresist to the sample surface, resist will tend to gather preferentially round the edge of the sample, forming a thicker crust - this is known as an edge bead. Removal of this edge bead with either a razor blade or a cotton bud with acetone is also important if optimum results are to be produced.

Another issue which was discovered in the process of optimisation was the tendency for the sample to stick to the mask during exposure, resulting in improper exposure. This was solved by securing the sample to a glass coverslip prior to resist spinning. This was also useful since it allowed handling of the sample without touching the delicate resist surface with tweezers which could easily damage it.

3.3 Chemically-assisted Ion-beam Etching

Once a pattern has been lithographically defined, it is necessary to transfer the desired design from the resist material to the semiconductor itself. The main method used in this thesis was chemically-assisted ion-beam etching (CAIBE) [2]. This process is

widely used in many areas of semiconductor device fabrication, such as in photonic crystal manufacture. One of the prime reasons for the usefulness of CAIBE is the accurate control that it provides over the etch profile.

CAIBE can be thought of as a hybrid technique, incorporating chemical and physical mechanisms to etch features into semiconductor material. Various gas mixtures can be utilised to allow different materials to be etched. The system used in the facilities in the university labs at St Andrews is designed for the processing of III-V type semiconductors. One suitable etchant of these compounds is chlorine gas. A sample which is to be processed is held under vacuum while chlorine gas is introduced to the evacuated chamber. At the same time, argon ions are accelerated towards the sample from above. A high vacuum (provided by a turbo-pump) is needed so that undesirable molecules, not intended to be involved in the etching are removed and cannot therefore affect this process.

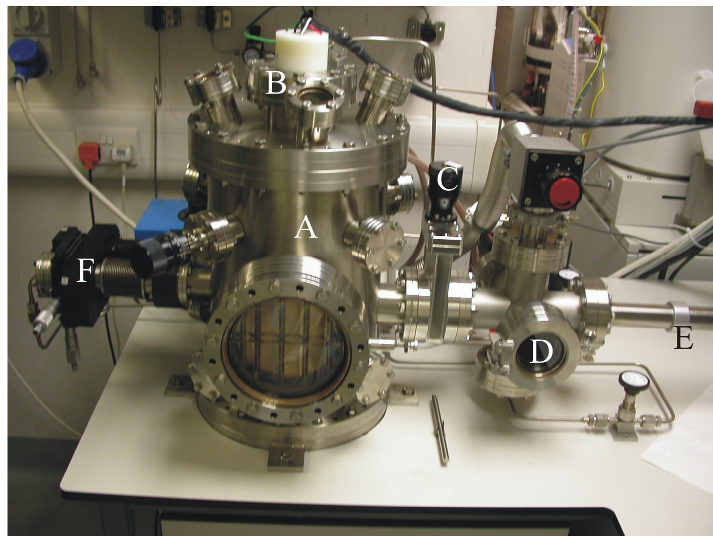

Figure 3.4. CAIBE system developed in St Andrews

The system used in the St Andrews facilities is shown above in Figure 3.4. Of the several key components that make up the system one is the low-vacuum chamber (D) this is used to perform the rough pumping stage, whereby the air pressure in the high

vacuum chamber is lowered from atmospheric pressure down to around $5x10^{-1}$ millibar. This pressure is too high to perform the etching process. Vacuum pumps capable of reaching these low etch suitable vacuums are unsuitable for operation at high vacuum and would be damaged if exposed to atmospheric pressure. It is therefore necessary to have a two-stage evacuation process initially using the roughing pump then once appropriate vacuum has been reached, a turbo-pump. Once the vacuum is deemed to be sufficiently low, the roughing pump is switched off. At this point, a valve (C) which separates the poor vacuum roughing chamber from the main etching chamber (A) can be opened safely. The sample is then moved into this main compartment by means of a movable arm (E). Once this has been accomplished and the arm retracted, the valve is closed.

The main etching chamber (A) consists of a stage upon which the sample rests, connected to a heating coil. Directly above this stage is an aluminium ring, designed to deliver the etchant chlorine gas to the sample. The position of this ring may be altered by use of three micro positioning stages (F). At the top of the main chamber lies the ion gun (B). Essentially this consists of a discharge chamber, where the argon gas is ionised. These ions are then extracted and accelerated towards the bottom of the chamber and the sample by the potential difference. A series of magnetic coils are used to control the focus and collimation of the beam. At all times, the main chamber is kept under a very low vacuum by the use of the turbo pump.

Considered in isolation and assuming that GaAs is the material to be etched, areas exposed to chlorine gas will undergo chemical reactions governed by the following relationships [3].

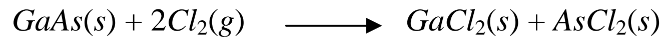

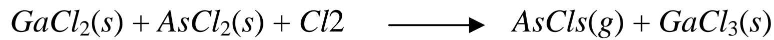

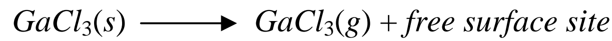

Without the addition of argon ions, this chemical etching would proceed at a slow rate – typically several nanometres per minute. As the temperature of the sample is increased, this rate will increase. In addition, the use of chemical etching as the sole mechanism for sample processing will tend to produce an anisotropic etch profile which bulges out at the sides, as is visible in Figure 3.5. The reason for this is that the etching gas will etch the sides of the trench more quickly than its floor. Movement of fresh gas to the bottom of the trench will be restricted by the trench itself. This restriction is less for the sides of the trench.

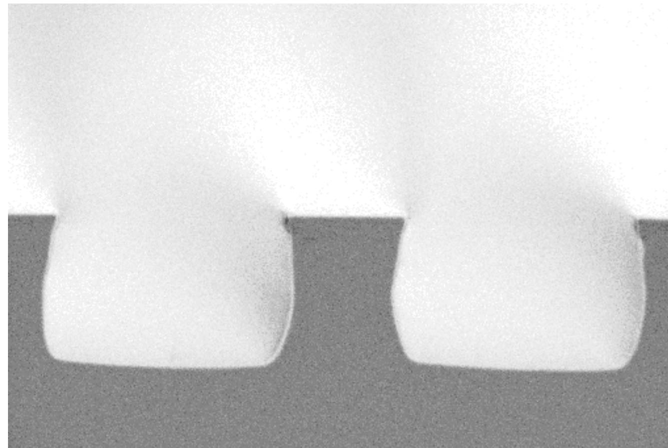

Figure 3.5 – Anisotropic etching caused by an imbalance between chemical and physical etch components, in this case an excess of chemical etching causes the formation of bowed walls

With the addition of physical etching provided by the accelerated argon ions, the etch rate increases significantly (> 100 nm/min). Used in isolation, this physical

etching which is also known as ion milling would produce an etch profile which decreased in width as the etch depth increased. This is because there is insufficient etching perpendicular to the direction of ion movement and poor removal of sputtered material.

CAIBE utilises both chemical and physical etching. Careful control of both components allows features to be etched with vertical sidewalls. Experimenting with different sample temperatures and chlorine gas flow rates allows the chemical component to be constrained. Conversely, by altering the beam voltage and current we change the kinetic energy of argon ions contained in the plasma, this allows control over the physical component of the etch.

As the etch proceeds, the sample will be heated by the presence of the plasma. This will result in a corresponding increase in chemical etch rate. Thus, an empirical set of criteria or a recipe can be developed to produce the desired etch parameters. In the work carried out here, straight, smooth consistent etching was an essential requirement.

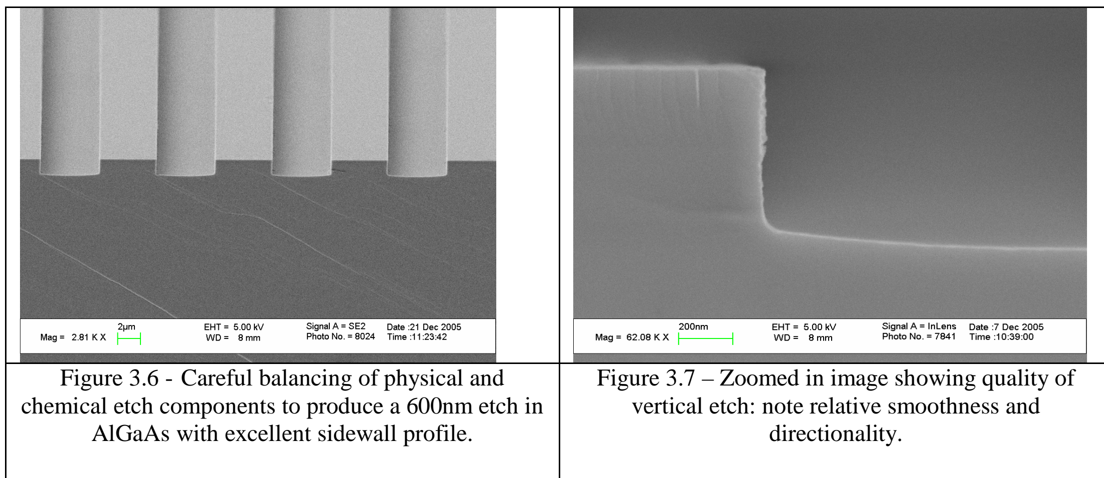

Figure 3.6 - Careful balancing of physical and chemical etch components to produce a 600nm etch in AlGaAs with excellent sidewall profile.

Figure 3.7 – Zoomed in image showing quality of vertical etch: note relative smoothness and directionality.

Figures 3.6 and 3.7 display SEM images of the type of optimised etch parameters required. A variety of etch parameters was investigated before a suitable

set giving the desired results was obtained. This process and its outcomes are described below.

In the work described in this thesis, two distinct types of CAIBE etches were required, in the case of the samples manufactured to create a periodically-switched nonlinearity, where etches are required to define both the grating and waveguide. One etch recipe was found to be suitable for both purposes. This relatively fast etch was capable of removing in excess of 3 microns of material, provided that the thicker SR 1818 resist was used as a mask. The recipe developed is shown below in table 3.2:

Beam Voltage	1450 V
Beam current	15 mA
Argon flow rate	10 sccm (standard cubic centimetres per minute)
Chlorine flow rate	5 sccm
Etch rate	420 nm/min

Table 3.2. Etch recipe for waveguide etching and PSN grating formation

This etch recipe is an adaptation of that detailed in [4], which was developed to create photonic crystal devices. As such, the selectivity of the of the process is high (as much as 50:1 in terms of mask selectivity). This figure is quoted for the case for photonic crystal fabrication in GaAs, where a silica hard mask is required to transfer patterns from the soft electron beam resist pmma (polymethylmethacrylate) into the GaAs material. Electron beam resists such as pmma are rarely tough enough to be used directly as masks for CAIBE [5, 6]. In the case of the photoresists used in this work, their toughness allows them to be used directly without the need for an intermediate mask, which allows for more simple manufacture of devices. Also, since the mask will not be etched away by the chlorine gas, its etch rate is solely determined by the incident ions from the ion beam.

The second type of etch developed was designed to accurately and reproducibly remove significantly smaller amounts of material – of the order of 100 nm. For this, a far less energetic ion beam and lower gas flow rates combine to give an etch which proceeds in a much slower manner. This etch recipe was adapted from one developed for etching of shallow waveguides for the formation of lasers as in the thesis of McGreehin [7]. The recipe for this etch is shown below in table 3.3.

Beam Voltage	350 V
Beam current	10 mA
Argon flow rate	10 sccm
Chlorine flow rate	2.5 sccm
Etch rate	170 nm/min

Table 3.3. Etch recipe developed for shallow etch OP-GaAs grating

These recipes were developed by utilising existing etch recipes for other III-V semiconductor materials already in use by colleagues, then systematically varying the etch temperature, gas flow rate and ion beam characteristics, analysing the results by microscopy until optimal results are obtained.

In general, the CAIBE technique can be optimised to give excellent selectivity as detailed above and in [4]. The smoothness of etches obtained can also be extremely high since roughness caused by argon ion impacts is to a large extent smoothed out by the chemical component of the etch. The resolution required by the fabrication detailed in this thesis does not approach the limits of the CAIBE system at St Andrews, where in photonic crystal etches routinely produce features demonstrating excellent smoothness which are around 250 nm in diameter [8]. As such, in this thesis,

I was able to use CAIBE to very accurately transfer the mask patterns into the semiconductor material.

3.4 Ion Implantation

The technique of ion implantation can be implemented to produce a variety of effects in semiconductor material. The basis of the technique is the introduction of ions of a certain species into material of differing composition. This implanting of ions can alter both the chemical and physical properties of the material.

One common use for the process in to enable quantum-well intermixing. Here, spatially selective implantation of ions into the material causes a local modification of the semiconductor bandgap, creating localised passive device areas at locations of choice. This then allows the creation of passive (non-absorbing) mirrors which reduce the possibility of catastrophic optical damage [9].

Typical ion implantation equipment will resemble the diagram shown below in Figure 3.8. Plasma is created by passing a high current through some elemental species. The liberated ions are then extracted and propelled through the machine. A series of magnets then steer the beam through the mass analysing slit. Here, the desired ion variety, charge and isotope are selected. After this, the ions are accelerated to the desired energy by a potential gradient. Magnetic lenses then shape the beam as required. The target material is held in a vacuum chamber upon a stage.

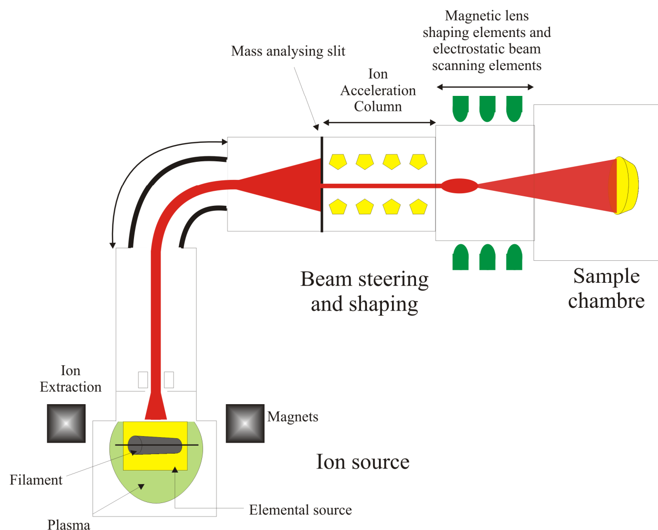

Figure 3.8. Diagram of a typical ion implantation machine. Image adapted from http://www.spirecorp.com/spire-biomedical/surface-treatment/technology-overview/ion-implantation.php

A wide range of ion doses and energies can be employed depending on the application requirements. The depth of penetration of ions in a material is typically less than a micron, but, by varying the energy of the ions, this can be controlled. In my work, the penetration depth was tailored to be around 1 micron.

As expected, increasing the energy of the ions allows deeper penetration into the material. The dose of ions refers to the time integral of the ion current and is essentially the total number of ions incident on the target material surface during the process. The degree of modification to the chemical and physical properties of bombarded material is related to this dose factor. (Interestingly, it is possible for ions to penetrate more deeply into a material than should be possible for a particular energy. Given a sufficiently high ion dose, a resonant transfer of energy can occur between ions in the material with the result of modification to the material occurring at depths greater than the maximum penetration of the implanted ions [10].)

Following the implantation process, it is often necessary to subject the samples to thermal annealing. This is because ion implantation tends to cause significant

structural damage to the target material in addition to a desired effect - ion impacts cause defects to form in the material which increase the loss. By annealing the material, repair of some of this damage can be achieved while still preserving the desired specific functionality gained by performing the implantation. Within the context of my project, the type of implantation undertaken is of the most aggressive kind, because of the desire to amorphise specific areas of the target material. This is discussed in greater depth in Chapter 7.

3.5 Analytical tools

The two main methods employed to quantify the dimensions of fabricated structures were scanning electron microscopy (SEM) and atomic force microscopy (AFM) [11]. SEM imaging was used to measure the depth of etched features and to assess the quality of surfaces after processing. Scanning electron microscopy was first developed as an analytical tool in thhe 1930s, with commercial systems not becoming available till the 1960s due to the complicated electronics involved with beam scanning [12]. In a scanning electron microscope, a high energy beam of electrons (with typical energies in the kV range) is directed at the surface of the material of interest. Interactions between incident electrons and the material surface are then detected through mechanisms such as backscattering and secondary electron emission. This allows an image of the material surface to be constructed. The resolution of the microscope is determined by the focal spot of the electron beam which can be a small as 10s of nanometres. The shorter characteristic wavelength of electrons compared with a visible photon accounts for the higher resolutions attainable in SEM [13].

Calibration of the system with a laser interferometer allows the SEM to be used for precision measurements in conjunction with its imaging capability.

Some of the structures fabricated were difficult to evaluate accurately using SEM because features present on the surface were both shallow and wide in nature. Atomic force microscopy (AFM) provided a useful alternative measurement technique capable of accurately examining these challenging features. In an AFM, a small cantilever with a fine tip is scanned across the surface of the material of interest. Forces act on the tip when it comes into close proximity to the surface resulting in a deflection of the cantilever given by Hooke's law [14]. A laser beam reflected off the tip of the cantilever onto an array of photodiodes records any movement as shown below in Figure 3.9.

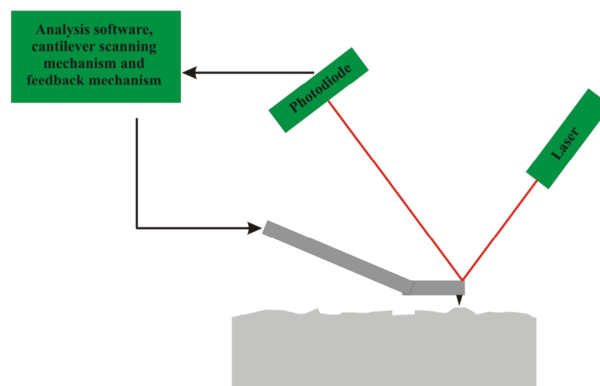

Figure 3.9. Principal of operation for atomic force microscopy. Image adapted from http://en.wikipedia.org/wiki/Atomic_force_microscope

A feedback mechanism is employed to maintain an optimal distance between tip and material, avoiding grounding of the tip or loss of signal due to too great a separation. A piezoelectric motor provides the ability to move the tip in the plane of the material, mapping out the surface and this technique can provide sub-nanometre resolution in three dimensions [15]. The field of view is more restricted than in SEM, typically limited to around 100 μm x 100 μm but this can generally provide more information

as to the vertical profile of a surface. AFM is best employed for viewing surfaces with small changes in vertical profile (less than 500 nm) and where fine detail is required about the topography, due to the sub Angstrom vertical resolution possible using the technique [11].

3.6 Concluding Remarks

As stated at the outset of this chapter, this overview type of summary relating to these principal fabrication techniques should be seen as a backdrop to the particular procedures that I deployed in preparing a range of optoelectronic structures and devices in my PhD project. The next two chapters build on the ideas developed here to describe the fabrication and testing of ultrashort-pulse quantum-dot (QD) lasers where my work starts with an investigation of the electronic state transition dynamics in an optically-pumped QD laser.

References

1. Alferov, Z.I., V.M. Andreev, and N.N. Ledentsov. *Semiconductor heterostructures, Ioffe Physico-Technical Institute,* http://edu.ioffe.ru/edu/alferov.html
2. Tyrrell, G.C., et al., *Chemical routes to GaAs etching with low energy ion beams.* Journal of Condensed Matter, 1991. **3**: p. 179 - 186.
3. O'Faolain, L., *The fabrication of microstructures for ultrashort pulse generation in monolithic modelocked semiconductor lasers*, PhD Thesis, *School of Physics and Astronomy*. 2005, University of St Andrews
4. Kotlyar, M.V., et al., *High-aspect-ratio chemically assisted ion-beam etching for photonic crystals using a high bean voltage-current ratio.* Journal of vacuum science and technology B, 2004. **22**(4): p. 1788-1791.
5. Kotlyar, M.V., *Photonic crystal waveguides and tunable filters in InP*, *PhD Thesis, School of Physics and Astronomy*. 2005, University of St Andrews: St Andrews.
6. Avary, K., et al., *Deeply etched two-dimensional photonic crystals fabricated on GaAs/AlGaAs slab waveguides by using chemically assisted ion beam etching.* Microelectronic Engineering, 2002. **61-62**: p. 875 - 880.
7. McGreehin, S.J., *Integrated optical manipulation in microfluidics*, *PhD Thesis, School of Physics and Astronomy*. 2006, University Of St Andrews.
8. O'Faolain, L., et al., *Low-loss propagation in photonic crystal waveguides.* Electronics Letters, 2006. **42**(25): p. 1454-1455.
9. *Quantum- Well intermixing overview, Intense Photonics,* http://www.intenseco.com/technology/default.asp
10. Peng, N., *Personal communication*, *2004-2008*
11. Binnig, G., C.F. Quate, and C. Gerber, *Atomic Force Microsciope.* Physical Review Letters, 1986. **56**(9): p. 930 - 934.
12. *Electron microscopy,* http://www.unl.edu/CMRAcfem/em.htm.
13. Halliday, D., R. Resnivk, and J. Walker, *Fundamentals of Physics*. 4 ed. 1993: Wiley. 1306.
14. *Baselt, D. Atomic force microscopy,* http://stm2.nrl.navy.mil/how-afm/how-afm.html#General%20concept
15. Wikipedia.org. *Atomic force microscope*. 2008. http://en.wikipedia.org/wiki/Atomic_force_microscope

Chapter 4 Properties of Quantum-dot Materials

This chapter begins with a description of the basic physics that underlies the operation of semiconductor diode lasers. This lays the foundation for the development of quantum confinement in one dimension as a method for improving device performance. I then go on to discuss implications of this confinement with regard to practical quantum-dot (QD) devices. After this groundwork has been done, I discuss my own investigations into QD material within the particular context of the generation of ultrashort pulses. This comprises a study of the transition dynamics of femtosecond optically-pumped quantum-dot material and a discussion of how this new information can be applied to develop QD lasers that can produce ultrashort optical pulses. Some of this work has been published in Applied Physics Letters and it was the featured article within that issue [1]. The work was also presented IEEE Annual Meeting 2005 in Sydney and was selected to be published in supplementary virtual journals [2].

4.1 Background Semiconductor Physics

It is well known that the properties of a semiconductor lie between the 'extreme' charge-carrier characteristics of metals and insulators. A semiconductor (at room temperature) possesses a full valence band and an empty conduction band, much like an insulator. However, the gap between valence and conduction bands is sufficiently small such that under increased temperatures, electrons may be thermally excited across the energy gap into the conduction band. There exist several comprehensive texts covering the subject of semiconductors and semiconductor lasers [3-6], but I will present only the key features that are relevant to the development of semiconductor lasers.

The numbers of free carriers in a semiconductor can be controlled by the introduction of donor impurity atoms into the semiconductor host material. Dopant atoms are chosen with a number of valence electrons such that when they form bonds with the host atoms in the semiconductor material, not all of the bonding requirements of the system are satisfied. This leaves loosely bound charges that can be excited

readily across the band gap and thus have mobility within the material. The process of n-type doping involves adding small concentrations of atoms with additional electrons while p-type doping involves adding small amounts of atoms with fewer valence electrons than the host material resulting in the creation of free positive entities called holes. The addition of impurities to semiconductor material allows the formation of a p-n junction that represents a configurational option that is key to the operation of semiconductor diode lasers.

4.1.1 The p-n Junction

A p-n junction is formed at the interface between a section of p-doped semiconductor material and a section of n-doped material. Initially, a carrier imbalance exists in the depletion region of junction interface. Electrons and holes diffuse across the p-n interface to redress this and in doing so, establish the in-built junction electric field. Figure 4.1 shows the various biasing states possible for the junction.

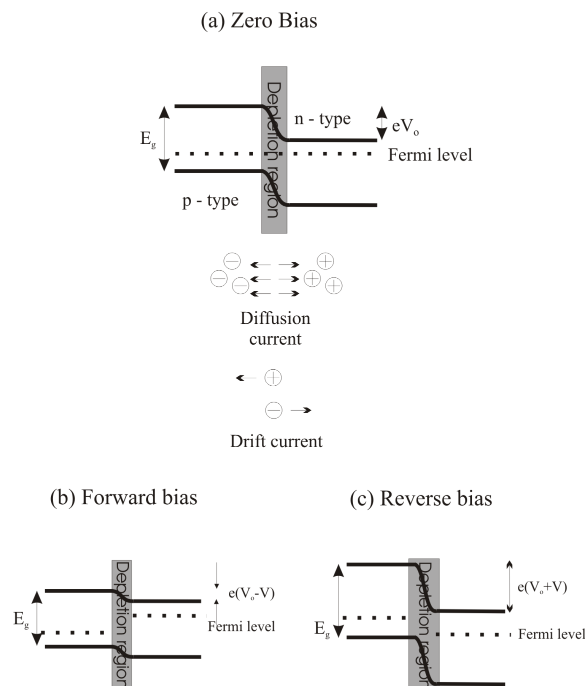

Figure 4.1. p-n junction under (a) equilibrium conditions and under (b) forward and (c) reverse biasing conditions. This picture is adapted from [3].

When no external voltage is applied to the material, free electrons in the n-type material will diffuse into the p-doped region. In interacting with a hole, the electron will occupy the vacancy. This initial movement of carriers constitutes a diffusion current. Now, positively charged ions in the n-type region left behind after their corresponding free electron diffuses across the junction act as potential barriers, making it increasingly more difficult for subsequent free carriers to diffuse across the junction. They form an electric field which acts to decrease diffusion across the junction. This electric field manifests itself in the form of a drift current shown above; acting to make electrons move from the p-region to the n-region. This is the origin of the space charge (depletion) region between p-type and n-type materials which becomes devoid of free charges. With reference to figure 4.1 (a), it can be seen that the Fermi level (which is the energy level which is situated in such a position so as its probability of occupancy is 50%) of the junction is constant across the interface. In the equilibrium situation the drift and diffusion currents balance each other, resulting in a total current density of zero. The absence of carriers in the space charge region therefore "effectively" makes the junction appear as an insulator.

A photon incident on the junction may be absorbed, promoting an electron/hole pair across the bandgap by the photoelectric effect. The photon will impart energy given by:

$$E_g = hc/\lambda = eV \qquad 4.1$$

In the above expression E_g corresponds to the energy gap in electron volts between the valence and conduction bands. V is the voltage generated in the device and e is the charge of the electron. The quantities h, c and λ refer to Planck's constant, the speed of light and the wavelength of photon absorbed respectively.

Under forward biased conditions as in figure 4.1(b), charges are swept across the junction, attracted to the opposite side. Given a large applied voltage, carriers can overcome the in-built potential barrier of the unbiased junction and a current can flow. In addition, the shape of the valence and conduction bands change and the Fermi level is no longer constant across the junction.

In a reverse-biased diode configuration (figure 4.1(c)), the applied field acts to pull each majority carrier away from the p-n interface. Given these conditions, the

diffusion current is reduced to negligible levels and the dominant process is the drift current [7]. This causes an increase in the potential barrier which electrons and holes must overcome to cross the p-n junction. Under these conditions the p-n junction again effectively acts as an insulator, similar to the case of an isolated junction. With the dominance of the drift current, the junction now acts to extract carriers.

4.1.2 Recombination

Both forward and reverse biasing of p-n junctions are of great importance to the work described in this thesis. They are central to the ability of semiconductor material to act as a vehicle for both optical gain and loss processes [6]. When the junction is in a forward-biased configuration, carriers are promoted into the conduction band. This creates gain due to stimulated emission processes. The physical mechanism of recombination concerns an electron in the conduction band recombining with a hole in the valence band. If the electron and hole recombine by a radiative process, a photon will be released with energy given by equation 4.1, which is clearly the opposite to the absorption effect discussed previously. In the reverse bias situation, the junction behaves as an absorber and the photo-generated carriers are swept out by the applied voltage. Once a certain number of photons have been absorbed by the material, the previously available empty states are occupied by the photo-generated carriers and the absorption subsequently saturates.

4.2 Semiconductor Diode Lasers

Semiconductor diode lasers consist of a forward-biased pn junction made from heavily doped material such the Fermi level in the n-type (p-type) region lies in the conduction (valence) band. Semiconductor laser materials such as GaAs are grown epitaxially in well ordered crystal lattices. Cleaving along crystallographic axes forms high quality optical facets which provide sufficient optical feedback for laser action to be established and sustained. The earliest homojunction semiconductor lasers exhibited threshold current densities which were of the order of 100 kA cm^{-2}.

To create more efficient diode lasers, the carriers and photons were confined separately in double heterostructure device configurations which were pioneered by

Alferov. This improved confinement geometry shown in figure 4.2 increases the density of states for a given transition, increasing the gain of the laser at that wavelength.

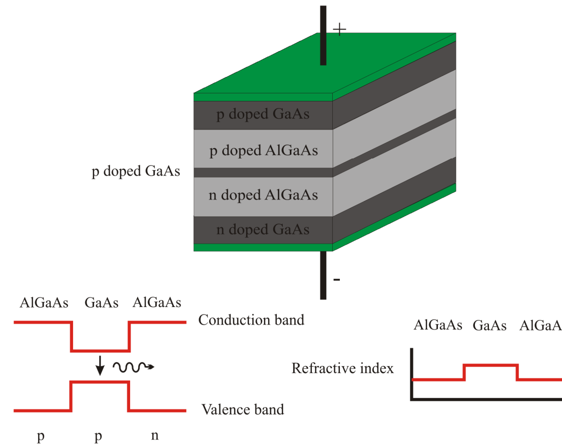

Figure 4.2 Material composition, refractive index profile and band structure of double heterostructure laser device. This shows the twin features of the DH concept, namely carrier confinement due to the larger bandgap of the cladding region and optical confinement due to the higher refractive index of the core region.

4.3. Quantum Confinement

If the thickness of the active region is reduced to about 10nm (of the order of the de Broglie wavelength for an electron), its energy levels become subject to quantum effects [8]. In one dimension, the system may be understood as a particle in a well. The result of the quantisation effect is a modification in the density of states and corresponding energy level structure associated with the material as is shown below in figure 4.3.

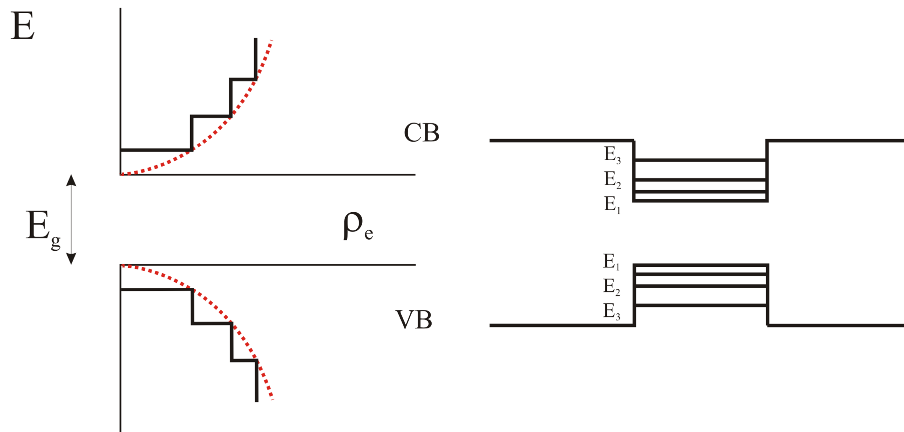

Figure 4.3 Energy versus density of states for bulk (dotted) and quantum-well material and energy level structure for QW material

The density of states for bulk semiconductor material is shown with a dotted red line and shows the density of states ρ_e increasing in proportion with the square root of the energy. This is underpinned by the physics of particles trapped in potential wells. The case of a quantum well device is shown with a solid black line. The density of states function still follows the general trend of the bulk case, but the quantum confinement now imposes an additional staircase-like structure on top resulting in a reduction in the density of states. Fewer carriers are therefore required to create a population inversion in the material at the lasing wavelength. For this reason, a quantum-well laser exhibits even lower threshold current values than a bulk double heterostructure device.

QW devices also exhibit high differential gain since there are fewer states to occupy. This allows fast switching of the device and fast modulation which is of benefit to pulsed applications. The lasing wavelength in a QW device is governed by a combination of the bandgap energy in the material and the quantisation energy in the well. Some tuning of the emission wavelength can therefore result from variation of the well thickness.

Threshold current densities in QW devices are typically of the order of 80 – 100 Acm^{-2} [9, 10]. Several single wells are often used in a multiple-quantum-well configuration to provide higher gain, but this in turn increases the threshold current.

4.3.1 Additional Quantum Confinement – Dots

Quantum dots (QD) provide further confinement of the carriers by limiting the degrees of freedom for the carriers in all three dimensions. Single quantum dots exhibit dimensions which are of the order of several nanometres in each direction. [11]. Such severe limitations have a corresponding effect on the density of states function as is shown below in figure 4.4. The simplest case for the energy level structure of a QD, assuming a cubic dot confined in three dimensions in infinite potentials is as follows.

$$E_{n_x,n_y,n_z} = \frac{\hbar^2\pi^2}{2}\left(\frac{n_x^{\;2}}{m_{cx}L_x^{\;2}} + \frac{n_y^{\;2}}{m_{cy}L_y^{\;2}} + \frac{n_z^{\;2}}{m_{cz}L_z^{\;2}}\right) \qquad 4.2$$

In the above expression, m_c is the effective mass of the electron, $\hbar$ is Planck's constant divided by 2π. $L_{x.y.z}$ is the size of the dot in the x, y and z directions respectively while n is a quantum number (n = 1, 2, 3…). In the case of a QW laser, only one direction would be represented in this equation.

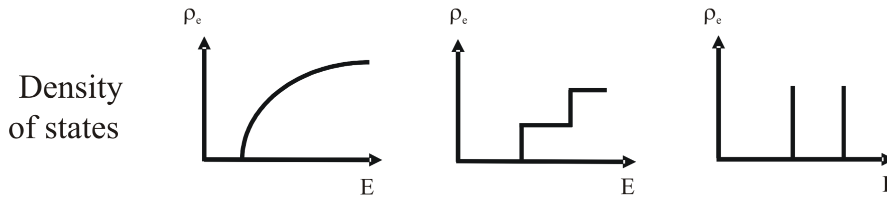

Figure 4.4. Density of states in bulk material (3D), QW material (2D) and QD material (0D) [12]. The QD case is for ideal dots which are identical in size. However, real dots exhibit size fluctuations leading to a broadening in the energy level structure.

Single QDs are sometimes called artificial atoms. QD lasers exhibit high material and differential gain [13]. Like their QW counterparts, QD lasers require some sort of separate confinement structure to limit the spreading out of charges and light from the dots. Figure 4.5 below shows the evolution of diode laser thresholds since their invention, documenting the major innovations leading to improvements in performance.

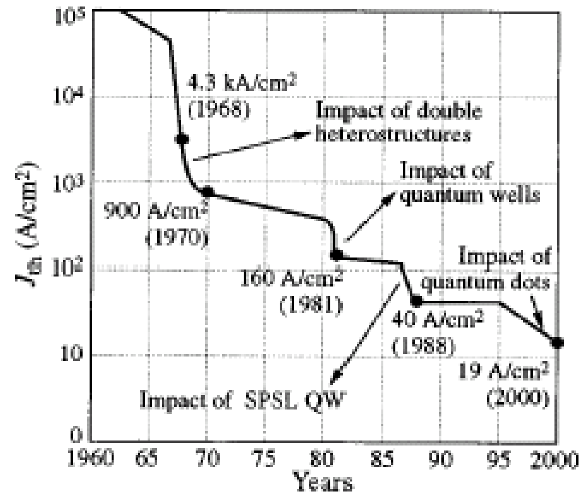

Figure 4.5. Threshold current density of diode lasers since their invention till the turn of the century. Major breakthroughs such as the development of the double heterostructure led to dramatic reductions in threshold current densities. The image is adapted from [10].

4.3.2 Self-organised Growth (Stranski-Krastanow [S-K])

The major breakthrough in the growth of quantum-dot material was the discovery and inclusion of self-organised growth (SOG) in QD wafer growth [14]. SOG allows the formation of very high quality layers of dots by exploiting the strain which occurs as the result of growing mismatched layers, such as GaAs and InAs (having a 7 % lattice mismatch, as shown above in figure 4.6) on top of one another. Growth of the InAs on a GaAs substrate occurs in two distinct phases [15]. Initially, growth takes place in a layer by layer manner. This is what is known as the *wetting layer* in quantum-dot material. As the growth proceeds, the total accumulated strain increases. After a critical thickness of InAs has been deposited, the growth morphology changes. Small three-dimensional islands of InAs form on a nanoscale dimension on top of the wetting layer. Once these islands of InAs are formed, they are covered with additional layers of GaAs to create isolated, 3D quantum confined structures. InGaAs/InAs QD systems with a GaAs substrate emit light in a wavelength range of approximately 1 μm to 1.3μm. Also, because the number of states in a QD system is limited and the dots grown by S-K can be quite low in density (typically between 10^9 cm^{-2} and 10^{11} cm^{-2} [16]), the gain can be saturated before lasing is achieved. For this reason, multiple layers of dots are grown to increase the available gain.

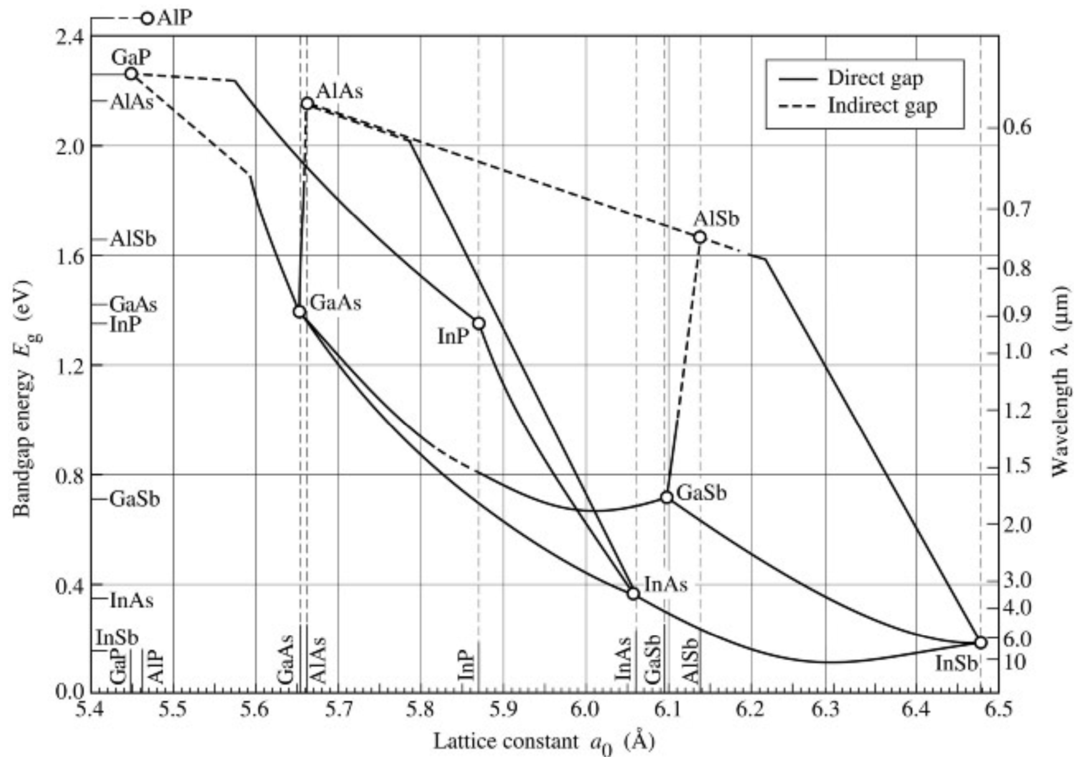

Figure 4.6. Bandgap energy and optical wavelength versus lattice constant for some well known semiconductor materials. Adapted from http://www.ee.ucla.edu/~wu/ee174/images/Bandgap-vs-Lattice%20Constant.jpg

Self-organised growth suffers from a dispersion of dot sizes. This is because dot formation is a natural process, governed by strain relaxation which will lead to a range of sizes. Dots of different size exhibit a different energy level structure and therefore give rise to optical transitions over a range of wavelengths. Thus, one can state that there is inhomogeneous broadening of the energy levels of the QDs. Typically, the dispersion is around 10% [12]. An additional effect of this broadening process is that for any given wavelength, the devices will display lower gain.

At low temperatures, QD lasers exhibit very low thresholds. This is because the carriers lack the thermal energy to escape the dots. The energies confining the carriers to the dots are in fact larger than the thermal energy which the carriers possess. In this regime, several authors have demonstrated threshold current densities which are of the order of 10's of A/cm^2 [17, 18]. Even lower values have been quoted for more aggressively cooled systems the value of 6 A/cm^2 at 4 K (25 A/cm^2 at room temperature) [19]. As the temperature is increased, carriers possess more thermal energy and some escape the dots into the surrounding material, leading to an increase

in threshold current [12]. This effect is investigated in some of the work covered in Chapter 5. Even at room temperature however, devices still exhibit low thresholds. As far as gain characteristics of QD lasers are concerned, studies have shown that the material gain is around an order of magnitude higher than for a QW laser under the same injection current density [20]

An additional advantage of QD lasers is that they display significantly suppressed carrier diffusion compared to their QW counterparts due to the increased confinement of carriers to the dots [21]. Importantly, this allows lasers to be fabricated using deep etching through the active region without suffering the penalties of increased surface recombination (which results in increased non-radiative recombination) displayed by QW devices with similar geometries [22]. This should allow QD lasers to be readily integrated with additional monolithic components such as photonic crystals or chirped facet mirrors that may provide pulse shaping capabilities.

Interestingly, QD lasers have also shown the capability of lasing at both their ground state (GS) and excited state (ES) wavelengths [23]. The ES exhibits higher gain than the GS since there are more states to occupy. This is analogous to the difference in the allowed numbers of electrons in the p-states compared with the s-states in the energy manifold of an atom. The existence of this excited state, and in particular the characterisation of its transmission dynamics in relation to those of the ground state, is the topic covered in the next section.

4.4 Investigation of the Transition Dynamics of Quantum-dot Material

4.4.1 Motivation

The development of QD lasers optimised for ultrashort pulse production demands a full understanding of all the contributing factors that affect the performance in terms of both the gain and saturable absorption. In a QD device, with lasing contributions provided by more than one electronic transition, it is therefore important to understand the relationships between the transitions that arise. To be specific, my research

involved the study of the evolution of the output of a QD laser in terms of contributions from its component states and their associated temporal characteristics. To put this into context, it is useful to mention the work of others who have also investigated various aspects of these behaviours.

Markus *et al* demonstrated dual-state lasing from an InAs/GaAs QD laser [23]. They showed that device length was important in determining which state constituted the laser output. Short devices exhibited ES lasing due to insufficient gain at the GS wavelength while longer devices initially displayed GS emission followed by ES lasing at higher pumping densities.

Several authors have investigated the temporal behaviour of emission from QD devices. Initially, it was thought that the phonon bottleneck would result in QD devices displaying long characteristic recovery times [24]. Experiments, however, have shown otherwise, namely that the variety of recombination paths available to carriers coupled with ultrafast relaxation of carriers in higher states allows an ultrafast recovery of both gain and absorption [25]. For example, Borri *et al* demonstrated ultrafast gain recovery in quantum dot semiconductor optical amplifiers (QDSOAs) happening on a timescale of 150fs [26]. They also showed recovery of the first excited state happening on a similar ultrafast timescale [27]. Further work by Rafailov *et al* investigated for the first time the transition dynamics of QD material in a passive absorber configuration [28] and Figure 4.7 shows this absorption recovery as a function of time.

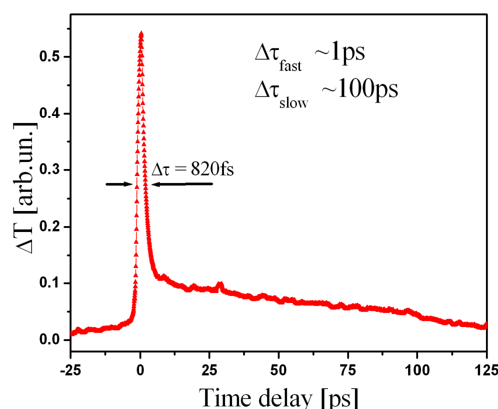

Figure 4.7. Pump-probe measurements carried out at 1μm. The initial fast recovery occurs on a time scale measured to be 820fs. After this initial rapid recovery, a much slower relaxation process taking place in excess of 100ps manifests itself. [This figure is reproduced from [28] with the authors' permission.]

Malins *et al* showed that the total recovery time decreases with increasing reverse bias [29]. They attribute this to a faster sweep out of carriers from the absorber caused by varying contributions of thermionic emission and tunnelling processes. This also agrees with the absorption recovery behaviour observed in QD SOAs [26]. The recovery of the absorption in an QDSOAs is very similar to the recovery in [29] under zero-bias conditions as expected. This is consistent with the observations of Cataluna *et al* [30] and Thompson *et al* [31] who reported that the durations of mode-locked pulses obtained from a two-section laser decreased as the reverse bias applied to the absorber section was increased.

Exploring the QD device in a lasing configuration and assessing the characteristics of pulses emitted from the different states of the device can be expected to give some insights into the way the different states in the QD laser contribute to the lasing process.

4.4.2 Sample Growth

The QD sample was grown by molecular beam epitaxy as discussed in Chapter 3. The active region of the device contained ten layers of InAs QDs separated by 33nm thick GaAs spacer layers The structure was grown on a (100) GaAs substrate. The dots were typically around 7 – 10nm in diameter. The material was grown by innolume GmbH in Germany. Chemically assisted ion beam etching (CAIBE) (which was also described in Chapter 3) was then used at the cleanroom facility in St Andrews to define waveguides of width 6, 12 and 16μm in the material by etching trenches of depth 2.6μm and 50μm width in the material. Etching to a depth of 2.6μm ensured that we etched through the active region of the material, maximising the waveguiding capability of the structure. The CAIBE etching parameters (beam current/voltage, sample temperature and etchant gas flow) were optimised to fabricate waveguides with vertical sidewalls. The precise details of the CAIBE etch are identical to those listed in table 3.2. The material was then cleaved into devices. The resulting structure was thus a ridge waveguide Fabry-Pérot resonator terminated at both ends by uncoated semiconductor facets. Both 1mm and 2mm long devices were fabricated to give some versatility in the available gain of the devices and to allow a comparison between the two. A graphic of a finished device is shown below in figure 4.8.

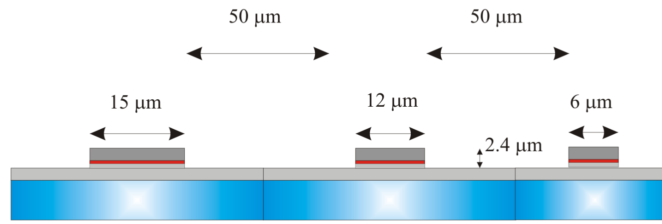

Figure 4.8. End elevation of waveguide QD Fabry- Pérot laser.

The finished devices were then mounted p-side up on a copper heatsink and were secured onto a thermoelectric cooler. This maintained the temperature of the samples at a constant 20°C. This step was undertaken to ensure that temperature effects were minimised and the working lifetime of the device maximised.

4.4.3 Experimental Assessment

A mode-locked titanium-sapphire laser was used as a pump source for the assessment. Ultrashort pulsed laser sources exhibiting high peak powers have been used in the past to investigate the behaviour of QD material, demonstrating that gain can be achieved by optical pumping [32] and that pulsed pumping can result in the production of a gain switched output pulse from the QD device [33]. These high peak powers allow investigation of QD laser emission characteristics such as the spectral and temporal characteristics of excited states which do not manifest themselves under cw pumping.
The Ti:sapphire laser used in this work delivered 1.2W average power at a wavelength centered on 790nm. It was operated in both cw unmode-locked and mode-locked regimes. In the latter, it delivered pulses with durations of around 150fs which had a repetition frequency of 84MHz with the typical characteristics shown below in figure 4.9. The $Ti:A1_20_3$ pump laser pulses were passed through a neutral density filter wheel to give fine control over the pump intensity incident on the QD laser and focused down onto the top of the device using a cylindrical lens. This created a pump illumination on the structure of roughly 40μm by 1mm. A diagram of the experimental setup is shown below in figure 4.10.

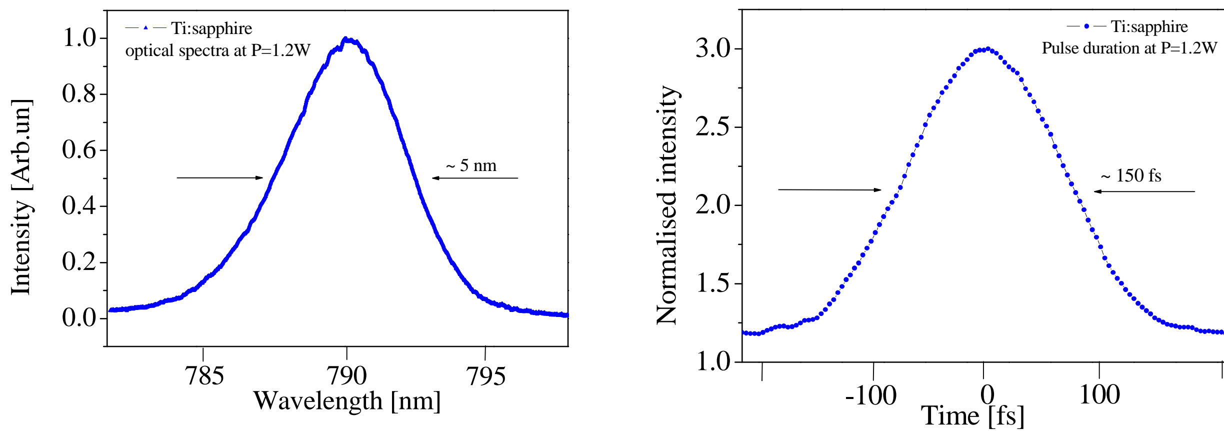

Figure 4.9. Optical spectra and pulse duration characteristics of the Ti:sapphire pump laser

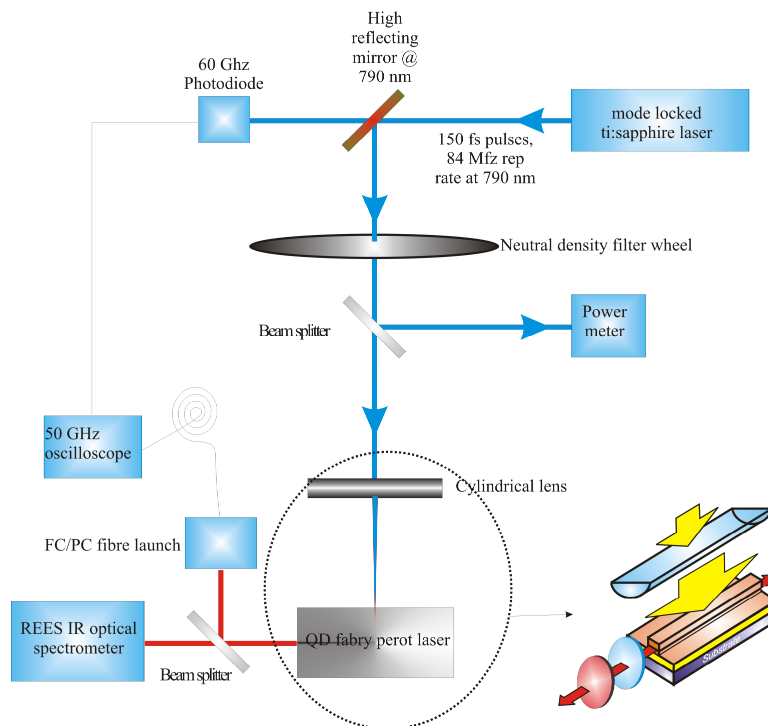

Figure 4.10. Experimental setup for the optical-pumping experiment

Output from the quantum-dot laser was then collimated and passed through a filter to remove any stray light from the pump source. This QD laser output was then spectrally analysed using a REES infrared spectrometer. The temporal characteristics

of the emission were investigated using a Hewlett Packard 50GHz oscilloscope, triggered from the Ti:sapphire pump source via a 60GHz photodiode.

4.5 Results

Light-light characteristics were obtained from the laser under both continuous and mode locked pumping. This is shown below in figure 4.11. It can be seen that lasing is initiated at much lower incident pumping densities in the case of the excitation by the ultrashort light pulses. This is because these optical pulses have a very high peak intensity that excites lots of carriers essentially simultaneously to produce an inversion with modest average pump powers. At the same time, saturation is reached at lower average power levels in the pulsed case than in the constant intensity counterpart. This is due to the fact that, all available states are filled efficiently by excitations caused by the intense pulses. This can be better understood once we also consider the optical spectra of the QD laser at low and high optical pump densities in both pumping configurations as shown in figure 4.12.

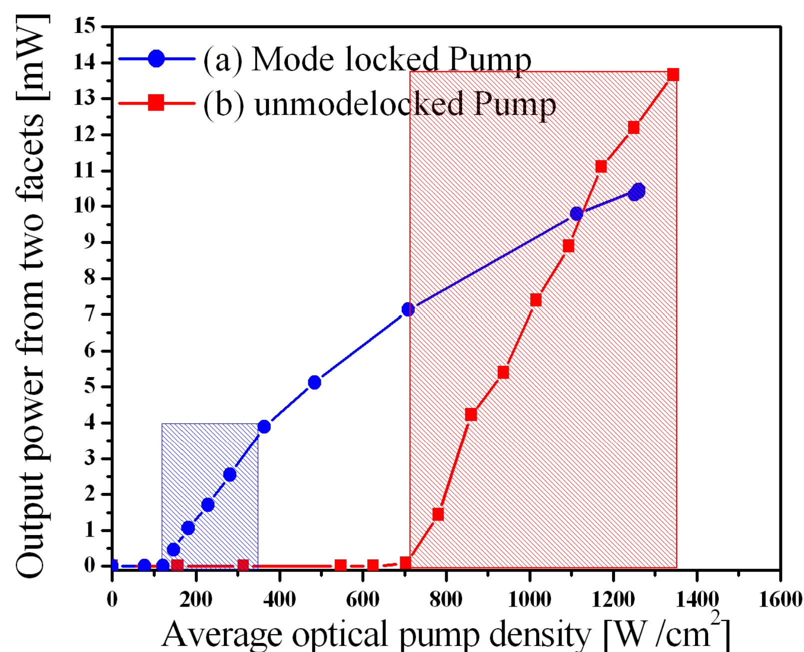

Figure 4.11. Power output from 2 mm long QD laser in (a) mode-locked and (b) unmodelocked (cw) pump configuration as a function of average optical density. The shaded areas show regions of linear increase of output power under both pumping regimes.

Comparing the spectral differences between pumping regimes side by side as in figure 4.12, we see that in the unmodelocked (continuous wave) case, the GS lasing wavelength is shifted to longer wavelengths than in the pulsed case. This can be explained by heating effects. A small shift to longer wavelengths at higher pumping also occurs in the pulsed case but the reduced heating effects associated with pulsed pumping mean that this shift is far less significant than in the unmodelocked case. These effects are also moderated by the raising of the Fermi level which may occur at higher pump intensities.

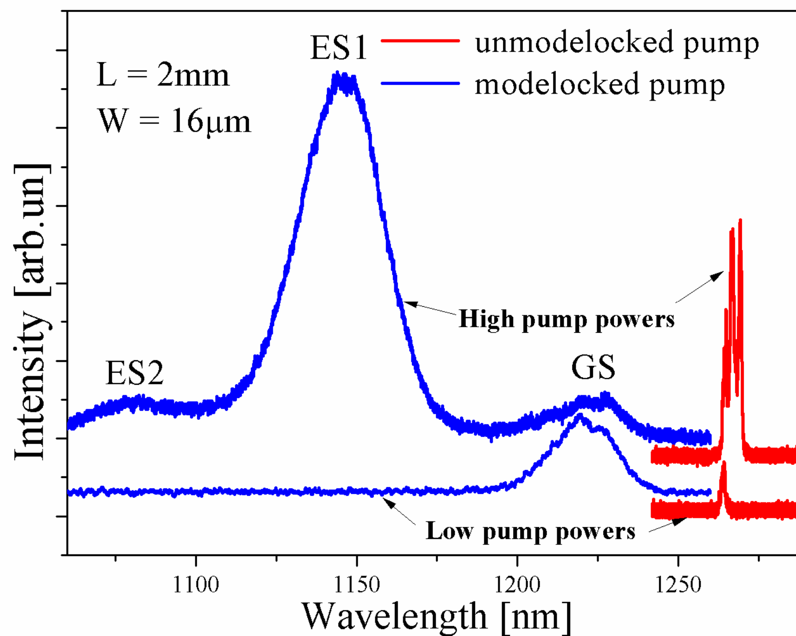

Figure 4.12. Optical spectra in both pulsed and cw configurations at low and high optical pump densities.

Figure 4.13 shows the evolution of the QD laser output under non-modelocked pumping. We see that the spectra broaden slightly and shift to longer wavelengths at higher pump powers. The red-shift can be explained by thermal expansion of the material. Non modelocked pumping imparts a large amount of energy onto the QD laser material. A proportion of this energy will serve to heat up the device. This heating increases the interatomic spacing of atoms in the structure which in turn will decrease the potential experienced by electrons. This reduction

manifests itself as a lowering of the bandgap of the material and hence leads to a shift towards longer, wavelengths [34].

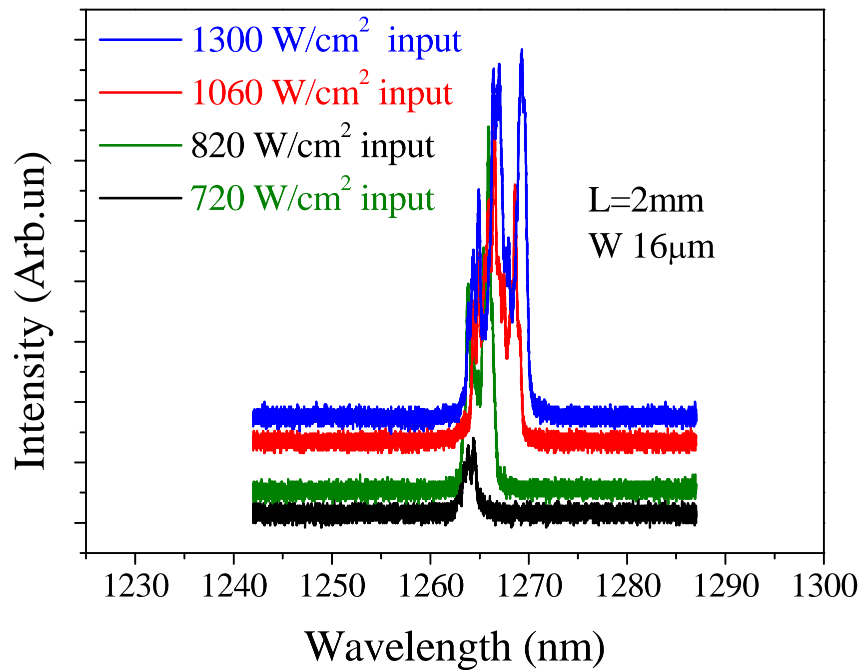

Figure 4.13. Optical spectra under increasing non modelocked (cw) case.

In QD material, this shift will be more pronounced than in bulk material due to the dependence of output wavelengths on the dot size distribution. Under continuous wave operation we can only impart enough energy to the device for ground state (GS) lasing.

If we now examine the spectra from the QD laser under modelocked pumping conditions, we observe significantly different behaviour to the unmodelocked case. Below, in figure 4.14, the lasing behaviour of the QD laser can be seen to depend on the incident pump density on the structure. Emission begins from the GS (1250nm) at low pump powers. As the pump power is increased, the contribution at the GS wavelength grows, and the power from the laser increases linearly. The GS gain, however, remains clamped at threshold. At the same time, the number of carriers in the excited states increases. At this stage, gain in the excited states is not large enough to achieve threshold, but, as the power is further increased, the first excited state (ES1) starts to lase at around 1175nm. Fortunately, while the gain in the lasing GS was clamped at threshold, the gain at ES1 and ES2 was not constrained, and thus increased with the pump intensity level [23]. Eventually, this increase became larger

than the total losses and lasing occurred. At still higher pump powers, the emission associated with ES1 became dominant over the GS emission and the second excited state (ES2) appeared at around 1100 nm. When this occurred, it became evident that the GS transition had become saturated. Finally, further increases serve to further increase contributions from (ES2). At this point, emission from the GS has all but ceased. It is thought that the effect is connected with the lower degeneracy and lower gain of the GS in comparison to the ESs [35]. At higher pumping levels, fast relaxation from ESs to the GS becomes prevalent. Since this effect happens on shorter time scales than the radiative decay from the GS, the states of the GS become blocked, thus suppressing emission [36].

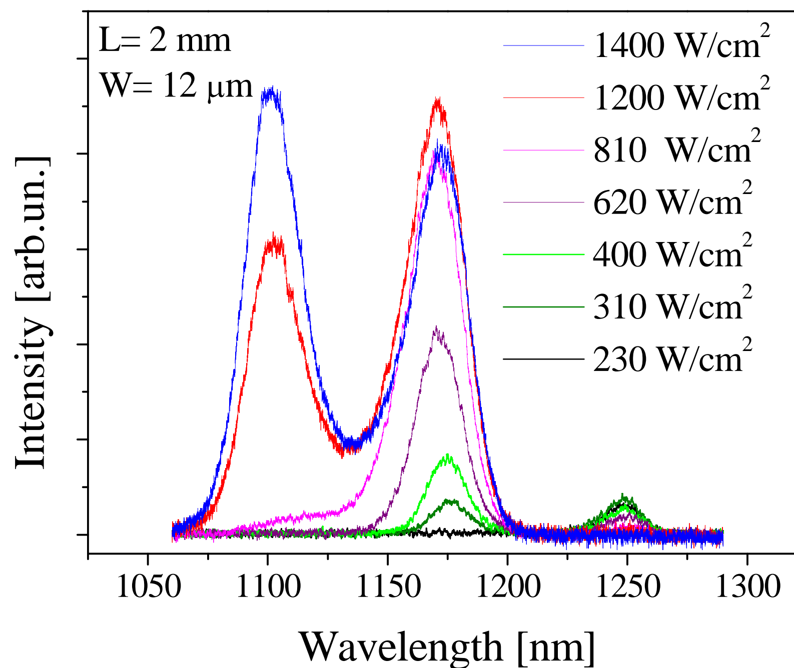

Figure 4.14. Evolution of pulsed spectra as a function of incident optical pump intensity

Given that there are a finite amount of states to be occupied, the act of continually increasing the photon flux incident on the QD laser will eventually use up the available gain. This breaks up the linear relationship between pump power and output power and it also explains the differing shapes of the light-light curves for the pumping regimes illustrated in figure 4.11. The non-modelocked case (b) shows a linear relationship which remains unchanged even at maximum pumping energies.

Here, the GS contribution is still increasing. The energy transferred to the QD laser is not high enough to saturate the GS or reach ES1 threshold. In contrast, with a modelocked pump (a), GS saturates under far lower pump intensities. In this case, contributions from three lasing states mean that the light-light relationship is far from linear. When ES1 is lasing in addition to the GS, the slope efficiency of the laser decreases further. It is thought that the prevalence of non-radiative processes from ES1 compared with GS was responsible for this [37].

With the spectral characteristics of the device now better understood, an investigation was made into the temporal characteristics of such lasers. When pumped in a non-modelocked configuration, the quantum-dot laser also produced light continuously and exhibited the same dependence on the nature of pumping applied when a modelocked optical input was used. It was pumped with a KLM Ti:Sapphire laser as discussed previously, but no mechanism was utilised to mode-lock the QD laser itself. Under pulsed pumping the device thus operated in a gain-switched configuration as outlined in Chapter 2. The gain-switched pulses were characterised for different optical pump densities. The development of this pulsed behaviour under increasing optical excitation is illustrated below in figure 4.15. Corresponding optical spectra are also shown to aid understanding of the behaviour.

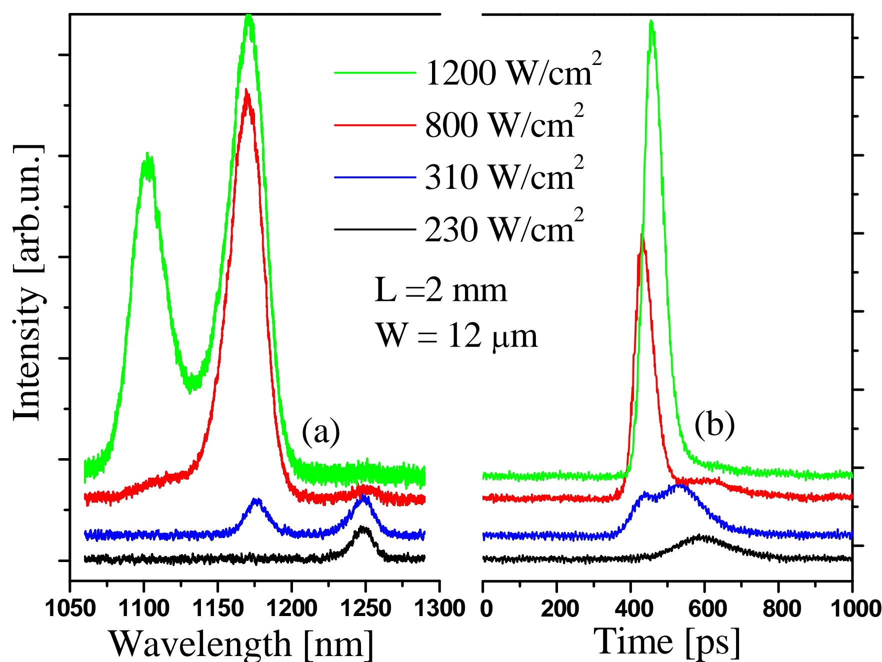

Figure 4.15. Evolution of (a) optical spectra and (b) pulse characteristics with increasing optical pump density.

We see that at low pump intensities where only the ground state makes contributions, a broad pulse is emitted. Upon increasing the pump power such that laser action within ES1 begins, we observe some very interesting behaviour. At around 310W/cm^2, both GD and ES1 are contributing roughly equally to the laser output according to their spectra. The time-resolved measurements show that the laser is emitting two distinct pulse trains at this point, corresponding to the two contributing states. As before, we observe a pulse due to the GS emission at about 550ps (slightly shifted forward in time compared to the GS pulse emitted with 230W/cm^2) but now additionally, we observe a second pulse, produced earlier[3] in time at around 440ps due to ES1 emission.

This is due to the order of the energy levels in the QD material. Carriers excited by the intense pumping at 790nm will first relax into the ES1 and can undergo stimulated emission. Additional time is required for carriers to relax into the GS, accounting for the delay between pulses from ES1 and GS. This result had been predicted in simulation prior to experimental verification for an electrically pumped single section device capable of operating on the GS and ES1 [38]. The authors claim the reason for this is that when both states are lasing, the higher gain of ES1 allows very rapid build of carrier density in the state. When ES1 is lasing, there must also be a significant population in the GS. This increases the time taken for carriers to relax from ES1 to GS through Pauli blocking. This allows significant population in ES1. When coupled with the high gain of ES1, this implies a faster switch-on time and thus the earlier production of an optical pulse.

Under further excitation, we see the emergence of ES1 as the dominant state in the lasing process due to its higher gain. This corresponds to the production of a more intense pulse at 440ps (ES1 pulse) and a barely detectable increase from the average light output at around 550ps connected with the saturated GS emission. At maximum incident pump intensities (~1200W/cm^2 limited by the maximum output from the titanium sapphire laser), the ES2 lasing contribution is similar in magnitude to that of ES1. This leads to the production of intense pulses centred at around 455ps that were around 60ps in duration. We see no evidence of a double pulse at these pump powers, but, since there are two states involved in the lasing, prior observations would indeed suggest the presence of dual pulses. It is possible that the pulse measured here is

[3] This was erroneously reported as *later* in [1]

actually a superposition of two pulses overlapping in time. Because of the electronic detection method used in this work, it was not be possible to temporally resolve dual pulses with the temporal separation involved.

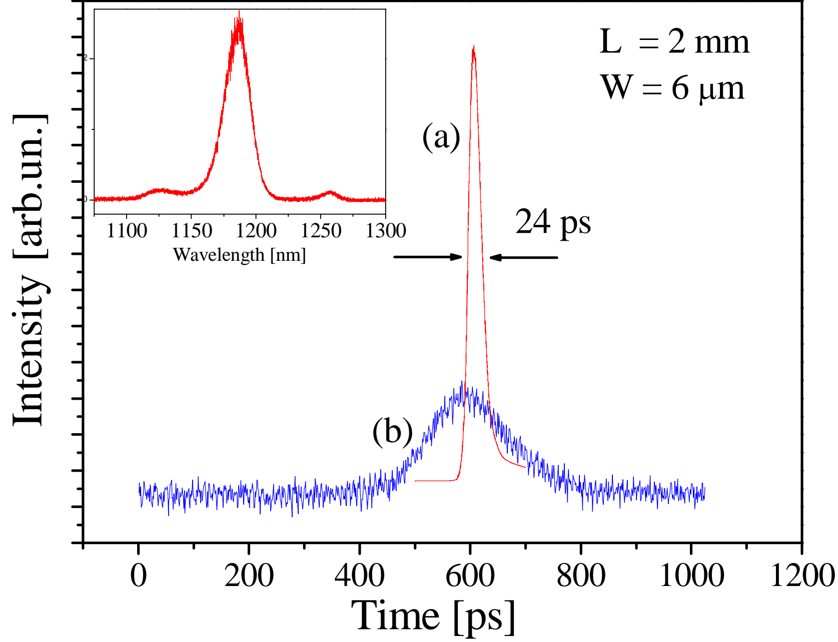

Figure 4.16. Shortest ES1 pulse (a) produced from the device with typical GS pulse (b) for comparison. The inset shows the corresponding optical spectra in the case of (a).

Figure 4.16 shows a trace of the shortest pulse duration achieved (24ps). This was achieved for a 6μm wide waveguide of 2mm length. The inset to the figure shows that this minimum pulse duration is achieved when ES1 transitions are dominant. A pulse produced solely from GS emission is also shown for comparison. The reason for the shorter nature of pulses from ES1 can be found by studying the dynamics of gain-switched semiconductor lasers. For instance, Downey *et al* show that the rise time of a gain-switched pulse is related to the differential gain by the following expression.

$$\tau_r = \frac{1}{g\Gamma(N - N_{th})} \quad 4.3$$

We see from the above that an increase in the differential gain causes a decrease in the rise time of the generated pulse together with a reduction in the duration of the pulse as a whole [39].

This measurement is limited by the resolution of the photodiode and oscilloscope used. It is possible that the pulses produced were slightly or even significantly shorter than the measured values reported. [The pulse duration shown is after appropriate deconvolution has been applied.] The real pulse duration is linked to the measured pulse duration by the following relationship.

$$\tau_{measured} = \sqrt{\left[\left(\tau_{real}\right)^2 + \left(\tau_{resscope}\right)^2 + \left(\tau_{resphoto}\right)^2 \right]} \qquad 4.4$$

In the above expression, $\tau_{measured}$, τ_{real}, $\tau_{resscope}$, $\tau_{resphoto}$ stand for the measured pulse duration, the real pulse duration, the temporal resolution of the oscilloscope and the temporal resolution of the photodiode respectively. From this we can see that the resolution of the measurement apparatus is of paramount importance. If the real pulse duration is shorter than the resolution of the measurement then the measured pulse duration will be significantly different from the actual value. Expression 4.4 assumes a Gaussian pulse shape.

Intensity autocorrelation measurements were carried out to try to measure the temporal behaviour with greater accuracy. Simple autocorrelation techniques can allow the characterisation of pulses which are of the order of 100fs in length. Unfortunately, due to the relatively low peak power of the pulses from the QD laser, it was not possible to measure the pulses on the autocorrelator that had been constructed. It was, however, possible to measure the duration of the pulses produced by the pump laser (figure 4.10). This indicates that this inability was due to the device parameters rather than any error in the experimental technique. Given that the autocorrelation method relies upon a nonlinear intensity dependent effect, the peak power of the device is of key relevance. I believe that this was the key factor in the inability to autocorrelate these pulses.

These measurements confirm that the intrinsic carrier transitions from different states in QD lasers occur on distinctive time scales. This also shows that the quantum-dot emissions from the GS and those involving transitions from ES1 are not mutually coherent. Despite the fact that the different states are pumped by the same source, the timescales associated with recombination from each state as well as their related relaxation times into each state from higher energy states such as the wetting layer result in the QD laser functioning as three relatively separate lasing processes.

The measurements show, however, that ES1 pulses are significantly shorter than those arising from emission from the GS. This should be considered when operating QD lasers in a mode-locked configuration. These results suggest that a QD laser operating at the ES1 could potentially produce shorter pulses than one operating from the GS. This may be connected to the higher gain available at the ES1.

4.6 Future work and conclusions

By carrying out this investigation into the transition dynamics of a QD laser under gain conditions during laser operation, a greater understanding of the carrier dynamics can be gained. Taken in conjunction with the work done on the gain recovery dynamics of QD material in semiconductor optical amplifier configurations and its behaviour as an absorber, there now exists a clearer picture of the recovery characteristics of the material. We showed that the higher differential gain of ES1 and the rapid state filling coupled with increased relaxation times to the GS result in the production of ultrashort pulses from ES1 which were measured to be less than 24ps in duration. These pulses were produced earlier in time than pulses from the GS.

From the perspective of ultrafast laser physics, the realisation that the different states emit light on different time scales has important implications. Because the states are behaving effectively as separate lasers (albeit operating from the same charge reservoir), it does not seem possible to engage both the GS and ES1 in the same mode-locking interactions. Thus the wider bandwidths hoped for are not yet accessible. Despite this, the design of QD material in which there exists more of a spectral overlap between GS and ES1 emission could result in a significant increase in 'cross talk' between these interacting states. This could thus have the potential to enable the exploitation of considerably wider spectral bandwidths in mode locking that could be "designed" to facilitate the generation of significantly shorter pulses. It should be noted here that in order for shorter pulses to result, there would need to also be some attempt to better control the dispersion in the system.

There are a number of steps that could be taken to further the findings of my investigations into this type of material structure. Autocorrelation measurements carried out with a more sensitive instrument would give a high resolution time-resolved picture of the pulses produced, possibly revealing additional temporal

features in the pulse profiles that may have become hidden due to the limited resolution of the measurement technique employed here.

Additionally, through the use of laser quality filter elements placed after the QD laser, it should be possible to severely attenuate the light from one quantum energy level. For example, the use of a filter blocking light below 1100nm would remove visible spectral and temporal contributions from ES2. By then operating the device at high pump powers, it would be possible to examine the pulse profile solely due to ES1 contributions. Likewise, the employment of a filter that blocks wavelengths above 1125nm would allow the study of ES2 in isolation.

In this chapter I have outlined an investigation into the transition dynamics from the different states in QD material with a view to engaging an enlarged bandwidth of two states for mode-locked operation. As mentioned previously, another important factor limiting the performance of QD lasers is the large positive chirp brought about by the carrier-induced slow self-phase modulation caused by a pulse passing through the device. Intracavity-based strategies to overcome the high amounts of positive frequency chirp in QD mode-locked lasers are very important if QD lasers are to be able to fulfil their potential. In Chapter 5 I will describe a preliminary investigation made into an external cavity based mode-locked QD laser. This more versatile cavity design allowed the inclusion of various elements designed to improve the performance of the device through stabilisation and feedback and intensities within the cavity.

References

1. Rafailov, E.U., et al., *Investigation of transition dynamics in a quantum-dot laser optically pumped by femtosecond pulses.* Applied Physics Letters, 2006. **88**(4).
2. Rafailov, E.U., et al. *Investigation of Transition Dynamics in a Quantum dot laser optically pumped by femtosecond pulses*. *LEOS Annual meeting,* 2005, *Paper ThN4* .
3. Neamen, D.A., *Semiconductor Physics and Devices*. Third Edition ed.: McGraw Hill. 2003
4. Bhattacharya, P., *Semiconductor Optoelectronic Devices*. 2 ed. Prentice Hall. 614. 2003
5. Agrawal, G.P., *Semiconductor Lasers Past, Present and Future*. Theoretical and Applied Optics, ed. W.T. Rhodes. AIP Press. 2003
6. Casey, H.C. and M.B. Panish, *Heterostructure Lasers Part A: Fundamentals and Principles*. Quantum Electronics - Principles and Applications, ed. P.F. liao and P. Kelley. Academic Press INC. 272. 2003
7. Wilson, J., Hawkes, J., *Optoelectronics an introduction*. 3 ed. Prentice hall. 1998
8. Holonyak, J.R., et al., *Quantum-Well Heterostructure Lasers.* IEEE Journal of Quantum Electronics, 1980. **16**(2): p. 170 - 186.
9. Gilor, J., et al. *Very low threshold current density for pseudomorphic quaternary AlInGaAs single QW lasers using a growth parameters optimisation technique*. in *15 th IEEE International Semiconductor Laser Conference,* 1996, *Paper P9*. Hafia, Israel.
10. Weisbuch, C., *The Development of Concepts in Light-Emitting Devices.* Brazilian Journal of Physics, 1996. **26**(1): p. 21 - 42.
11. Bimberg, D. and C. Ribbat, *Quantum Dots: lasers and amplifiers.* Elsevier Microelectronics Journal, 2003. **34**: p. 323 - 328.
12. Ledentsov, N.N., et al., *Quantum-Dot Heterostructure Lasers.* IEEE Journal of Selected Topics in Quantum Electronics, 2000. **6**(3): p. 439 - 451.
13. Asada, M., Y. Miyamoto, and Y. Suematsu, *Gain and the Threshold of 3-Dimensional Quantum-Box Lasers.* IEEE Journal of Quantum Electronics, 1986. **22**(9): p. 1915-1921.
14. Bhattacharya, D., et al., *Spectral and dynamic properties of InAs-GaAs self-organised quantum-dot lasers.* IEEE Journal of Selected Topics in Quantum Electronics, 1999. **5**(3): p. 648 - 657.
15. Goldstein, L., et al., *Growth by Molecular-Beam Epitaxy and Characterization of Inas/Gaas Strained-Layer Superlattices.* Applied Physics Letters, 1985. **47**(10): p. 1099-1101.
16. Cataluna, M.A., *Ultrashort-pulse generation from quantum-dot semiconductor diode lasers*, PhD Thesis, *School of Physics and Astronomy*. 2007, University of St Andrews: St Andrews.
17. Caroff, P., et al., *High-gain and low-threshold InAs quantum-dot lasers on InP.* Applied Physics Letters, 2005. **87**(24).
18. Shimizu, H., et al., *InAs quantum dot lasers with extremely low threshold current density (7A/cm(2)/layer).* Japanese Journal of Applied Physics Part 2-Letters & Express Letters, 2005. **44**(33-36): p. L1103-L1104.

19. Park, G., et al., *Room-temperature continuous-wave operation of a single-layered 1.3 mu m quantum dot laser.* Applied Physics Letters, 1999. **75**(21): p. 3267-3269.
20. Kirstaedter, N., et al., *Gain and differential gain of single layer InAs/GaAs quantum dot injection lasers.* Applied Physics Letters, 1996. **69**(9): p. 1226-1228.
21. Moore, S.A., et al., *Reduced surface sidewall recombination and diffusion in quantum-dot lasers.* IEEE Photonics Technology Letters, 2006. **18**(17-20): p. 1861-1863.
22. Ouyang, D., et al., *High performance narrow stripe quantum-dot lasers with etched waveguide.* Semiconductor Science and Technology, 2003. **18**(12): p. L53-L54.
23. Markus, A., et al., *Simultaneous two-state lasing in quantum-dot lasers.* Applied Physics Letters, 2003. **82**(12): p. 1818-1820.
24. Benisty, H., C.M. Sotomayortorres, and C. Weisbuch, *Intrinsic Mechanism for the Poor Luminescence Properties of Quantum-Box Systems.* Physical Review B, 1991. **44**(19): p. 10945-10948.
25. Morris, D., N. Perret, and S. Fafard, *Carrier energy relaxation by means of Auger processes in InAs/GaAs self-assembled quantum dots.* Applied Physics Letters, 1999. **75**(23): p. 3593-3595.
26. Borri, P., et al., *Ultrafast gain dynamics in InAs-InGaAs quantum-dot amplifiers.* IEEE Photonics Technology Letters, 2000. **12**(6): p. 594-596.
27. Schneider, S., et al., *Excited-state gain dynamics in InGaAs quantum-dot amplifiers.* IEEE Photonics Technology Letters, 2005. **17**(10): p. 2014-2016.
28. Rafailov, E.U., et al., *Fast quantum-dot saturable absorber for passive mode-locking of solid-state lasers.* IEEE Photonics Technology Letters, 2004. **16**(11): p. 2439-2441.
29. Malins, D.B., et al., *Ultrafast electroabsorption dynamics in an InAs quantum dot saturable absorber at 1.3 mu m.* Applied Physics Letters, 2006. **89**(17).
30. Cataluna, M.A., et al., *Temperature dependence of pulse duration in a mode-locked quantum-dot laser.* Applied Physics Letters, 2007. **90**(10).
31. Thompson, M.G., et al., *Subpicosecond high-power mode locking using flared waveguide monolithic quantum-dot lasers.* Applied Physics Letters, 2006. **88**(13).
32. Lingk, C., et al. *Stimulated emission dynamics in self-assembled InAs/GaAs quantum dots*. in *Quantum electronics and laser science conference,* 2000. *Paper QMJ7*.
33. Lingk, C., et al. *Quantum dot laser dynamics after pulsed optical excitation*. in *Lasers and Electro-optics. CLEO' 01*. 2001 Paper CWK4. Baltimore.
34. Van Zeghbroeck, B. *Principles of Semiconductor devices*. 1997 .
35. Zhukov, A.E., et al., *Long-wavelength lasing from multiply stacked InAs/InGaAs quantum dots on GaAs substrates.* Applied Physics Letters, 1999. **75**(13): p. 1926-1928.
36. Tartakovskii, A.I., et al., *Dynamics of stimulated emission in InAs quantum-dot laser structures measured in pump-probe experiments.* Applied Physics Letters, 2002. **81**(22): p. 4118-4120.
37. Maximov, M.V., et al. *GaAs based 1.3 micron InGaAs quantum dot lasers: A status report*. 2000

38. Mao, M.H., et al. *Spectrally resolved two state lasing in quantum-dot lasers*. in *Lasers and electro-optics society, 2005, LEOS 2005, Paper MB4*. Sydney, Australia.
39. Downey, P.M., et al., *Picosecond Dynamics of a Gain-Switched Ingaasp Laser.* IEEE Journal of Quantum Electronics, 1987. **23**(6): p. 1039-1047.

Chapter 5 All-quantum-dot, external-cavity, mode-locked laser

5.1 Introduction

To decrease the duration of pulses obtained from semiconductor lasers, several approaches are currently being investigated. In the previous chapter, I discussed temporal characteristics of pulses emitted from the first excited state (ES1) and the ground state (GS) of an optically pumped QD laser. I showed that pulses produced by first-excited state transitions evolve on a shorter timescale than those from the GS. This implies some potential advantages for ES1 operation in pulsed configurations such as those that apply to mode locking. In this chapter, I perform a preliminary investigation into a mode-locked, external-cavity laser based entirely on quantum-dot materials. The laser is mode locked using a quantum-dot intracavity SESAM. As such, this is described as an all-quantum-dot mode-locked external cavity laser. Given that advances in techniques such as molecular beam epitaxy (MBE) have made it possible to fabricate quantum-dot devices with characteristics suitable for many different purposes, it is now possible not only to produce high quality quantum-dot lasers but also to manufacture saturable absorber mirrors containing QDs. The chapter begins with a description of the motivation for the external-cavity configuration and the use of a quantum-dot SESAM mode locking element. I next discuss the experimental setup and the assessment techniques, followed by results and a discussion on their significance. After this, I describe some of the other work in which I was involved in respect of quantum-dot laser development, specifically the temperature insensitive operation of monolithic mode-locked, two-section lasers.

I then discuss where this work could possibly be taken in the future. I should also mention here that the research described as the main thrust of this chapter has been published in the Electronics Letters journal [1] and was also presented as a conference paper at the IEEE Annual Meeting 2006 in Montreal [2] and at the annual semiconductor and integrated optoelectronics (SIOE) conference in Cardiff [3].

5.2 Motivation

5.2.1 Advantages of external-cavity configurations

One of the principal advantages of semiconductor lasers is their inherent structural simplicity. A monolithic device is not susceptible to misalignment because the mirrors are formed from cleaved facets rather than as separate components. This can make this laser type very stable and robust as well as compact, and so it is particularly suitable for applications where the end user has no detailed knowledge of laser physics. The exceptionally small footprints of semiconductor lasers coupled with their unbeatable efficiencies under electrical injection and the potential for mass production are compelling reasons as to why these devices are so important to the future growth of the optical communications market. It therefore may seem counterintuitive to employ a semiconductor laser in a non-monolithic configuration.

In the developmental phase of a mode-locked laser system, however, operation in a more elaborate cavity arrangement can provide additional insight into the physics that governs the operation. An example of this could be where, for example, one of the facets of the monolithic laser chip has been antireflection coated and an external mirror is used for feedback.

Freedom to explore multiple configurations

Use of an external mirror allows tuning of cavity length and adjustment of the feedback into the cavity to optimise performance. It also offers the freedom to place additional elements within the cavity, thus tailoring the behaviour of the system. This can be used to provide valuable information about the dynamic process ongoing within the laser cavity.

One element commonly placed within an external cavity is a diffraction grating. This can be used to reduce the laser linewidth or to tune the operating wavelength [4]. Recently, a grating was used in an external cavity QD laser to provide a means of selecting either ground, excited or dual state lasing [5]. The lasing state was determined by driving conditions and the presence or otherwise of the grating which was designed to be resonant with GS. This idea has been further

developed by the incorporation of a grating in a mode-locked external cavity system. In this system, switching of mode-locked output between GS and ES1 was dependent on the grating angle. The authors of this work explain that reliable, ultrafast switching between these two states would allow this system to be used as a source for a dual-band clock recovery source in telecommunications applications [6].

Intracavity compensation of frequency chirp

Several authors have explored the use of an external-cavity section *in addition* to the laser cavity in order to compensate for the frequency chirp introduced by self-phase modulation connected with the carrier induced refractive index change mentioned in Chapter 2 section 2.1.4 [7]. Other studies have shown that this phenomenon in conjunction with other ultrafast effects associated with gain dynamics is the limiting factor pertaining to ultrashort pulse generation in semiconductor lasers [8].

Delfyett *et al* routinely employed an external cavity to compensate for accumulated intracavity frequency chirp [9]. The reasoning behind this is that it is perhaps more straight forward to externally compress and amplify a chirped pulse than to try to overcome the associated problems in an intracavity configuration. This strategy involves three distinct stages. Firstly, within the mode-locked laser, chirped pulses are produced. Next, these chirped pulses are amplified in an external Semiconductor Optical Amplifier (SOA) element. The chirped pulses will exhibit relatively low peak power and therefore will largely avoid problematic gain saturation effects associated with amplification of intense optical pulses. These amplified pulses can then be readily directed through dispersion compensating components to remove the frequency chirp, thus increasing the peak power [10]. By using this technique, pulses as short as 250 fs have been obtained from a semiconductor laser that was mode-locked using a quantum-well-based saturable absorber [11]. In a separate publication, the same authors also demonstrated 590 fs pulses with 1.4 kW of peak power from a colliding pulse mode-locked semiconductor laser, where the output pulses were subject to the eXtreme chirped pulse amplification technique [12].

One of the advantages of the external system I investigated is that it has the potential to be used to provide *intracavity* dispersion compensation. By using

this technique, it is in principle possible to obtain shorter pulses than with an external cavity scheme such as that used by Delfyett *et al* [9-11]. In an *external* dispersion compensation/compression scheme, chirped pulses *with an already defined spectral bandwidth* can be dechirped to produce bandwidth-limited pulses. Once the pulses have exited the laser resonator, their spectral bandwidth cannot be increased, they can only be shortened to a degree supported by the bandwidth they had upon emerging from the cavity.

In a resonator with *intracavity* dispersion management, pulses are chirp compensated as they evolve in the cavity. This active management of dispersion allows the possibility of phase locking a larger number of longitudinal modes. As a result of this increase in bandwidth, lasers with intracavity dispersion compensation are capable of supporting shorter pulses than those relying solely on external compression schemes. This can be seen clearly in mode-locked solid-state laser systems where intracavity dispersion-management enables the production of femtosecond pulses. Dispersion compensation can be obtained by prisms or chirped mirrors as outlined in Chapter 2 (2.2.5).

Control over peak power

Another important feature of an external cavity system is that the peak power of the optical pulses can be altered by changing the cavity length as shown in the following expression.

$$P_{pk} = P_{av} \, {}^{\tau_{RT}}\!/_{\tau_{pulse}} \qquad 5.1$$

In expression 5.1, P_{pk} and P_{av} are the peak and average powers respectively while the τ_p represents the pulse duration and τ_{RT} is the cavity round-trip time. By increasing the peak power of the laser, for example, the energy contained in the laser pulses will also be increased which can assist in optimum saturation of the saturable element. Here I only consider the case of passive mode locking by a saturable absorber element.

I employed an intracavity semiconductor saturable absorber mirror device as the mode-locking element in this work. One of the requirements for mode locking previously outlined in Chapter 2 – equation 2.22 was that the loss is saturated faster than the gain. By using an external-cavity configuration, there is the facility to alter the spot size on the SESAM whilst maintaining a constant spot size in the gain

material. This means then the ratio between the saturation energies can be adjusted, giving a more favourable regime for mode locking. Assuming a constant average power, decreasing the spot size will increase the intensity on the absorber, resulting in a greater saturation effect. In the laboratory setup employed here, the minimum spot sizes obtainable will be similar to those inside the waveguided gain section; but, by using a wider, tapered gain section, the external cavity would allow a proper exploration of this ratio.

Ability to separate gain and absorber behaviour

In an external cavity configuration, the part of the laser responsible for the gain and that which provides the saturable absorption are separate. This allows the absorber to be tailored to meet the requirements in order to facilitate optimal mode locking behaviour. If required, the absorber can be made of different material than the gain section. This was the case in the work of Keller *et al,* where a quantum-dot SESAM was used to mode-lock a quantum-well based vertical extended cavity laser to produce 3.3 ps pulses [13]. In this work, the authors explain that the low saturation fluence of the quantum-dot SESAM allows the laser to operate at a 50 GHz repetition rate while avoiding the tight focusing required and thermal problems associated with a comparable quantum-well SESAM based system.

In addition, since the absorber and gain are separate, there exists the option to temperature tune the SESAM or laser to either optimise the overlap of absorption and gain profiles or by increasing the SESAM temperature, decrease its recovery time as discussed in [14]. It is well known that as the temperature of quantum-dot devices is increased, their operating wavelength is red-shifted due to a lowering of their bandgap, as is the case for Bulk and quantum-well-based devices. In the paper by Klopf *et al*, the authors measure the tuning rate for quantum-dot lasers to be around 0.16 nm/K which is claimed to be less than half the typical value for a GaAs/AlGaAs quantum-well laser [15]. Small changes in absorption/emission wavelengths can thus be achieved by modest changes in operating temperature.

It should be noted however that other additional operating parameters of the laser device or SESAM will also change with temperature. For instance, the refractive index of the SESAM Bragg mirror will also change with temperature, leading to a tuning of the resonant properties of the SESAM with temperature. Since this effect

will exhibit a different tuning rate to the tuning of the peak absorption, eventually an offset will develop between the two [16].

It is useful to note that external-cavity systems also exhibit improved noise characteristics when compared to monolithic mode-locked laser devices of equivalent optical length [17]. This is because with an external cavity, large parts of the cavity can comprise passive elements or empty space therefore allowing lower repetition rates without altering the length of the semiconductor chip [18]. Lower noise operation can be useful in the limitation of ASE noise as discussed in Chapter 1. This could be useful for applications where low pulse timing-jitter values are important.

5.3 The Quantum-dot SESAM

I used a single section semiconductor optical amplifier designed for operation at 1270 nm as a gain element, placed in an optical cavity with a quantum-dot-based SESAM at one end. In the past, SESAMs have been used to achieve mode locking in solid-state lasers. For operation around 1µm, InGaAs quantum wells on AlGaAs mirrors are used. At 1.3µm and above, however, these systems exhibit very high non-saturable loss due to high strain (see Chapter 4, figure 4.6). To operate at this wavelength, the required indium concentration is too high to be able to readily incorporate the InGaAs QW into the Bragg stack.

The issue of low non-saturable loss is very important for solid-state lasers due to their low gain. By contrast, in semiconductor lasers the gain is significantly higher so this issue is less important. However, a high non-saturable loss will be detrimental to the efficiency and stability of the laser in a pulsed regime. In addition, the non-saturable losses will most likely be manifested in the form of scattering or two-photon absorption. This will increase the SESAM temperature, with implications for the reflectivity of the Bragg stack and absorption spectrum of the absorber layer. It follows that it is always best to strive to construct a SESAM having negligible non-saturable loss. An alternative to the InGaAs/AlGaAs material system would be to use SESAMs based on InGaAsP material, but due to the low index contrast between the layers, these devices exhibit quite narrow bandwidth reflectivity [19].

Two types of SESAMs offering improved performance at these wavelengths have been developed recently. The first of these are QW structures based on GaInNAs which are grown on GaAs mirrors. The inclusion of small amounts of nitrogen reduces the non saturable loss of the system by lowering the strain. I was involved in the utilisation of one of these structures to facilitate the mode-locked operation of a Cr^{4+}:YAG laser to produce 140 fs pulses, but this is not discussed here as it is outside the remit of this thesis [20, 21].

The second type of device is based on quantum-dot material. These possess excellent properties for the mode locking of lasers such as large spectral bandwidth (the precise details of which can be controlled by epitaxy) and ultrafast recovery as discussed previously. Since the initial demonstration of an epitaxially grown quantum-dot absorber mirror [22], several authors have utilised the technology in other laser systems. Interestingly, it has been shown that a QD-based SESAM incorporating a p-n junction displays similar pulse shortening abilities upon the increase of reverse bias as has been discussed earlier for monolithic QD lasers [23]. This is because increasing the reverse bias applied to the SESAM enhances the sweep-out of carriers from the device.

QD SESAMS have also been successfully deployed at 1.3μm to mode lock both Cr^{4+}:Forsterite [24] and $Nd:YVO_4$ lasers [25]. In the former work, McWilliam *et al* developed lasers that produced femtosecond pulses. They observed in preliminary measurements with a structure containing 20 dot layers that the shortest pulses were produced when the cavity was arranged such that the SESAM was at an angle of 45° to the path of the beam rather than at normal incidence. This allowed better overlap between the laser output spectrum and the absorption spectrum of the SESAM. The ability to angle-tune demonstrated a useful technique that may be used to tune the absorption of resonant cavity QD SESAMS to lower wavelengths. The authors then implemented a new, optimised QD SESAM containing 25 layers of dots where the gain of the laser and absorption spectra of the SESAM overlapped at zero incidence.

More recently, a quantum-dot SESAM was implemented in a $Yb^{3+}:KY(WO_4)_2$ laser system that produced mode-locked femtosecond pulses. The authors accurately measure the saturation fluence of this 9-QD layer device to be 25 μJ/cm^2 and its modulation depth to be 2.3% [26]. A fibre laser has also been mode locked using a

QD SESAM of this design. The higher gain of this type of structure demanded a higher modulation depth of 17.8% and a saturation fluence of 591 μJ/cm^2. This high fluence value was facilitated by the 80 layers of quantum-dots which constituted the absorbing region of the device [27].

QD SESAMs have also been implemented as previously mentioned in the mode locking of vertical extended cavity surface emitting lasers (VECSELS). In this work, the modulation depth and saturation fluence of the device of the SESAM used were around 3 % and 1.7 μJ/cm^2 respectively. This device contained a single layer of quantum-dots in its absorbing layer and allowed the production of pulses measuring 2.8 ps. [28].

We see from the above that QD SESAMs with a variety of modulation depths have been used to mode lock different laser systems. Low gain systems such as the solid-state vibronics and VECSELs require modulation depths of anywhere between 1% and 3% depending on the stimulated emission cross sections of each gain material and the absorption cross section of the SESAM at the operating wavelength. At this point, it is worth noting that despite the fact that VECSELs have high gain semiconductor material as a gain medium, the short length of their gain sections delivers less round-trip gain than a conventional edge-emitting semiconductor laser. In contrast, the high overall gains that can accessed in fibre lasers demand a stronger modulation of their gain to instigate mode locking.

In the system investigated in my project, I have sought to for the first time, to exploit a quantum-dot SESAM to mode lock a quantum-dot edge-emitting laser Moreover, I made an initial attempt at marrying the parameters important for mode locking with QD gain material to those qualities most readily offered by QD SESAMs. I had predicted that a modulation depth of around 10% would be sufficient to initiate mode locking where this estimate takes account of the gain of the active material relative to those discussed above. For this initial investigation, I used the same 25 layer quantum-dot SESAM as deployed for the work reported in reference [29][4].

As will be shown later, this device demonstrated characteristics which suggested its potential suitability. The versatility of the external cavity was one of the

[4] In references [1] and [2], it was stated that the SESAM contained 30 planes of dots and slightly different dimensions, however recent dialogue with the device grower revealed that this was not the case.

keys to the success of the investigation of this laser system allowing the demonstration of high-power mode locked operation.

5.4 Material description

The initial QD gain-section chips used in this work were grown by molecular beam epitaxy (MBE) on a GaAs (100) substrate by a commercial company (Innolume GmbH). They contained 9 layers of self-organised dots with a dot density of 5 $x10^{10}$ cm^{-2}. The dots were typically 7 nm high and had a 15 nm base. Into this material, single section ridge waveguides of width 10 μm were shallow-etched. The gain chips were then cleaved into devices of length 2.8 mm. One face of these single section gain chips was left as cleaved while the other was given an antireflection coating such that feedback was reduced to below 0.5 % for GS emission.

The QD SESAM used in this work was grown by MBE using a Riber 32P machine at the Ioffe-Physico Technical Institute in St Petersberg. The material structure comprised (in order of growth) a GaAs(100) substrate, followed by a GaAs buffer layer then a distributed Bragg reflector (DBR) with reflectivity from 1250 nm to 1400 nm and a peak reflectivity of 99.5 %, then a first 0.23 μm thick GaAs matrix layer, 25 planes of InAs/InGaAs QDs separated by 50 nm thick GaAs spacer layers. After the dot layers, a second 81.5 nm thick GaAs matrix layer, a 0.2 μm thick $Al_{0.4}Ga_{0.6}As$ barrier layer, and finally a 10 nm thick GaAs cap layer were grown to complete the structure. The DBR consisted of 25-period quarter-wave $Al_{0.95}Ga_{0.05}As$/GaAs stack. The QD plane was formed by deposition of 2.3 monolayers of InAs followed by a 5 nm thick $In_{0.16}Ga_{0.84}$ As covering layer. This is shown below in figure 5.1.

The density of dots in the QD SESAM material is similar to that of the QD gain section. In order to characterise the QD SESAM, it was placed in a photo-spectrometer. The resulting reflectivity traces for different areas on the SESAM surface are shown below in figure 5.2 for a probe beam at normal incidence. The obvious dip around 1250 nm corresponds to the absorption area of the SESAM. The total losses of the SESAM (saturable plus non- saturable) are around 10.5 – 11%. This SESAM was previously used to mode lock a Cr^{4+}:Forsterite laser, producing 160 fs pulses at 1280 nm. The authors measured the saturation fluence of the SESAM to be

280 μJ/cm^2 [30]. We can also assume that the device exhibits low non-saturable losses.

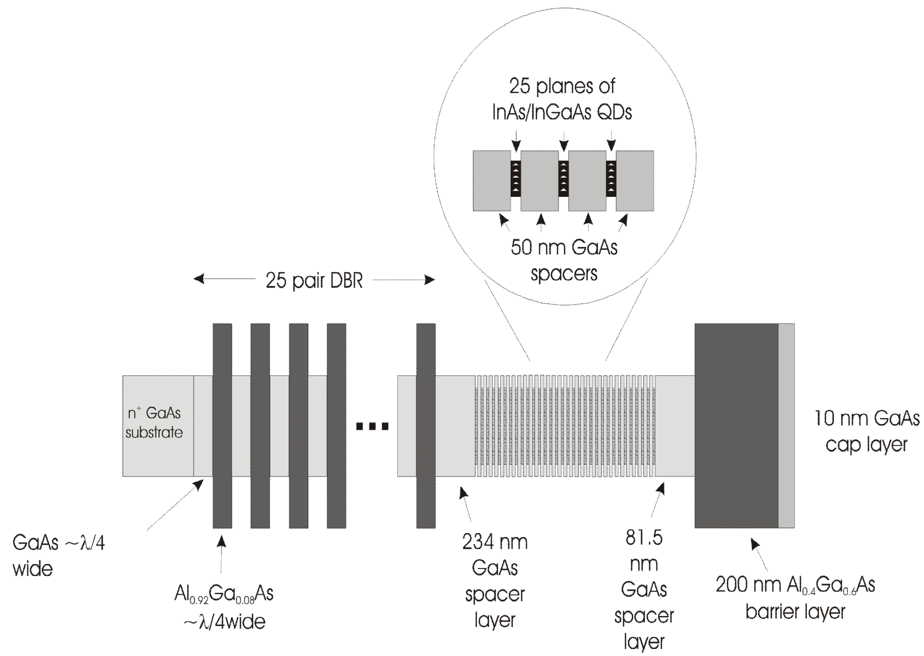

Figure 5.1. QD SESAM material structure

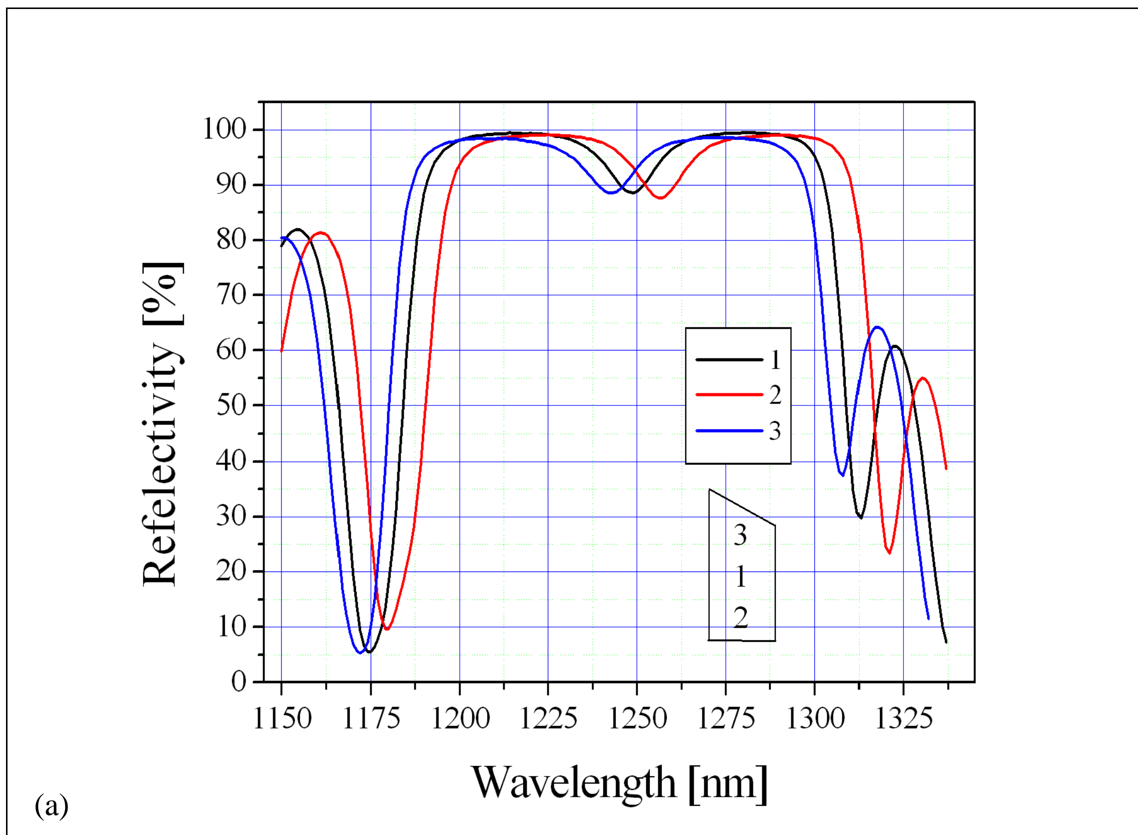

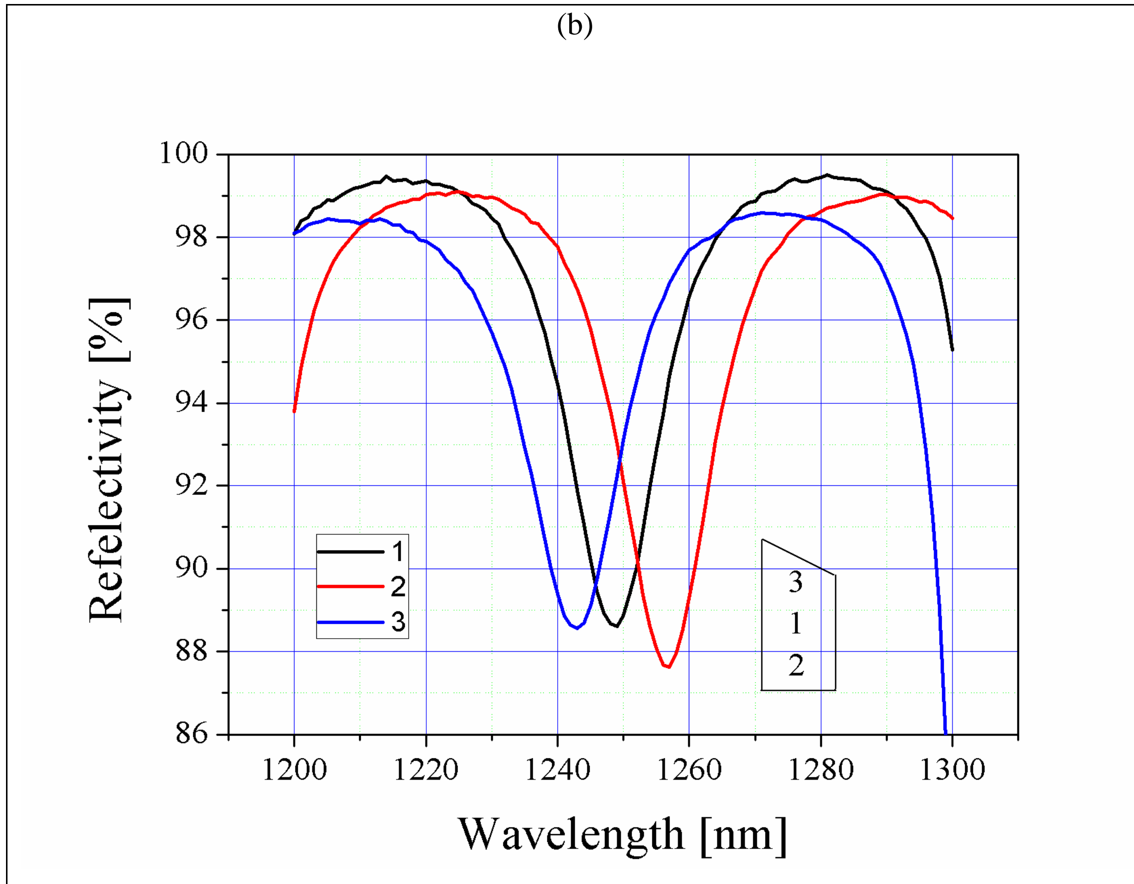

Figure 5.2. (a) Reflectivity of QD SESAM as a function of wavelength for different positions on wafer fragment and (b) zoomed in trace. This measurement is distinct to that reported in reference [29] where the author states the total losses to be around 0.03 in arbitrary units.

5.5 Experimental setup

The corresponding experimental setup is shown below in figure 5.3. The cleaved, antireflection coated gain chips were mounted p-side up on a copper heatsink. A thermoelectric cooler was then used to maintain the temperature of these devices at a constant 20 deg C. The QD SESAM was mounted on two linear stages to give control of position of the incident light on the SESAM. This was then attached to a wide span motorised linear stage to give some control over the cavity length and spot size as discussed above. Light reflected back from the SESAM is coupled into the facet of the gain section by a X40 aspheric lens. Output from the as-cleaved facet of the laser is then collimated by means of another X40 aspheric lens. After the laser cavity terminates, an optical isolator is used in order to eliminate unwanted back reflections into the cavity The laser output is then coupled into single transverse mode optical

fibre where the fibre end is angled by 8 degrees away from the normal to further eliminate back reflections. The diagnostic equipment used consisted of a Rees optical spectrum analyser with a resolution of 0.4 nm and capable of measuring signals above 10 μW in power. The RF spectra were measured using a Rhode & Schwarz FSP 40 radio frequency spectrum analyser capable of measuring signals up to 40 GHz and with a resolution bandwidth variable between 1 Hz and 10 MHz and a 1 Hz noise level of -155 dBm. A Melles Griot universal optical power meter fitted with a Ge head was used to measure the power from the laser. It had a sensitivity of 10 μW. An HP54750A oscilloscope (with 50 GHz bandwidth) was used to measure the temporal characteristics of the emission. The oscilloscope was used in conjunction with a Newport D-30IR-FC photodetector with a minimum response time of 30 ps and was triggered with a Newport D-15IR-FC photodetector with a minimum response time of 15 ps. This would allow far easier pulse measurement to be carried out than is possible with the autocorrelator, especially given the long duration and low peak power of the pulses described later in the chapter. A representation of the setup is shown below in figure 5.3.

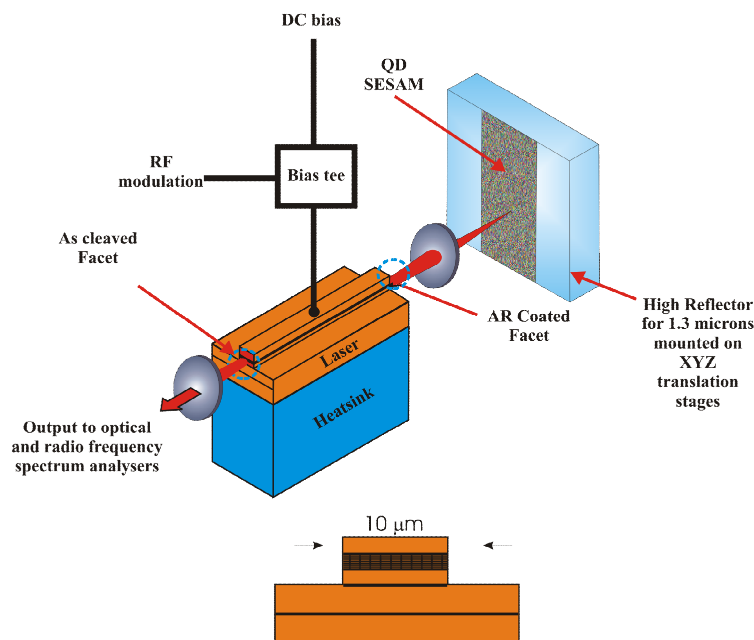

Figure 5.3. Experimental setup

5.6 Results

First investigations into the performance of this system began with obtaining light-current characteristics. Figure 5.4 shows such graphs for two different QD gain chips where it can be seen that there was no evidence of overheating of the device or rollover of the output power.

The threshold current for both devices is significantly higher than one would expect for a monolithic device. This can be partially attributed to the additional losses introduced by the external cavity configuration. Device (b) exhibits a slightly higher threshold current than device (a) but displays a better slope efficiency, pointing to higher mirror reflectivity. It was unclear as to whether this was due to variations in the devices which were from the same batch of commercially purchased lasers. A great deal of difficulty was found in sourcing reliable, high quality devices for this work. This was punctuated by the failure of device (b). Subsequent work therefore was carried out using device (a).

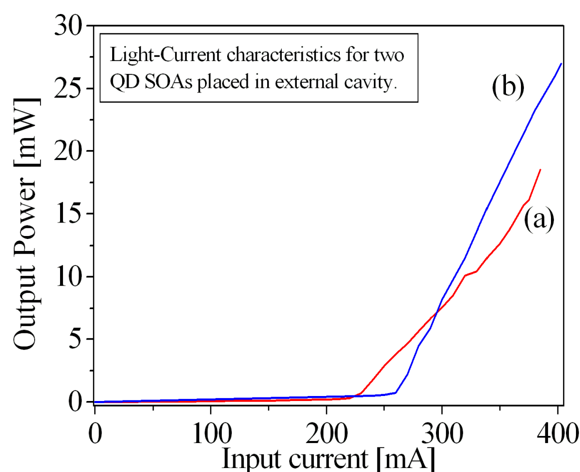

Figure 5.4. Light-current characteristic from two theoretically identical QD gain chips a and b.

Optical spectra of the emission from the laser were obtained and are shown below in figure 5.5 for both the cw case and the mode-locked cases. Mode-locked spectra correspond to reflection by the QD SESAM whereas cw operation corresponds to reflection from a high relectivity (R = 99%) mirror.

We see from the optical spectra that emission from the QD laser is centred at 1205 nm. This corresponds to ES1 rather than GS emission. This further explains the high threshold of the device shown in figure 5.4. It can be speculated that gain in the GS is too low to compensate for the total losses of the cavity. This conclusion can be reached because of previous investigations into the state-switching dynamics in quantum-dot lasers [31]. In this work, Markus *et al* explored the cw lasing behaviour of quantum-dot lasers of varying lengths. In devices below 1.5 mm in length, there was insufficient gain to observe any ground state lasing. Lasing thus commenced through the first excited-state at high current densities of around 710 Acm^{-2} In longer devices, lasing proceeded at far lower threshold currents (210 $Acm^{-2)}$ from the ground state with excited-state emission becoming apparent at higher pumping currents. The shorter cavity lasers possessed insufficient gain to allow GS lasing.

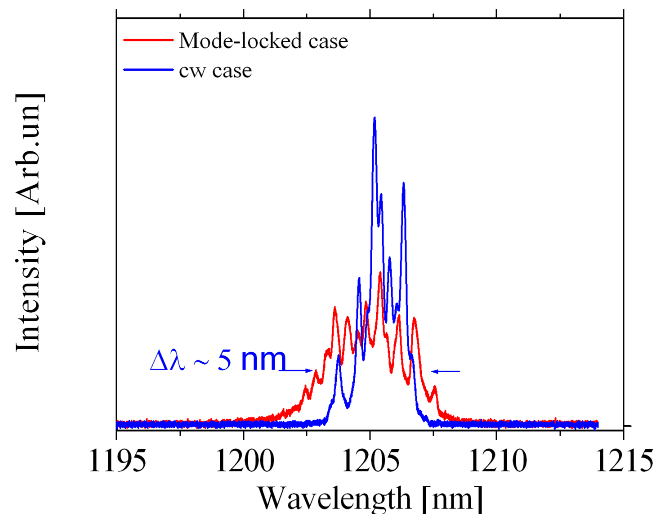

Figure 5.5. Optical spectra in cw and mode-locked case at a bias current of 385 mA. This shows the wide, inhomogeneously broadened nature of the laser emission from quantum-dot devices.

This increase in loss is also apparent if we compare the threshold current of the external cavity laser studied in this work to that of a typical monolithic mode-locked quantum dot laser as in [32], where the measured threshold current 25 mA at 298° K. The active region in this device was 2.1 mm in length.

A comparison of the two spectra reveals a significant broadening when the QD SESAM is used as a reflector and the FWHM is approximately 5 nm. This bandwidth would be capable of supporting Gaussian pulses with durations of around 430 fs if the pulses were bandwidth limited. To verify pulsed operation, I obtained an RF spectrum

(fig. 5.6 below) and there is clear evidence of a repetition frequency of around 860 MHz. This corresponds to a total optical cavity length of 17.2 cm. Higher harmonics of this fundamental frequency are also visible confirming the stability of the mode locking. The height of the RF peaks – in excess of 40 dBm - is also indicative of the strength of the mode-locked pulsations. In the figure below, there is a clear discontinuity in the measured spectrum at around 3 GHz. This is due to the internal workings of the spectrum analyser used in the work. The Rohde & Schwarz FSP-40 steps through its frequency range, not in one continuous large sweep, but rather in a series of smaller ones. Each one of these has a slightly different noise-floor value. The boundary between two of these sweep fields happens to reside at around 3 GHz, which results in the observed discontinuity seen in the RF trace. This discontinuity was also visible when no signal was input to the RF analyser, further demonstrating that this is an artefact of the measurement device. It was possible to observe mode locking at fundamental frequencies ranging from 350 MHz to around 1.5 GHz but the optimum performance was observed at the frequencies shown in the figure. This corresponds to an estimated spot size of 50 x 15 μm.

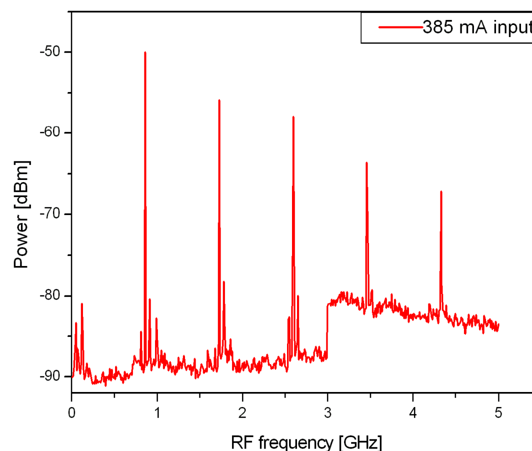

Figure 5.6. RF spectrum from an external-cavity laser

The optical and RF spectra show clear evidence of instabilities. Judging by the additional sub-peaks present in the RF spectra and spikes in the optical spectrum, it was concluded that the mode locking was not optimised. At this point, a fast oscilloscope and photodiode similar to that used in Chapter 3 was employed to try to observe the temporal behaviour of the laser. Unfortunately, due to the poor stability of the mode locking, it was not possible to measure the pulse duration.

The most likely explanations for this instability are related to the characteristics of the QD SESAM. Comparing figures 5.5 and 5.2, the output of the laser is centred at 1205 nm whereas the absorption of the SESAM is centred at around 1250 nm, depending on the position on the SESAM surface. Although the QD material in the SESAM possesses a broad spectral bandwidth which is capable of mode-locking at wavelengths corresponding to ES1, the SESAM does not perform optimally at this wavelength. Away from its design wavelength, the SESAM would not allow access its full modulation depth of around 10 %. The small modulation thus available was insufficient to properly mode-lock semiconductor lasers of the type explored here. In addition, the high threshold current and excited-state exclusive lasing behaviour of the quantum-dot gain chip suggested that this device was not of the highest quality. This was likely to be a factor in the poor performance of the laser system as a whole.

An attempt to improve the stability of the mode locking involved imposing an additional RF field was applied to the laser field by means of an RF signal generator and a bias tee. This imposed a modulation on the current injected into the device. This technique is known as hybrid mode-locking and is a widely used method of stabilising the operation of mode-locked semiconductor lasers [33]. The strength of the imposed modulation was controlled by adjusting the power of the signal coming from the generator. A RF modulation of approximately 13 dB was superimposed onto the drive current of the laser, attempting to impedance match the impedance of the RF modulator and bias tee. The match was not however ideal.

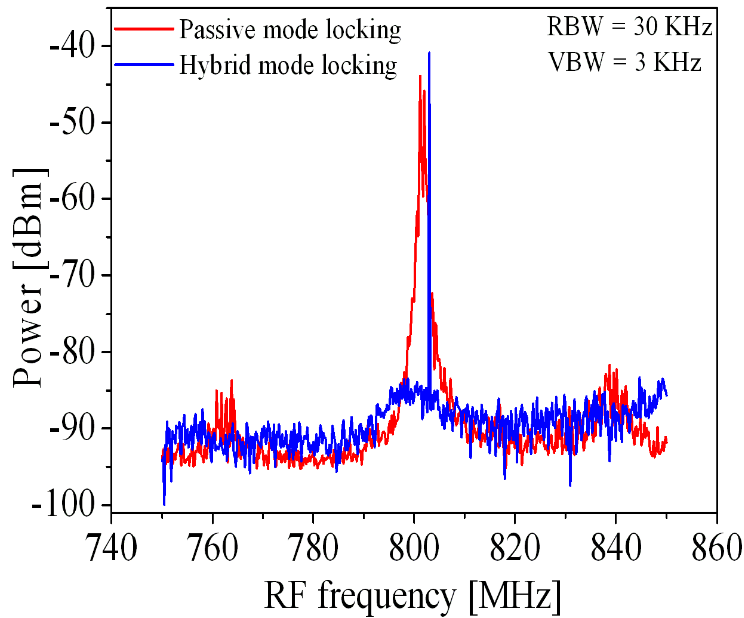

Figure 5.7. RF spectra under passive (wider) and hybrid (narrower) mode locking at a bias current of 385 mA.

One advantage of this method is that it allows easy synchronisation of the laser pulses with external diagnostic equipment. RF spectra under passive mode-locked conditions (only the QD SESAM) and Hybrid conditions (with additional electrical RF modulation) are shown above in figure 5.7. When the additional RF modulation is applied to the system, we observe a significant narrowing in the width of the RF peak. This suggests that the additional RF biasing was aiding the stability of the device. At this stage an attempt was made to once more try to measure the duration of pulses produced by this system by autocorrelation. Unfortunately, however, the improvement in the appearance of the RF frequency did not allow the temporal characteristics to be explored in this way.

At this stage, a new quantum-dot SOA device was purchased from Innolume GmbH and incorporated inton the external cavity setup with the existing SESAM structure. The quantum-dot SOA comprised of a single section 5 μm wide ridge waveguide structure, 3.5 mm in length. The facets of the SOA were both antireflection coated and angled at 7 degrees from the normal to prevent lasing without additional feedback. The device contained 10 layers of quantum-dots in a 450 nm thick active region with a dot densitiy and typical dot dimensions similar to that

previously described. The robust, high quality nature of this new SOA allowed injection currents of up to 650 mA to be applied.

The external cavity was then redesigned to try to increase the fluence on the SESAM which in turn would then increase the modulation it could provide to the laser field. A representation of the refined cavity design is shown below in figure 5.8.

In initial experiments, the SOA had one facet which was uncoated and this provided feedback into the laser. Since the new SOA has dual antireflection coatings, additional mirrors can be used on both ends of the cavity to provide feedback without the additional reflected field encountered if one of the facets is 'as-cleaved'. While on one side of the cavity, feedback was provided by the SESAM/HR as before, on the other side, varying degrees of feedback were provided by changing the transmission of the output coupling mirror. By reducing the transmission of the output coupler, the intracavity power will be increased which will increase the power incident on the SESAM. In addition, on the end of the cavity containing the SESAM, a secondary lens of equal power to the SOA coupling lens is used to tightly focus the output from the SOA to a considerably smaller spot than is possible with the one lens configuration used in the initial experiments. The dimensions of the spot on the SESAM are estimated to be approximately 2 microns x 20 microns. This smaller spot will increase the fluence on the SESAM, enhancing its saturation without altering the fluence inside the SOA. To further improve the ability to finely adjust the feedback into the cavity, the coupling and focusing lenses were affixed to mounts allowing angular control in addition to the existing XYZ positioning.

The diagnostic equipment was then improved in order to gain more accurate information regarding the lasing behaviour. An Agilent 86140A optical spectrum analyser with a wavelength resolution of ±0.025 nm and a sensitivity at 1300 nm of -90 dBm was used for characterisation of optical spectra.

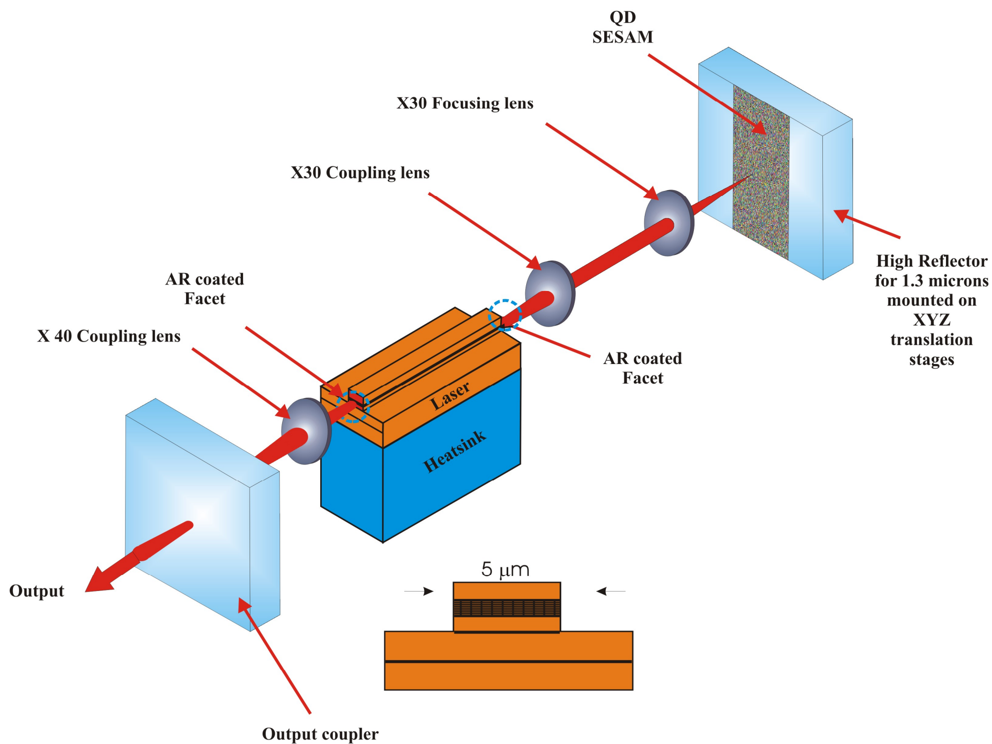

Figure 5.8. Improved external cavity design

Below in figure 5.9 are plots of output power as a function of input current for different cavity feedback conditions. We see that when no feedback is employed (zero mirror configuration) the SOA does not reach lasing threshold. We see a steady linear increase in output with increasing current. An examination of the optical spectra in this configuration revealed that the SOA did not reach lasing threshold. This is in accordance with expectations for an SOA device with no feedback supplied to it. The one mirror configuration corresponds to the case when feedback is supplied to only one side of the cavity by means of the SESAM/HR mirror while all light emerging from the opposite facet is output coupled.

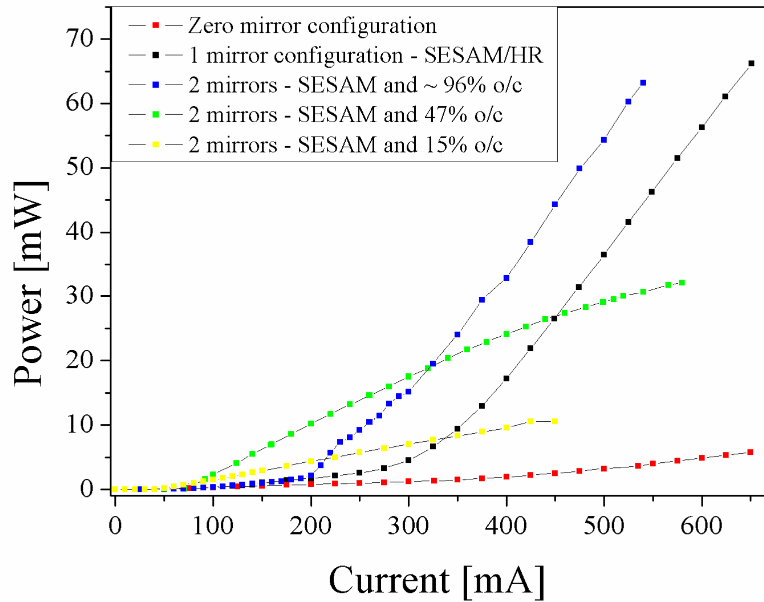

Figure 5.9. Light-current characteristics for various cavity feedback conditioons

We do not observe any rollover behaviour except when the 47.5% and 15% output couplers are used. In these cases, overheating occurs at around 570 mA and 400 mA respectively. Clearly, as the transmittance of the output coupler is decreased, the output power from the laser decreases, while at the same time the power circulating within the cavity increases. This explains why the threshold lasing current decreases as the transmittance of the output coupler decreases. At the same time, decreasing the transmittance of the output coupler also decreases the slope efficiency of the laser. This is because a lower output coupling mirror results in an increased influence by intracavity losses and less of the circulating laser field is being output coupled.

This new device was capable of producing light from both ground and excited states, depending on the injection current and feedback conditions employed. When the laser is operated in a 1 mirror configuration or with a glass slide output coupler, the evolution of the laser output behaves in a similar manner as was outlined for the optically pumped quantum-dot laser discussed in Chapter 4 or indeed that described by Markus *et al* [31]. Emission begins from the GS, increasing in intensity with pump current. At higher injection currents around 400 mA, emission from ES1 begins. At high input currents (650 mA) output from GS does not cease but the emission is

dominated by contributions from ES1. The output spectra for low and high pump currents are shown below in figure 5.10.

When the quality factor of the cavity is increased by changing the output coupler to a 47% o/c or the 15% transmitting o/c, the laser operates solely on GS with no contribution from ES1, even when the input current is high enough to produce overheating in the SOA. In the case of the 15% output coupler this is partially due to the point of device overheating occurring at low pump currents where ES1 contributions may not have been taking place. Another contributing factor is that cavity losses are reduced as more highly reflecting output couplers are used, allowing the contribution from the GS to use up the additional carriers as the input current is increased.

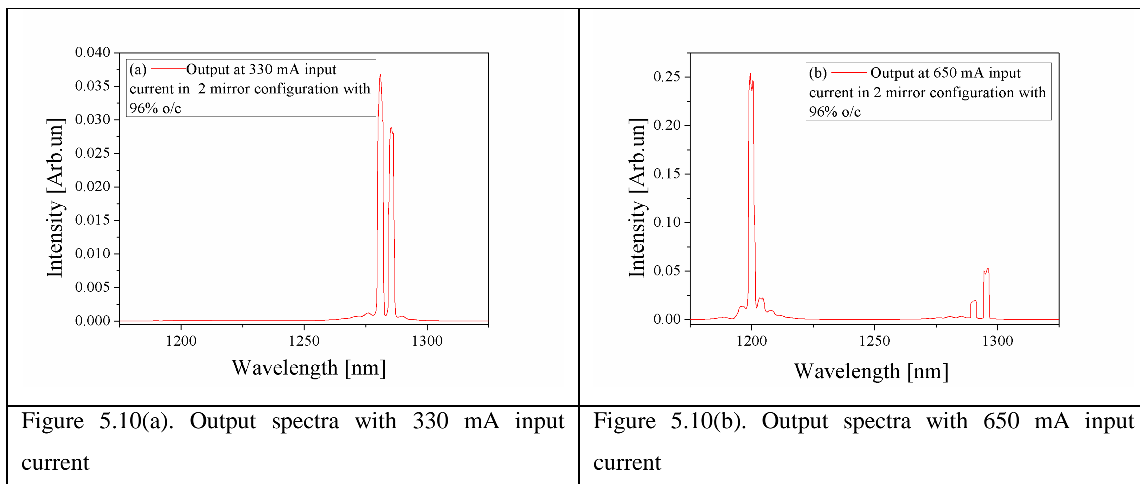

Figure 5.10(a). Output spectra with 330 mA input current	Figure 5.10(b). Output spectra with 650 mA input current

With the continuous wave lasing behaviour understood, we then investigated the mode locking behaviour of the external cavity system. When operated in a single mirror configuration, no evidence of pulsed operation was seen. It is thought that here, the double pass geometry coupled with the low fluence on the SESAM was not sufficient to allow mode locking. The cavity was then altered to incorporate the second mirror. This would not only increase the circulating intracavity power but also increase the cavity length. In this configuration with a 96% output coupler, a strong modulation was visible on the RF analyser at around 1.1 GHz. This was also visible on the oscilloscope. Plots of these are shown below along with optical spectra in figure 5.11.

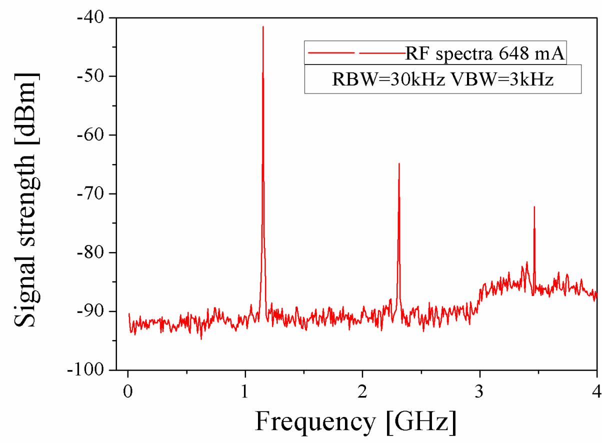

Figure 5.11(a). RF spectra at 648 mA input current with 96% o/c

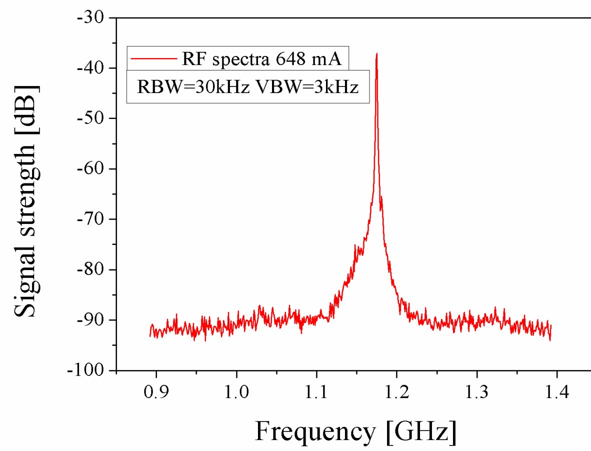

Figure 5.11(b). Zoomed in RF spectra at 648 mA input current with 96% o/c

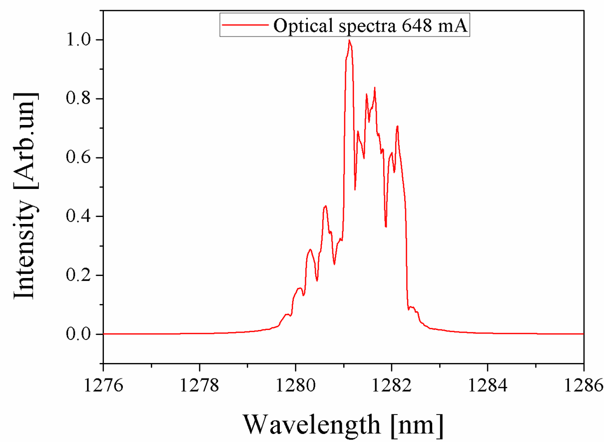

Figure 5.11(c). Optical spectra 648 mA input current with 96% o/c

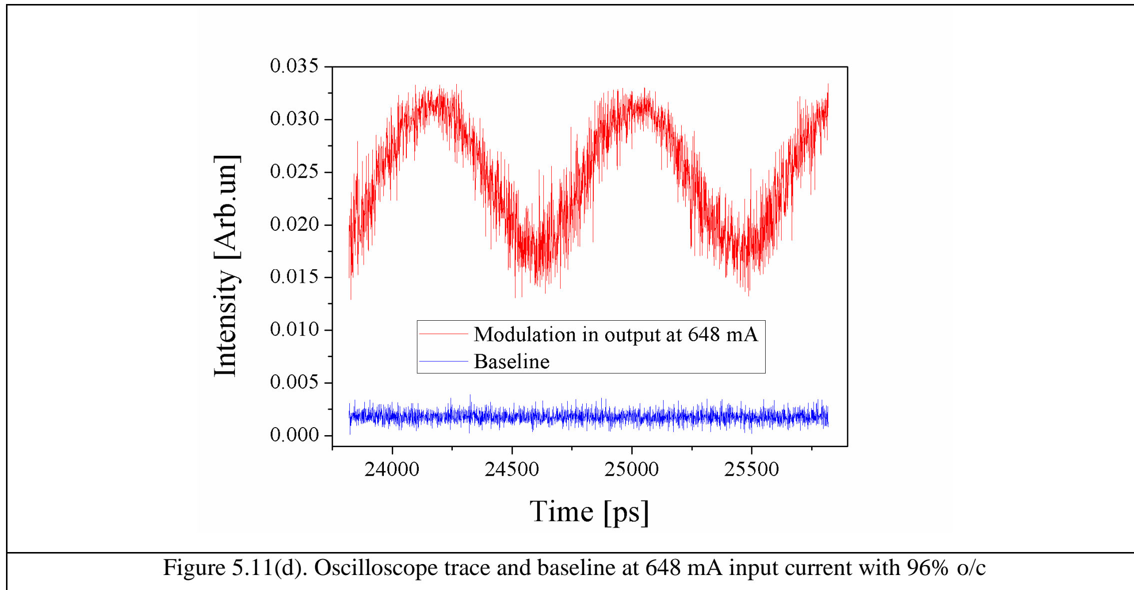

Figure 5.11(d). Oscilloscope trace and baseline at 648 mA input current with 96% o/c

Looking at the oscilloscope trace, there is a substantial offset from zero in the pulses and there is overlap between one pulse and the next. The pulses are not properly formed and appear as a modulation on top of the laser output rather than separate discrete pulses. As a result of this, it is difficult to make measurements regarding the duration of the pulses. If we assume that the bottom end of the modulation corresponds to what would be the FWHM of the 'pulses' then we can estimate that the duration is of the order of 800 ps. This result was obtained at maximum injection current. It was theorised that increasing the intracavity power in this configuration might improve the performance; potentially yielding shorter pulses where the oscilloscope signal returned to zero between pulses.

Implementing these ideas, the 96% o/c was replaced with a 47% o/c which increased the intracavity power by a factor of 13. This step lead to a significant increase in performance as the SESAM was more effectively saturated. On this occasion, the pulses produced displayed the return to zero behaviour described above and were visible for a wide range of input current values. A typical data set for an input current of 280 mA is shown below in figure 5.12.

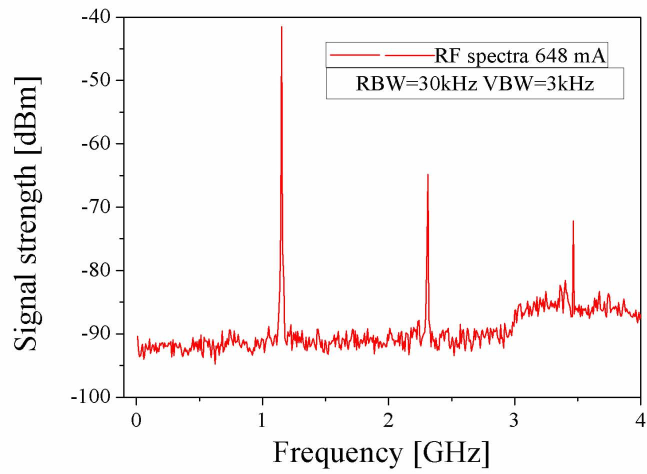

Figure 5.12(a). RF spectra at 260 mA

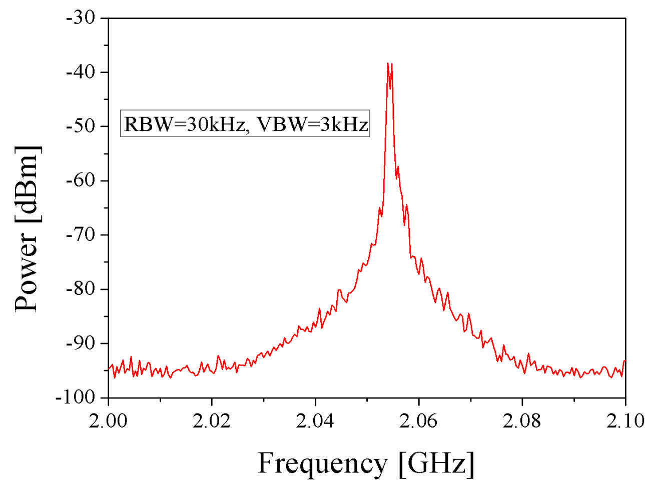

Figure 5.12(b). Zoomed in RF spectra at 260 mA

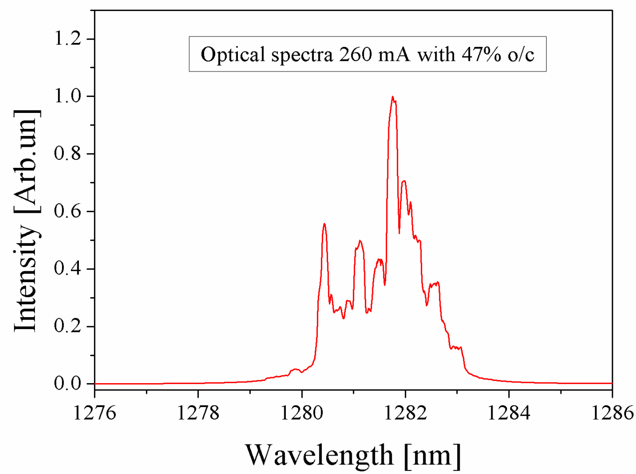

Figure 5.12(c). Optical spectra at 260 mA

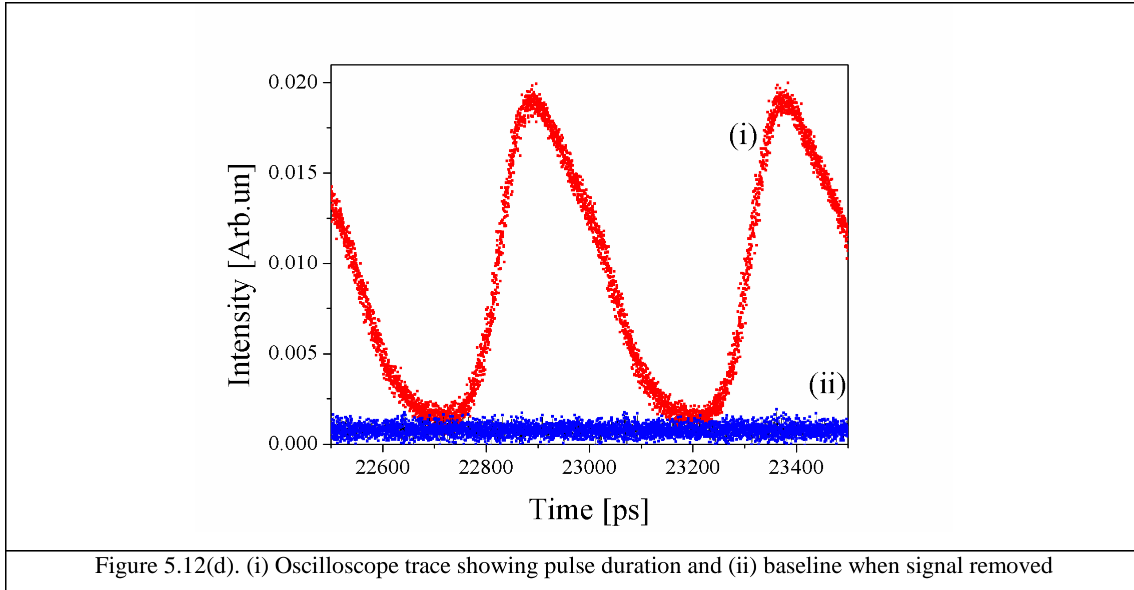

Figure 5.12(d). (i) Oscilloscope trace showing pulse duration and (ii) baseline when signal removed

As we can see, pulses of duration around 200 ps are produced in this configuration. Interestingly, from the RF spectrum, we see that the pulses repetition frequency is about 2 GHz which is twice the cavity round trip frequency. There are two sets of pulses propagating in the cavity which in this case is an indication of non-optimised mode locking. In addition, looking at the oscilloscope trace, the pulses are misshapen on their trailing edge which is indicative of there being multiple pulses overlapping within the visible scope.

To try to gain a better understanding of the processes involved, I then performed a series of measurements on the pulse duration as the input current was increased. The result is shown below in figure 5.13.

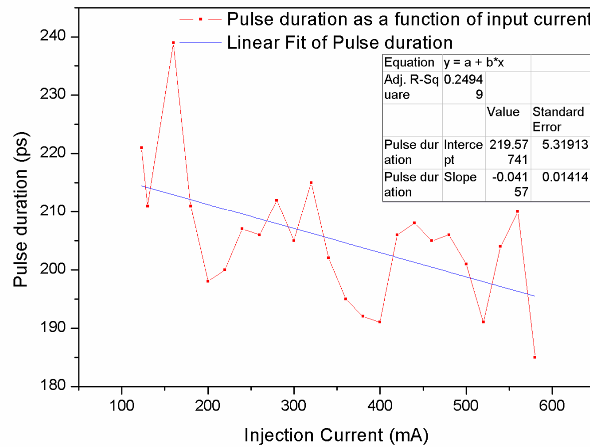

Figure 5.13. Pulse duration as a function of injection current

A slight trend of decreasing pulse duration with increasing injection current is visible from the plot. Taking a line of best-fit, there is roughly a 20 ps drop in pulse duration over the range of currents investigated.This can be explained by the increased fluence on the SESAM with increasing injection current. Correspondingly, the fluence on the SESAM increases from 3.5 μJ/cm^2 to 25.4 μJ/cm^2 over the range of injection currents investigated. However, since there are multiple pulses present in the oscilloscope trace, it is unclear whether this apparent shortening is actually due to one or more of the constituent pulses becoming narrower or if the constituent pulses are moving with respect to one another within the envelope, altering their degree of overlap and thus the width of the whole envelope.

At this point, the 47% output coupler was replaced with a 15% o/c to further increase the intracavity power. Unfortunately, no pulsing behaviour was observed on either the RF analyser or the oscilloscope.

A possible explanation is that when the 47% o/c was in use, the SESAM was possibly already providing the maximum modulation possible at the lasing wavelength. From looking at figure 5.2, at 1280 nm, the SESAM possesses a maximum modulation depth of 1.4%. When the output coupler was then changed to a 15% o/c, the amount of modulation provided by the SESAM could not then increase because this was already its maximum value, but the intracavity power increased, which would then require a larger modulation to instigate mode locking.

This work is a useful demonstration of the different mode locking requirements of semiconductor lasers in comparison to their vibronic counterparts. As previously mentioned, the SESAM used in this work was used to mode lock a Cr^{4+}:forsterite laser at 1278 nm. At this wavelength, the SESAM possesses a maximum modulation depth of 1.5 % [29]. This is in obvious contrast to the 200 ps pulses we obtained from our external cavity quantum-dot laser. It should also be noted however that the fluences incident on the SESAM are considerably different in the vibronic and semiconductor laser cases. In the case of the Cr^{4+}:forsterite, the fluence where modelocking first appears is 280 μJ/cm^2 (at1280 nm) [30]. In the case of the quantum-dot external cavity laser, the maximum fluence obtainable with the 47% o/c is 25.4 μJ/cm^2 at 1281 nm, assuming a pulse duration of 200 ps, a repetition frequency of 2 GHz, an average output power of 30 mW and an elliptical spot on the SESAM

with semi-major axes measuring 2 μm and 20 μm respectively. This is roughly a factor of 10 lower than is required at this wavelength to fully saturate the SESAM.

We therefore conclude that the SESAM is not optimised for operation in this particular laser system. The amount of modulation this SESAM can superimpose on the laser field is insufficient to optimally mode lock the quantum-dot laser at the wavelength and power levels at which the quantum-dot laser operates.

The SESAM-based semiconductor external cavity laser system has been explored previously by several authors such as Shen *et al* [34] and Adams *et al* [35]. Both authors attempt to mode lock a semiconductor laser using a SESAM device. Interestingly neither of the authors report mode locking when the SESAM is used in isolation. In the work of Shen *et al*, they also use a reverse biased section in the laser chip to mode lock the laser while in the work of Adams *et al* they impose an additional RF bias on the laser to see mode locking.

In the paper by Shen *et al*, the SBR is employed to allow the production of shorter pulses than are possible when the multisection laser is used in conjunction with a normal high reflector mirror.

Despite this disappointment, these initial results demonstrated the potential of this all-QD external cavity system. These results bear testament to both the quality and versatility of this laser gain chip and SESAM. This work also demonstrated for the first time to my knowledge the operation of a QD SESAM designed for operation close to the QD GS in an ES1 mode locking regime. In addition, I was able to show that a mode locking element designed specifically for use with low gain laser materials was able to induce strong though ultimately unoptimised mode-locked laser pulses in a high gain semiconductor laser.

5.7 Additional work on quantum-dot lasers

In conjunction with my investigations into external cavity-based mode-locked quantum-dot lasers, I was also involved in investigating the behaviour of monolithic two–section quantum-dot laser systems containing an integrated quantum-dot saturable absorber formed by a split electrical contact. These studies were performed in collaboration with colleagues, Dr Maria Ana Cataluna and Dr Edik Rafailov. Significant results obtained included the demonstration of the shortest pulses

obtained directly from a mode-locked quantum-dot laser [36][5], mode locking in both GS and ES1 regimes in a monolithic laser [37, 38] and the enhancement of GS modelocking by simultaneous emission from ES1 [39].

I had significant involvement into studies of the temperature resilience of quantum-dot material. This work was connected with one of the original hypotheses of quantum-dot performance, namely that of temperature insensitive operation [40]. A defining aim was therefore to examine the performance of a mode locked quantum-dot laser under increasing temperature. For example, simplification of optical communications technology could be achieved by the inclusion of temperature insensitive laser transmitters. This would allow the removal of cooling equipment employed to stabilise temperature and performance. If quantum-dot lasers could be utilised in this way, then this would allow them to be used in the next generation of simplified ultrafast communication systems.

Initially, a value of the characteristic temperature of the laser was determined as a measure of its temperature insensitivity. By using the following expression, a value of $I_0=\infty$ would correspond to a truly temperature insensitive device.

$$I_{th} = I_{th0} \exp(\frac{T}{T_0}) \qquad 5.2$$

In the above, I_{th} is the threshold current, I_{th0} is the threshold at a reference temperature, which is a constant. T is the temperature in Kelvin, T_0 is the characteristic temperature. A value of 41 K was found for the characteristic temperature. This was found to be accurate for up to 70 °C, beyond which, thermal excitation of carriers results in a departure from this value. This trend of a constant T_0 at low temperatures followed by a departure from this at higher T is consistent to that found in the literature [41]. This low value for the characteristic temperature is lower than that calculated for quantum-dot laser devices in the literature [42]. The comparatively poor performance of our device reflects the fact that it was not designed with temperature-insensitive operation in mind.

The quantum-dot laser was then investigated in a mode locked configuration at various heatsink temperatures. The gain section and saturable absorber were balanced so as to give stable mode-locked operation with an average output power of 7 mW at each of the heatsink temperatures investigated.

[5] This work was completed prior to my arrival and is included here to give a flavour of the types of investigation being carried out.

Stable mode locking was demonstrated in a temperature range spanning 50 °C from 20 °C through to 70 °C, with signs of deterioration only emerging for operation at 80 °C. This is shown above in figure 5.14 as presented by my colleague Dr Cataluna. We notice that as the temperature is increased, the optical spectrum is red-shifted as previously documented in semiconductor lasers [43]. The second point to note about figure 5.8 a) is that as the temperature increases from 50 °C to 70 °C, the width of the optical spectrum decreases dramatically. This phenomenon has been subject to extensive study elsewhere. Sakamoto and Sugawara suggest that this can be explained by an increase in homogeneous broadening at higher temperatures leading to suppression of lasing [44]. However, Patane et al suggest an alternative mechanism, namely that changes in carrier relaxation from dots at increased temperature results in a narrowing of the dot laser mode distribution [45].

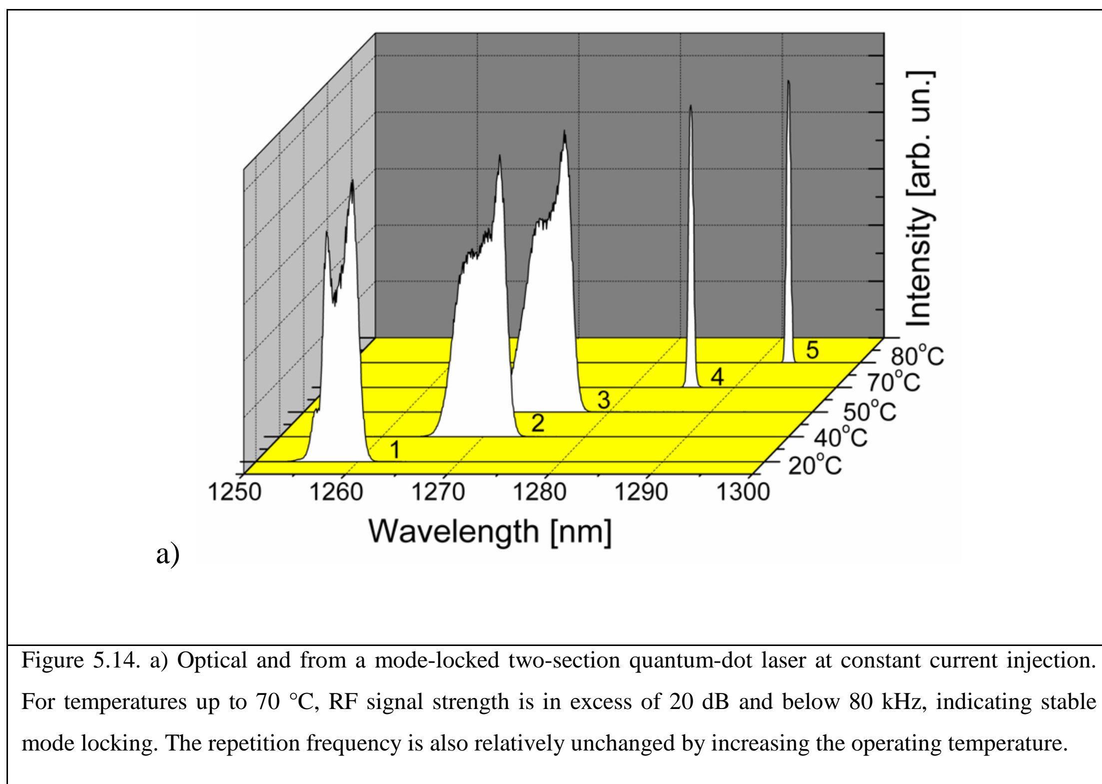

Figure 5.14. a) Optical and from a mode-locked two-section quantum-dot laser at constant current injection. For temperatures up to 70 °C, RF signal strength is in excess of 20 dB and below 80 kHz, indicating stable mode locking. The repetition frequency is also relatively unchanged by increasing the operating temperature.

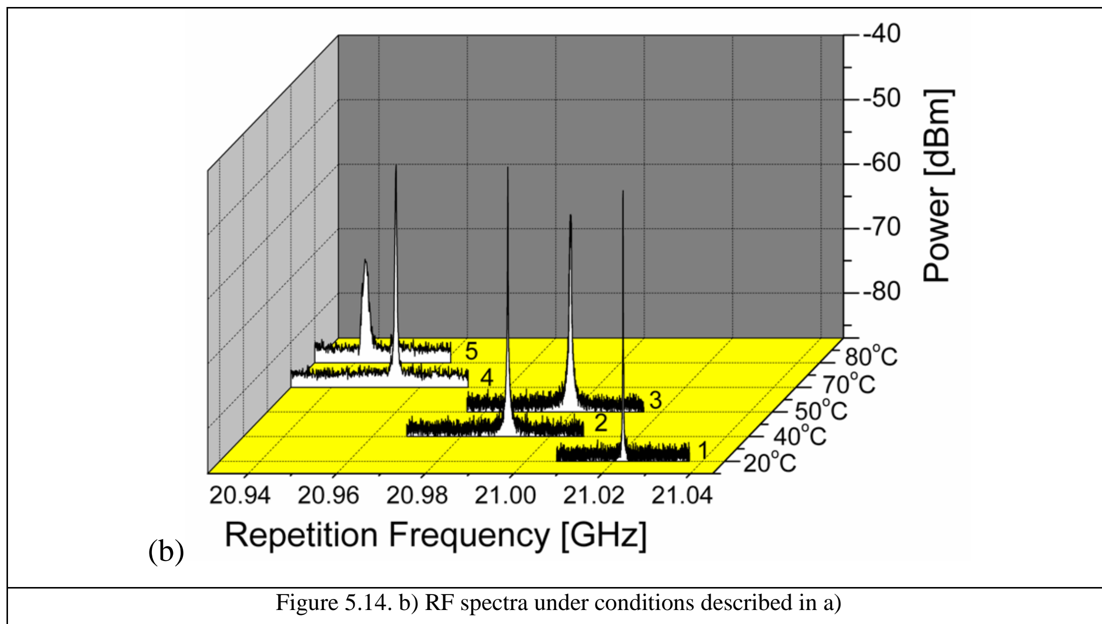

Figure 5.14. b) RF spectra under conditions described in a)

The RF spectrum is seen to remain relatively constant throughout the range of temperatures studies. This is attributed to a balancing of two counteracting effects. An increase in temperature will serve to increase the length of the laser cavity and lead to a decrease in RF frequency. At the same time, semiconductor material exhibits a refractive index which decreases with increasing temperature. Coupled with the afore-mentioned red-shifting of emission wavelength with increasing temperature, this serves to increase the RF frequency. The result is a repetition frequency which decreases slightly with increasing temperature.

5.8 Conclusions and future work

In this chapter I have shown the potential of the all-quantum-dot external cavity mode-locked laser system. From these initial assessments, it is evident that quantum-dot SESAMS are suitable for the mode locking of QD lasers, but have not yet proven their advantage over a monolithic absorber element. A wide range of measures could be implemented in order to improve the performance of the system.

The fundamental limitation of the current experiment is the incompatability of the SESAM and gain chip. Primarily, a SESAM is required which possesses an absorption bandwidth coincident with the output from the laser at normal incidence. Additional work is also required to better match the saturation fluence and modulation depths of SESAM to the requirements of the output power and gain of the gain

section. While the initial estimate for a suitable modulation depth required was sensible, further investigation would allow this to be refined. The introduction of additional layers of quantum-dots would allow the SESAM to introduce a greater modulation, potentially phase locking a larger number of longitudinal modes.

The SESAM used in this work is a resonant device, meaning that at the top semiconductor-air interface in the device, there is an antinode in the field intensity pattern. This causes an enhancement of the field inside the SESAM which in turn allows this type of device to exhibit both lower saturafion fluences and larger modulation depths than comparable antiresonant devices [46]. Unfortunately, this also causes this type of SESAM to exhibit very high levels of dispersion when utilised at wavelengths not coincident with the design wavelength. By contrast, antiresonant devices display flat, near-zero group velocity dispersion over a wide range of wavelengths which is advantageous [46]. It is therefore possible that an antiresonant SESAM could yield short pulses in this system.

Another approach which could yield improved performance relates to the inclusion of an extra reverse biased element in the laser in order to provide additional modulation to the laser field as described previously. Several authors have described the tendency for external cavity mode-locked lasers to operate in a multi-pulse configuration [47, 48]. The reason they cite for this occurrence is the imperfect performance of the SOA antireflection coatings giving rise to back-reflections within the SOA [48]. This causes additional pulses to appear with spacing equal to the round trip time of the SOA. The inclusion of the reverse biased section helps to suppress this multiple-pulse behaviour. The estimated additional pulse spacings within the laser system investigated here do not correspond to the round trip time of the SOA indicating that this mechanism does not appear to be at work in this particular system.

With suitable components in place, several steps can be taken to further improve performance such as the inclusion of intracavity dispersion management, tuning of SESAM absorption and the emission wavelength of the laser by altering their temperature or by additional RF modulation as applied above. There also exists the option to incorporate additional optical elements to correct the astigmatic beam from the diode such that a circular spot of minimum area is made on the absorber. This technique is employed by Adams *et al* [35].

This has shown that QD SESAMS are versatile components suitable for use with QD lasers. Further investigations will attempt to fulfil the potential shown here

and successfully incorporate quantum-dot based material in laser systems with quantum-dot based material.

Regarding the additional work I was involved in relating to quantum-dot lasers, it has been demonstrated that stable mode locked operation can be achieved over a wide temperature range. Further work by colleagues on this topic went on to show the dependence of pulse duration on temperature from this laser system and a theoretical model was formulated to explain the observed behaviour [49]. They explain how a decrease in the absorber carrier escape rate with increasing temperature allows the pulse duration to decrease with increasing temperature for a constant injection current.

This chapter concludes my investigations into quantum-dot based semiconductor material as a vehicle for obtaining ultrashort laser pulses. Chapter 6 introduces the concepts of nonlinear optics. An understanding of these is vital if semiconductor material is to be utilised as a vehicle for parametric nonlinear processes.

References

1. McRobbie, A.D., et al., *HIgh power all-quantum-dot-based external cavity modelocked laser.* Electronics Letters, 2007. **43**(15): p. 812 - 813.
2. McRobbie, A.D., et al. *High power all-quantum-dot-based external cavity mode-locked laser*. *LEOS'06*. 2006, Paper ref THJ4, Montreal, Canada.
3. McRobbie, A.D., et al. *All-quantum-dot based external cavity mode locked laser*. *SIOE'07*. 2007. Paper ref WE3, Cardiff, UK.
4. Hawthorn, C.J., K.P. Weber, and R.E. Scholten, *Littrow configuration tunable external cavity diode laser with fixed direction output beam.* Review of Scientific Instruments, 2001. **72**(12): p. 4477-4479.
5. Fan, H.S., et al., *Opposite temperature effects of quantum-dot laser under dual-wavelength operation.* Applied Physics Letters, 2007. **90**(18).
6. Kim, J., M.T. Choi, and P.J. Delfyett, *Pulse generation and compression via ground and excited states from a grating coupled passively mode-locked quantum dot two-section diode laser.* Applied Physics Letters, 2006. **89**(26).
7. Delfyett, P.J., *Ultrafast single and multiwavelength modelocked semiconductor lasers: Physics and Applications*, *Ultrafast lasers:technology and applications*, M.E. Fermann, A. Galvanauskas, and G. Sucha, Editors. 2003, Marcel Dekker Inc: New York. p. 219-321.
8. Cataluna, M.A., *Ultrashort-pulse generation from quantum-dot semiconductor diode lasers*, PhD Thesis, *School of Physics and Astronomy*, 2007, University of St Andrews: St Andrews.
9. Choi, M.T., et al., *Ultrashort, high-power pulse generation from a master oscillator power amplifier based on external cavity mode locking of a quantum-dot two-section diode laser.* Applied Physics Letters, 2005. **87**(22).
10. Delfyett, P.J., *Ultrafast single and Multiwavelength modelocked semiconductor lasers:physics and applications*, *Ultrafast lasers: Technology and applications*, M.E. Fermann, A. Galvanauskas, and G. Sucha, Editors. 2002, Marcel Dekker. p. 800.
11. Gee, S., et al., *Ultrashort pulse generation by intracavity spectral shaping and phase compensation of external-cavity modelocked semiconductor lasers.* IEEE Journal of Quantum Electronics, 2000. **36**(9): p. 1035-1040.
12. Kim, K., S. Lee, and P.J. Delfyett, *1.4 kW high peak power generation from an all semiconductor mode-locked master oscillator power amplifier system based on eXtreme chirped pulse amplification (X-CPA).* Optics Express, 2005. **13**(12): p. 4600 - 4606.
13. Lorenser, D., et al., *50-GHz passively mode-locked surface-emitting semiconductor laser with 100-mW average output power.* IEEE Journal of Quantum Electronics, 2006. **42**(7-8): p. 838-847.
14. Malins, D.B., et al., *Ultrafast electroabsorption dynamics in an InAs quantum dot saturable absorber at 1.3 mu m.* Applied Physics Letters, 2006. **89**(17).
15. Klopf, F., et al., *Correlation between the gain profile and the temperature-induced shift in wavelength of quantum-dot lasers.* Applied Physics Letters, 2002. **81**(2): p. 217 - 219.
16. Tropper, A.C. and S. Hoogland, *Extended cavity surface-emmitting semiconductor lasers.* Progress in Quantum electronics, 2006. **30**: p. 2 - 43.

17. Derickson, D.J., et al., *Short Pulse Generation Using Multisegment Mode-Locked Semiconductor-Lasers.* IEEE Journal of Quantum Electronics, 1992. **28**(10): p. 2186-2202.
18. Choi, M.-T., et al., *Ultrashort, high power pulse generation from a master oscillator power amplifier based on external cavity mode locking of a quantum-dot two-section diode laser.* Applied Physics Letters, 2005. **87**: p. 221107.
19. Sun, H.D., et al., *Low-loss 1.3-mu m GaInNAs saturable Bragg reflector for high-power picosecond neodymium lasers.* Optics Letters, 2002. **27**(23): p. 2124-2126.
20. Lebum, C.G., et al. *Low-loss GaInNAs saturable Bragg reflector for femtosecond modelocking of a Cr4+:YAG laser*. *Photon 06/ QEP 17*. Paper ref LTE716:15, Manchester.
21. Lebum, C.G., et al. *Self-starting femtosecond Cr4+YAG laser mode locked with a GaInNAs saturable bragg reflector*. in *Advanced Solid state Photonics (ASSP'07)*,Paper ref WA6, Vancouver.
22. Rafailov, E.U., et al., *Fast quantum-dot saturable absorber for passive mode-locking of solid-state lasers.* IEEE Photonics Technology Letters, 2004. **16**(11): p. 2439-2441.
23. Lagatsky, A.A., et al., *Quantum-dot-based saturable absorber with p-n junction for mode-locking of solid-state lasers.* IEEE Photonics Technology Letters, 2005. **17**(2): p. 294-296.
24. McWilliam, A., et al., *Quantum-dot-based saturable absorber for femtosecond mode-locked operation of a solid-state laser.* Optics Letters, 2006. **31**(10): p. 1444-1446.
25. Su, K.W., et al., *InAs/GaAs quantum-dot saturable absorber for a diode-pumped passively mode-locked Nd : YVO4 laser at 1342 nm.* Optics Letters, 2005. **30**(12): p. 1482-1484.
26. Lagatsky, A.A., et al., *Low-loss quantum-dot-based saturable absorber for efficient femtosecond pulse generation.* Applied Physics Letters, 2007. **91**(231111).
27. Herda, R., et al., *Semiconductor quantum-dot saturable absorber mode-locked fiber laser.* IEEE Photonics Technology Letters, 2006. **18**(1-4): p. 157-159.
28. Lorenser, D., et al., *Towards wafer-scale integration of high repetition rate passively mode-locked surface-emitting semiconductor lasers.* Applied Physics B-Lasers and Optics, 2004. **79**(8): p. 927-932.
29. McWilliam, A., *Femtosecond Cr4+:forsterite laser for applications in telecommunications and biophotonics*, PhD Thesis, *School of physics and Astronomy*. 2007, University Of St Andrews: St Andrews.
30. Lagatsky, A.A., et al. *1-μm and 1.3-μm femtosecond lasers mode-locked using quantum-dot-based saturable absorbers*. *CLEO Europe*. 2007., CA2-5-MON, Munich, Germany.
31. Markus, A., et al., *Simultaneous two-state lasing in quantum-dot lasers.* Applied Physics Letters, 2003. **82**(12): p. 1818-1820.
32. Cataluna, M.A., et al., *Stable mode-locked operation up to 80 degrees C from an InGaAs quantum-dot laser.* IEEE Photonics Technology Letters, 2006. **18**(13-16): p. 1500-1502.
33. Delfyett, P.J., et al., *High-Power Ultrafast Laser-Diodes.* IEEE Journal of Quantum Electronics, 1992. **28**(10): p. 2203-2219.

34. Shen, J.L., et al., *Mode-locking of external-cavity semiconductor lasers with saturable Bragg reflectors.* Journal of the Optical Society of America B-Optical Physics, 1999. **16**(7): p. 1064-1067.
35. Adams, L.E., et al., *Mode locking of a broad area semiconductor laser with a multiple quantum well saturable absorber.* Optics Letters, 1993. **18**(22): p. 1940-1942.
36. Rafailov, E.U., et al., *High-power picosecond and femtosecond pulse generation from a two-section mode-locked quantum-dot laser.* Applied Physics Letters, 2005. **87**(8).
37. Cataluna, M.A., et al., *Stable mode locking via ground- or excited-state transitions in a two-section quantum-dot laser.* Applied Physics Letters, 2006. **89**(8).
38. Cataluna, M.A., et al. *Ground and excited-state modelocking in a two-section quantum-dot laser*. *LEOS annual meeting*. 2005, Paper ref *ThS2,* Sydney Australia.
39. Cataluna, M.A., et al. *New mode locking regime in a quantum-dot laser: enhancement by simultaneous cw excited-state emission. CLEO'06, Paper ref CThH3* Longbeach, USA.
40. Arakawa, Y. and H. Sakaki, *Multidimensional Quantum Well Laser and Temperature-Dependence of Its Threshold Current.* Applied Physics Letters, 1982. **40**(11): p. 939-941.
41. Mowbray, D.J. and M.S. Skolnick, *New physics and devices based on self-assembled semiconductor quantum dots.* Journal of Physics D-Applied Physics, 2005. **38**(13): p. 2059-2076.
42. Shchekin, O.B. and D.G. Deppe, *1.3 mu m InAs quantum dot laser with T-o=161 K from 0 to 80 degrees C.* Applied Physics Letters, 2002. **80**(18): p. 3277-3279.
43. Kim, J.S., et al., *Room-Temperature operation of InP-based InAs quantum dot laser.* IEEE Photonics Technology Letters, 2004. **16**(7): p. 1607-1609.
44. Sakamoto, A. and M. Sugawara, *Theoretical calculation of lasing spectra of quantum-dot lasers: Effect of inhomogeneous broadening of optical gain.* IEEE Photonics Technology Letters, 2000. **12**(2): p. 107-109.
45. Patane, A., et al., *Thermal effects in quantum dot lasers.* Journal of Applied Physics, 1999. **85**(1): p. 625-627.
46. Spuhler, G.J., et al., *Semiconductor saturable absorber mirrir structures with low saturation fluence.* Applied Physics B-Lasers and Optics, 2005. **81**: p. 27 - 32.
47. Derickson, D.J., et al., *Suppression of multiple pulse formation in external-cavity mode-locked semiconductor lasers using intrawaveguide saturable absorbers.* IEEE Photonics Technology Letters, 1992. **4**(4): p. 333-335.
48. Yvind, K., et al., *Performance of external cavity mode-locked semiconductor lasers employing reverse biased saturable absorbers.* Physica Scripta, 2002. T101: p. 1290132.
49. Cataluna, M.A., et al., *Temperature dependence of pulse duration in a mode-locked quantum-dot laser.* Applied Physics Letters, 2007. **90**(10).

Chapter 6 Nonlinear Frequency Conversion Theory

In the previous chapters the subject matter has concerned the direct emission from laser devices that can exhibit very high powers and where the optical beams can be focused to very small spot sizes. In this chapter the emphasis is directed towards induced nonlinear optical phenomena and frequency conversion in particular. Following the invention of the laser in 1960 by Maiman *et al* [1], it became apparent that these new optical tools could be used to produce fascinating phenomena, based on the fact that previously unobtainable intensities could be achieved. One branch of physics that was driven by this laser development is nonlinear optics. A telling indication of this is how quickly the first experimental demonstration of second harmonic generation in 1961 followed the birth of the laser [2]. Prior to this, nonlinear optics consisted largely of theoretical work, because the required intensities were difficult to produce. In this chapter, I will describe the use of laser light for nonlinear frequency conversion.

6.1 Polarisation

When an electric field is applied to a charge- neutral dielectric material, the positive and negative charges are separated, leading to the formation of electric dipoles. The electric polarisation is then defined as the net average dipole moment per unit volume. In terms of Maxwell's equations, the induced polarisation is represented by an extra term added onto the end:

$$\frac{\partial^2 E(z,t)}{\partial z^2} = \mu_0 \varepsilon_0 \varepsilon_r \frac{\partial^2 E(z,t)}{\partial t^2} + \mu_0 \frac{\partial^2 P(z,t)}{\partial t^2} \qquad 6.1$$

Equation 6.1 is called the nonlinear wave equation (when the polarisation varies nonlinearly with E), with E, the electric field, expressed as a function of space (z) and time (t). P is the polarisation and ε_r is the dielectric permeability. A solution to equation 6.1 which applies in the linear case is shown below:

$$P(t) = \varepsilon_0 \chi E(t) \qquad 6.2$$

Both the polarisation and electric field are vectors in the above expression and ε_0 is the permittivity of free space. χ is the electric susceptibility of the material and is a

measure of how easily the dielectric polarises under the influence of an applied electric field. At low optical intensities, there is a linear relationship between the electric field and the polarisation. Thus, linear optics describes phenomena such as refraction and absorption.

6.2 Nonlinear Polarisation Response

When an electromagnetic field incident on a dielectric becomes comparable to the inter-atomic field ($\sim 10^6$ V/m) [3], the polarisation response of the material can no longer be expressed by equation 6.2 and instead must be represented by a power series of the electric field as shown below in equation 6.3:

1st order   2nd order   3rd order

$$P(t) = \varepsilon_0(\chi^{(1)}E(t) + \chi^{(2)}E^2(t) + \chi^{(3)}E^3(t) + ...) \qquad 6.3$$

The extra terms in the expression describe the nonlinear polarisation response of the material to the electric field. Typically, the second-order response term is several orders of magnitude smaller than the linear contribution and so forth for higher-order nonlinearities, underlining the need for intense optical fields. Physically, this means that the dipole response of the material is no longer responds linear with the incident electromagnetic field.

The nonlinear optical properties exhibited by a material are strongly dependent on its structure. For instance, in centrosymmetric crystals, the even-order terms in equation 6.3 are zero. As such, the material used in my project is non-centrosymmetric. The work covered in this chapter concerns materials where the second-order terms are non-zero, while the subject matter in other chapters contains references to third-order nonlinear processes, notably the optical Kerr effect.

Looking at the second-order contribution alone, it has the form below:

$$P^{(2)}(t) = \varepsilon_0 \chi^{(2)} E^{(2)}(t) \qquad 6.4$$

If we consider two incident light fields, one at frequency ω_1 the other at frequency ω_2, as shown in equation 6.5, this results in a second-order polarisation response as shown in equation 6.6:

$$E(t) = E_1 \cos(\omega_1 t) + E_2 \cos(\omega_2 t) \qquad 6.5$$

In the above, $\omega_{1,2}$ are the angular frequencies of the driving electromagnetic fields.

$$
\begin{aligned}
&P^{(2)}(t) = E_1 \cos(\omega_1 t) + E_2 \cos(\omega_2 t) \quad \{1\} \\
&+\varepsilon_0 \chi^{(2)}[\cos(\omega_1 + \omega_2) + \cos(\omega_1 - \omega_2)t]E_1 E_2 \quad \{2\} \\
&+\frac{1}{2}\varepsilon_0 \chi^{(2)} E_1^{\ 2} \cos(2\omega_1 t) \quad \{3\} \\
&+\frac{1}{2}\varepsilon_0 \chi^{(2)} E_2^{\ 2} \cos(2\omega_2 t) \quad \{4\} \\
&+\frac{1}{2}\varepsilon_0 \chi^{(2)} E_1^{\ 2} + \frac{1}{2}\varepsilon_0 \chi^{(2)} E_2^{\ 2} \quad \{5\}
\end{aligned}
\qquad 6.6
$$

The second-order nonlinear polarisation response shown in equation 6.6 will cause the material to emit radiation at frequencies of ω_1, ω_2, $2\omega_1$, $2\omega_2$, $\omega_1+\omega_2$ and $\omega_1-\omega_2$. The fields at twice the frequencies are produced by what is called second harmonic generation (SHG). The field at $\omega_1+\omega_2$ is called a sum-frequency mixing process (SFM) and the field at $\omega_1-\omega_2$ is called a difference frequency mixing process (DFM). The DC terms account for the process known as optical rectification. The two processes most relevant to my project are SHG and optical parametric generation (OPG).

OPG involves the interaction of a strong input pump beam at angular frequency ω_3 with a weak field at ω_1 (called the idler) generating a field at the difference frequency ω_2(called the signal), by $\omega_2= \omega_3 - \omega_1$. At the same time, another mixing process occurs whereby fields with frequencies ω_2 and ω_3 interact through $\chi^{(2)}$ to give gain at ω_1 by $\omega_1= \omega_3 - \omega_2$. The result of these two processes is that the signal and idler waves experience gain while the pump wave is depleted. A simpler way of picturing the OPG process is to think of the photons themselves, rather than the light fields. In this paradigm, the pump photon, which has energy E_3 is split into two lower frequency photons with energies that add up to E_3 i.e. $E_{pump}=E_{signal}+E_{idler}$.

6.3 The Coupled-wave Equations

The physical processes governing the relationships between the interacting fields in nonlinear process including OPG and SHG are described by the coupled-wave equations. Detailed derivations of the coupled-wave equations can be found in references such as [4-6], but I only present here the main results and their implications

for my particular area of study. The basic form of the coupled-wave equations is shown below:

$$\frac{\partial E_1(z)}{\partial z} = -i\frac{d_{eff}\omega_1}{cn_1}E_3(z)E_2^*(z)e^{-i(\Delta kz)}$$
$$\frac{\partial E_2^*(z)}{\partial z} = i\frac{d_{eff}\omega_2}{cn_2}E_3(z)E_1^*(z)e^{i(\Delta kz)} \qquad 6.7$$
$$\frac{\partial E_3(z)}{\partial z} = -i\frac{d_{eff}\omega_3}{cn_3}E_1(z)E_2(z)e^{i(\Delta kz)}$$

In the above, n_j is the refractive index experienced by each interacting wave. The quantity d_{eff} is the effective nonlinear dielectric scalar with the subscript *eff* denoting that the value of d and hence the induced nonlinear polarisation depends on the direction of propagation through the crystal. Δk is the wave vector mismatch and is defined as follows where k_i are the wavevectors of each field, respectively:

$$\Delta k = k_3 - k_2 - k_1 \qquad 6.8$$

The electric field and induced polarisation are vector quantities and are not necessarily parallel to each other. The susceptibility, which relates the two, is therefore represented by a tensor. The second-order polarisation response is then represented by the following:

$$P_i = \varepsilon_0 \chi^{(2)}{}_{ijk} E_j E_k \qquad 6.9$$

It is normal practice to represent the susceptibility in terms of the nonlinear dielectric tensor d_{ijk}:

$$d_{ijk} = \frac{\chi^{(2)}{}_{ijk}}{2} \qquad 6.10$$

$d_{i,j,k}$ describes the nonlinear coupling of fields along the *j* and *k*-axes generating a polarisation along the *i*-axis. In a typical 3-wave mixing process detailed by expression 6.7, the nonlinear susceptibility is represented by a 3x3x3 tensor. Fortunately, several simplifications exist that reduce this tensor to something more manageable. Firstly, the order of the driving fields in this type of nonlinear interaction is not important [7] This is called the *piezoelectric contraction*:

$$d_{ijk} = d_{ikj} \qquad 6.11$$

This means that the subscripts *j* and *k* can be replaced by a single suffix *l*, with values 1 to 6.

jk	11	22	33	23,32	13,31	12,21
l	1	2	3	4	5	6

The *piezoelectric contraction* allows the 3x3x3 tensor to be reduced to a 3x6 matrix. A second simplification known as *Kleinman's conjecture* states that in a lossless medium, all d_{ijk} coefficients related by a simple reordering of *i*, *j* and *k* will be equivalent. This means that the number of coefficients needed to represent χ and therefore d is further reduced to a maximum of 10 elements [8]:

$$d_{ijk}= d_{ikj} =d_{kji} =d_{kij}=d_{jik} =d_{jki}$$

The final simplification that can be made concerns the application of crystal symmetries. If the crystal is unaffected after a symmetry operation, that is, if there exists symmetry in the crystal structure, some elements in the matrix will be zero; others will be equal in magnitude with opposite sign. This is why the nonlinear dielectric tensor that describes real crystalline materials usually contains less than 10 elements and sometimes as few as 2 or 3. Altogether, this means that the calculation of d_{eff} is reduced from what at first sight seems very complicated to a weighted multiplication of only a few matrix elements.

6.3.1 Solving the Coupled-wave Equations for Second Harmonic Generation

To understand how the electric fields evolve as they propagate through the crystal, we solve the coupled-wave equations of 6.7. Full solutions of equations 6.7 can be found in several texts including [5, 6] but I will only present an abridged version of their solution here. In the case of SHG, we have $\omega_1=\omega_2=\omega$ and $\omega_1+ \omega_2=\omega_3$. We then make the assumption of low conversion efficiency i.e. the pump field is not depleted significantly. Under this condition, the following applies:

$$\frac{\partial E_1}{\partial z} = \frac{\partial E_2}{\partial z} = 0 \qquad 6.12$$

This means that we only need concern ourselves with

$$\frac{\partial E_3(z)}{\partial z} = -i\frac{d_{eff}\omega_3}{cn_3}E_1(z)E_2(z)e^{i(\Delta kz)} \qquad 6.13$$

We use the trial solution of

$$E_3(z) = a\exp(i\Delta kz) + b \qquad 6.14$$

With substitution and the application of the initial boundary condition of $E_3=0$ at z=0, we are able to extract expressions for coefficients a and b where:

$$a = -\frac{2\omega_1 d_{eff}E_1E_2}{cn_3\Delta k} = -b \qquad 6.15$$

Therefore the solution for the amplitude of the generated wave as a function of z is

$$E_3(z) = \frac{2\omega_1 d_{eff}E_1E_2}{cn_3\Delta k}[1-\exp(i\Delta kz)] \qquad 6.16$$

The intensity distribution along z I(z) can then be readily obtained by application of $\mathrm{I(z)} \propto \mathrm{E(z)}^2$:

$$I_3(z) = \frac{4\omega_1^2 d_{eff}^2 I_\omega z^2}{c^2 n_3^2}\sin c^2\left(\frac{\Delta kz}{2}\right) \qquad 6.17$$

The crucial part of expression 6.16 is the sinc^2 dependency. This is considered in more detail in section 6.5.

6.3.2 Solving the Coupled-wave Equations for the Case of Difference-frequency Generation

Difference-frequency generation (DFG), which is shown below in figure 6.1, involves the mixing of a strong pump wave, denoted by the frequency ω_3 with a weaker wave at ω_1 to produce an output at ω_2.

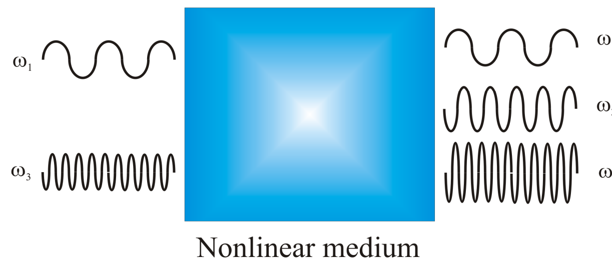

Figure 6.1. Difference-frequency generation

In this instance, solving the coupled-wave equations is more complicated. We thus assume perfect phase matching and no depletion of the pump wave. This means that the coupled-wave equations take the form below:

$$\frac{\partial E_3}{\partial z} = 0$$

$$\frac{\partial E_1}{\partial z} = i\kappa_1 d'_{ijk} E_3 E_2^* \qquad \text{Where } \kappa_j = -\frac{\omega_j}{n_j c} \tag{6.18}$$

$$\frac{\partial E_2}{\partial z} = i\kappa_2 d'_{ijk} E_1 E_3^*$$

By selecting solutions of the form $E = \exp(\Gamma z)$, where $\Gamma = \sqrt{\kappa_1 \kappa_2 d'^{\,2}_{ijk} \, | E_3 |^2}$ and using specific trial solutions of

$E_1 = E_1^+ \exp(\Gamma z) + E_1^- \exp(-\Gamma z)$
$E_2 = E_2^+ \exp(\Gamma z) + E_2^- \exp(-\Gamma z)$
Boundary conditions (6.19)
$E_2(z=0) = 0$ (no DFG wave at crystal entrance)
$E_1(z=0) = E_1(0)$ (amplitude of weak wave (1) is constant at crystal entrance)

The solutions obtained for the two waves E_1 and E_2 are then as follows:

$$E_1 = E_1(0)\cosh(\Gamma z)$$

$$E^*_2 = -i\sqrt{\frac{\kappa_2}{\kappa_1}} E_1(0)\sinh(\Gamma z) \tag{6.20}$$

Examination of the real parts of both these expressions, shows that with increasing z, both E_1 and E_2 grow at the expense of E_3, which explains the ability to achieve gain at the signal and idler wavelengths at the expense of the pump.

6.4 The Manley-Rowe Relations

In section 6.2, the idea of viewing difference-frequency generation and the related optical parametric generation processes in terms of photon splitting was introduced. In the simplest case, one pump photon is split in two, forming a signal and idler photon without loss of energy.

Returning to the coupled-wave equations (6.7) and multiplying each of the three expressions by its complex conjugate electric field and n_i/ω_i, we obtain the following expression:

$$\frac{n_1\partial |E_1|^2}{\omega_1\partial z} = \frac{n_2\partial |E_2|^2}{\omega_2\partial z} = -\frac{n_3\partial |E_3|^2}{\omega_3\partial z} = -id'_{ijk}E^*{}_1E^*{}_2E^*{}_3\exp(-i\Delta kz) \qquad 6.21$$

The intensity associated with an electromagnetic wave is given by

$$I = nc\varepsilon_0 |E|^2/2 \qquad 6.22$$

Applying this to equation 6.20 and cancelling off terms, we arrive at the common form of the Manley-Rowe relations:

$$\frac{1}{\omega_1}\frac{\partial I_1}{\partial z} = \frac{1}{\omega_2}\frac{\partial I_2}{\partial z} = -\frac{1}{\omega_3}\frac{\partial I_3}{\partial z} \qquad 6.23$$

Consider a crystal of length δz and cross cross-section A with N_i photons per second entering the material and a corresponding number N_o leaving the crystal. Rewriting equation 6.22 in terms of photon number we obtain the following:

$$\frac{\Delta N_1}{A\partial z} = \frac{\Delta N_2}{A\partial z} = -\frac{\Delta N_2}{A\partial z} \qquad 6.24$$

This shows that the number of photons created per second at ω_1 or ω_2 is exactly balanced by the number consumed every second at ω_3. This is the most general case of this expression. If we instead define a new variable N_T which is the sum of N_1,N_2 and N_3 and we recall that $\omega_3 = \omega_1 + \omega_2$, then we can write the following expression:

$$\frac{\Delta N_T}{\partial z} = \frac{\Delta N_1}{\partial z} + \frac{\Delta N_2}{\partial z} + \frac{\Delta N_3}{\partial z} = 0 \qquad 6.25$$

This confirms that there is no net change in photon number. The Manley-Rowe relations are a theoretical ideal and do not take into consideration any detrimental factors such as losses which reduce the efficiency of the conversion process.

So far the analysis presented here has neglected the wave vectors of the interacting waves. In analogy with second harmonic generation, however, it is evident that wave vectors and therefore the phases of the electromagnetic fields involved are of crucial in these types of nonlinear optical interactions.

6.5 Phase Matching

Phase matching is of paramount importance for efficient nonlinear frequency conversion. Looking back at equation 6.17, it follows that the amplitude of the

converted field has a sinc-type dependency. As mentioned previously, the wavevector mismatch is given by:

$$\Delta k = k_3 - k_2 - k_1 = \frac{n_3\omega_3}{c} - \frac{n_2\omega_2}{c} - \frac{n_1\omega_1}{c} \qquad 6.26$$

Plotting the part of equation 6.17 which concerns wavevector mismatch illustrates its importance in the frequency conversion process. This is shown illustratively below in figure 6.2.

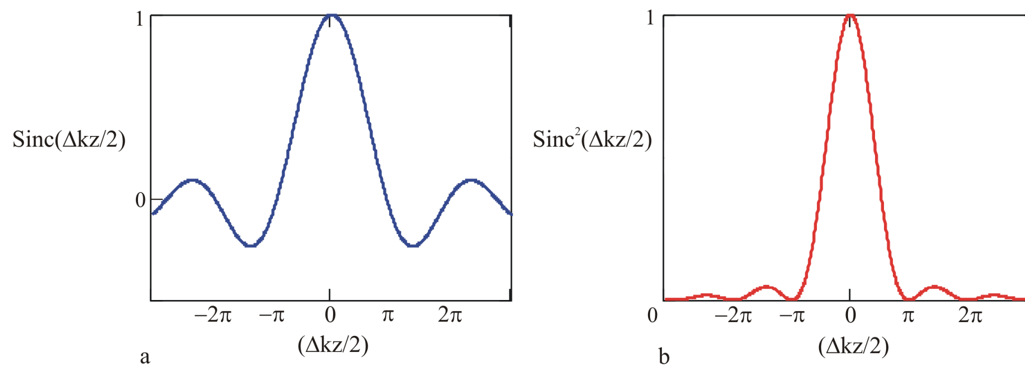

Figure 6.2. Normalised plots of (a) sinc(Δkz/2) (amplitude) and (b) $sinc^2$(Δkz/2) (intensity) as functions of Δkz/2. The functional dependence of this curve is the same for the case of sum-frequency generation as it is for DFG.

There is maximum conversion where the wave vector mismatch is zero. Any deviation from Δk=0 results in a rapid reduction in the y-value of the each function and therefore a similar reduction in the amount of converted field. Secondly, in the case of a non-zero Δk, as z increases, eventually the point will be reached when Δkz/2=π. At this point the sinc function crosses the x axis, and changes sign. This corresponds to a reversal in the direction of the frequency conversion process. Instead of energy being transferred from the pump wave to the generated wave, the opposite happens.

6.5.1 Refractive-index Dependence on Wavelength

Because of the dependence of Δk on refractive index, one can readily see how the wavelength dependence of the refractive index n – otherwise known as chromatic

dispersion - plays a crucial role. The normal dispersion curve for GaAs is shown below in figure 6.3

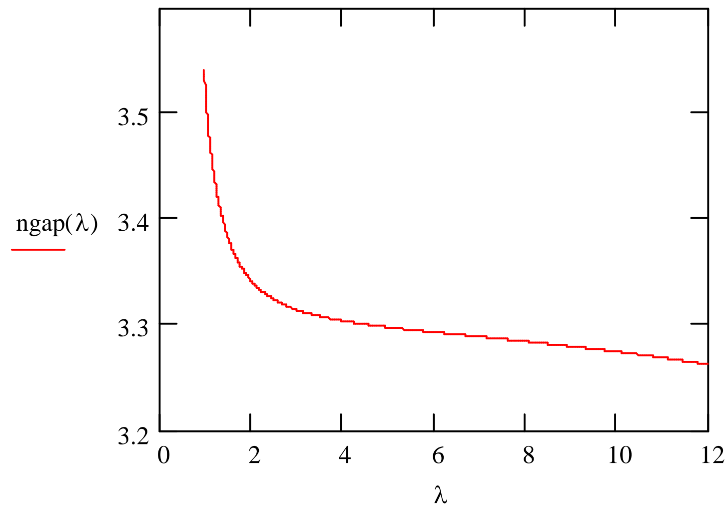

Figure 6.3. Refractive index of GaAs as a function of wavelength. For most transparent materials, the shape of the trend is similar to the above. The sharp increase in index for wavelengths shorter than 1 micron corresponds to the band edge of GaAs, where the material absorbs incident radiation. The above graph was produced by using mathcad and the Sellmeier equation for GaAs.

Under normal conditions, interacting waves of differing wavelengths will experience different refractive indices and will therefore propagate through the medium with different phase velocities (given by $v_\lambda = c/n_\lambda$), and relative phase differences will arise. Given that the k-vector of each mode is given by $k_{mode} = k_0\ n_{mode}$, the simple k-conservation rule expressed in equation 6.26 is then violated and very little converted light is produced.

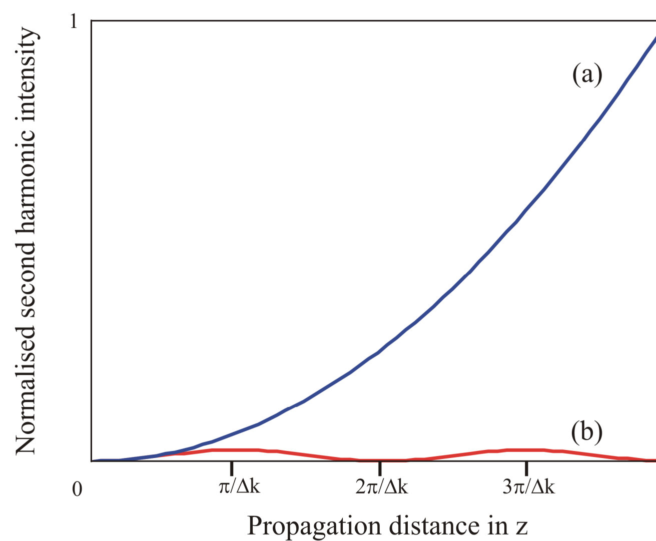

Figure 6.4. Second harmonic intensity as a function of z in (a) phase matched and (b) non phase matched cases.

In the phase matched case, there is a quadratic relationship between the converted field and propagation in z. However, in the absence of a phase-matching relationship, the amount of converted light varies in a sinusoidal form. In case b, in the region $n\pi/\Delta k < z < 2n\pi/\Delta k$, where n is odd, energy is transferred from the second harmonic wave to the fundamental wave - in a direction opposite to what is desired. At a distance of $z = \pi/\Delta k$, the amount of energy in the second harmonic field reaches a maximum. This distance is defined as the coherence length L_c.

If we plot the normalised converted field as a function of propagation distance through the crystal with and without phase matching, we obtain figure 6.4. Phase matching can be obtained by several methods, two of which are discussed here.

6.5.2 Birefringent Phase Matching

Birefringent phase matching (BPM) was the first phase-matching method to be considered and applied in practice[9]. It exploits the birefringence of some materials, i.e. the fact that they display more than one refractive index value, depending on the polarisation state and the direction of propagation of the electromagnetic wave. Birefringent materials can be either uniaxial or biaxial in nature, depending on how the refractive index changes with propagation direction. The BPM technique seeks to engineer the condition:

$$\Delta k_{BPM} = k_3 - k_2 - k_1 = \frac{n_3\omega_3}{c} - \frac{n_2\omega_2}{c} - \frac{n_1\omega_1}{c} = 0 \,. \qquad 6.27$$

In the simplest case of a uniaxial material, there are two distinct refractive indices. In two directions, the crystal is isotropic, but in the third dimension, the refractive index depends on angle of propagation through the material.

Looking below at figure 6.5 which shows a plot of the ordinary and extraordinary refractive indices of BBO (a commonly used nonlinear material) as a function of wavelength, we can see how birefringent crystals can be employed to achieve phase matching and subsequent nonlinear frequency conversion.

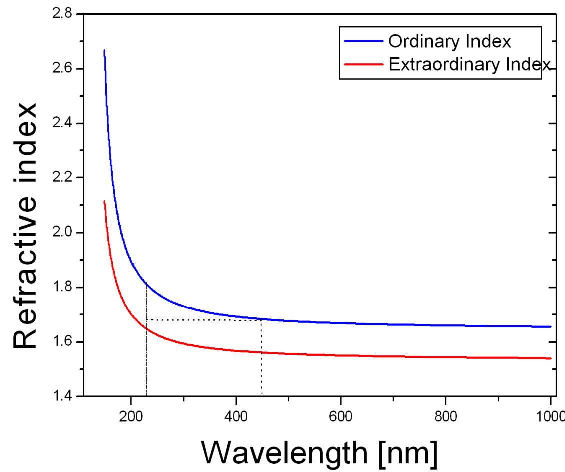

Figure 6.5. Ordinary and extraordinary refractive indices of BBO as a function of wavelength.

To achieve this effect, which is commonly referred to as type 1 collinear phase matching for second harmonic generation, we require the fundamental and second harmonic wave to experience the same refractive index. Using the example depicted above, we use a pump source at around 450nm and aim to produce the second harmonic at 225nm. We notice that the ordinary index at 450 nm is larger than the extraordinary index at 225 nm. If the fundamental wave into the crystal is polarised to experience the refractive index n_o, it can give rise to a second harmonic polarised perpendicularly to the fundamental wave through the nonlinear dielectric tensor. If this wave then experiences a refractive index $n_e(\theta)_{SHG}$, where $n_{0fundamental}=n_e(\theta)_{SHG}$, then the two waves become phase matched. Uniaxial crystals represent the simpler of the two classes of nonlinear crystal. Other crystals are biaxial in nature, where all three crystallographic axes exhibit different refractive indices - $n_x \neq n_y \neq n_z$. Careful choice of the polarisations and propagation angles can thus facilitate phase matching, but since BPM was not used in this project, no further discussion is included.

6.5.3 Quasi-phase Matching (QPM)

Quasi-phase matching is the main phase-matching technique employed in my project. Rather than properly matching the phases of the interacting waves, QPM employs periodic modification of the nonlinear material to reset the phase difference between the interacting waves to zero at well defined, repeat intervals. Initially proposed by Armstrong *et al* and described in their seminal paper[7], QPM was initially difficult to demonstrate experimentally due to the high demands it places on material properties, as outlined below.

With reference to figure 6.4, we recall that in case (b), the amount of converted field reaches a maximum when $z = \pi/\Delta k = L_c$. After this point, when the pump and converted fields have accumulated a phase difference of $\Delta\phi = \phi_3 - \phi_2 - \phi_1 = \pi$, energy begins to be returned to the pump field. It follows that if we consider a bulk crystal as a series of blocks of thickness L_c and apply the above, in the first block, we would get conversion from the pump to the converted wave. At the end of the first block, the direction of conversion reverses. If we were able to cancel phase differences after the first slab of material, then instead of getting back conversion in the second slab, we would get more forward conversion. In terms of the coupled wave equations, this can be achieved mathematically by simply adding an extra $i\pi$ into the argument of the exponents on the right hand side of the equations 6.28:

$$\begin{aligned}
\frac{\partial E_1(z)}{\partial z} &= i\frac{d_{eff}\omega_1}{cn_1}E_3(z)E_2^*(z)e^{i(\Delta kz + i\pi)} \\
\frac{\partial E_2(z)}{\partial z} &= i\frac{d_{eff}\omega_2}{cn_2}E_3(z)E_1^*(z)e^{i(\Delta kz + i\pi)} \\
\frac{\partial E_3(z)}{\partial z} &= i\frac{d_{eff}\omega_3}{cn_3}E_1(z)E_2(z)e^{-i(\Delta kz + i\pi)}
\end{aligned} \qquad 6.28$$

This method is termed *quasi* because the phases are not matched properly. Instead, QPM ensures that the phases are never allowed to become too dissimilar as to impede relatively efficient conversion. If we were to plot the QPM solutions of the coupled-wave equations for the case of second harmonic generation (The cases of difference and sum-frequency conversion are very similar), we would obtain the characteristic shown in figure 6.6, which is based on the analysis from references 4 and 10].

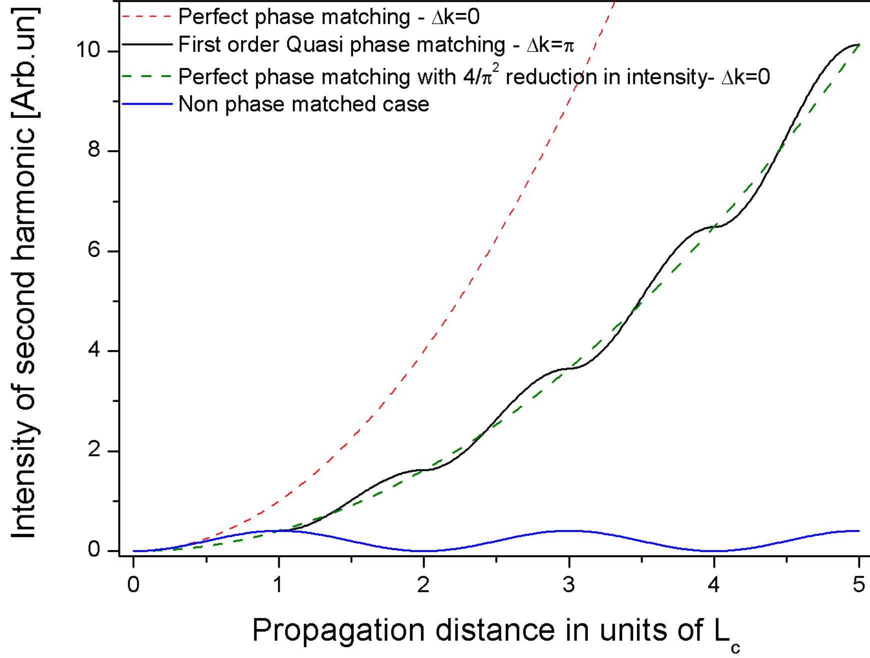

Figure 6.6. Plot of second harmonic intensity as a function of distance through the crystal for various values of Δk

The perfect phase matching case and the non-phase matched cases are reproduced from figure 6.5. As expected, growth of the second harmonic is slower in the case of QPM than in the perfectly phase matched case. In fact, the converted field growth in the quasi-phase-matched case oscillates around that generated by a perfectly phase matched interaction with a $4/\pi^2$ reduction in efficiency. This is explained by substituting values for L_c and Δk into the function $\text{sinc}(\Delta kz/2)^2$, yielding a value of $4/\pi$, so the efficiency of a QPM system is a factor of $4/\pi^2$ lower than a perfectly phase matched system with the same nonlinear coefficient.

The phase matching condition for QPM has the following dependence:

$$\Delta k_{QPM} = k_3 - k_2 - k_1 - \frac{2\pi}{\Lambda_g} = 0 \qquad 6.29$$

where $\Lambda_g = 2L_c = 2\pi/\Delta k$. The extra term Λ_g is the grating period that compensates for the fact that the refractive indices are not equal. By utilising different grating periods, QPM can be achieved for a variety of input wavelengths. The only limitation is that Λ_g must be large enough to be definable through lithography. Importantly, given that Λ_g is largely independent of the crystal properties, one may choose any propagation

direction through the crystal, unlike in birefringently phase-matched systems. This allows the propagation direction to be chosen to coincide with that giving the maximum nonlinear coefficient, which is a significant advantage of QPM over BPM. Also, by choosing the propagation direction to be along a crystal axis, the effect of beam walk-off can be ignored. In the majority of materials, QPM allows one to exploit higher nonlinear coefficients, so QPM systems generally demonstrate higher gain.

Reordering the material on such short length scales is a technically demanding process. Early techniques involved the stacking of plates of material and rotating the crystal orientation in alternate plates, which has the effect of changing the sign of the nonlinear dielectric tensor d_{ijk} and therefore changes the direction of the frequency conversion process. So, when the fundamental and second harmonic waves accumulate a phase difference of π, a plate of opposite orientation is used.

Fortunately, in ferroelectric crystals, there is an easier method to obtain this domain inversion which does not rely on stacking of plates of alternating orientation. Ferroelectric materials exhibit a spontaneous dipole moment; one can control the direction of this moment, switching it between different states by the application of an electric field. This process is called poling and it is harnessed by using high Voltage in conjunction with patterned electrodes that induce the desired ordering of the material. The technique is shown below in figure 6.7.

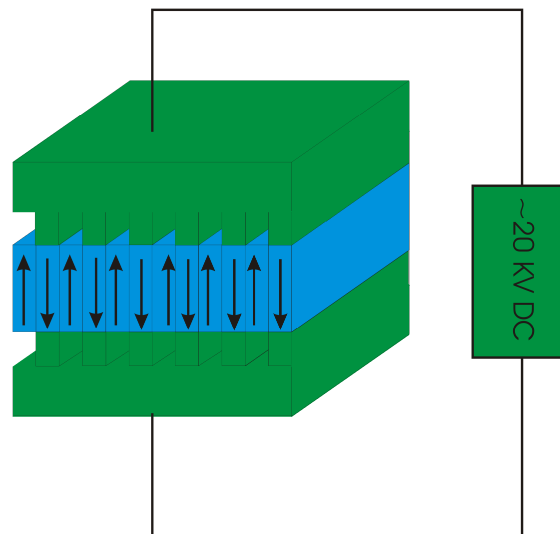

Figure 6.7. Representation of periodically poled material with patterned electrode

The metal contacts can be defined lithographically. This technique was first experimentally demonstrated experimentally by Yamada et al [11] and has been

successfully developed and utilised in commercial systems. One problem with poling is that the thickness of periodically poled (pp) crystals is typically limited to around 0.5 – 1mm by the spreading out of the electric field lines. This limits accurate control over the crystal domain orientation in arbitrarily thick crystals, so pp crystals typically have a small input face that requires tight focusing of the input beams, as well as limiting the diameters of the propagating beams inside the material and giving a divergent output. Another problem relates to the high voltages required to initiate the domain reversal effect. If the poling voltage is close to the breakdown voltage of the material, the crystal may be damaged. As mentioned earlier, most periodically poled materials also require to be operated at elevated temperatures for optimal performance.

Periodically-poled OPO systems with a wide range of properties have been widely available on a commercial basis for about the last 5 years. Concentrating specifically on pulsed periodically-poled $LiNbO_3$ (PPLN) systems, current systems such as the opal femtosecond OPO from Spectra physics can generate hundreds of milliwats of average output power with typical pulse durations of about 250 fs.

6.6 Optical Parametric Oscillation

In section 6.2.1, we discussed how the signal (ω_2) and idler (ω_1) waves may build up from background noise by means of the parametric amplification process. If the nonlinear medium was placed in an optical cavity that was resonant at one of the generated wavelengths, then this would lead to a device with similarities to a laser oscillator. The difference is that while a laser operates by the principles of stimulated emission, the oscillator discussed here relies on parametric processes to provide optical gain. After many passes of the cavity, significant power could be converted from the pump to the generated down-converted wavelengths. This is the basic principle of operation of an optical parametric oscillator (OPO), a basic diagram of which is shown below in figure 6.8.

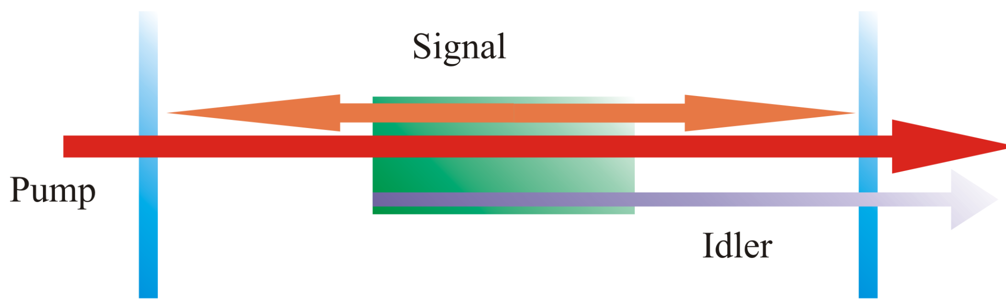

Figure 6.8. Basic OPO cavity.

Despite enhancements in technology used to implement the technique, the basic methods and design facilitating OPOs are very similar to that outlined by the first paper on the subject by Giordmaine and Miller [12]. Figure 6.8 shows a singly resonant OPO, for which only one of the down-converted waves (in this case the signal wave ω_2)is resonant in the cavity. The resonant wave can make many trips around the cavity while the in the case of non-resonant waves, only one pass is made.

The singly resonant oscillator (SRO) is the simplest type of OPO. With only one resonant condition to satisfy, the SRO can be tuned continuously, making the device perform consistently as system parameters such as crystal angle (in a birefringent system) or temperature are altered. As we can see from Figure 6.8, only the pump beam is externally fed into the cavity and the signal and idler beams build up from noise. Therefore, because of the weak nature of these two signals and the non resonant nature of the pump beam, a very powerful pump, typically of the order of several Watts, is required to achieve oscillation threshold) in this configuration [13] (although sub-Watt threshold pump levels have been demonstrated [14]).

Alternate OPO cavity configurations exist based on different cavity geometries and resonant characteristics that are able to operate with a far lower threshold, thus requiring a less specialist pumping laser. These different geometries impose additional constraints on the system, but these can have implications on the performance and characteristics of the device. As a general rule, oscillators with more resonating waves exhibit lower thresholds than their simpler counterparts but must consequently pay the price of ever more stringent confinements on the cavity parameters.

6.9 Conclusions

In this chapter I have outlined the underlying physics for nonlinear optical frequency conversion where the origins of the nonlinear polarisation and its implications have been discussed. Equations describing fields generated by this polarisation were shown and solved and the phase relationships between interacting waves as well as methods to control it were outlined. In Chapter 7 I will describe semiconductor-based nonlinear frequency conversion devices that I fabricated for this type of work. Beginning from design considerations, I then proceed to present information on how these devices were fabricated and subsequently evaluated.

References

1. Maiman, T.H., *Stimulated optical radiation in Ruby.* Nature, 1960(4736): p. 493 - 494.
2. Franken, P.A., A.E. Hill, C.W. Peters, and G. Weinreich, *Generation of optical harmonics.* Physical Review Letters, 1961. **7**(4): p. 118-120.
3. Wilson. J., H.P., *Optoelectronics an introduction*. 3 ed. Prentice hall. 1998
4. Lindsay, I.D., *High Spatial and Spectral Quality Diode-Laser-Based Pump Sources for Solid-State Lasers and Optical Parametric Oscillators*, PhD Thesis, *School of Physics and Astronomy*, 1999, University of St Andrews: St Andrews.
5. Sutherland, R.L., *Handbook of nonlinear optics*. Optical Engineering, ed. B.J. Thompson. 1996: Marcel Dekker, Inc. 685.
6. Reid, D.T., *Nonlinear optics and modulators*, MSc module course notes, 2001 *Department of Physics*., Heriot Watt University: Edinburgh. p. 49.
7. Armstrong, J.A., N. Bloembergen, J. Ducuing, and P.S. Pershan, *Interactions between light waves in a nonlinear dielectric.* Physical Review Letters, 1962. **127**(6): p. 1918 - 1939.
8. Kleinman, D.A., *Nonlinear dielectric polarisation in optical media.* Physical Review Letters, 1962. **126**(6): p. 1977-1979.
9. Maker, P.D., R.W. Terhune, M. Nisenoff, and C.M. Savage, *Effects of dispersion and focusing on the production of optical harmonics.* Physical Review, 1962. **8**(1): p. 21 - 23.
10. Fejer, M.M., G.A. Magel, D.H. Jundt, and R.L. Byer, *Quasi-Phase-Matched 2nd Harmonic-Generation - Tuning and Tolerances.* IEEE Journal of Quantum Electronics, 1992. **28**(11): p. 2631-2654.
11. Yamada, M., N. Nada, M. Saitoh, and K. Watanabe, *1st-Order Quasi-Phase Matched Linbo3 Wave-Guide Periodically Poled by Applying an External-Field for Efficient Blue 2nd-Harmonic Generation.* Applied Physics Letters, 1993. **62**(5): p. 435-436.
12. Giordmaine, J.A. and R.C. Miller, *Tunable coherent parametric oscillation in LiNbO3 at optical frequencies.* Physical Review, 1965. **14**(24): p. 973 - 976.
13. Gross, P., M.E. Klein, T. Walde, K.J. Boller, M. Auerbach, P. Wessels, and C. Fallnich, *Fiber-laser-pumped continuous-wave singly resonant optical parametric oscillator.* Optics Letters, 2002. **27**(6): p. 418-420.
14. Batchko, R.G., D.R. Weise, T. Plettner, G.D. Miller, M.M. Fejer, and R.L. Byer, *Continuous-wave 532-nm-pumped singly resonant optical parametric oscillator based on periodically poled lithium niobate.* Optics Letters, 1998. **23**(3): p. 168-170.

Chapter 7 Nonlinear frequency conversion Experimental

In this chapter I deal with the design, fabrication and testing of ridge waveguide, semiconductor-based nonlinear frequency conversion structures for infra-red light generation. The techniques adopted here are all based on quasi-phase-matching (QPM) which is covered in chapter 6. I begin with an explanation of the periodically-switched nonlinearity (PSN) concept and a description of structures previously designed which employed a PSN methodology using regrown material. I then discuss the structures that I designed and fabricated, beginning with the design procedure employed to determine the dimensions of the structure. This is followed by descriptions and discussion concerning the fabrication and post-processing steps as well as the assessments undertaken to determine their characteristics. The focus then shifts to work on domain-inverted or orientation-patterned GaAs material, which was a new approach developed recently by groups in the USA and Japan [1, 2]. Recognising the elegance of this new approach and its potential to produce devices with high efficiencies, I began a study of its implications and applicability in the context of my project. This chapter concludes with a comparison of the methods investigated then possible future steps to improve both methods are discussed.

7.1 PSN Concept

The periodic switching of nonlinearities, being a variant of quasi-phase matching (QPM), is a method of controlling the interactions of waves in a medium that offers transparency to the wavelengths involved. QPM is frequently achieved by periodic-poling, where the use of patterned electrodes allows control over the sign of the relevant nonlinear coefficient, thereby facilitating continued forward conversion from the pump beam into a frequency-converted field. The non-ferroelectric nature of GaAs, coupled with its optical isotropy does not permit the application of this or other conventional phase matching methods. However, the PSN method is applicable and this can be illustrated by plotting nonlinear coefficient as a function of propagation distance or converted field as a function of propagation distance as shown below in figures 7.1 and 7.2.

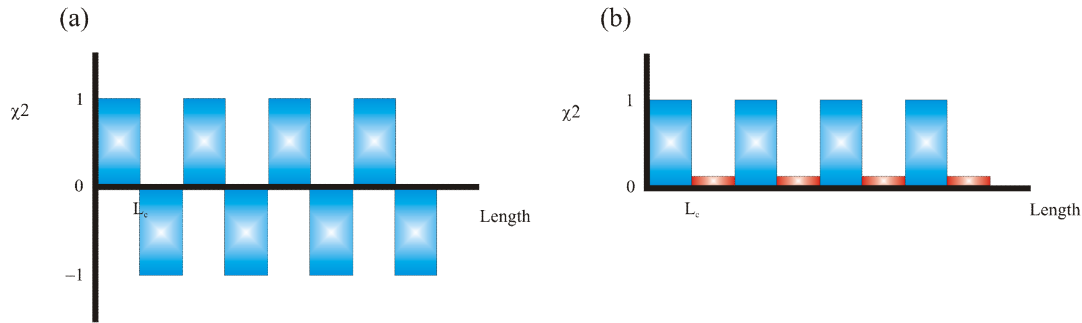

Figure 7.1. Magnitude of normalised nonlinear coefficient as a function of distance in (a) QPM scheme and (b) PSN scheme. Modulation of nonlinear coefficient occurs on the same length scale in each method.

In Chapter 6, the coherence length L_c was defined as the distance at which the interacting waves have become π out of phase with each other, thus reversing the direction of the nonlinear frequency conversion process. In the original QPM case shown in (a), the *sign* of nonlinear coefficient changes every L_c allowing continued forward conversion when the waves are out of phase. In the PSN case (b), it is the *magnitude* of the nonlinear coefficient that is modulated every coherence length. Within the coherence length, the nonlinear coefficient is at its normal high value and forward conversion will occur. Beyond L_c, the magnitude of the nonlinear coefficient is decreased significantly to minimise backward conversion. At the end of another coherence length L_c, the nonlinear coefficient is reset to its initial high value and so on. The result is that over $2L_c$, there is a net gain in converted light. More light is forward converted in high χ^2 (in phase) regions of the material than is lost in low χ^2 (anti-phase) sections. If we consider for a moment a PSN system and periodically poled conventional QPM systems manufactured from the same material, it is clear that the conventional system would display twice the efficiency of the PSN method. The key advance comes with the inclusion of materials with higher nonlinear coefficients than in conventional QPM systems such that the PSN method delivers a higher frequency conversion factor per grating period.

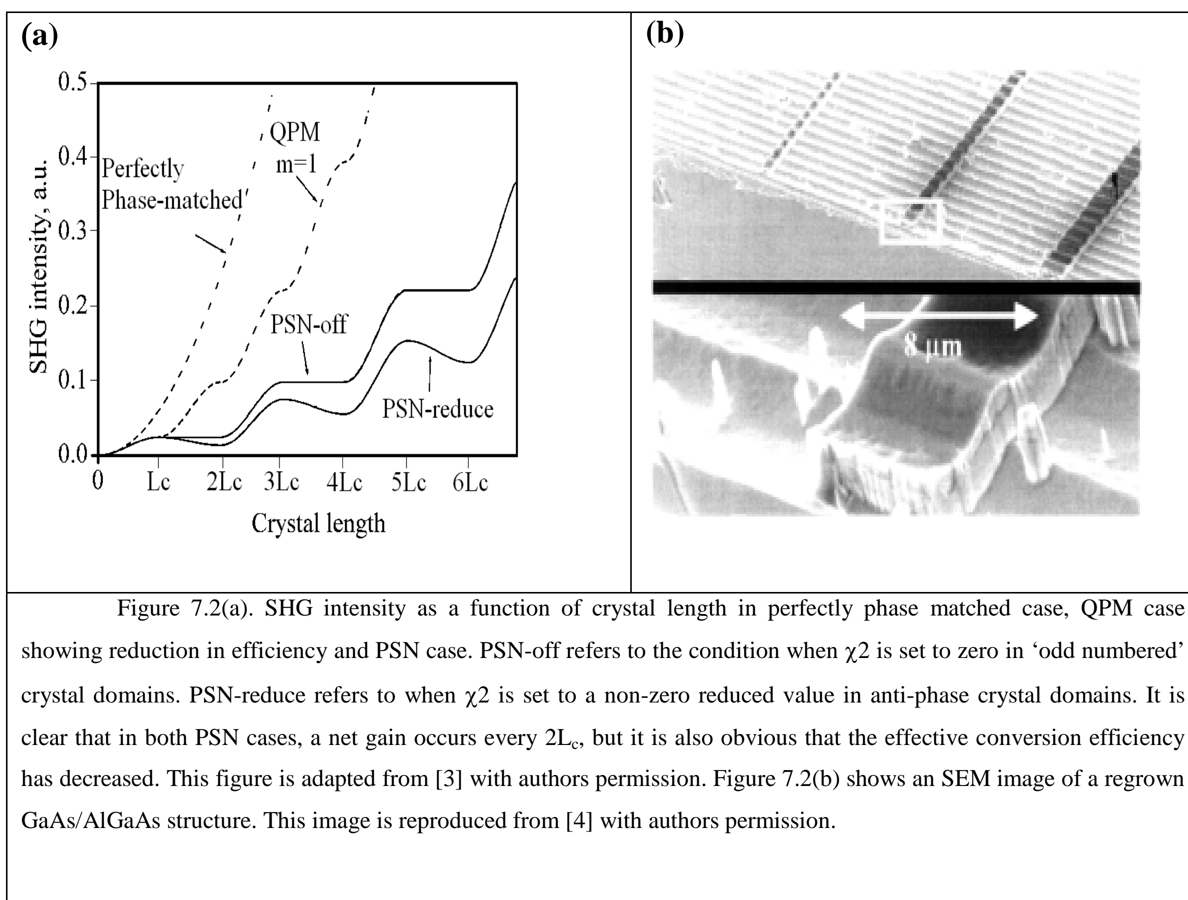

Figure 7.2(a). SHG intensity as a function of crystal length in perfectly phase matched case, QPM case showing reduction in efficiency and PSN case. PSN-off refers to the condition when $\chi2$ is set to zero in 'odd numbered' crystal domains. PSN-reduce refers to when $\chi2$ is set to a non-zero reduced value in anti-phase crystal domains. It is clear that in both PSN cases, a net gain occurs every $2L_c$, but it is also obvious that the effective conversion efficiency has decreased. This figure is adapted from [3] with authors permission. Figure 7.2(b) shows an SEM image of a regrown GaAs/AlGaAs structure. This image is reproduced from [4] with authors permission.

Previous work on a QPM system (shown above in figure 7.2(b)) involved the development of a waveguide structure where the active region of the device consisted of an alternating GaAs/AlGaAs grating [4]. The nonlinear coefficient of AlGaAs decreases with increasing Al content in accordance with Miller's rule. Thus by fabricating a structure where the in-phase regions were made from GaAs and the anti-phase regions are made from AlGaAs, the authors obtained a structure with a periodic modulation in χ^2 and were able to demonstrate SHG at 975 nm. The authors demonstrated a high quality interface between regions of GaAs and AlGaAs, but the etch and regrowth method they used involved selective removal and regrowth of the active region of the device. As such, there were significant associated losses. Additionally, reflections at the interfaces between regions of GaAs and AlGaAs were thought to be a limiting factor in the performance of the device.

7.2 Ion-implantation for Destruction of Nonlinear Coefficient

Ion implantation induced amorphization provides a means of periodically destroying the nonlinear coefficient of the waveguide devices while at the same time avoiding the inherently lossy regrowth discussed in reference [4]. Previous work on ion implantation in AlGaAs investigated the effect of high doses of ions on the second harmonic response of the material [5]. Materials displaying inversion symmetry in their structure do not exhibit a second-order nonlinear coefficient. Heavy ion bombardment should therefore be able to amorphize a material to such an extent that it is transformed from a non-centrosymmetric material into one displaying inversion symmetry. It was confirmed that this occurs when the vacancy concentration induced in the material by implantation becomes comparable to the atomic density of the target material. An ion dose of between 10^{14} and 10^{15} cm^{-2} is found to be sufficient to achieve this. These correspond to ion concentrations in the range of 10^{18} to 10^{19} per cubic centimetre. Given that each ion can be involved in multiple collisions, the vacancy concentration introduced by the ion doses used is calculated to be comparable to the atomic density of the target material (The atomic density of GaAs which is 4.5×10^{22} atoms/cm^{-3} [6]). The drop in nonlinear response was quantified by measuring the second harmonic light produced by the material in a reflection experiment. The authors then measured the propagation losses of the devices in a waveguide configuration and found that devices exhibited high losses (around 30 dB cm^{-1}), so the reduction in second-order susceptibility by ion induced amorphization incurs a significant loss penalty which severely limited the amount of converted light obtained.

I sought to take this work to the next stage by using this method of selective ion implantation to create a selective spatial amorphization, resulting in the modulation in χ^2 needed for a PSN-off nonlinear frequency conversion structure. I then studied different annealing temperatures with the aim of finding a “sweet spot’ of reduced nonlinearity and low loss.

7.3 Design and Calculations

The PSN method involves a modulation of the value of χ2. This can be achieved by a combination of selective etching and appropriate choice of ion dose and energy.

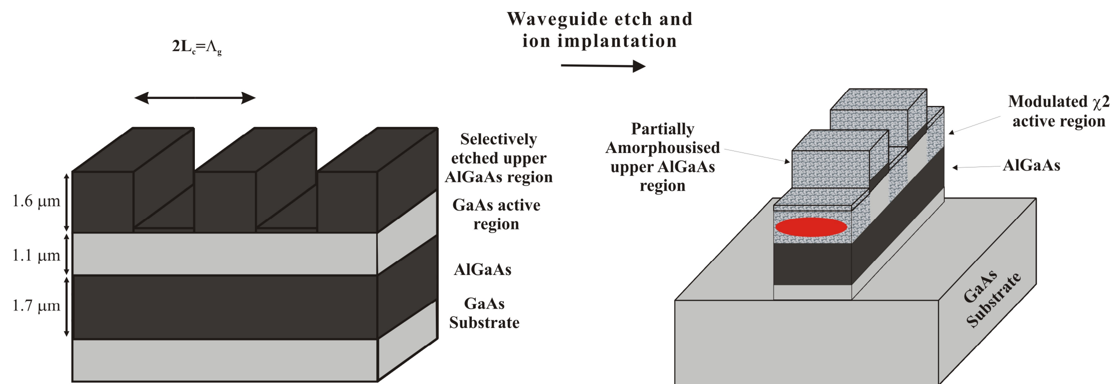

Figure 7.3. Graphic showing the manufacturing process of a PSN device. The graphic on the left shows the device after the grating etch step whereas the right hand image shows a completed device after ion implantation and definition of a ridge waveguide.

Figure 7.3 shows the basis of the technique. I chose a material consisting of a GaAs substrate and active region with $Al_{0.25\text{-}0.45}Ga_{0.75\text{-}0.55}As$ layers providing vertical confinement. A thin GaAs cap layer prevents oxidation of the AlGaAs. The top layer of AlGaAs is thicker than would normally be the case in a double heterostructure waveguide because it serves as a protective mask, shielding the active region from ion implantation. By periodically etching away sections of the top AlGaAs layer, one can obtain the structure illustrated in figure 7.3. The theoretical calculations below demonstrate the higher figure of merit of the PSN-off method in comparison to a periodically-poled lithium niobate crystal (PPLN). The figure is a result of calculations undertaken to investigate the relative merits of the PSN system in comparison to standard PPLN [3]. In this work, Artigas *et al* studied QPM devices from a theoretical perspective. Beginning from coupled-wave equations, the authors applied a Fourier expansion of the relevant coefficients, thus deducing the governing averaged equations and a figure of merit for PSN structures of arbitrary design. They demonstrate that, despite the implicit reduced conversion efficiency of the PSN method, the overall efficiency is still higher because of the higher χ^2 of GaAs-based material.

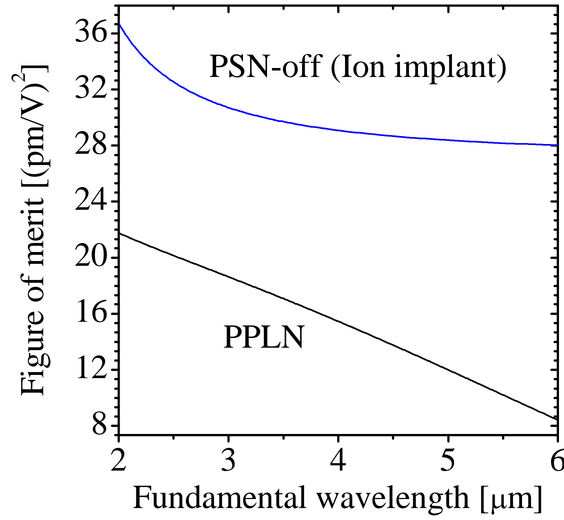

Figure 7.4. Figures of merit for PPLN and PSN-off structure. The figure of merit is used is the effective nonlinear coefficient $(D_{H,1})^2 = \left[\frac{2}{i\pi}\left(\frac{d_1}{n_{F1}\sqrt{n_{H1}}}\frac{l_{c1}}{\Lambda} - \frac{d_2}{n_{F2}\sqrt{n_{H2}}}\frac{l_{c2}}{\Lambda}\right)\right]^2$ - 7.1. where d_q is the nonlinear coefficient, $n_{i,q}$ is the refractive index, l_{cq} is the coherent length and the period $\Lambda = l_{cq} + l_{cq}$ for the fundamental and harmonic waves (i = F or H) in each domain (q= *1* or *2*). This was previously calculated in [3, 7, 8] where, for analysis purposes, nonlinear coefficients of d_{14}=170 pm/V for GaAs and d_{33}=27 pm/V for PPLN were used

7.3.1 Ion implantation calculations

The ion dose and energy are chosen such that 100% disordering can be achieved in the active region, below the etched windows, while at the same time, ions are stopped in the top AlGaAs layer to leave the active region in unetched areas unharmed. Colleagues at the University of Surrey used *Stopping Range of Ions in Matter* (SRIM) analysis, to calculate a dose of around $5\text{x}10^{14}$ cm^{-2} and energy equal to 1.750 MeV for the implantation process. The ion species chosen were doubly charged As^+ ions. It was calculated that these conditions would yield the desired disordering over the required depths of material.

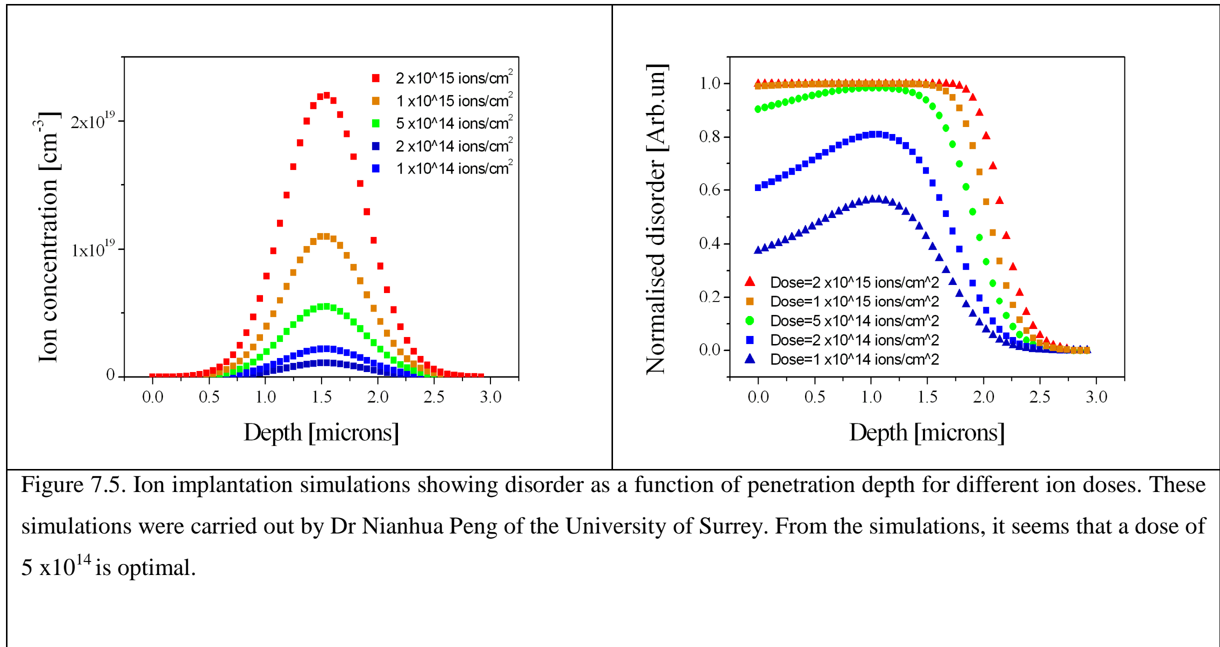

Figure 7.5. Ion implantation simulations showing disorder as a function of penetration depth for different ion doses. These simulations were carried out by Dr Nianhua Peng of the University of Surrey. From the simulations, it seems that a dose of 5 $x10^{14}$ is optimal.

We investigated a selection of Ion doses between $1x10^{14}$ and $2x10^{15}$ as an added degree of freedom. Doses of $1x10^{14}$, $2x10^{14}$, 5 $x10^{14}$, 1 $x10^{15}$ and 2 $x10^{15}$ are chosen at constant ion energy, giving a variety of disordering as shown in the figure**.** The degree of disorder is calculated by considering the energy loss experienced by ions as they penetrate into the material and the different mechanisms causing this loss as functions of ion concentration. The impact of implanted ions with the molecules in the implanted structure causes displacement of these molecules and thus introduces disorder to the structure, altering the previously well devined molecular structure. The implanted ions themselves also add to this disorder, coming to rest in the material at a position dictated by a combination of the statistical spread of their kinetic energy and the spacing of collisions they undergo.

7.3.2 Phase matching calculations

The desired operating wavelengths determine the period of the modulation in the PSN structure required such that phase-matching is achieved. Using the Sellmeier equation for GaAs in conjunction with equation 6.29 from Chapter 6, we can determine the dimensions of L_c for the PSN structure. The pump wavelength λ_p was chosen as 1.064 μm since suitable sources are available. The signal and idler

wavelengths were chosen to produce light at a variety of IR wavelengths in an optical parametric generation. Corresponding second-harmonic pump inputs resulting in an output of around 1 μm were also calculated for each coherence length and an additional set of coherence lengths designed specifically for SHG production at 1.064 microns. The results of these calculations are summarised below in figure 7.6. [The actual calculations are added as Appendix A at the end of this thesis.]

N	Pump Wavelength λ_p [μm]	Coherence length (grating half period) l_c [μm]	Signal Wavelength λ_s [μm]	Idler Wavelength λ_i [μm]	Second harmonic λ_{SHG} [μm]
1	1.064	5	1.40	4.43	2.318
2		4.45	1.50	3.66	2.241
3		4	1.65	3.00	2.172
4		3.85	1.80	2.60	2.149
5		3	N/A	N/A	2.00
6		6	1.30	5.86	2.45
7		7	1.25	7.15	2.5675
8		8	1.21	8.82	2.6765

Figure 7.6. Table of grating coherence lengths and wavelengths of the interacting waves.

7.4 Sample Preparation

Photolithography is used to pattern the surface of the material with the desired structure.

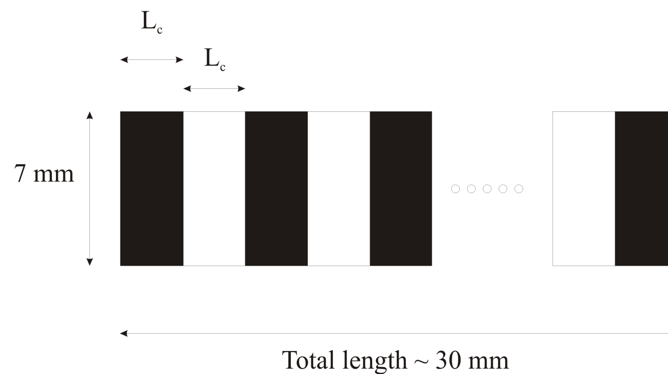

Figure 7.7. Mask design

Using the values displayed in figure 7.6, a photolithography mask was designed using *Wavemaker* software with dimensions as shown above in figure 7.7. The pattern on this mask is transferred onto the material surface. It is critical that the grating period defined in the mask is accurately and uniformly reproduced in the semiconductor. It is also very important that the depth of etch be fit for purpose.

The material structure is as shown in figure 7.8. On the far right side of the figure is the surface of the material which consists of an AlGaAs/GaAs/AlGaAs heterostructure with a 1.1 μm thick core region. After lithographic patterning and etching, a grating is created in the material, i.e. etched into the top layer of AlGaAs.

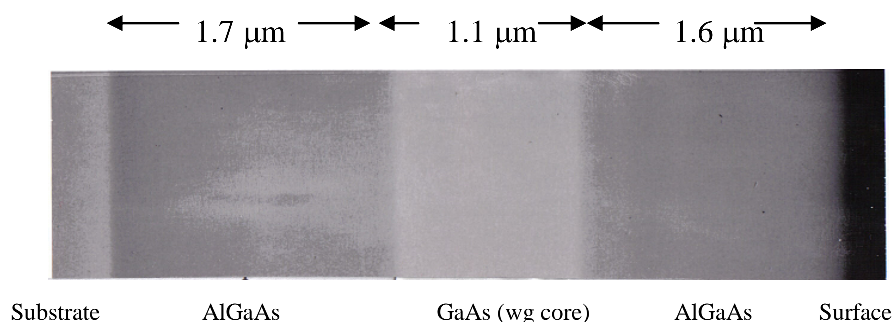

Figure 7.8. - Material structure for Ion implantation method

For the frequency conversion work, it is necessary to etch most of the way through this top layer of material. The etching work was done using a specially developed CAIBE process, ensuring smooth, vertical sidewalls while at the same time preserving

the integrity of the active region underneath. A beam voltage of 1450 V, beam current of 15 mA and gas flow rates of 10 sccm and 5 sccm for Argon and Chlorine gasses, respectively, were used. The etch rate for these conditions is approximately 420 nm/minute. An etch duration of approximately 3.3 minutes was sufficient to etch to a depth of 1.4 microns. Cross-sections of the material after etching are as shown in fig. 7.9.

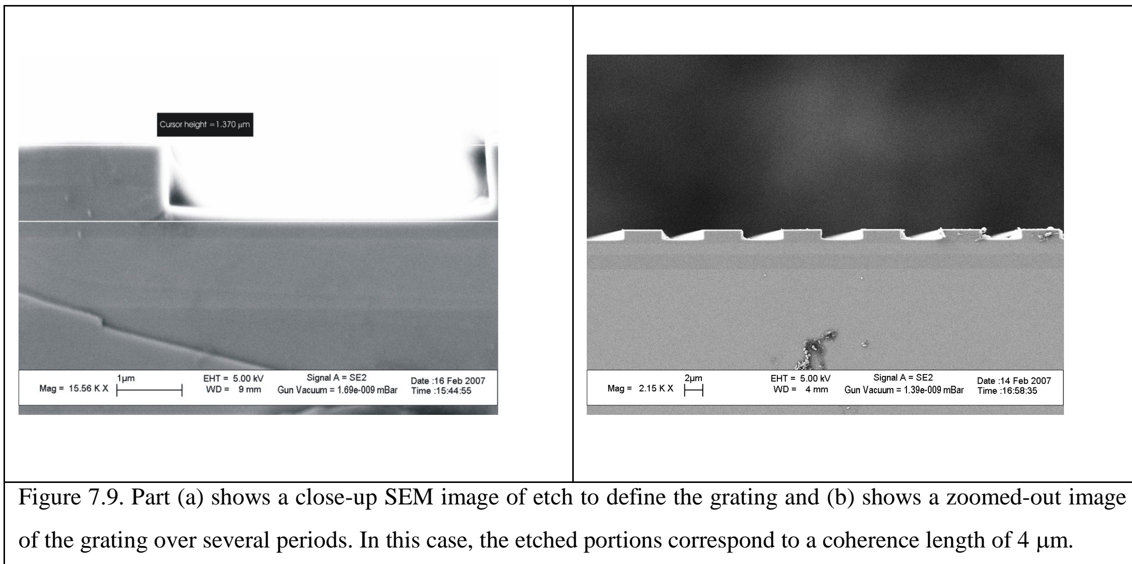

Figure 7.9. Part (a) shows a close-up SEM image of etch to define the grating and (b) shows a zoomed-out image of the grating over several periods. In this case, the etched portions correspond to a coherence length of 4 μm.

The etch depth is 1.37 microns. The slightly brighter layer of material just below the annotation line in figure 7.9(a) is the active region, so the grating is etched through most of the top waveguiding layer but not into the active region. From figure 7.9(b), we can see that the period of the mask has been accurately reproduced and as such I have fabricated a structure close to the desired profile shown in figure 7.3(a).

With the fabrication of the grating completed, the next step was to create deeply etched ridge waveguides. These provide the horizontal confinement for the waveguide mode. Waveguides of width 4, 6, 9, 12 and 15 μm were defined in the material, again using of both photolithography and CAIBE with the same etching recipe, except for using a higher process temperature. To define the mesa waveguides, it was necessary to etch down to a depth of greater than 2.7 μm. The etching parameters gave a rate of approximately 550 nm/min, meaning that an etch time of around 5 minutes was sufficient to achieve the desired depth. An SEM image of a device taken at completion of the etching process is shown below in figure 7.10.

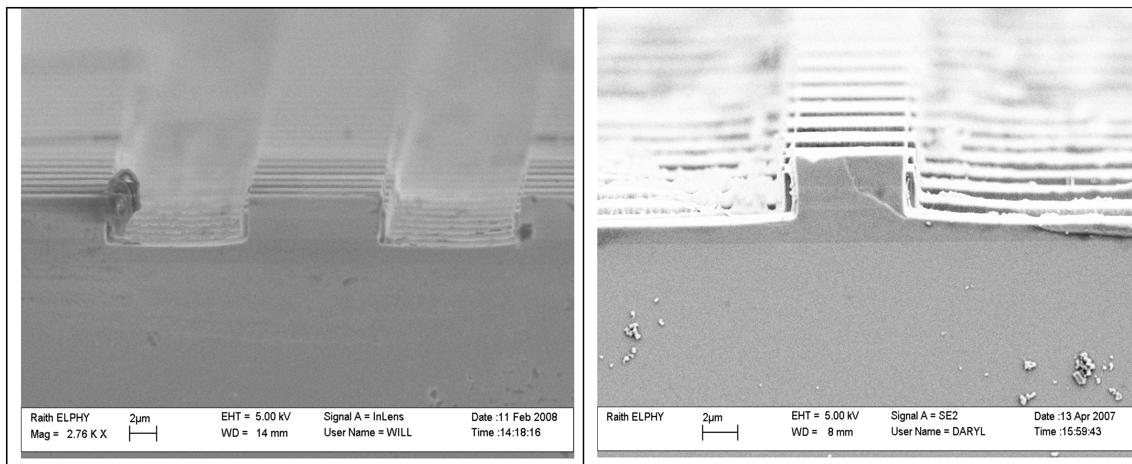

Figure 7.10. SEM images of a completed structures. The grating pattern defined in the previous etch is clearly visible. On the waveguide on the right, we can see three distinct layers, corresponding to the three layers of the material. We can clearly see that the waveguide etch has been sufficiently deep.

Following the waveguide etch, the material was ready to undergo selective amorphization by ion implantation. However, before subjecting the samples to ion implantation, the quality of the devices was assessed to ensure that each behaved as expected, and to identify losses introduced by the implantation process.

7.5 Linear-loss experimental setup and technique

Despite the fact that the devices were designed to operate with an input wavelength of 1064 nm, testing was carried out at 1500 nm using low power cw light sources. This was due to the ability of the sources to evaluate the properties of the samples without the risk of damage. It can be assumed that the performance and waveguiding capabilities at 1500 nm will be similar to that at 1064 nm because this is far from the absorption edge of GaAs and the waveguides are large and simple in their design. Thus, if an optical mode were supported at 1500 nm, it would also be supported at 1064 nm since the mode size would be smaller at the shorter wavelength. This assumption was confirmed by using a 2D commercial mode-solving package to plot the transverse electric field of the fundamental mode at a range of wavelengths as shown below in figure 7.11

a) b) c)

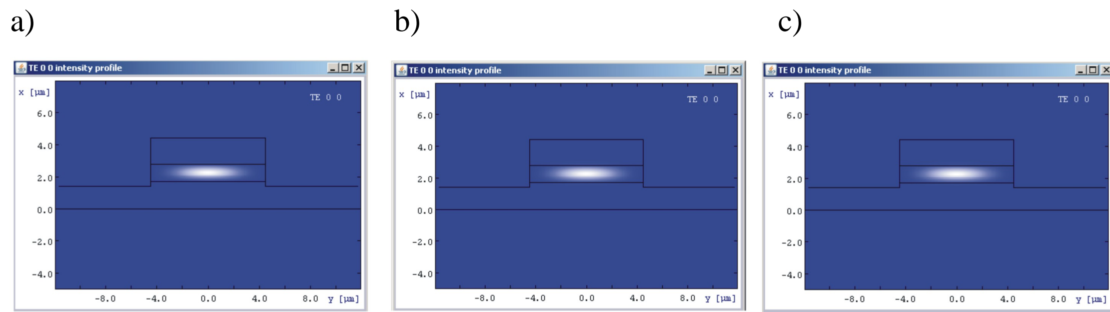

Figure 7.11. Simulations of fundamental TEM00 mode in 9 µm waveguide structure at propagation wavelengths of a)1µm, b)1.5 µm and c)3 µm respectively. Clearly, the waveguide supports the fundamental mode at all three wavelengths. This was done using an online mode-solving program available at http://wwwhome.math.utwente.nl/~hammer/eims.html. The package uses well defined algorithms and is routinely used for these sorts of calculations

A diagram of the experimental setup is shown below in figure 7.12 which consisted of a broadband amplified spontaneous emission source with a bandwidth of around 30 nm at 1550 nm.

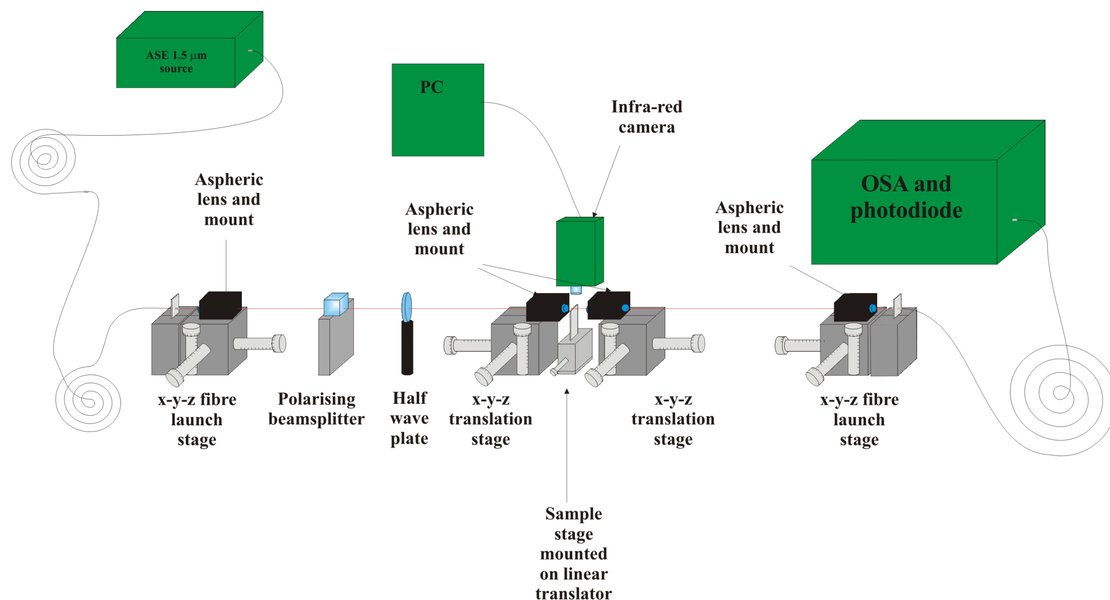

Figure 7.12. Experimental setup for linear-loss evaluation of frequency conversion samples.

This light was coupled into single mode optical fibre and launched into a collimating 10 X aspheric lens. The light was then passed through a polarising beam splitter and half wave plate to allow the selection and optimisation of an arbitrary linear polarisation. Coupling into one of the waveguides was achieved through use of either

60 X or 40 X aspheric lenses mounted on an XYZ positioning stage. The aspheric lenses produced a spot size of about 2 μm.

Alignment was aided by the use of an infra red camera, which was sensitive from 400 nm up to 1.9 μm, and which was situated above the sample and focused in the plane of the waveguides. Using these tools, both the input spot and any output could be viewed directly by the camera, which greatly helped in determining the precise coupling conditions. A dense, bright spot at both the input and output facet of the waveguide was a very strong sign that successful ridge waveguide coupling was taking place. This is shown in figure 7.13b. Light emerging from the waveguide was then collected by a second aspheric lens and collimated. Proper alignment was ensured by launching light in a counterpropagating direction and looking for input and output spots as before (on the facets of the forward direction aligned waveguide). Once the input and output lenses were correctly positioned, the transmitted light was collected by a second fibre launch stage and analysed.

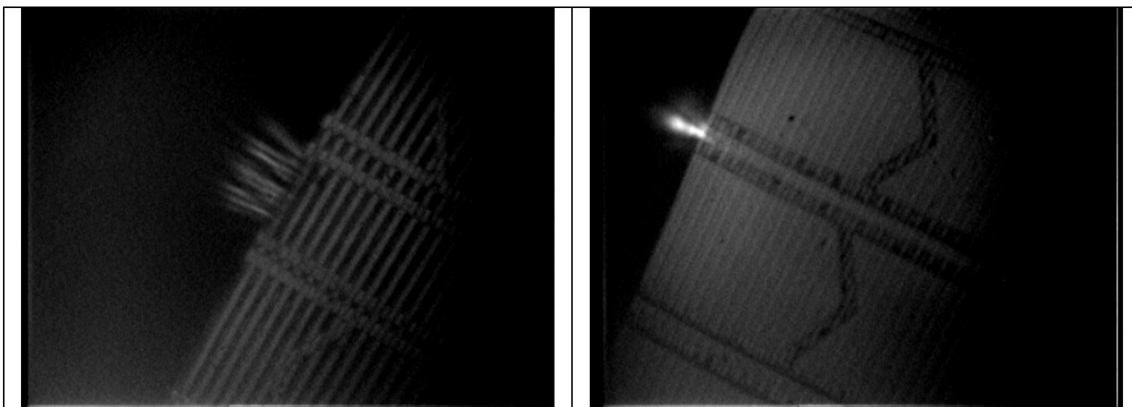

Figure 7.13 (a) Guiding in Bulk material and (b) in ridge waveguide. Clearly visible in the right –hand picture are V-shapes etched into the material that are designed to suppress wave-guiding in bulk material.

7.5.1 Fourier analysis loss method

The loss was analysed via the Fabry Perot (F-P) fringe spectrum produced by the waveguides, in particular using the method developed by Hofstetter and Thornton [9], They derive the expression for the Fourier transform of a Fabry Perot spectrum and the key points of the technique are summarised here and an in-depth analyses of the technique is provided in both the original paper itself and in the thesis of Kotlyar [10].

If we consider a F-P structure of length L, with two parallel facets of reflectivity R and absorption and refractive indices α and n respectively, the

transmitted intensity of the electric field resonant in the structure from [9] is as follows:

$$I(\beta) = \frac{(1-R)^2 \exp(-2\alpha L\beta) + 4\sin^2(\psi)}{\left[1 - R\exp(-2\alpha L\beta)\right]^2 + 4R\exp(-2\alpha L\beta)\sin^2(\psi + nL\beta)} \quad - \quad 7.2$$

In the above expression the quantity β is the wave number given by $\beta = \frac{2\pi}{\lambda}$. The phase change experienced by waves upon reflection is described by $\psi = \tan^{-1}(\frac{-2\alpha}{n^2 + \alpha^2 - 1})$. Information in the F-P spectrum pertaining to the length of the resonator is related to the spacing between the peaks in the spectrum. For a cavity with length L, the frequency spacing between the F-P fringes is given by $f = \frac{c}{2nL}$, where c is the speed of light and n is the refractive index as before. Rewriting the expression to show the spacing in terms of wavelength, the expression becomes as follows:

$$\Delta\lambda = \frac{\lambda^2}{2L\mathrm{n}} \quad - \quad 7.3$$

The loss associated with the cavity can be extracted by a more rigorous examination of the F-P spectrum. Shown below is a F-P spectrum recorded for a blank deeply etched ridge waveguide structure. The waveguide is etched using identical conditions to that described in section 7.4. As such, this structure is identical to a PSN waveguide except that it does not contain a grating. My initial intention was to calculate the losses by application of the cut-back method, whereby otherwise identical devices are cleaved into different lengths and then their transmitted power measured [11]. In this method, the loss is then proportional to the length of the device since the devices are otherwise identical, assuming identical coupling conditions. Unfortunately, due to the high-loss nature of the devices, only the very shortest devices transmitted any light. This meant that it was not possible to utilise this method in my investigations.

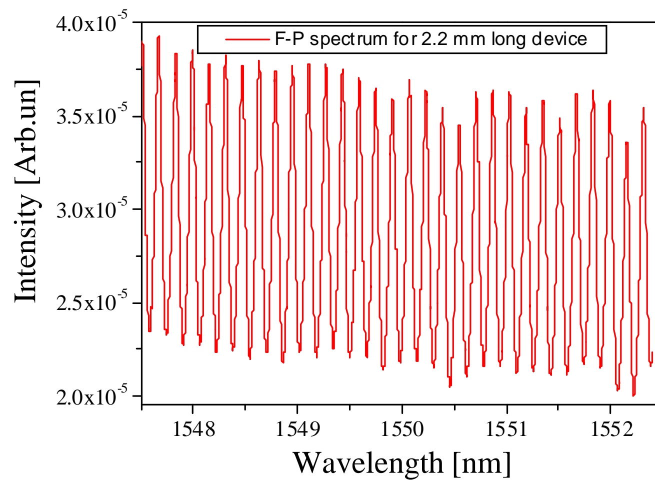

Figure 7.14. F-P fringe spectrum from a 2.2 mm long waveguide device taken with a resolution of 0.01nm and a span of 5 nm. The fringes show the maxima and minima of the F-P function. The fringe spacing is inversely proportional to the length of the F-P structure.

A fast Fourier transform (FFT) of the k values of the F-P spectrum yields a series of symmetric peaks which decrease in magnitude. Each of these harmonic peaks corresponds to a round trip of light inside the cavity. If these are plotted on a logarithmic scale, there is a linear relationship between the sizes of the peaks. Below is the Fourier transform of the above F-P fringe spectrum.

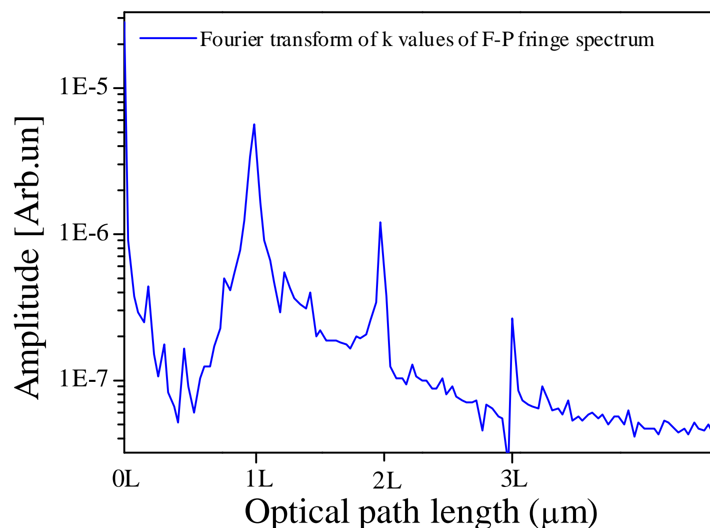

Figure 7.15. Fast Fourier transform of above F-P fringe spectrum on a logarithmic scale. Each peak corresponds to a successive round trip of the cavity. The distance between the peaks is proportional to the length of the F-P structure.

In the above figure, the x and y axes represent the number of points used to calculate the FFT and the amplitude of the harmonics respectively. The ratio between adjacent peak amplitudes is related to the loss of the cavity. As the loss is calculated from the relationship between the peaks, this method is independent of the coupling conditions. The relationship between the total cavity loss and the ratio between peaks is described by the harmonic amplitude ratio (HAR).

$$HAR = \mathrm{R}\exp(-\alpha L) \quad - \quad 7.4$$

In the above expression, $R = \sqrt{r_1 r_2}$, where $r_{1,2}$ are the reflectivities of facet 1 and 2 respectively. The quantity α is the total loss of the structure, taking into account both propagation loss and losses due to transmission at the facets. To obtain the HAR in the case of figure 7.15, the ratio of Pk_2/Pk_1, Pk_3/Pk_2 and Pk_4/Pk_3 would be calculated and an average taken. Reflectivities of the facets of the structures fabricated in this thesis are estimated to be 30% by a calculation of the Fresnel reflection. Blank, deeply etched GaAs based waveguides were found to exhibit a typical loss value of around $\alpha = 2.5$ cm^{-1}. This loss value – in units of inverse length - can be converted into a value in decibels per unit length by the following formula.

$$\alpha(dB/cm) = 4.31\alpha(1/cm) \quad - \quad 7.5$$

Thus, the above value corresponds to a loss in decibels around 10 dB/cm. This value compares well with loss values obtained by other researchers using similar equipment within the group [12]. Since the waveguides I fabricated are mesa structures, where the waveguide is etched through the active region, this has implications for their loss. When comparing to state of the art shallow etched waveguides, the losses are significantly higher [13]. This is because, in a deeply etched waveguide, the optical mode experiences much more of an interaction with the etched waveguide boundary than in a weakly guided, shallow etched waveguide, where losses can be as low as 0.1 dB/cm [13].

The accuracy of the method is limited by both the resolution of the F-P scan. The better the resolution of the F-P scan, the more information there is to provide the Fourier transform. A better resolution means that the fringes of the F-P spectrum will be more accurately represented, resulting in a Fourier transform which is more representative of the actual fringe pattern and thus a more accurate loss value. This

effect will result in an increased error in the measured loss value and consequently also in the measured loss value itself. As a general rule, one should use the best resolution available as this will give the most accurate representation of the fringes.

Using this method to examine PSN structures prior to ion implantation, we record an average loss value of 28 dB/cm. This loss is somewhat higher than for unstructured waveguides but unlikely to be of serious detriment to the ultimate performance of the devices in this proof-of-concept phase as they still were able to transmit an easily measurable amount of light in the μW scale.

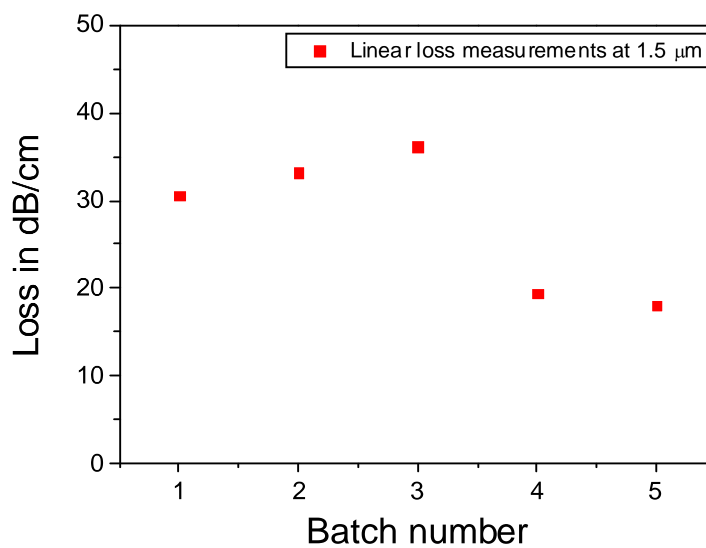

Figure 7.16. Linear loss of waveguide devices prior to ion implantation. The batch numbers refer to separate etches in the CAIBE machine which can explain the variations in loss value between different batches.

Possible reasons for the greater loss of the structures containing the grating are likely to be as a direct consequence of the extra etch step involved in their fabrication. In deeply etched waveguides, the mode has more of an interaction with the sidewalls than in a shallow etched structure. Rough sidewalls cause increases in losses because they increase scattering. This is why smoothly etched sidewalls are of particular importance when defining deeply etched waveguides. The structures containing the grating exhibit considerably more roughness in their sidewalls compared to a blank ridge waveguide with identical dimensions defined by lithography. This increase in roughness can be expected to increase the losses of the waveguide. Another factor that may act to increase the loss is the possibility of ion induced defects in the upper AlGaAs layer caused by the CAIBE. In waveguide structures, a proportion of the

guided mode can propagate in the cladding layers. The PSN waveguide structures have the upper cladding layer periodically removed and this has obvious implications if light is propagating. The presence of the grating itself is also likely to introduce losses.

7.6 Ion implantation and thermal annealing

With the quality of the samples now assured, ion implantation post-processing was then used as detailed in section 7.3 to bring about the modulation in susceptibility. The samples were divided into batches and subjected to various degrees of thermal annealing to repair the ion-induced damage. The first batch of devices was annealed at 500º C, for 30 seconds. This anneal was chosen after consultation with colleagues at the University of Surrey, who carried out both the implantation and subsequent annealing. They regularly used such an anneal on various materials for the removal of unstable defects.

After annealing, these devices were retested in the linear-loss setup. Unfortunately, none of the devices transmitted any light. The devices were then cleaved as short as possible (down to around 400 μm in length) to try to minimise the compound loss. This approach proved fruitless as the losses were still too high for any output to be observed. This anneal was thus deemed to be ineffective in repairing the ion-induced damage.

By consulting the literature, I was able to suggest a new type of annealing The authors of reference [5] investigated various annealing steps to attempt to reduce this loss while maintaining the modification of the nonlinear coefficient such that practicable devices could still be produced. They found that an anneal at 600 °C for 10 minutes was required to produce an improvement in the losses of an AlGaAs waveguide implanted uniformly with 2×10^{14} ions cm^{-2}. Due to the high ion dose required to cause the desired modulation in nonlinear coefficient, significant damage is caused to the target material. This thus requires high temperature annealing to repair.

The next batch of samples was annealed using this recipe and then assessed using the same linear-loss testing procedure. Initial tests did not yield any samples which transmitted light, but, once the devices were cleaved to very short lengths,

some output was observed. By taking a FFT of the resulting fringe spectrum, a very high average loss value of 250 dB/cm was deduced. It therefore seems that annealing at 600ºC for 10 minutes is insufficient to repair the damage caused to the active region in the PSN devices. Given that the loss of these devices was so high, it was not possible to measure a nonlinear output in the manner discussed in section 7.7.

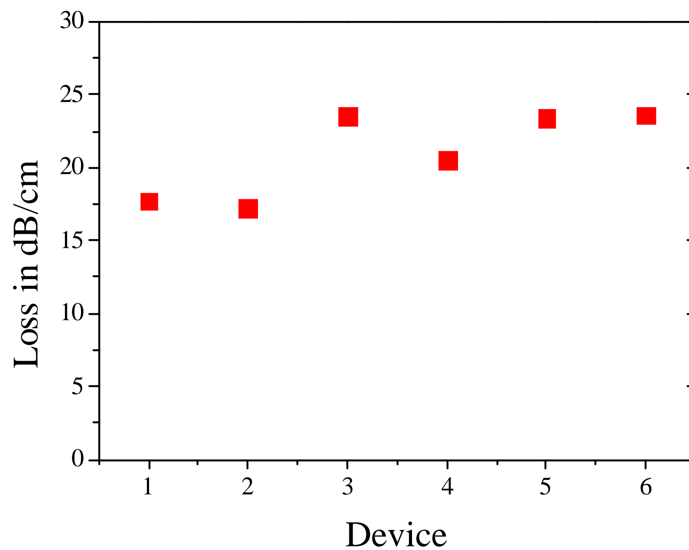

Figure 7.17. Losses of devices annealed at 800 °C

The remaining option was to increase the temperature of the anneal in excess of 600 ºC. Colleagues at the University of Surrey suggested that higher temperature anneals should be able to remove more of the ion induced defects in the material and reduce the loss. Such extreme temperatures have the potential to damage GaAs material, and so steps were required to minimise this risk. For this reason, this final small batch of samples which were all implanted with a dose of 5 $x10^{14}$ ions/cm^2 was coated with a protective 50 nm layer of SiN3 and subjected to a 10 min 800 ºC anneal. The transmissive properties of these samples were then evaluated and found to be vastly improved in comparison to those annealed at lower temperatures. They exhibited an average loss value of 23 dB/cm as shown above, which is similar to that measured prior to implantation.

7.7 Assessment of nonlinear optical properties.

The samples fabricated were capable of operation in both an OPG configuration pumped at 1.064 µm and SHG being pumped at around 2.1 µm. The first method used involved the parametric generation. In this configuration, both the pump beam and the generated signal wave are visible both on the IR viewing camera and on commercially available IR viewing cards. This was of great assistance in the alignment of the experimental setup which is shown below in figure 7. 18.

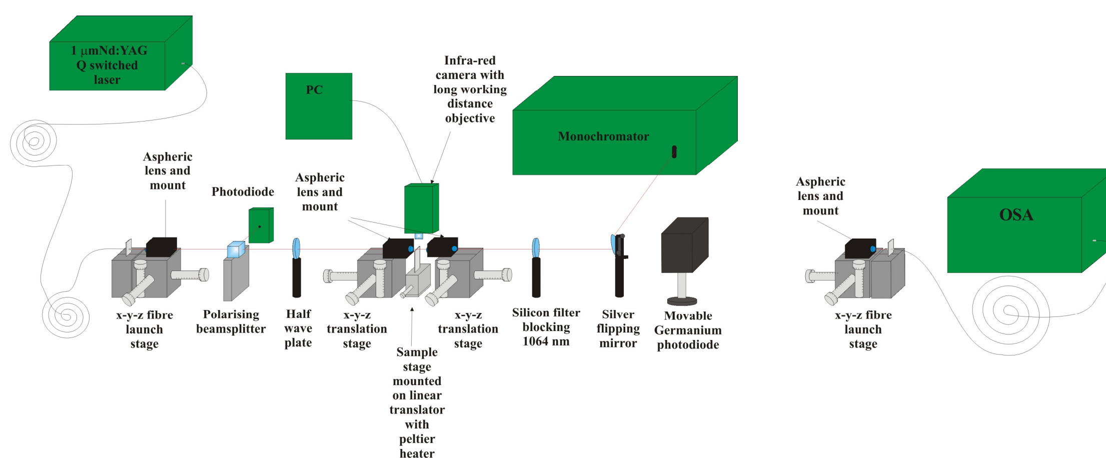

Figure 7.18. Experimental setup for OPG nonlinear evaluation

The output of a Q switched Nd:YAG laser was fibre coupled for ease of alignment and passed through a polarising beam splitter and a half-wave plate. This allowed the input power to be monitored by a photodiode and an arbitrary linear input polarisation selected. By following the alignment steps outlined in section 7.5, laser light could be coupled into a waveguide successfully and the output collected. Given that the aim was to observe frequency converted light from the output facet, it was necessary to tune the position of the output lens to allow optimal coupling for the frequency converted light. Alignment was aided here by the use of a 1.5 micron laser source. This enabled the output lens to be positioned at approximately the correct position to collect any frequency converted light. A germanium photodiode placed after a silicon filter was used to detect the converted signal wave which from figure 7.6 would be the region of 1.2 – 1.8 µm. The sensitivity of this measurement was increased by the use of a lock-in amplifier synchronised with the pump laser repetition frequency. By varying the input power in a linear fashion, a corresponding nonlinear output signal would indicate frequency converted light. The use of a Digikrom 480 monochromator

allowed the recording of the optical spectra from the waveguides and a typical pump spectrum is shown below in figure 7.19. The pump source was also implemented in a free space arrangement, allowing higher powers to be directed at the sample.

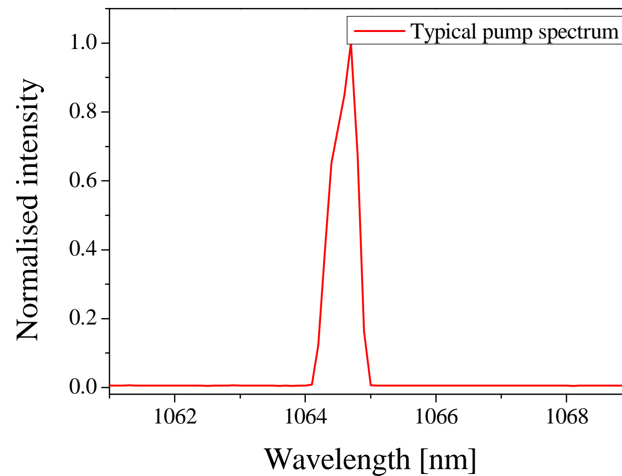

Figure 7.19. Typical pump spectrum from Q-switched Nd:YAG laser

Input powers could be varied from 10's of μW up to hundreds of mW. The high peak powers emitted by the pump laser in energetic nanosecond pulses in conjunction with the tight focusing required to successfully couple into the waveguide structures resulted in very high peak fluences incident on the input facets of the devices as shown below in table 7.1. This resulted in surprisingly low incident powers producing observable facet damage to the devices.

Average incident power (mW)	**Peak intensity W/m^2**	**Damage**
0.942	2 x10^{12}	No
1.2	2.54 x10^{12}	No
1.3	2.75 x10^{12}	Yes
1.5	3.18 x10^{12}	Yes

Table 7.1. Showing showing measured damage threshold for devices when using a X60 lens. This assumes a spot size of 2 μm radius.

The samples were also tested in an SHG configuration. An optical parametric oscillator tunable around 2 μm was used as the pump source providing harmonic generation at around 1 micron. A diagram of the experimental setup is shown below.

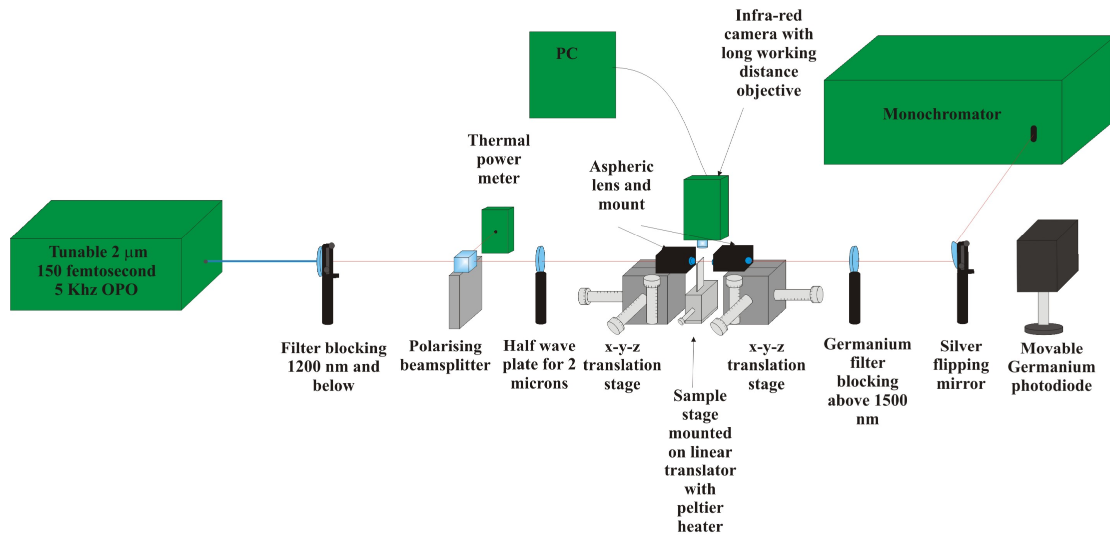

Figure 7.20. SHG experimental setup

The OPO produced output at several wavelengths; a signal beam at 1.2 µm which was used for alignment and the idler beam at around 2 microns which served as the pump beam for the semiconductor structures. Once alignment had been performed with the 1.2 µm beam, it was blocked and the position of the lenses adjusted to try to optimise coupling of the 2 micron beam into the structures. The Ge filter situated after the output collimating lens blocked any 2 micron light allowing the detector to measure only light produced due to SHG.

Despite using all appropriate measures to assess the nonlinear properties of the samples, no nonlinear signal could be measured. The samples annealed at 600 °C were too lossy, while the samples annealed at 800 °C did not produce any nonlinear signal, despite the losses being much lower. In addition to reducing the losses of the material, I must conclude that the anneal also restored the nonlinear coefficient to its initial value, thereby destroying the PSN. The conditions used in the implantation process were calculated using well established algorithms. Altering either the energy or the dose of the implant significantly should not therefore result in any improvements in performance. Rather, having introduced the disorder, the challenge was in developing an anneal process that compensated the huge optical losses while maintaining the nonlinear coefficient. From my investigations, it was, unfortunately, not possible to achieve this balance. The absence of similar work by other researchers also highlights the difficulties in pursuing this methodology.

7.8 Orientation-patterned GaAs

Orientation patterning (also called Sublattice Reversal Epitaxy SRE or 'periodically-poled' GaAs) allows the production of high quality domain inverted (quasi-periodically-poled) GaAs structures. The idea is to deposit a thin non-polar buffer layer such as germanium, followed by subsequent overgrowth of single phase GaAs in anti-phase to the substrate. Without this buffer, deposited GaAs layers nucleate in the same orientation as the preceding layer. Germanium is chosen because it has a very similar lattice constant to GaAs (~0.1% mismatch [14]), allowing the growth of low-strain, high-quality films. Normally, growth of a polar material such as GaAs on a non-polar material would occur with both phases of material nucleating at random on the surface. This would cause the formation of numerous randomly located anti-phase boundaries on the surface. Careful control of the growth conditions eliminates such boundaries such that single-phase material can be produced.
Selective etching through the anti-phase layer and Ge buffer to expose the in-phase material underneath then allows the regrowth of domain inverted GaAs material with inversion period definable arbitrarily through photolithography and etching. Regions of domain-inverted material exhibit sign reversal of all their non-vanishing nonlinear coefficients resulting in a nonlinear coefficient variation as shown in figure 7.1b. This case is identical to that of PPLN and provides forward conversion at each coherence length. Recognising the elegance and potential of this new orientation-patterned (OP) methodology, we began a study of its implications and applicability in the context of this project.

According to our calculations (shown below in figure 7.21) such devices demonstrate significantly higher efficiency than either PPLN or PSN devices. The modelling is based on that used in references [3, 8, 15] and was carried out by Dr David Artigas. Fresnel reflections at the low/high χ^2 boundary are also taken into account for the case of a regrown GaAs/AlGaAs structure. In the case of the ion-implanted structures, the contribution from Fresnel reflections is believed to be less.

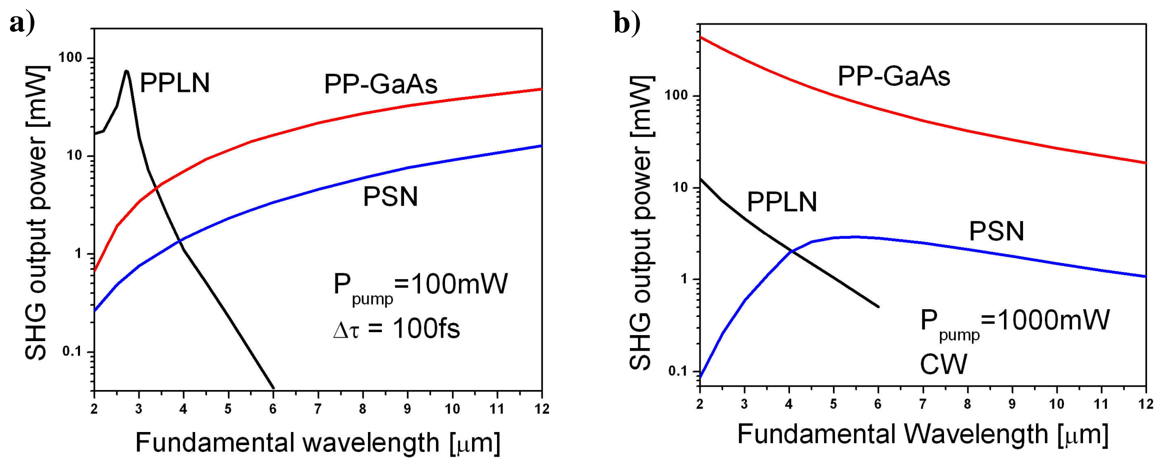

Figure 7.21. Calculated output SHG power versus pump wavelength for optimal crystal length with **(a)** a femtosecond pump beam and **(b)** a CW pump beam for pp-GaAs, PPLN and PSN crystals.. PPLN displays higher efficiencies in the pulsed regime below 3.5μm due to both large group velocity mismatch and high losses in GaAs at these wavelengths. This also means that the maximum device length for GaAs devices is less than for PPLN in the femtosecond pump case at these wavelengths. Interface reflections are especially detrimental to the performance of the PSN devices. In a CW regime, pp-GaAs is shown to be a considerably better nonlinear material than either PPLN or PSN material for the whole of the wavelength regime investigated.

7.8.1 Sample Preparation

Fabrication of pp-GaAs material involved a combination of precise and demanding MBE growth and similarly accurate etching. Our initial attempt used a combination of wet etching and CAIBE of lithographically defined structures performed at St Andrews, followed by regrowth at the national III-V facility in Sheffield. A schematic of the preparation procedure is shown below in figure 7.22.

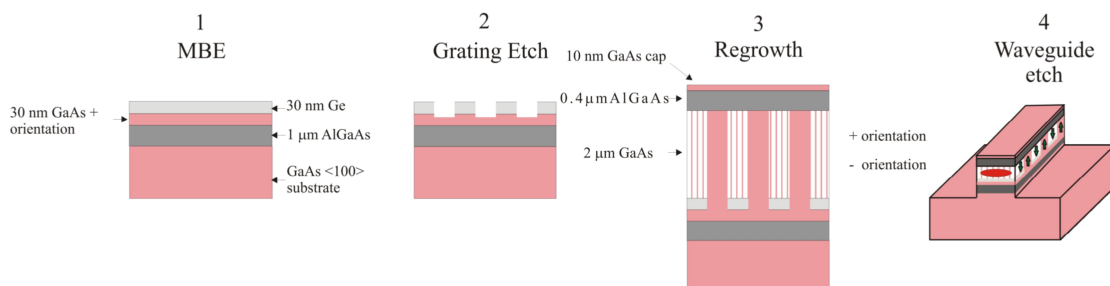

Figure 7.22. Initial attempt at creation of OP-GaAs material procedure

Initial growth was carried out at the national III-V centre in Sheffield, consisting of a GaAs <100> substrate with overgrown layers of AlGaAs (1μm), GaAs (30 nm) and finally 30 nm of Ge. A wet etching technique was then employed to transfer the

grating pattern in figures 7.4 – 7.5 into the material as in stage 2 of figure 7.22. A solution of H_2O_2/H_2O (50/50) was found to etch Ge material in a controllable, reproducible manner.

The low aspect ratio of etches performed made it difficult to accurately measure the depths etched using SEM techniques. Therefore, atomic force microscopy (AFM) was utilised.

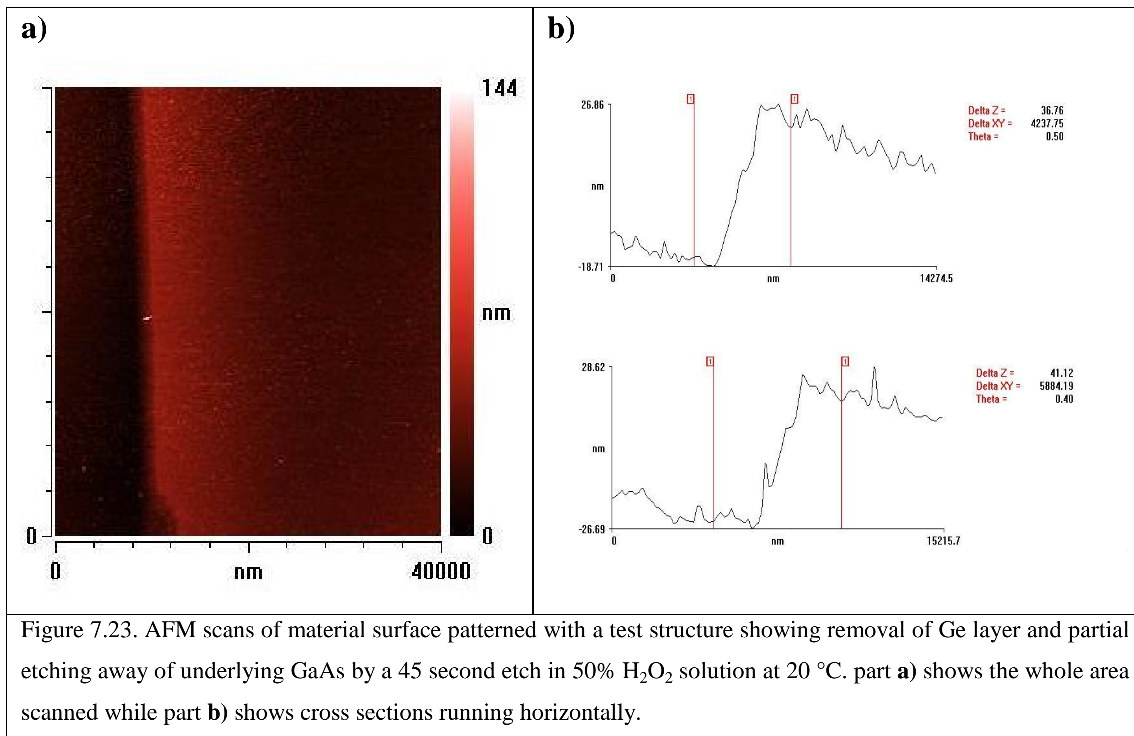

Figure 7.23. AFM scans of material surface patterned with a test structure showing removal of Ge layer and partial etching away of underlying GaAs by a 45 second etch in 50% H_2O_2 solution at 20 °C. part **a)** shows the whole area scanned while part **b)** shows cross sections running horizontally.

Since both horizontal scans show additional material being removed other than the 30 nm of Ge, some of the underlying GaAs must also be etched away. After the grating was etched into the material, it was sent to Sheffield for regrowth as shown in stage 3 of figure 7.22. After this, the samples were returned to St Andrews for the definition of ridge waveguides by CAIBE. A 5-min etch using the recipe developed for the PSN samples was found to be suitable for this purpose and corresponding images of finished devices are shown below.

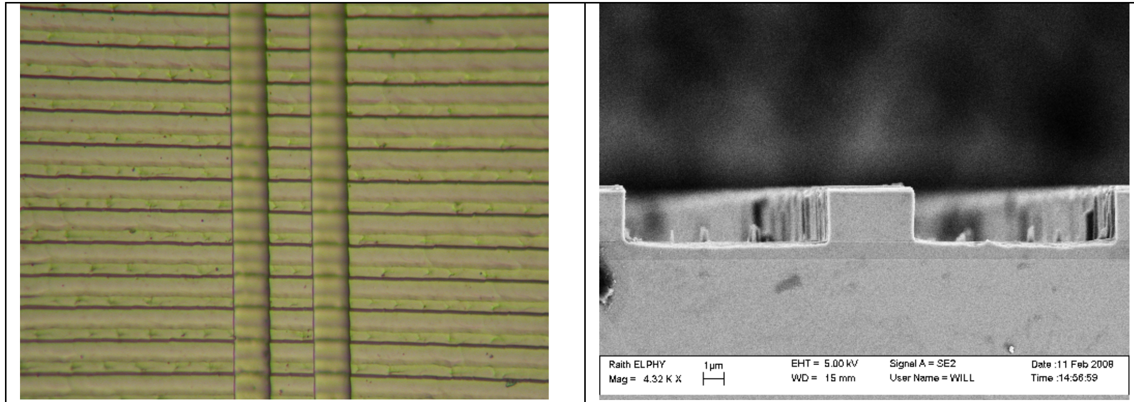

Figure 7.24. a) Top view of completed structure taken with an optical microscope. The ridge waveguide runs vertically while the grating is horizontal. Part b) shows an end elevation of a waveguide taken using SEM. The boundary between the active region ant the underlying waveguide is clearly visible.

Unfortunately, when the nonlinear properties of these samples were evaluated, no nonlinearity was observed. It was concluded that on this occasion there had been a failure in producing domain-inverted material. From figure 7.24, there does seem to be some visual difference between adjacent regions of GaAs, but this can be attributed to the different focal distances of these adjacent areas of material. It is thought that the defects visible on the surface of the material are randomly located anti-phase boundaries caused by nucleation of random phases of GaAs on the Ge material.

It was clear after this initial unsuccessful attempt that I needed a greater understanding of the processes involved in this type of epitaxial regrowth. I therefore conducted a search to find more information on regrowth of polar materials on non-polar specifically within the context of the GaAs/Ge system. From the literature [16-18], the key to growth of single phase polar material on non-polar layers is a combination of using thin buffer layers and growth on misoriented substrates. The precise growth conditions of the constituent layers are also of paramount importance to the success of the technique.

When growing GaAs on Ge on a misoriented substrate, there is preferential nucleation of Ga and As atoms at specific nucleation points on the Ge surface. This then favours growth of a particular domain of GaAs rather than the random process occurring with a <100>wafer. Depositing pre-layers of material and using specific growth temperatures then allows the overgrown layer to be in-phase or in anti-phase with the substrate.

In the light of this new information, discussions were arranged with our collaborators so that new approaches to the epitaxial growth work could be

implemented. Unfortunately, our primary collaborators in this work at the national III-V centre in Sheffield were in the process of moving to a new facility and could therefore not assist at this critical stage of my project. To mitigate the effect of this disruption some limited access to epitaxial growth facilities at the Ioffe Institute in St Petersburg was negotiated.

7.8.2 Sample Preparation 2

Given my lack of expertise in epitaxial growth, I provided our new collaborators with literature relevant to regrowth we required so they, being more familiar with the terminology, could tailor the growth procedures to suit. Following the process outlined in [7][16], a (100) GaAs wafer misoriented by 4° towards (111)B was purchased from a commercial semiconductor manufacturer. This was then sent for initial preparation to the Ioffe institute.

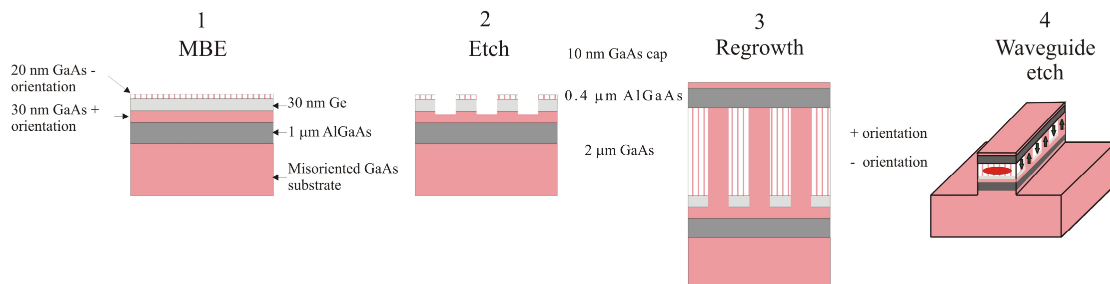

Figure 7.25. Sample preparation process for domain inverted structures based on [1, 17, 19]

Initial growth was performed in a Riber-32 machine and consisted of the deposition of 200 nm GaAs, 1 mm of $Al_xGa_{1-x}As$, x from 0.6 to 35 and then 30 nm of GaAs. All of this was performed at 570 °C. The wafer was then moved to the Supra-32 MBE machine in a dry nitrogen atmosphere. Once loaded into the machine, a degassing process was performed to purge the surface from any contaminants. Deposition of 30 nm of germanium then occurred at a temperature of 500 °C. The wafer was then transferred back to the Riber-32 machine for the final growth stage. A pre-deposition 5 Å layer of gallium was first deposited at 300 °C and the substrate subsequently annealed at 620 °C before the temperature was reduced to 570 °C for the 20 nm GaAs deposition. This precise growth procedure was designed such that the

final GaAs layer would be in anti-phase to the substrate, allowing subsequent definition of orientation patterned material. This completes stage 1 in figure 7.24.

Next, I performed photolithography and selective CAIBE etching to imprint the periodic grating described in figures 7.6 and 7.7. A suitable etching recipe with a rate of around 170 nm per minute was developed to remove reliably the small amount of material required. A beam voltage of 350 V, coupled with a beam current of 10 mA and gas flow rates of 10 sccm and 2.5 sccm for argon and chlorine gasses respectively were used for a period of 40 seconds. Etch tests showed that this particular blend of physical and chemical etching components resulted in smooth, straight sidewalls of reproducible depth.

Removal of the top anti-phase GaAs and Ge layers is essential to expose the in-phase 30 nm GaAs layer underneath. In this preliminary investigation however, overetching to remove the in-phase 30 nm GaAs layer and some of the underlying in-phase AlGaAs was performed as this was easier to achieve in reproducible fashion and should not have affected regrowth of in-phase material. This over etching would increase the corrugation in the waveguiding direction ultimately limiting the performance of the final devices but in this early stage, we wished to demonstrate that we possessed understanding and capability of the SRE growth method.

Below are typical AFM scans and pictures of the material surface taken with an optical microscope, showing the depth and quality of the etched grating.

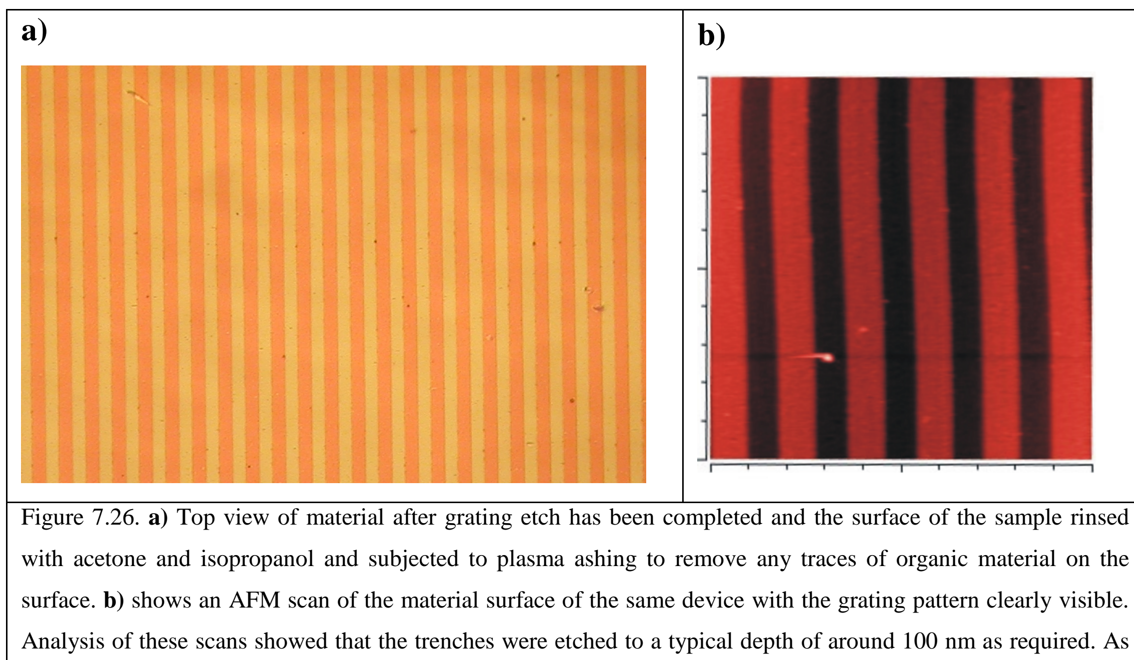

Figure 7.26. **a)** Top view of material after grating etch has been completed and the surface of the sample rinsed with acetone and isopropanol and subjected to plasma ashing to remove any traces of organic material on the surface. **b)** shows an AFM scan of the material surface of the same device with the grating pattern clearly visible. Analysis of these scans showed that the trenches were etched to a typical depth of around 100 nm as required. As

we can see from the image and the scan, the quality of the surface appears to be high.

With the material now patterned to selectively expose alternating regions of in-phase and anti-phase material, the next phase in the manufacture is regrowth to form the active region of the GaAs and subsequent AlGaAs deposition to form the upper waveguiding layer. Prior to transport to the Ioffe institute, the samples were all cleansed again and packed between sterile wipes in sealed sample cases in a nitrogen atmosphere.

The MBE regrowth consisted of 2 μm of GaAs followed by 400 nm of $Al_xGa_{1-x}As$, x from 0.6 to 35 and a 10 nm GaAs cap layer using the same procedure outlined above to ensure optimal growth quality. Once the samples growth was complete, they were returned to St Andrews for the waveguide etching step.

This was carried out using the recipe used to define the waveguide in the PSN case. A duration of 5 mins was again found to be sufficient to etch through the active region of the material to provide the required deeply etched waveguide. Upon inspecting the surface of the regrown material, we became concerned as to the quality of the deposited layers. Below in figure 7.27 are images of the regrown surface taken with an optical microscope.

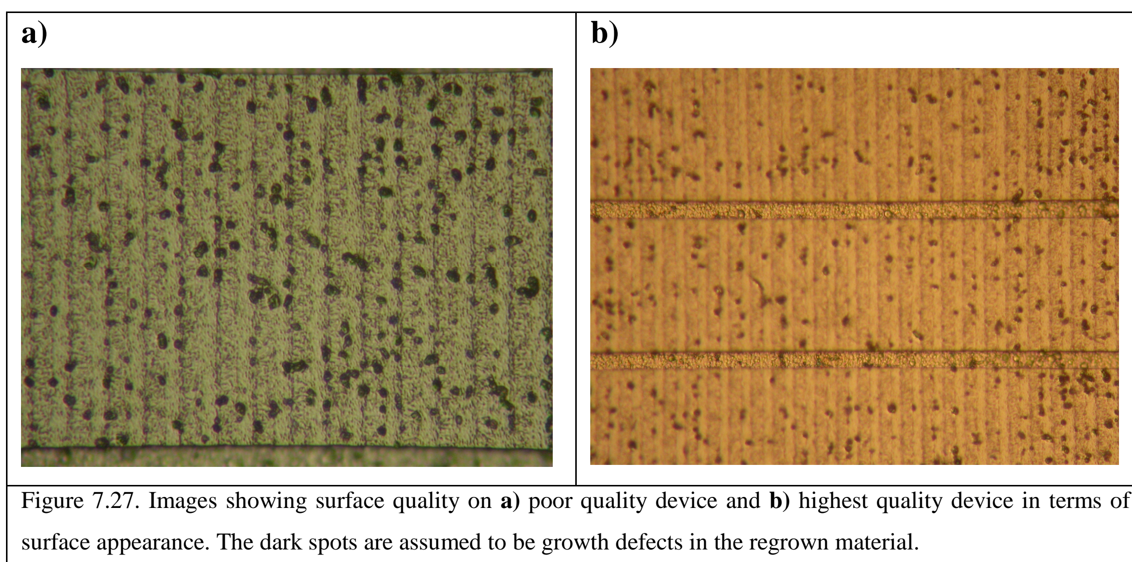

Figure 7.27. Images showing surface quality on **a)** poor quality device and **b)** highest quality device in terms of surface appearance. The dark spots are assumed to be growth defects in the regrown material.

In the figure, the material surface is covered in defects. These are far more pronounced than in the case of the sample on the <100> GaAs substrate.

Due to time constraints, a thorough analysis of these samples was not undertaken but a brief evaluation of the nonlinear properties of the highest quality device was performed using the methods outlined in section 7.7. During this nonlinear

evaluation, the sample was observed to be extremely lossy and no nonlinear signal was observed.

It can be concluded from the above that considerable advances need to be made in the development of the basic science and related technology to be able to reproduce the high-quality orientation-patterned material reported in the literature. It is unclear whether or not the initial material growth at Ioffe was successful in the production of such O-P material. Techniques such as stain etching should be able to give some insight into the success or otherwise of this step in the fabrication [16]. Significant improvements also must be made in the understanding of the regrowth procedure of the orientation-patterned active region because the large defects that are evident in figure 7.27 were not seen in figure 7.26 prior to regrowth.

7.9 Conclusions and Future Work

The investigations undertaken in this chapter sought to evaluate the suitability of two different types of semiconductor waveguide structure for nonlinear frequency conversion. Unfortunately, it was not possible to measure a nonlinear signal from any of the ion-implanted PSN structures. To obtain the required modulation in $\chi^{(2)}$ in my waveguide structure, a high dose of ions was needed, but, in addition to destroying the nonlinear coefficient of the material, the implant also severely affected its transmissive properties. In my investigations, I was unable to find an anneal process that simultaneously repaired the loss-induced defects while preserving the required modulation of the nonlinear coefficient. The huge losses introduced by the implantation process seem to be a fatal problem in terms of the viability of these devices.

There does remain, however, the possibility of implementing the PSN concept by using a different vector to achieve the variation in χ^2 such as regrowth. From theoretical work on the subject, these devices could potentially demonstrate higher efficiencies than $LiNbO_3$. Also, semiconductor materials with even higher nonlinear coefficients than GaAs exist that have even better figures of merit for nonlinear frequency conversion. An example is InAs which displays nonlinear coefficients as high as around 300 pm/V. It absorbs up to around 3.5 μm, however beyond this wavelength could prove to be an excellent nonlinear material [20].

Despite this promise, it is clear that any PSN system will demonstrate at the very most, 50% of the efficiency of an equivalent periodically-poled crystal system. This was one of the reasons why the orientation poling concept for GaAs became so compelling.

Given the elegance and potential performance of the O-P-GaAs system, it was extremely disappointing that my investigations proved fruitless. As stated previously, the principal reason for this was unoptimised epitaxial growth and regrowth, all of which were outside my direct control. Throughout my investigations, the MBE processes were treated essentially as 'given' procedures. Successful growth of O-P material by other groups has involved extensive testing and optimisation of regrowth procedures. Despite the fact that the authors of related papers have developed and published recipes for the fabrication of these material types, our attempts at putting them into practice illustrate the practical challenges in their implementation. It is my opinion that an integrated fabrication approach performed in its entirety at one facility coupled with a concerted effort into the understanding of the MBE processes is required to produce successful devices by this means.

At the very end of my involvement with the project, some collaboration was successfully negotiated with a company that has the technology to supply commercially grown OP-GaAs material [6]. This should greatly increase the simplicity of creating the low-threshold waveguide OPOs which were a principal end goal of this project. The greatest challenge in the optimisation of these devices will be the minimisation of corrugation and its associated losses in the waveguide core but this can be achieved by careful polishing of the material.

Recently, several groups have developed an alternative approach for the fabrication of O-P material. Instead of relying on sublattice reversal epitaxy or misoriented wafers, a precise etching, bonding and polishing strategy has been adopted to obtain orientation-patterned material which is free from corrugation [21]. A schematic of the fabrication procedure is shown below in figure 7.28.

[6] Schunemann, Peter G - peter.g.schunemann@baesystems.com

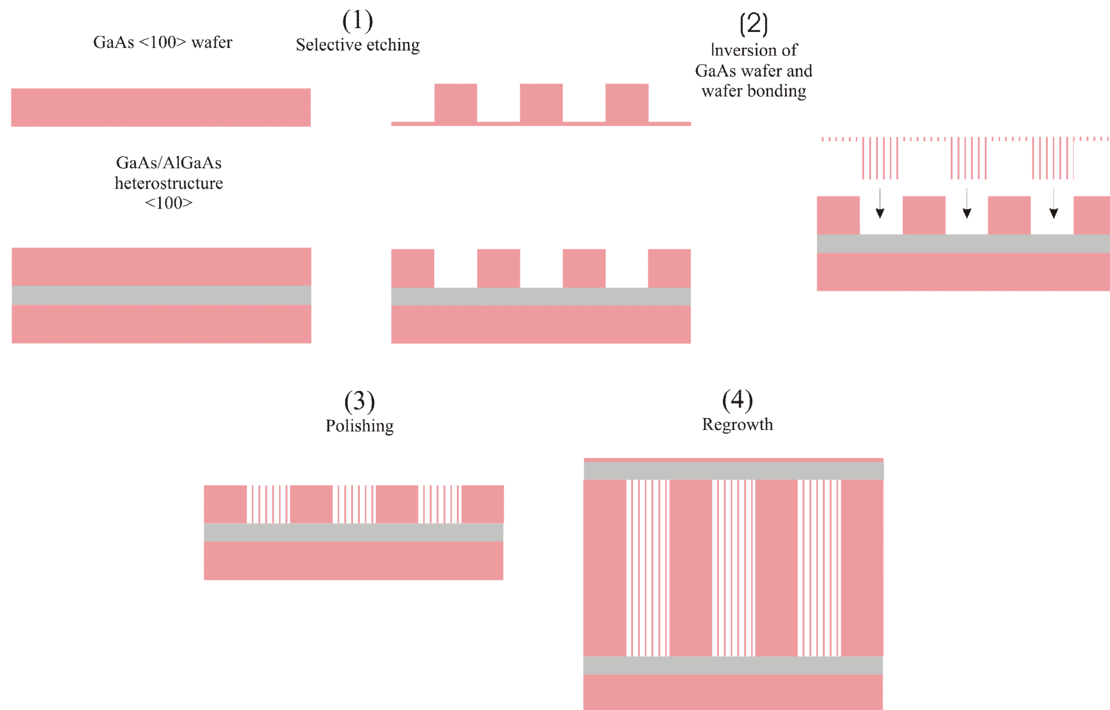

Figure 7.28. Orientation-patterned GaAs formed by bonding and polishing technique. The desired grating pattern and its inverse are etched into the heterostructure material and a GaAs <100> wafer respectively. The GaAs wafer is then turned upside down and bonded to the heterostructure such that the two join with no gaps. Polishing is then used to remove additional GaAs material leaving a domain inverted template with no corrugation. Regrowth is used to define the active region and upper waveguiding layers. It is worth noting that all overgrown layers will exhibit periodic domain inversion. [The respective layers are not shown to scale in the figure.]

This method requires a combination of very precise etching to define the grating and its complementary structure. In addition, advanced polishing techniques are required to remove the additional GaAs and leave the underlying material of high enough quality for subsequent regrowth. This method has shown extremely promising results and its successful optimisation could lead to the technique becoming more widely utilised.

References

1. Skauli, T., et al., *Measurement of the nonlinear coefficient of orientation-patterned GaAs and demonstration of highly efficient second-harmonic generation.* Optics Letters, 2002. **27**(8): p. 628-630.
2. Kondo, T. and I. Shoji, *Study on Wavelength Conversion by Compound-Semiconductor -Based Quasi Phase-Matching Devices*, *Photonics Based on Wavelength Integration and Manipulation*. 2005, IPAP. p. 151 - 160.
3. Artigas, D., et al., *Periodically switched nonlinear structures for frequency conversion: Theory and experimental demonstration.* IEEE Journal of Quantum Electronics, 2004. **40**(8): p. 1122-1130.
4. Rafailov, E.U., et al., *Second-harmonic generation from a first-order quasi-phase-matched GaAs/AlGaAs waveguide crystal.* Optics Letters, 2001. **26**(24): p. 1984-1986.
5. Janz, S., et al., *Modification of the 2nd-Order Optical Susceptibility in Alxga1-Xas by Ion-Beam-Induced Amorphization.* Applied Physics Letters, 1994. **65**(2): p. 216-218.
6. Kayali, S., *GaAs MMIC Reliability Assurance Guideline for Space Applications (Chapter 3 GaAs Material Properties)*. 1997, NASA Jet Propulsion Labatroatory: Pasadena. p. 17. http://parts.jpl.nasa.gov/mmic/contents.htm
7. Artigas, D., et al. *Design parameters of periodically-switched nonlinear structures for efficient nonlinear process*. in *Advanced solid state photonics*. 2005. Paper MB24, Vienna, Austria
8. Artigas, D., et al., *Design parameters of periodically switched nonlinear structures for efficient nonlinear processes*. OSA Trends in Optics and Photonics series. Advanced Solid-State Photonics, 2005 I. Sorokina Ed., 98, p.86-91.
9. Hofstetter, D. and R.L. Thornton, *Theory of loss measurements of Fabry-Perot resonators by Fourier analysis of the transmission spectra.* Optics Letters, 1997. **22**(24): p. 1831-1833.
10. Kotlyar, M.V., *Photonic crystal waveguides and tunable filters in InP*, PhD Thesis, *School of Physics and Astronomy*. 2005, University of St Andrews: St Andrews. p. 155.
11. *Integrated publishing, Electrical engineering training series, http://www.tpub.com/neets/tm/109-3.htm.*
12. Moore, S.A., et al., *Reduced surface sidewall recombination and diffusion in quantum-dot lasers.* IEEE Photonics Technology Letters, 2006. **18**(17-20): p. 1861-1863.
13. Deri, R.J. and E. Kapon, *Low-loss III-V semiconductor optical waveguides.* IEEE Journal of Quantum Electronics, 1991. **27**(3): p. 626 - 640.
14. Strite, S., et al., *Antiphase Domain Free Growth of Gaas on Ge in Gaas/Ge/Gaas Heterostructures.* Applied Physics Letters, 1990. **56**(3): p. 244-246.
15. Artigas, D., et al. *Design parameters of periodically switched nonlinear structures for efficient nonlinear processes*. in *Advanced solid state photonics*. 2005. Paper MB24, Vienna, Austria.

16. Eyres, L.A., *All-Epitaxially Orientation-Patterned Semiconductors For Nonlinear Optical Frequency Conversion*, PhD Thesis, *Department of Applied Physics*. 2001, Stanford University. p. 181.
17. Ebert, C.B., et al., *MBE growth of antiphase GaAs films using GaAs/Ge/GaAs heteroepitaxy.* Journal of Crystal Growth, 1999. **201**: p. 187-193.
18. Koh, S., et al., *GaAs/Ge/GaAs sublattice reversal epitaxy and its application to nonlinear optical devices.* Journal of Crystal Growth, 2001. **227**: p. 183 - 192.
19. Eyres, L.A., et al., *All-epitaxial fabrication of thick, orientation-patterned GaAs films for nonlinear optical frequency conversion.* Applied Physics Letters, 2001. **79**(7): p. 904-906.
20. Rafailov, E.U. 2008 Personal communication, *Alternative nonlinear materials*,
21. Li, J., et al. *Wafer-fused orientation-patterned GaAs*. in *Photonics west 07*. 2007. p 68750H, San Jose, California, USA

Chapter 8 Summary and Outlook.

In this work, semiconductor material was explored as a medium for both ultrashort-pulse production through the study of quantum-dot lasers and as a nonlinear medium for parametric optical processes. The work was motivated by the desire to further develop these materials for their inclusion in compact, efficient optical devices.

8.1 Mode-locked quantum-dot lasers

My work on quantum-dot material was concerned with the laser dynamics of the quantum states contributing to gain-switched emission from a device that had been optically pumped with femtosecond pulses [1, 2]. I observed the evolution of emission from low-energy states to excited states as this pump intensity was increased. I also demonstrated that pulses arising from emission from the first excited state had considerably shorter duration and were generated earlier in time than those due to ground-state emission. The pulses from ES1 had durations of 24 ps whereas those from the GS had durations of around 180 ps. The apparent faster excited-state lasing dynamics allude to potential advantages for operation of quantum-dot lasers under the conditions of excited-state mode locking. Subsequent investigations by other authors, however, have measured pulse durations from quantum-dot lasers operating in this regime and found that generally, they produce pulses of similar length or longer than those from the ground state [3-6]. This suggests that optimally short pulses are produced from ground-state emission as opposed to ES1, although the amount of work done in this area is still too limited to provide definitive conclusions. While there is some ambiguity with regard to the advantages of quantum-dot lasers operating in an ES1 mode-locked regime, recent work has shown the ability of un-mode-locked emission from the excited-state to improve the characteristics of GS mode locking through depletion of excited carriers by excited-state lasing [7].

My work on quantum-dot transition dynamics also demonstrated that the ground and excited states were acting essentially as independent laser transitions. However, with appropriate design of the quantum-dot material such that ground and excited states exhibited a greater degree of overlap, there exists the possibility of

creating a quantum-dot laser system with increased cross-talk between the electronic states, thus allowing the engagement of the entire bandwidth for the excited state plus the ground state during a fully optimised mode locking condition. This would be a very exciting prospect within the context of ultrashort-pulse semiconductor diode laser development.

I also investigated two mode-locked quantum-dot laser systems. The first was an external cavity mode-locked laser that incorporated a quantum-dot SESAM. Here, preliminary investigations in the unoptimised system demonstrated mode locking despite the apparent incompatibility of SESAM and gain material [8-10]. While this laser has not yet been fully unoptimised, this preliminary result indicates the potential versatility of an all-quantum-dot system in that the broad bandwidths of both gain section and absorber allow mode-locked operation even when the two are not ideally matched.

Additionally, I investigated two-section, mode-locked quantum-dot lasers where mode locking was achieved over a wide temperature range from 20 °C to 70 °C. This result showed that these devices display some resilience to temperature effects [11] and subsequent work by Cataluna and Viktorov explained the mechanisms governing this behaviour [12]. In basic terms, it was concluded that as the temperature increases the absorber carrier escape rate decreases thereby allowing shorter pulses to evolve.

Outlook

Quantum-dot lasers have been shown to outperform quantum-well lasers in several areas including pulse duration [5, 6, 13], and jitter [14]. The main challenge is to find ways to overcome the frequency-induced chirp arising from self-phase nodulation which is seen as the principal limiting factor on obtaining optimally short, transform-limited pulses from quantum-dot lasers [7]. Until this issue is addressed, it will be difficult to engage the whole inhomogeneously broadened gain bandwidth of quantum-dot devices during mode locking. Interestingly, recent work involving tunnel injection of cold carriers has demonstrated consistently lower linewidth enhancement factors at different operating conditions suggesting the potential of lower frequency chirps [15, 16]. Tunnel injection provides carriers directly into lasing states without the problems associated with relaxation down from higher energy states

such as the wetting layer. The introduction of multi-segment gain and absorption sections in monolithic quantum-dot lasers could also be of use. This would allow more precise control of the frequency chirp in the respective sections with a corresponding prospect for the generation of shorter pulses.

An alternative approach to engineering the dot material is to monolithically integrate intracavity dispersion compensating elements into the structure such as chirped-mirror structures. These elements would ideally allow comparable improvement in performance as obtained by similar intracavity schemes in different laser systems without compromising the monolithic nature of the device. Although this adds a degree of complexity to the laser, my view is that this would be more than compensated by the likelihood of a much superior performance in the mode locking regime.

Another challenge facing quantum-dot lasers is that of temperature resilience. As stated previously, initial theoretical work on quantum-dot lasers predicted an infinite value for T_0! In practice, however, the presence of additional energy levels inside the dot and surrounding wetting layer result in a value well removed from this ideal. This is especially pronounced at non-cryogenic temperatures where carriers can become thermally excited to a problematic degree [17]. One approach which leads to improvements in T_0 is to use p-doping of the quantum dots with beryllium, for example. The introduction of an excess hole concentration counteracts the close spacing of 'hole levels' [18]. This technique was used by Fathpour *et al* who demonstrated an infinite value of T_0 over a range from 5 to 75 °C [19].

Quantum-dot lasers are already capable of directly producing shorter pulses that any other diode based system and outperform quantum-well lasers in most areas with the exception of output power. The ultimate aim is for quantum-dot lasers to be capable of approaching the performance of vibronics lasers, such that when considered in conjunction with their small footprint and ability to be operated in turnkey configuration, they become the laser system of choice for a variety of applications. My experiments have helped to highlight some key issues related to achievement of this goal.

8.2. Nonlinear frequency conversion

The second part of my project concerned the selection of semiconductor material and structures that could be used for parametric nonlinear processes in the mid-infrared. This involved the design, manufacture and testing of novel quasi-phase-matched structures [20] and GaAs waveguides were fabricated with a periodically-switched nonlinearity created by ion implantation. The disappointing conclusion I reached was that it was not possible to simultaneously realise a waveguide having low optical losses and the necessary periodically-switched nonlinearity when using ion implantation.

During the course of my investigations into the nonlinear properties of GaAs, a new technology delivering re-orientated GaAs material emerged. This enabled the production of domain-inverted GaAs material with arbitrary inversion periods. Struck by the elegance of the technique and the impressive efficiencies it promised in simulation, this system was also investigated but considerable difficulties were encountered in implementing optimal epitaxial procedures for the fabrication of these structures. This was the fundamental limitation to our successful fabrication of a device of this type. Because epitaxial work was outsourced to collaborating institutions, this led to inevitable time delays, most notably when in the middle of my project the regrowth facility in Sheffield relocated to new premises resulting in a complete dismantling of their existing infrastructure.

My own conclusion from this is that, closer co-operation (possibly involving personnel exchange during important stages of fabrication) between partner institutions is vital to the success of this type of multi-stage, multi-disciplinary device production process. This is particularly the case when using non-standard materials and procedures. A fabrication process similar to that outlined below, performed in its entirety at one facility would therefore be the ideal case.

In the early stages of material growth, a thorough investigation of the epitaxial growth parameters leading to the production of orientation-patterned material is required. This will require the expertise of an epitaxial growth specialist. Once a successful process is established, definition of the inversion period grating can take place. It is important that this occurs under the close supervision of the epitaxial growth expert. This will ensure that at all times the semiconductor material is

maintained and conditioned optimally for subsequent regrowth. Overgrowth of the orientation patterned active region can then be performed, completing the epitaxial steps of the fabrication. Since the material has remained in the epitaxial facility, there will have been constant access to diagnostic equipment, ensuring the quality of the devices at every stage of the fabrication. Implementation of this sort of process should, given time lead to a dramatic improvement in the quality of devices produced.

Outlook

Semiconductor materials continue to provide ever more impressive efficiencies as fabrication techniques move towards maturity. Currently, several groups are investigating the sorts of bonding and polishing approaches outlined in Chapter 7, figure 7.26. These approaches are able to produce domain-inverted material without the need for non-polar buffer layers and represent a significant advance in the technological development [21, 22]. The lack of a buffer layer would allow this material to be patterned with ridge waveguides free from corrugations, drastically reducing the losses exhibited.

There is also the possibility of developing new semiconductor materials for nonlinear frequency conversion. An example of this is GaN. The wide transparency range of GaN makes it attractive for applications in the ultraviolet right through to the far infra-red and has already been implemented in an orientation patterned quasi-phase-matched configuration [23]. This is achieved in a similar way to that used in the fabrication of orientation patterned GaAs. In the case of GaN, an AlN buffer layer allows the growth of periodically-domain-inverted material.

Once a reliable, scalable technique has been developed which can produce low-loss material, the considerable advantages of GaAs and other semiconductor-based OPO systems such as high nonlinear coefficients, wide transparency and integrability will become more apparent to end users requiring such sources. This will open the door for orientation-patterned GaAs-based parametric devices to compete with and even replace the current breed of ferroelectric crystals as materials of choice in commercial systems.

The small footprints and inherently aligned nature of an all monolithic GaAs-based OPO device could also open up new opportunities for their implementation. Compact, ‘plug and play’ trace-gas detection kits could be of use for

instance in the search for fossil fuels or in the monitoring of pipes in petrochemical plants. In these environments, equipment needs to be able to function without continual optimisation and in an economic sense be deployed as is required at a modicum of expense.

Within this thesis I have reviewed the development of semiconductor-based materials and devices with a view to developing efficient new options that might offer some advantages over existing systems that are based on the well developed ferroelectric materials and solid-state laser gain media. Driving forces for investigations of this type include the integrability of and efficiencies obtainable through semiconductor devices.

The fact that semiconductor devices can be packaged in monolithic, ready to use configurations makes them ideal as reliable components in larger systems and also in situations where the deployment of currently existing ferroelectric-based devices would be impossible or impractical. Their monolithic nature and the fact that a semiconductor based system will comprise fewer components than equivalent alternative systems means that they are well suited to mass production. Where demand is present, this will allow a significant cost advantage for semiconductor-based solutions.

Further improvements in understanding of the underlying physics of this field will allow optimal utilisation of semiconductors in both new and existing applications, at the heart of a new class of compact, efficient devices.

References

1. Rafailov, E.U., A.D. McRobbie, M.A. Cataluna, L. O'Faolain, W. Sibbett, and D.A. Livshits. *Investigation of transition dynamics in a quantum-dot laser optically pumped by femtosecond pulses*. *LEOS annual meeting*. 2005, Paper ThN4. Sydney, Australia
2. Rafailov, E.U., A.D. McRobbie, M.A. Cataluna, L. O'Faolain, W. Sibbett, and D.A. Livshits, *Investigation of transition dynamics in a quantum-dot laser optically pumped by femtosecond pulses.* Applied Physics Letters, 2006. **88**(4).
3. Cataluna, M.A., W. Sibbett, D.A. Livshits, J. Weimert, A.R. Kovsh, and E.U. Rafailov, *Stable mode locking via ground- or excited-state transitions in a two-section quantum-dot laser.* Applied Physics Letters, 2006. **89**(8).
4. Kim, J., M.T. Choi, and P.J. Delfyett, *Pulse generation and compression via ground and excited states from a grating coupled passively mode-locked quantum dot two-section diode laser.* Applied Physics Letters, 2006. **89**(26).
5. Thompson, M.G., A. Rae, R.L. Sellin, C. Marinelli, R.V. Penty, I.H. White, A.R. Kovsh, S.S. Mikhrin, D.A. Livshits, and I.L. Krestnikov, *Subpicosecond high-power mode locking using flared waveguide monolithic quantum-dot lasers.* Applied Physics Letters, 2006. **88**(13).
6. Rafailov, E.U., M.A. Cataluna, W. Sibbett, N.D. Il'inskaya, Y.M. Zadiranov, A.E. Zhukov, V.M. Ustinov, D.A. Livshits, A.R. Kovsh, and N.N. Ledentsov, *High-power picosecond and femtosecond pulse generation from a two-section mode-locked quantum-dot laser.* Applied Physics Letters, 2005. **87**(8).
7. Cataluna, M.A., *Ultrashort-pulse generation from quantum-dot semiconductor diode lasers*, PhD Thesis, *School of Physics and Astronomy*. 2007, University of St Andrews: St Andrews.
8. McRobbie, A.D., M.A. Cataluna, S.A. Zolotovskaya, D.A. Livshits, W. Sibbett, and E.U. Rafailov. *All-quantum-dot based external cavity mode locked laser*. in *SIOE'07*. 2007. Session 1 quantum-dot devices, Talk 3,Cardiff, UK.
9. McRobbie, A.D., M.A. Cataluna, S.A. Zolotovskaya, D.A. Livshits, W. Sibbett, and E.U. Rafailov, *High power all-quantum-dot-based external cavity modelocked laser.* Electronics Letters, 2007. **43**(15): p. 812 - 813.
10. McRobbie, A.D., M.A. Cataluna, D.A. Livshits, W. Sibbett, and E.U. Rafailov. *High power all-quantum-dot based external cavity mode locked laser*. in *LEOS annual meeting*. 2006. Paper ThJ4, Montreal, Canada.
11. Cataluna, M.A., E.U. Rafailov, A.D. McRobbie, W. Sibbett, D.A. Livshits, and A.R. Kovsh, *Stable mode-locked operation up to 80 degrees C from an InGaAs quantum-dot laser.* IEEE Photonics Technology Letters, 2006. **18**(13-16): p. 1500-1502.
12. Cataluna, M.A., E.A. Viktorov, P. Mandel, W. Sibbett, D.A. Livshits, J. Weimert, A.R. Kovsh, and E.U. Rafailov, *Temperature dependence of pulse duration in a mode-locked quantum-dot laser.* Applied Physics Letters, 2007. **90**(10).
13. Laemmlin, M., G. Fiol, C. Meuer, M. Kuntz, F. Hopfer, A.R. Kovsh, N.N. Ledentsov, and D. Bimberg, *Distortion-free optical amplification of 20-80*

GHz modelocked laser pulses at 1.3 mu m using quantum dots. Electronics Letters, 2006. **42**(12): p. 697-699.

14. Choi, M.T., J.M. Kim, W. Lee, and P.J. Delfyett, *Ultralow noise optical pulse generation in an actively mode-locked quantum-dot semiconductor laser.* Applied Physics Letters, 2006. **88**: p. 131106.
15. Mi, Z. and P. Bhattacharya, *Analysis of the linewidth-enhancement factor of long-wavelength tunnel-injection quantum-dot lasers.* IEEE Journal of Quantum Electronics, 2007. **43**(5-6): p. 363-369.
16. Mi, Z., P. Bhattacharya, and S. Fathpour, *High-speed 1.3 mu m tunnel injection quantum-dot lasers.* Applied Physics Letters, 2005. **86**(15).
17. Asryan, L.V. and R.A. Suris, *Characteristic temperature of quantum dot laser.* Electronics Letters, 1997. **33**(22): p. 1871-1872.
18. Shchekin, O.B. and D.G. Deppe, *1.3 mu m InAs quantum dot laser with T-o=161 K from 0 to 80 degrees C.* Applied Physics Letters, 2002. **80**(18): p. 3277-3279.
19. Fathpour, S., Z. Mi, P. Bhattacharya, A.R. Kovsh, S.S. Mikhrin, I.L. Krestnikov, A.V. Kozhukhov, and N.N. Ledentsov, *The role of Auger recombination in the temperature-dependent output characteristics (T-0 = infinity) of p-doped 1.3 mu m quantum dot lasers.* Applied Physics Letters, 2004. **85**(22): p. 5164-5166.
20. Artigas, D., P. Loza-Alvarez, E.U. Rafailov, A.D. McRobbie, and W. Sibbett, *Design parameters of periodically switched nonlinear structures for efficient nonlinear processes*. OSA Trends in Optics and Photonics series Advanced Solid-State Photonics, 2005. I. Sorokina Ed., 98, p.86-91.
21. Li, J., D.B. Fenner, K. Termkoa, M.G. Allen, P.F. Moulton, C. Lynch, D.F. Bliss, and W.D. Goodhue. *Wafer-fused orientation-patterned GaAs*. in *Photonics west 07*. 2007. p 68750H, San Jose, California, USA: SPIE.
22. Oron, M.B., S. Shusterman, and P. Blau. *Periodically oriented GaAs templates and waveguide structures for frequency conversion*. *Photonics West 07*. 2007. p 68750F San Jose, California, USA
23. Chowdhury, A., H.M. Ng, M. Bhardwaj, and N.G. Weimann, *Second-harmonic generation in periodically poled GaN.* Applied Physics Letters, 2003. **83**(6): p. 1077-1079.

Appendix A

This program calculates period of the grating for Ion implanted PSN second-harmonic GaAs crystals

$\lambda := 2.318$

$$\mathrm{ngap}(\lambda) := \left[1 + 0.186\ln\left[\frac{\left[9\cdot(\lambda^2) - 1.537\right]}{2.039(\lambda^2) - 1.537} \right] + \left[\frac{39.194}{\left[9 - \frac{1.537}{(\lambda^2)}\right]} \right] + \left(\frac{136.08}{26.01 - \frac{1.537}{\lambda^2}} \right) + \left(\frac{0.00218}{0.00111 - \frac{1.537}{\lambda^2}} \right) \right]^{\frac{1}{2}}$$

This is the sellemeir equation for GaAs which calculates the refractive index of GaAs as a function of λ

$$\beta z1 := 2\cdot\frac{\pi}{\lambda}\cdot\mathrm{ngap}(\lambda)$$

$$\beta z2 := 2\cdot\frac{\pi}{\frac{\lambda}{2}}\cdot\mathrm{ngap}\left(\frac{\lambda}{2}\right)$$

$$\Delta Ko := \beta z2 - 2\cdot\beta z1$$

$$lc := \frac{\pi\cdot m}{\Delta Ko}$$

$lc = 4.997m$

$$\Delta n(\lambda) := \mathrm{ngap}\left(\frac{\lambda}{2}\right) - \mathrm{ngap}(\lambda)$$

$$\Lambda_{GaAs} := \frac{\lambda}{2\cdot\Delta n(\lambda)}$$

$\Lambda_{GaAs} = 9.994$

β is the wave vector, normally denoted by k. The subscripts z1 and z2 refer to the fundamental and second harmonic respectively

ΔKo is the wave vector mismatch

Λ is the grating period, determined by the interaction wavelength and the refractive index difference experienced by the fundamental and second harmonic

$\lambda := 2.241$

$$\beta z1 := 2\cdot\frac{\pi}{\lambda}\cdot\mathrm{ngap}(\lambda)$$

m is the order of phase matching. In this case, it is 1.

$$\beta z2 := 2\cdot\frac{\pi}{\frac{\lambda}{2}}\cdot\mathrm{ngap}\left(\frac{\lambda}{2}\right)$$

lc is thus the coherence length exhibited by a certain wave vector mismatch

$$\Delta Ko := \beta z2 - 2\cdot\beta z1$$

$$lc := \frac{\pi\cdot m}{\Delta Ko}$$

$lc = 4.456m$

The calculations below work out the coherence lengths required for a set of different fundamental wavelengths such that the fundamental and second harmonic wavelengths are phase matched in the QPM fashion i.e. this is not perfect phase matchng, rather, the sign of the nonlinear coefficient is reversed when the waves accumulate sufficient phase difference as to reverse the direction of the process.

$\lambda := 2.172$

$\beta z1 := 2\cdot\frac{\pi}{\lambda}\cdot ngap(\lambda)$

$\beta z2 := 2\cdot\frac{\pi}{\frac{\lambda}{2}}\cdot ngap\left(\frac{\lambda}{2}\right)$

$\Delta Ko := \beta z2 - 2\cdot\beta z1$

$lc := \frac{\pi\cdot m}{\Delta Ko}$

$lc = 4\,m$

$\lambda := 2.149$

$\beta z1 := 2\cdot\frac{\pi}{\lambda}\cdot ngap(\lambda)$

$\beta z2 := 2\cdot\frac{\pi}{\frac{\lambda}{2}}\cdot ngap\left(\frac{\lambda}{2}\right)$

$\Delta Ko := \beta z2 - 2\cdot\beta z1$

$lc := \frac{\pi\cdot m}{\Delta Ko}$

$lc = 3.854m$

$\lambda := 2.$

$\beta z1 := 2\cdot\frac{\pi}{\lambda}\cdot ngap(\lambda)$

$\beta z2 := 2\cdot\frac{\pi}{\frac{\lambda}{2}}\cdot ngap\left(\frac{\lambda}{2}\right)$

$\Delta Ko := \beta z2 - 2\cdot\beta z1$

$lc := \frac{\pi\cdot m}{\Delta Ko}$

$lc = 2.972m$

$\lambda := 2.45$

$\beta z1 := 2\cdot\frac{\pi}{\lambda}\cdot ngap(\lambda)$

$\beta z2 := 2\cdot\frac{\pi}{\frac{\lambda}{2}}\cdot ngap\left(\frac{\lambda}{2}\right)$

$\Delta Ko := \beta z2 - 2\cdot\beta z1$

$lc := \frac{\pi\cdot m}{\Delta Ko}$

$lc = 6.008m$

$\lambda := 2.5675$

$\beta z1 := 2\cdot\frac{\pi}{\lambda}\cdot ngap(\lambda)$

$\beta z2 := 2\cdot\frac{\pi}{\frac{\lambda}{2}}\cdot ngap\left(\frac{\lambda}{2}\right)$

$\Delta Ko := \beta z2 - 2\cdot\beta z1$

$lc := \frac{\pi\cdot m}{\Delta Ko}$

$lc = 7\,m$

$\lambda := 2.6765$

$\beta z1 := 2\cdot\frac{\pi}{\lambda}\cdot ngap(\lambda)$

$\beta z2 := 2\cdot\frac{\pi}{\frac{\lambda}{2}}\cdot ngap\left(\frac{\lambda}{2}\right)$

$\Delta Ko := \beta z2 - 2\cdot\beta z1$

$lc := \frac{\pi\cdot m}{\Delta Ko}$

$lc = 8.002m$

Program calculates coherence length and participating wavelengths in PSN OPG GaAs crystal

$L := 500$ mkm — L is the crystal length

$d := 3.4$ — d is the coherence length

$\Delta := 2 \cdot d$ — Δ is the grating period which is twice the coherence length

$m := 1$ — m is the order of QPM

$i := 0..150$ $\quad j := 0..500$ — i goes from 0 to 150, j goes from 0 to 500

$\lambda p_i := 0.95 + \frac{i}{1000}$

The signal wavelength begins at 1.2

$\lambda s_j := 1.2 + \frac{j}{100}$

p is pump, s is signal i is idler

$\lambda i_{i,j} := \frac{(\lambda s_j \cdot \lambda p_i)}{(\lambda s_j - \lambda p_i)}$

$\lambda p_{114} = 1.064$ — i = 114 correponds to a pump wavelength of 1064 nm

$\lambda i_{0,0} = 4.56$

The idler is 4.56 microns when the pump is 0.95 and the signal is 1.2

$\beta zg := \frac{2 \cdot \pi \cdot m}{\Delta}$

βzg is the grating vector - which is the extra wave vector needed for QPM since we are not perfectly phase matched here. Δ is the grating period which is 2x the coherence length

$$ngap_i := \left[1 + 0.186 \cdot \ln\left[\frac{\left[9 \cdot (\lambda p_i \cdot \lambda p_i) - 1.537\right]}{2.039 \cdot (\lambda p_i \cdot \lambda p_i) - 1.537}\right] + \left[\frac{39.194}{\left[9 - \frac{1.537}{(\lambda p_i \cdot \lambda p_i)}\right]}\right] + \left(\frac{136.08}{26.01 - \frac{1.537}{\lambda p_i \cdot \lambda p_i}}\right) + \left(\frac{0.00218}{0.00111 - \frac{1.537}{\lambda p_i \cdot \lambda p_i}}\right)\right]^{\frac{1}{2}}$$

$$ngas_j := \left[1 + 0.186 \cdot \ln\left[\frac{\left[9 \cdot (\lambda s_j \cdot \lambda s_j) - 1.537\right]}{2.039 \cdot (\lambda s_j \cdot \lambda s_j) - 1.537}\right] + \left[\frac{39.194}{\left[9 - \frac{1.537}{(\lambda s_j \cdot \lambda s_j)}\right]}\right] + \left(\frac{136.08}{26.01 - \frac{1.537}{\lambda s_j \cdot \lambda s_j}}\right) + \left(\frac{0.00218}{0.00111 - \frac{1.537}{\lambda s_j \cdot \lambda s_j}}\right)\right]^{\frac{1}{2}}$$

$$ngai_{i,j} := \left[1 + 0.186 \cdot \ln\left[\frac{\left[9 \cdot (\lambda i_{i,j} \cdot \lambda i_{i,j}) - 1.537\right]}{2.039 \cdot (\lambda i_{i,j} \cdot \lambda i_{i,j}) - 1.537}\right] + \left[\frac{39.194}{\left[9 - \frac{1.537}{(\lambda i_{i,j} \cdot \lambda i_{i,j})}\right]}\right] + \left(\frac{136.08}{26.01 - \frac{1.537}{\lambda i_{i,j} \cdot \lambda i_{i,j}}}\right) + \left(\frac{0.00218}{0.00111 - \frac{1.537}{\lambda i_{i,j} \cdot \lambda i_{i,j}}}\right)\right]^{\frac{1}{2}}$$

These are the sellemeir equations for GaAs for the pump, signal and idler

$$\beta zp_i := 2\cdot\frac{\pi}{\lambda p_i}\cdot ngap_i$$

$$\beta zs_j := 2\cdot\frac{\pi}{\lambda s_j}\cdot ngas_j$$

$$\beta zi_{i,j} := 2\cdot\frac{\pi}{\lambda i_{i,j}}\cdot ngai_{i,j}$$

β is the wave vector which would normally be called k. Again, p s and i denote pump signal and idler, so βzpi is the wave vector associated with the pump with the subscript i.

$$\Delta Ko_{i,j} := \beta zp_i - \beta zs_j - \beta zi_{i,j}$$

$\Delta Koi,,j$ is the wave vector mismatch

$$\Delta K_{i,j} := \Delta Ko_{i,j} - \beta zg$$

$\Delta Ki,j$ is the wave vector mismatch with the grating period taken into account - setting up the QPM

$$lc_{i,j} := \frac{\pi\cdot m}{\Delta Ko_{i,j}}$$

lci,j is the coherence length

$$PM_{i,j} := \left(\frac{\sin\left(\frac{\Delta K_{i,j}\cdot L}{2}\right)}{\frac{\Delta K_{i,j}\cdot L}{2}}\right)^2$$

This is the phase matching sinc equation.

$\lambda i_{114,20} = 4.433$

$\lambda i_{114,30} = 3.661$

$\lambda i_{114,45} = 2.996$

$\lambda i_{114,60} = 2.602$

$\lambda i_{114,10} = 5.861$

$\lambda i_{114,5} = 7.151$

$\lambda i_{114,4} = 7.496$

$\lambda i_{114,1} = 8.818$

$lc_{114,20} = 4.96$

$lc_{114,30} = 4.436$

$lc_{114,45} = 4.032$

$lc_{114,60} = 3.839$

$lc_{114,10} = 5.979$

$lc_{114,5} = 6.909$

$lc_{114,4} = 7.157$

$lc_{114,1} = 8.092$

$\lambda p_{114} = 1.064$

j = 20 corresponds to a signal wavelength of 1400 nm
j = 30 is 1500 nm
j=45 is 1650 nm
j=60 is 1800 nm
j=10 is 1300 nm
j=5 is 1250 nm
j=4 is 1240 nm
j=1 is 1210 nm

These calculated coherence lengths correspond to those from figure 7.5